

THERMOMECHANICAL PROCESSING, ADDITIVE MANUFACTURING AND
ALLOY DESIGN OF HIGH STRENGTH MG ALLOYS

Sivanesh Palanivel

Dissertation Prepared for the Degree of
DOCTOR OF PHILOSOPHY

UNIVERSITY OF NORTH TEXAS

May 2016

APPROVED:

Rajiv S. Mishra, Major Professor

Rajarshi Banerjee, Committee Member

Marcus L. Young, Committee Member

Sundeeep Mukherjee, Committee Member

Kevin J. Doherty, Committee Member

Andrey Voevodin, Chair of the Department of

Materials Science and Engineering

Costas Tsatsoulis, Dean of the College of Engineering

Costas Tsatsoulis (interim), Dean of the Toulouse Graduate School

Palanivel, Sivanesh. *Thermomechanical Processing, Additive Manufacturing and Alloy Design of High Strength Mg Alloys*. Doctor of Philosophy (Materials Science and Engineering), May 2016, 205 pp., 18 tables, 59 figures, references, 25 titles.

Mg-Y-Nd alloys have been promising due to their ability to form strengthening precipitates on the prismatic plane. In this dissertation, these terminologies are discussed in detail. A simple calculation showed that the microstructural efficiency in Mg-4Y-3Nd alloy is 30% of its maximum potential. Guided by the definitions of alloying and microstructural efficiency, the two prime objectives of this thesis were to: (i) to use thermomechanical processing routes to tailor the microstructure and achieve high strength in an Mg-4Y-3Nd alloy, and (ii) optimize the alloy chemistry of the Mg-rare earth alloy and design a novel rare—earth free Mg alloy by Calphad approach to achieve a strength of 500 MPa. Experimental, theoretical and computational approaches have been used to establish the process-structure-property relationships in an Mg-4Y-3Nd alloy. In addition, the investigation on the interaction between dislocations and strengthening precipitate revealed that, specific defects like the I_1 fault aid in the accelerated precipitation of the strengthening precipitate in an Mg-4Y-3Nd alloy. Also, the effect of external field (ultrasonic waves) was studied in detail and showed accelerated age hardening response in Mg-4Y-3Nd alloy by a factor of 24. As the bottleneck of low strength is addressed, the answers to the following questions are discussed in this dissertation: What are the fundamental micro-mechanisms governing second phase evolution in an Mg-4Y-3Nd alloy? Is defect engineering critical to achieve high strength Mg alloys? Can application of an external field influence the age hardening response in an Mg-4Y-3Nd alloy? Can a combination of innovative processing for tailoring microstructures and computational alloy design lead to new and effective paths for application of magnesium alloys?

Copyright 2016

by

Sivanesh Palanivel

ACKNOWLEDGEMENTS

Reaching the finish line in a doctoral degree is a self-gratifying experience. Though, only my name appears on the cover page, this dissertation would not have been possible without the selfless support extended by my advisor, sponsors, family, colleagues, and friends. First and foremost, I would like to extend my deep sense of gratitude to my advisor, Dr. Rajiv S. Mishra. I am grateful to him for not only providing me the opportunity to work with him but also for pushing me towards the unknown space most of the times. I would also like to thank Mrs. Mishra for her care and affection. Thanks for the beautiful memories.

If this dissertation has reached this stage, it is primarily because of the ARL team (Dr. Raymond Brennan, Dr. Kevin Doherty, and Dr. Kyu C. Cho). I would like to thank each of them for their financial support and also for the invaluable discussions during the course of my PhD. Special thanks to Mr. Yuri Hovanski and Dr. K.K Sankaran for their constant encouragement. I would also like to thank my committee members for their valuable time during my PhD.

I would also like to acknowledge all the MTSE faculty and staff for their help. In addition, much of this dissertation was possible due to the useful discussions and help from colleagues and friends. I would like to thank them all. Special thanks to Swetha, Vikram, Ramakrishna, Pratyush and Aditya for their continued support throughout my PhD. I would also like to thank my undergraduate friends, teachers and mentors who have played an important role towards my choice of pursuing a doctorate.

Last, but not the least, thank you Mom, Dad and Chintu (brother) for the love, affection, and care that you have always showered on me. If not for all of your sacrifices, I'd be nowhere near where I am. I am indebted to you forever. Thanks everyone. It has been a memorable journey!

TABLE OF CONTENTS

| | |
|---|-----|
| ACKNOWLEDGEMENTS..... | iii |
| LIST OF TABLES..... | ix |
| LIST OF FIGURES..... | xi |
| CHAPTER 1: BACKGROUND AND MOTIVATION..... | 1 |
| 1.1 Introduction..... | 1 |
| 1.2 Concepts of ‘Alloying Efficiency’ and ‘Microstructural Efficiency’ from the Perspective of Strength..... | 4 |
| 1.3 Brief Description on the Deformation Modes and Precipitate Descriptors in WE43 Alloy...6 | |
| 1.4 References..... | 8 |
| CHAPTER 2: EFFECT OF PROCESSING PARAMETERS ON THE MICROSTRUCTURAL EVOLUTION AND JOINT EFFICIENCY OF A WE43 ALLOY DURING FRICTION STIR PROCESSING..... | 9 |
| 2.1 Introduction..... | 9 |
| 2.2 Experimental Details..... | 11 |
| 2.3 Results and Discussion..... | 13 |
| 2.3.1 Initial Microstructure: T5 Temper (As rolled +Aged) | 13 |
| 2.3.2 Friction Stir Welding (FSW)..... | 14 |
| 2.3.3 Mechanical Properties and PWHT (Post Weld Heat Treatment)..... | 19 |
| 2.4 Conclusions..... | 20 |
| 2.5 References..... | 20 |

| | |
|--|----|
| CHAPTER 3: EFFECT OF INITIAL MICROSTRUCTURE ON THE MICROSTRUCTURAL EVOLUTION AND NUGGET EFFICIENCY OF A WE43 ALLOY DURING FRICTION STIR WELDING..... | 24 |
| 3.1 Experimental Details..... | 24 |
| 3.2 Results and Discussion..... | 26 |
| 3.2.1 Path Dependent Microstructural Evolution during Rolling..... | 26 |
| 3.2.2 Effect of Initial Microstructure on the Nugget Efficiency after FSW..... | 31 |
| 3.2.3 Strain Rate Sensitivity of Rolled WE43 Alloy..... | 40 |
| 3.3 Conclusions..... | 42 |
| 3.4 References..... | 44 |
| CHAPTER 4: FRICTION STIR ADDITIVE MANUFACTURING OF MG-4Y-3Nd ALLOY FOR HIGH STRUCTURAL PERFORMANCE THROUGH MICROSTRUCTURAL CONTROL..... | 45 |
| 4.1 Introduction..... | 45 |
| 4.1.1 Current Metal based Additive Manufacturing Techniques and Key Challenges..... | 45 |
| 4.1.2 Structural Performance: Future of Additive Manufacturing..... | 48 |
| 4.1.3 Mg alloys: Lightweighting for Structural Applications..... | 49 |
| 4.2 Process Description and Experimental Procedure..... | 50 |
| 4.3 Results and Discussion..... | 55 |
| 4.3.1 Nugget Macrostructure and the Effect of Welding Parameter on the Formation of Defects..... | 55 |
| 4.3.2 Banding and its Origin..... | 60 |

| | | |
|--|---|-----|
| 4.3.3 | Peak Temperature, Strain Rate and Zener-Hollomon Parameter..... | 67 |
| 4.3.4 | Effect of Welding Parameter on the Mechanical Properties of a Built Structure.. | 71 |
| 4.4 | Characterization of Interfacial and Non-Interfacial Microstructures..... | 77 |
| 4.5 | Conclusions..... | 96 |
| 4.6 | References..... | 97 |
| CHAPTER 5: A FRAMEWORK FOR SHEAR DRIVEN DISSOLUTION OF THERMALLY STABLE PARTICLES DURING FRICTION STIR WELDING/PROCESSING..... | | 107 |
| 5.1 | Introduction..... | 107 |
| 5.2 | Experimental and Computational details..... | 109 |
| 5.3 | Results and Discussion..... | 111 |
| 5.4 | Conclusions..... | 124 |
| 5.5 | References..... | 125 |
| CHAPTER 6: DISLOCATION TYPES AND CONFIGURATION IN A FRICTION STIR PROCESSED Mg-4Y-3Nd ALLOY..... | | 129 |
| 6.1 | Introduction..... | 130 |
| 6.2 | Experimental Methods..... | 131 |
| 6.3 | Results and Discussion..... | 133 |
| 6.3.1 | Room Temperature Stress-Strain Curve and Peak Temperature during FSP..... | 134 |
| 6.3.2 | Dislocation Structures after FSP..... | 135 |
| 6.4 | Conclusions..... | 141 |
| 6.5 | References..... | 142 |
| CHAPTER 7: DISLOCATION MEDIATED PRECIPITATION IN A FRICTION STIR PROCESSED Mg-4Y-3Nd ALLOY..... | | 144 |

| | |
|--|-----|
| 7.1 Introduction..... | 144 |
| 7.2 Experimental Procedures..... | 146 |
| 7.3 Results and Discussion..... | 147 |
| 7.3.1 Strength and Ductility in Friction Stir Processed and Aged Conditions..... | 147 |
| 7.3.2 Defect Mediated Precipitation..... | 149 |
| 7.3.2.1 β_1 Nucleation on the I_1 Stacking Fault..... | 152 |
| 7.3.2.2 Nucleation of Precipitate on $\langle c+a \rangle$ Dislocations..... | 156 |
| 7.4 Conclusions..... | 158 |
| 7.5 References..... | 159 |
| CHAPTER 8: ENHANCED AGE HARDENING RESPONSE IN A WE43 ALLOY BY IN-SITU ULTRASONIC AGING..... | 162 |
| 8.1 Introduction..... | 162 |
| 8.2 Experimental Details..... | 163 |
| 8.3 Results and Discussion..... | 165 |
| 8.3.1 Effect of Power and Sonication Time on the Age Hardening Response of WE43 Alloy..... | 165 |
| 8.3.2 Microstructure of the Ultrasonically Aged Specimen..... | 168 |
| 8.3.3 Conceptual Thermodynamic and Kinetic Hypothesis for Accelerated Age Hardening Response under the Influence of Sound Waves..... | 171 |
| 8.4 Conclusions..... | 173 |
| 8.5 References..... | 174 |
| CHAPTER 9: COMPUTATIONAL DESIGN OF HIGH STRENGTH LOW ALLOY MAGNESIUM ALLOYS..... | 176 |

| | |
|---|-----|
| 9.1 Introduction..... | 176 |
| 9.1.1 Microstructural Efficiency of WE43 Alloy..... | 178 |
| 9.2 Background: Formation of β_1 Precipitate from α —Mg Solid Solution and the Concept of Microalloying..... | 179 |
| 9.3 Theoretical Methodology: Thermo-Physical-Structure-Kinetic Approach to Select Microalloying Elements for Design and Optimization of WE43 Alloy..... | 183 |
| 9.4 Computational Design to Achieve High Strength Mg Alloys..... | 189 |
| 9.4.1 Basic Principle of Calphad Based Approach..... | 189 |
| 9.4.2 Computed Mg-rare Earth Alloy Space Based on Strength and Cost Considerations..... | 190 |
| 9.4.3 Design of a Cheaper Mg-Al-Ca Alloy for High Strength..... | 194 |
| 9.5 Conclusions..... | 195 |
| 9.6 References..... | 196 |
| CHAPTER 10: CONCLUDING REMARKS AND FUTURE DIRECTIONS..... | 198 |
| LIST OF RELATED PUBLICATIONS..... | 205 |

LIST OF TABLES

| | |
|--|-----|
| Table 1.1. Precipitation sequence in WE43..... | 7 |
| Table 2.1. Equations for process parameters based calculations..... | 15 |
| Table 2.2. Summary of process parameter based calculations..... | 16 |
| Table 3.1. Comparison of mechanical properties and the microstructural characteristics as a function of rolling history..... | 30 |
| Table 4.1. Key potential benefits of friction stir additive manufacturing as compared to ultrasonic additive manufacturing and fusion based additive techniques..... | 51 |
| Table 4.2. Summary of the tool dimensions and estimated material specific variables to compute the peak temperature..... | 68 |
| Table 4.3. Summary of welding parameter based calculations during FSAM..... | 71 |
| Table 4.4. Experimentally and empirically determined parameters after tensile deformation... | 77 |
| Table 4.5. Summary of EDS results from Fig 10 (a) | 78 |
| Table 4.6. Location specific grain size distribution in the 1400/102 build manufactured by FSAM..... | 89 |
| Table 4.7. Location specific Schmid factor of basal and non-basal slip system having two different tensile directions..... | 95 |
| Table 6.1. g.b values for selected reflections (g) in an hcp metal..... | 132 |
| Table 7.1. Summary of tensile properties from Figure 1..... | 148 |
| Table 8.1. Comparison of age hardening response between conventionally aged and ultrasonically aged specimen..... | 167 |
| Table 9.1. Theoretical screening of potential microalloying elements for the design of high strength Mg alloys..... | 186 |

| | |
|--|-----|
| Table 9.2. Ranking the microalloying additions on the basis of crystallographic and thermodynamic criterion for the nucleation of β_1 precipitate a Mg-rare earth alloy..... | 187 |
| Table 9.3. Theoretically predicted vs. experimentally observed effect of trace elements in a few Mg alloys. Note that the effect of predicted elements is in good agreement with experiments.. | 188 |
| Table 9.4. Summary of the computed mass fractions of different phases for WE43 and predicted alloy from Figure 6..... | 192 |

LIST OF FIGURES

| | |
|---|----|
| Figure 1.1. A comprehensive chart showing the strength in the current Mg alloys. Note that high strength Mg alloys with a value greater than 350 MPa are rapidly solidified. Strength achieved in cast WE43 is 200 MPa and is a low value. Furthermore, strength achieved by wrought processes is also limited to ~300 MPa [3-10]. | 2 |
| Figure 1.2. Current standing of Mg and Al alloys in terms of strength [11]. | 4 |
| Figure 1.3. Schematic diagrams showing (a and b) effects of the orientation of precipitate plates on interparticle spacing for dislocation slip on basal plane of the magnesium matrix phase (taken from Nie [11]). This can be extended to discuss the microstructural efficiency. | 6 |
| Figure 2.1. (a) Scanning electron (SE) micrograph depicting shear localization and precipitation gradients (b) Back scattered electron (BSE) micrograph showing cuboidal $Mg_2YZr_{0.3}$ and plate shaped $Mg_{41}Nd_5Zr$ intermetallics. | 14 |
| Figure 2.2 EBSD micrographs of (a) 600/102, (b) 800/102 and (c) IPF color code. | 17 |
| Figure 2.3. SEM micrographs of different conditions; (a) AR+T5 (210 °C/48h), (b) 600/102 SZ, (c) 600/102 TMAZ, (d) 800/102 SZ, (e) 800/102 TMAZ. | 18 |
| Figure 2.4. Microhardness data for as processed and PWHT samples. | 19 |
| Figure 3.1(a) Schematic illustration of friction stir welding. (b) Tool used in the current study. | 25 |
| Figure 3.2. Path dependent microstructural and strength evolution in a WE43 alloy. Note that alloy numbering through 1-4 is representative of different rolling reductions of a WE43 alloy. | 27 |
| Figure 3.3. (a) SEM micrograph of alloy 1 showing the extent of inhomogeneity, and (b) enlarged image of the circled portion in (a). Diffraction pattern is shown in the inset and corresponds to extremely fine grains, (c) HAADF-STEM image showing coarsened precipitates in the size range of 100-150 nm. These images have been recorded after peak aging at 180°C for | |

| | |
|---|----|
| 60 hours. | 28 |
| Figure 3.4. (a & b) Precipitate descriptors in alloy 4 after peak aging at 180°C for 60 hours. | 30 |
| Figure 3.5. (a, b & c). Influence of initial microstructure on the mechanical properties during friction stir welding at 2000 rpm and 102 mm/min. The initial microstructures were in their peak aged condition. Post weld aging treatment was performed after FSW for further strengthening. Peak aging was done for all the conditions at 180°C for 60 hours. | 32 |
| Figure 3.6. $\langle 0001 \rangle$, $\langle 10 \bar{1} 0 \rangle$ and $\langle 11 \bar{2} 0 \rangle$ pole figures of (a) alloy 1 (ARA), (b) alloy 4 (ARA), (c) alloy 1 (FSWA) and (d) alloy 4 (FSWA). | 35 |
| Figure 3.7. Yield anisotropy factor calculated by using the TSL-OIM software for alloy 1 after FSW at 2000 rpm and 102 mm/min (2000/102). (a) cluster showing higher tendency of basal slip, and (b) cluster showing higher tendency of non-basal slip. | 36 |
| Figure 3.8. Hardness profiles across the centerline in the Y-Z plane for specimen welded at (a) 700/102 and (b) 2000/102. | 37 |
| Figure 3.9. Effect of process parameters on the strength and ductility of (a) alloy 3, (b) alloy 4. | 38 |
| Figure 3.10. HAADF-STEM images showing the precipitate descriptors after FSW for alloy 4 welded at (a) 700/102, (b) 2000/102. Bright field images showing (c) higher amount of retained dislocation density in a sample welded at 2000/102, (d) the diffracting grain with the image recorded parallel to $[0001]$ and (e) diffraction pattern showing the orientation relationship of the coarsened precipitates with the matrix. These precipitates are found to the equilibrium β precipitates (Mg_{12}NdY) with an orientation relationship of $[0001]_{\alpha} // [1-1-2]_{\beta}$ and $(-111)_{\alpha} // (10-10)_{\beta}$ | 40 |
| Figure 3.11. Strain rate jump test in the ARA condition for (a) alloy 3, (b) alloy 4. Effect of rate of loading on the tensile properties in, (c) alloy 4. | 41 |

| | |
|--|----|
| Figure 4.1. Temporal evolution of metal based additive technologies and a listing of key challenges [3-9]. | 47 |
| Figure 4.2. (a) Schematic illustration of the friction stir additive manufacturing (FSAM) process. Note that the build direction is perpendicular to the welding direction. (b) Photograph and dimensions of the tool used in the current study. | 52 |
| Figure 4.3. Defects in the 1400 /102 build specimen. The TMAZ-base metal interface at the bottom-right of the picture shows debonding. | 56 |
| Figure 4.4. Transverse section macrograph of the friction stir welded build structures manufactured at (a) 1400/102, and (b) 800/102 specimens. Dashed horizontal white lines represent the original interface positions/locations. | 56 |
| Figure 4.5. Forge forces, during the welding of the different interfacial lap joints, plotted against the distance along the weld line. | 58 |
| Figure 4.6. Spatial dependence of material flow and the microstructural features for a build manufactured at 1400 rpm and 102mm/min using FSAM. | 61 |
| Figure 4.7. (a) Cyclic variation in the microstructure at 800/102, (b) Band spacing and the difference in precipitation density, (c) Chemical composition of the marked positions in (b) by EDS. | 62 |
| Figure 4.8. (a) Spatial variation of strain across the pin diameter. Spatial periodicity and variation of the traverse force(x) and the spindle torque over the welding distance for a build manufactured at (b) 800/102 and (c) 1400/102. To be in line with the observed micrographs in Fig 6 & 7, these process responses have been plotted for the stacking of the third layer and hence are representative of layer 2-3 interface. | 66 |
| Figure 4.9. Hardness profiles along the build direction of (a) 800/102 stack, and (b) 1400/102 | |

stack. The vertical line is representative of the hardness in the base material after aging and corresponds to 97HV. (c) Comparison between the uniaxial tensile stress-strain curves of the rolled and 1400/102 stack after aging, (d) work hardening behavior of the ARA sheet and build manufactured at 1400/102, and (e) net flow stress vs true strain to evaluate the strain hardening exponent. Testing was done parallel to the rolling/welding direction.75

Figure 4.10. SEM micrographs showing, (a) Mg_2Y intermetallic cluster in the rolled state with their compositions tabulated in Table 4, (b) necklace structure along the grain boundaries after aging, (c) HAADF - STEM micrograph of the inset in (b) representative of the inhomogeneity in the rolled and aged condition.78

Figure 4.11. BSE images showing distribution of precipitates in (a) layer 4, (b) layer 3-4 interface, (c) two-pass region in layer3, (d) one pass region in layer 3, (e) layer 2-3 interface, (f) layer 1-2 interface and (g) layer 1. The examined regions have been annotated in the legend adjacent to these micrographs. EDS results for the grain boundary precipitates in Figure (d & g) have been shown in (h).81

Figure 4.12 (a, b and c). HAADF-STEM images showing the precipitate descriptors after FSAM at interface 2. These images have been recorded after peak aging at 180°C for 60 hours.83

Figure 4.13 (a, b). HAADF-STEM images showing the precipitate descriptors at the bottom layer after FSAM. (c) Enlarged image of the location shown in (b). (d) A typical dark field micrograph obtained from the local area in figure (c). The reflection corresponding to the image has been marked in the diffraction pattern shown in the inset. Images were recorded parallel to [01-10]. These images have been obtained after peak aging at 180 °C for 60 hours. Note that the examined region corresponds to the highest hardness and strength of 400 MPa.86

Figure 4.14. IPF maps depicting the distribution of grains in (a) layer 4, (b) layer 3-4 interface,

(c) layer 1 corresponding to the tensile curve, and (d) thermo mechanically affected zone (TMAZ). The dark black lines and the faint white lines represent the high angle (HAGB) and low angle grain boundaries (LAGB). These analyzed regions have been annotated in the legend adjacent to these micrographs. Color correspondence scale and the sample coordinate system have been shown in (e) & (f).88

Figure 4.15. Back scattered electron (BSE) images showing, (a) bottom layer and (b) interface for a build manufactured using 800 rpm and 102 mm/min.90

Figure 4.16. $\langle 0001 \rangle$, $\langle 10\bar{1}0 \rangle$ and $\langle 11\bar{2}0 \rangle$ pole figures of (a) shoulder affected layer 4 (top), (b) layer 3-4 interface, (c) pin affected layer 1 (bottom) and (d) thermo mechanically affected zone (TMAZ) after FSAM.92

Figure 4.17. Schematic illustration of the crack propagation path along the trace of the basal plane at the nugget-TMAZ interface.94

Figure 5.1. Back scattered electron images show thermally stable Mg_2Y intermetallics in (a) rolled, and (b) solutionised conditions. FSP leads to (c) dissolution of the intermetallic phase on the advancing side, and (d) fragmentation on the retreating side. (e) Predicted thermal cycle by numerical model shows lower peak temperature ($435^\circ C$) and shorter times for diffusion in comparison to solutionising treatment.112

Figure 5.2. Theoretical model showing the basic mechanisms that dissolve particles during FSW/FSP.113

Figure 5.3. (a) Velocity profile and streamline used for computation of strain and strain rates during FSW/FSP, (b) calculated value of effective strain on Mg_2Y particle using Eqs (5, 6), and (c, d) computed strain and strain rate components on the particle situated at a distance of $60\ \mu m$ from the pin surface within the shear layer.116

| | |
|---|-----|
| Figure 5.4. Schematic plot showing 2-D geometric straining of the Mg_2Y particle around the surface of the pin during FSW/FSP. The strain values are quantified at selected positions for a process parameter of 800 rpm and 102 mm/min. These positions can be cross-referenced with Figure 3(a) to enhance understanding. Negative sign of the strain value indicates that the particle is under compression. | 118 |
| Figure 5.5. (a) Evolution of mobile and immobile dislocation density with strain calculated using Eqs. (5-8). (b) Processing strain captured in the form of high dislocation density in an Mg-4Y-3Nd alloy, (c) Departure side pinning supporting the mechanism of interfacial transport of solute atoms, and (d) Number of dislocations arriving at the particle, and solute atoms dissolving away from Mg_2Y as a function of strain. | 121 |
| Figure 6.1. (a) Room temperature uniaxial tensile stress-strain curves of a friction stir processed specimen, and (b) computed thermal cycle in the shear layer during FSP. | 133 |
| Figure 6.2. (a) Typical dislocation density in a friction stir processed specimen, (b) high density of $\langle c \rangle$ or $\langle c+a \rangle$ dislocations visible using $g=0002$ reflection, and (c) $\langle a \rangle$ type helical screw dislocations formed by absorption of vacancies during processing. | 134 |
| Figure 6.3. Weak beam dark field images recorded for an area using $g = 0002$ and $g = \bar{1}2\bar{1}0$ near $[10\bar{1}0]$ zone axis in a friction stir processed WE43 alloy showing (a) a mixture of I_1 stacking fault and $\langle c \rangle$ dislocations, and (b) the presence of basal $\langle a \rangle$ dislocations and I_2 stacking fault near I_1 fault. Note the possible nucleation of pyramidal $\langle c+a \rangle$ dislocation at the I_1 fault. | 135 |
| Figure 6.4. (a) Selected grain for analysis of dislocation substructure after FSP. (b-g) Detailed investigation of the Burgers vector using two beam imaging conditions show dissociation and formation of $\langle c+a \rangle$ to/from $\langle c \rangle$ and $\langle a \rangle$ dislocations. Investigated area is enclosed in a square box and enlarged in the inset of respective micrographs. Solid arrows in the inset point towards | |

the nodes and the dashed arrow shows grain boundary nucleation of $c+a$, and (h) a schematic of the dislocation reactions contained within enclosed square highlighted in the TEM image....138

Figure 7.1. Age hardening response of an Mg-4Y-3Nd after friction stir processing. Note that the strength increases at a faster rate for the first eight hours from 208 to 268 MPa. Further aging leads to minimal rise in strength and a compromise in ductility.148

Figure 7.2. (a, b) Heterogeneous nucleation of β_1 precipitates on dislocations, (c, d) Micrograph at later stages after pinching off showing well aligned array of β_1 precipitates (e) Diffraction pattern of the micrograph in (d) recorded along the $[01\bar{1}1]$ zone axis showing superlattice reflections arising from β_1 precipitates.150

Figure 7.3. (a) Hexagonal network formed by the reactions between $a/3 \langle 11\bar{2}0 \rangle$ type screw dislocations, (b) Formation of β_1 precipitates on these individual dislocation lines as confirmed by the (c) diffraction pattern recorded along the $[10\bar{1}0]$ zone axis. (d) shows the six orientation variants resulting from three correspondence variants.151

Figure 7.4 (a-d). Weak beam dark field images recorded with a series of two beam conditions showing the presence of an I_1 stacking fault bounded by a pyramidal Frank partial. The arrows point towards the same position in the above micrographs. Note that the feature is invisible in (d) which highlights the dark field image captured using $g = [1\bar{2}12]$ reflection, as well as (e) selected area diffraction (SAD) patterns recorded parallel to $[10\bar{1}0]$ of α -Mg, showing β_1 spots generated within the I_1 stacking fault.154

Figure 7.5. A schematic showing the driving force to nucleate β_1 on I_1 basal stacking fault. Note that the fault is terminated by a sessile Frank partial dislocation. Each individual layer/plane has been color coded.155

| | |
|--|-----|
| Figure 7.6 (a-c). Dark field images captured using two beam conditions, with the highlighted arrows pointing towards a $\langle c+a \rangle$ dislocation (d) a diffraction pattern recorded parallel to the $[10\bar{1}0]$ zone axis confirming nucleation of unidentified precipitate on the dislocation with a Burgers vector of $1/3 \langle 11\bar{2}3 \rangle$ (e) an inset displaying the region of SAD aperture centering. ... | 157 |
| Figure 8.1. Custom built in-situ ultrasonic aging set up for studying the age hardening response of a WE43 alloy under the influence of sound waves. | 164 |
| Figure 8.2. Effect of ultrasonic power on the age hardening response of a WE43 alloy for a sonication time interval of (a) 60 s, (b) 30 s, and (c) 15 s. Note that increasing the power from 100 W to 400 W accelerates the time to peak hardness. Furthermore, decreasing the sonication time from for 60 seconds to 30 seconds accelerates the hardening response. | 166 |
| Figure 8.3. (a) TEM micrograph of as processed specimen showing a cleaner matrix with the absence of strengthening precipitates. TEM micrographs tracking the evolution of microstructure for a specimen aged at 210°C using a power of 400 W after (b) 15 minutes of aging showing pockets rich in Nd, (c, d) 30 minutes of aging showing the formation of hexagonal networks and Nd rich regions, (d) 60 minutes of aging showing well aligned β_1 precipitates. Note that the inset in (d) labelled as (e) corresponds to the dashed square and shows well grown β_1 precipitates with a plate diameter of 50 nm. This is further confirmed from the diffraction pattern in (f) which shows bright superlattice reflections emerging from (e). (g) shows a high number density of well aligned precipitates after ultrasonic aging for two hours. Note the accelerated nucleation and growth of the β_1 precipitates under the influence of ultrasonic stress which otherwise takes 48 hours to reach peak aged condition during conventional aging. | 170 |
| Figure 8.4. Stress wave induced transportation of solute enhancing the diffusional rate and hence the precipitation kinetics. | 172 |

| | |
|--|-----|
| Figure 8.5. (a) Effect of stress on G-X plot of a binary AB alloy (b) Correlation of growth kinetics to stress modified G-X plot ($\Delta\mu$: chemical potential, M: interface mobility, v: Interface velocity). | 173 |
| Figure 9.1. Comprehensive summary of strength in Magnesium alloys [1-9]. | 177 |
| Figure 9.2. Calculated microstructural efficiency in a WE43 alloy. | 178 |
| Figure 9.3. Schematic showing (a) transformation of α -Mg to β_1 in a WE43 alloy and, (b) relieving transformation strain by diffusion of a larger atom to the expansion and a vacancy to a compression region. | 181 |
| Figure 9.4. Design framework for architecting high strength Mg alloys. | 184 |
| Figure 9.5. Potential microalloying elements based on (a) solute-vacancy binding energy—solubility, and (b) solute vacancy-binding energy—size plots for Mg. The data for plotting is taken from [14-18]. | 185 |
| Figure 9.6. Calphad based optimized alloy space for an Mg-Y-Nd system. Note that a reduction in Y and Nd content with Nd:Y ratio greater than 2 results in higher yield strength and reduced cost. | 191 |
| Figure 9.7. Computed mass fraction of metastable and stable phases in the commercially available WE43 and predicted EW alloy. | 192 |
| Figure 9.8. A comparison on the computed driving force for precipitation of $Mg_{12}R$ and other relevant phases in WE43 and the predicted alloy at the aging temperature (180 °C). Note that the driving force to precipitate $Mg_{12}R$ is an order of magnitude higher in the predicted alloy when compared to WE43. | 193 |
| Figure 9.9. Design optimization of Mg-Al-Ca alloy system to achieve strength greater than 400 MPa. | 194 |

CHAPTER 1

BACKGROUND AND MOTIVATION

1. Introduction

The recent emphasis on magnesium alloys can be appreciated by following the research push from several agencies and editorial efforts. References [1] and [2] capture two such efforts. The NSF workshop produced a final report [1] emphasizing the knowledge gaps and future research directions. A similar discussion is captured in the “Viewpoint set no. 47 Magnesium Alloy Science and Technology” in Scripta Materialia [2]. To set up the context of this dissertation regarding magnesium alloys, the following set of statements can be helpful:

- Magnesium alloys provide the opportunity for lightweighting of structural components because of the low density.
- The science and technology of magnesium alloys have lagged aluminum alloys and the NSF workshop report [1] highlights – “The key quote of the workshop: “Al alloys of incredible strength were developed by Edisonian trial and error, over the course of 80 years. The science and engineering community will only permit us 5-10 years to make similar improvements to Mg alloys.” --- J.F. Nie”.
- If the specific properties are normalized with cost, then the advantage of magnesium alloys compared to aluminum alloys are not attractive.
- Rare earth magnesium alloys have better properties in comparison to other alloys. But, can use of effective processing strategies and tailoring microstructural evolution paths transform the alloy chemistry-microstructure-property relationship in magnesium- alloys leading to better performance?
- The cost of magnesium alloys depends on the level of alloying elements and processing

route. Simple Mg-Al-Zn alloys are less costly, but the performance levels are low. Rare-earth elements have better properties and reduce anisotropy, but increase the cost. Can computational alloy design address this issue?

From the above statements, it is clear that, to achieve a real breakthrough in the use of magnesium alloys, its performance has to be increased. Though performance can be gaged by various properties like flammability, corrosion resistance, formability etc., the focus of this dissertation is on enhancing strength. In other words, the objective of this dissertation is to achieve high strength magnesium alloys using thermo-mechanical processing techniques, external fields and computational alloy design. Figure 1.1 shows a comprehensive plot summarizing the reported strength values in magnesium alloys from the available literature.

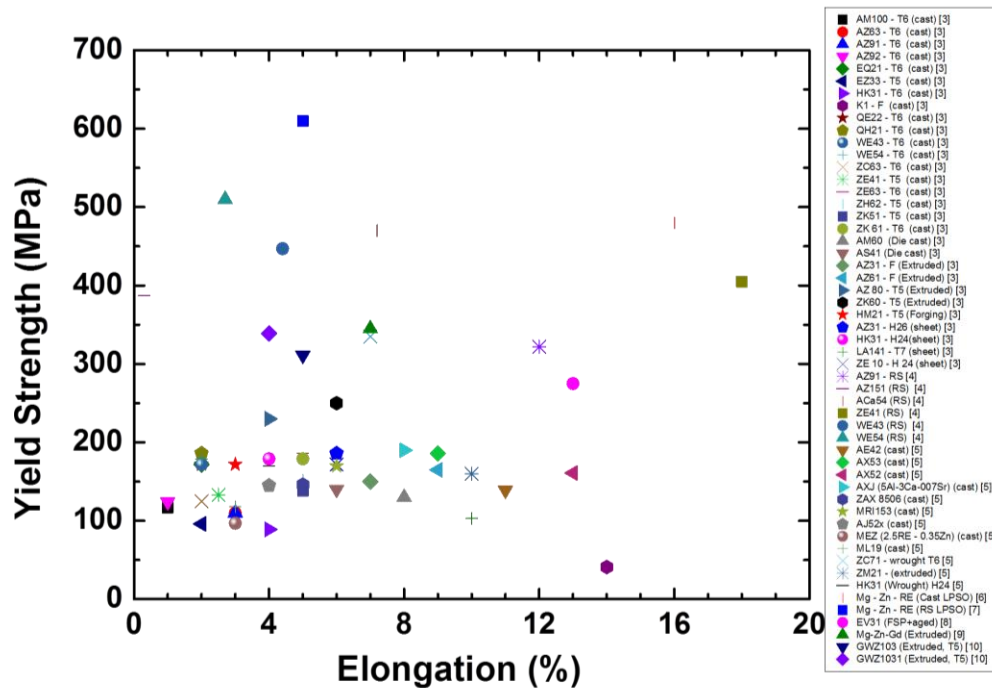


Figure 1.1 A comprehensive chart showing the strength in the current Mg alloys. Note that high strength Mg alloys with a value greater than 350 MPa are rapidly solidified. Strength achieved in

cast WE43 is 200 MPa and is a low value. Furthermore, strength achieved by wrought processes is also limited to ~300 MPa [3-10].

As highlighted from the figure, the inability to achieve high strength by conventional thermomechanical processing route is a key challenge as stated earlier. Therefore, the objective of this dissertation is to understand the fundamentals of microstructural evolution in an Mg-Y-Nd alloy and extract the maximum potential of this system by thermomechanical processing, additive manufacturing, and application of external fields. This alloy system was chosen due to the growing interest of the Mg community towards Mg-rare earth alloys and also due to the formation of precipitates on the prismatic planes which would serve as effective obstacles to the movement of basal dislocations. Furthermore, towards the later portions of the dissertation, a materials by design approach is highlighted to accelerate the discovery and deployment of high strength Mg alloys.

As the bottleneck of low strength is addressed, the answers to the following questions are actively chased in this dissertation. These are:

1. What are the fundamental micro-mechanisms governing second phase evolution in magnesium alloys?
2. Can application of an external field influence the nucleation and growth rate of strengthening precipitates during aging?
3. Can the external field increase the number density of precipitates?
4. Is defect engineering critical to achieve high strength Mg alloys?
5. Can a combination of innovative processing for tailoring microstructures and alloy design

by computation lead to new and effective paths for application of magnesium alloys?

Figure 1.2 compares the strength between Mg and Al alloys and it is evident that Mg alloys are inferior in comparison to the Al alloys. The reason for reduced strength in Mg alloys can be understood based on the concepts of alloying and microstructural efficiency which is detailed in the next section.

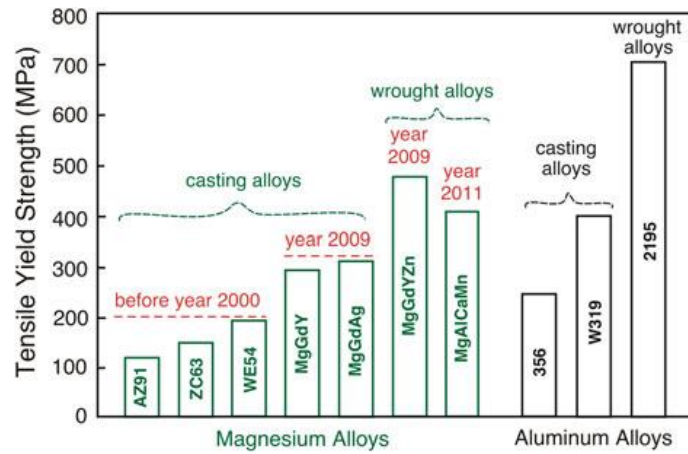


Figure 1.2. Current standing of Mg and Al alloys in terms of strength [11]

1.2 Concepts of ‘Alloying Efficiency’ and ‘Microstructural Efficiency’ from the Perspective of Strength

The terms ‘alloying efficiency’ and ‘microstructural efficiency’ are not commonly used in metallurgical literature [12]. Since the dissertation relies heavily on these two terms, it is important to define them. What is alloying efficiency? If we consider the context of precipitation-strengthening, the strength is dictated by uniform distribution of fine precipitates. The volume fraction of the second phase may depend on the type of precipitate. For example, if the alloying element X makes a phase Mg_3X and the alloying element Y makes a phase Mg_2Y ,

then alloying element X has higher alloying efficiency. It gives more volume fraction of precipitate per atom% of addition. A comparison of aluminum alloys with magnesium alloys is very illustrative. Considering the ballpark figures, one can argue that pure aluminum has strength level of 100 MPa, which increases to 200 MPa when 4 wt.% of Mg is added as in 5XXX series alloys. The strength of 2XXX alloys goes to 400 MPa and that of 7XXX goes to 550 MPa. On the other hand, for Mg alloys, going from pure magnesium to AZ31, AZ91 and WE43, one finds that strength does not cross 320 MPa. AZ91 has 10 wt.% alloying element compared to AZ31, which has only 4 wt.%. The increase of alloying content does not proportionately increase the strength. So, the alloying efficiency in AZ91 is low and the reason is microstructural (in)efficiency, the next keyword.

‘Microstructural efficiency’ can be defined in generic terms or in the context of a system. For the present proposal, let us consider Mg as the matrix. Figure 1.3 is taken from a review by Nie [11]. It clearly illustrates the nature of precipitates in magnesium alloys and this is one of the reason for lack of effective strengthening per at.% of alloying element. For example, to block the basal dislocations, fine needle-shaped precipitates in the prismatic orientation or very fine spherical precipitates would be most effective. As mentioned earlier, since WE43 alloys have strengthening precipitates on prismatic planes, this system was chosen for study.

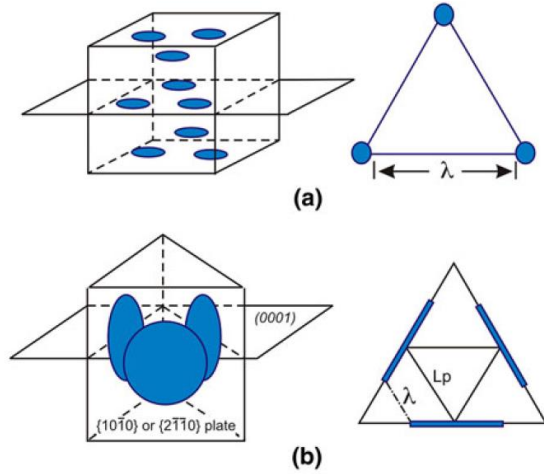


Figure 1.3. Schematic diagrams showing (a and b) effects of the orientation of precipitate plates on interparticle spacing for dislocation slip on basal plane of the magnesium matrix phase (taken from Nie [11]). This can be extended to discuss the microstructural efficiency.

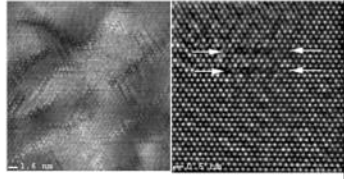
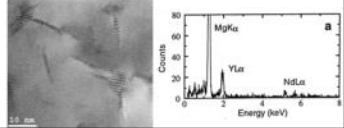
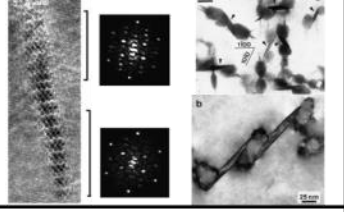

The dissertation is heavily inspired from these concepts of alloying and microstructural efficiency and will be recalled throughout the document to explain the observations. Before proceeding to the results, it is important to have an informed picture of the deformation modes and the precipitate descriptors in a WE43 alloy. Section 1.3 details this aspect.

1.3 Brief description of the deformation modes and precipitate descriptors in WE43 alloy

Mg has an hcp crystal structure with limited slip systems such as $(0001) \langle 11\bar{2}0 \rangle$ basal slip, $(10\bar{1}2) \langle 10\bar{1}1 \rangle$ pyramidal twinning, and more complex slip on prismatic $(10\bar{1}0)$ and pyramidal $(10\bar{1}1)$ planes [13,14]. In comparison to the prismatic and pyramidal slip, the basal slip system is most easily activated due to its lower critical resolved shear stress (CRSS) [15]. Moreover, in comparison to Al alloys, the Hall-Petch coefficient for Mg alloys is higher and would result in a greater contribution to strength by grain size refinement. Therefore, a process like friction stir would be suitable for increasing the strength by virtue of grain refinement. Since, the major contribution to strength in WE43 arises from second phases; the text to follow would lay its focus on discussing precipitation strengthening.

From the concepts of alloying and microstructural efficiency mentioned in section 1.1, the basic minimum requirement to increase strength is to maximize these terms. However, to realize this objective, it is necessary to understand the precipitation sequence in WE43. Table 1.1 shows the precipitation sequence by reviewing and compiling the literature available on WE43. Based on Table 1.1, it can be concluded that a uniform dispersion of β' and β_1 will be most desirable due to a higher alloying efficiency leading to a greater number density and a favorable orientation in the form of prismatic plates resulting in a higher microstructural efficiency.

Table 1.1. Precipitation sequence in WE43 [16,17]

| Precipitate type & shape | Microstructure | Composition | Structure | Orientation relationship | Interface |
|---|---|--|---|--|---------------|
| β'' , platelets, 150°C/1324 h or 200°C/2h, |  | $Mg(Y_{0.85}Nd_{0.15})$, Mg_3X type | DO19, $a=2a_{Mg}$, $c=c_{Mg}$, Forms by chemical ordering | Forms on (11-20) and monoatomic layers on (1-100) | coherent |
| β' , globular and irregularly faceted, 250°C/2h |  | $Mg_{12}NdY$ | bco, $a=0.640nm$, $b=2.223$, $c=0.521nm$ | $(100)_{\beta'} // (1-210)_{\alpha}$, $[001]_{\beta'} // [0001]_{\alpha}$ 3 variants | coherent |
| β_1 , plates, 250°C/48h |  | $Mg_{14}Nd_2Y$, Isomorphous with Mg_3X , where X represents Nd, Ce, La, Pr, Dy, Sm. | Fcc, $a=0.74nm$ | $(-112)_{\beta_1} // (1-110)_{\alpha}$, $[110]_{\beta_1} // [0001]_{\alpha}$, 6 variants | Semi-coherent |
| β equilibrium plates, extended aging at 250°C |  | $Mg_{14}Nd_2Y$, Isomorphous with Mg_5Gd | Fcc, $a=2.2nm$ | $(-112)_{\beta} // (1-110)_{\alpha}$, $[110]_{\beta} // [0001]_{\alpha}$ | Incoherent |

In subsequent chapters, effect of thermomechanical processing, additive manufacturing and external field effects on the microstructure is detailed. In the last section, a theoretical and computational approach is laid to design high strength Mg alloy.

1.4. References

1. Mg Science and Technology Workshop, May 19-20, 2011, Arlington, VA, Sponsored by the National Science Foundation, report accessed from <http://www.virginia.edu/ms/research/agnew/conferences/>
2. S.R. Agnew, J.F. Nie, Scripta Materialia 63 (2010), 671-673
3. ASM Handbook on Mg alloys (Desk edition)
4. C. Sanchez, G. Nussbaum, P. Azavant, H. Octor, Mater. Sci. Eng A 221 (1996)
5. Z. Yang, J. P. Li, J.X. Zhang, G.W. Lorimer, J. Robson, Acta Metall.Sin. 21 (2008) 313-328
6. T. Honma, N. Kunito, S. Kamado, Scripta Mater. 61 (2009) 644
7. Y. Kawamura, K. Hayashi, A. Innoue, T. Masumoto, Mater. Trans. 42 (2001) 1172
8. T.A Freeney, R.S. Mishra, Metall and Materials Trans. A 41 (2010) 73-84
9. M. Yamasaki, T. Annan, S. Yoshimoto, Y. Kawamura, Scripta Mater. 53 (2005) 799-803
10. X. B. Liu, R.S. Chen, E.H. Han, Journal of Alloys and Compounds 465 (2008) 232-238
11. J.F. Nie, Metallurgical and Materials Transactions A 43 (2012) 3891-3939
12. S. Palanivel, R.S. Mishra, Unpublished work (2013)
13. S.R. Agnew, and O. Duygulu: Int. Jour. of Plast. 21 (2005), 1161-1193
14. E.F. Emley: Principles of Magnesium Technology, Elsevier Science & Technology, 1966.
15. X.Y. Lou, M. Li, R.K. Boger, S.R. Agnew, and R.H. Wagoner: Int. Jour. of Plast. 23 (2007) 44-86.
16. C. Antion, P. Donnadieu, F. Perrard, A. Deschamps, C. Tassin, A. Pisch, Acta Mater. 51 (2003), 5335-5348
17. J.F Nie, B.C Muddle, Acta mater. 48 (2000), 1691-1703

CHAPTER 2

EFFECT OF PROCESSING PARAMETERS ON THE MICROSTRUCTURAL EVOLUTION AND JOINT EFFICIENCY OF A WE43 ALLOY DURING FRICTION STIR WELDING[†]

Overview: The processing parameters play an important role in determining the spatial and temporal evolution of the microstructure during friction stir welding (FSW). The overall kinetics of microstructural evolution is location sensitive and the effect of the process strain, strain rate and thermal cycle creates complexity. In the present study, magnesium-based WE43 alloy was processed using two processing conditions. Joint efficiency was subsequently evaluated. The results have been correlated with detailed microstructural information obtained from SEM and OIM-EBSD. The influence of microstructural evolution on strength has been analyzed. This framework provides an approach to maximize joint efficiency.

2.1. Introduction

The onset of many desirable features like fuel efficiency, high specific strength and numerous others are driving Mg-based alloys towards being a potential replacement in the future. It is known that the rule of thumb for the selection of any alloy system in a majority of applications is confined to strength restrictions. As a result, the strength comparison of the Mg alloys with their counterparts has triggered intensive research for their use in engineering

[†] This chapter is presented in its entirety from S. Palanivel, R.S. Mishra, B. Davis, R. Delorme, K.J. Doherty, K.C. Cho, “Effect of initial microstructure on the microstructural evolution and joint efficiency of a WE43 alloy during friction stir welding”, Friction Stir Welding and Processing VII, TMS, San Antonio, TX, 2013 with permission from John Wiley and Sons.

applications. WE43 is currently touted to be one of the most promising Mg-based alloys due to their good elevated temperature properties, creep performance, flammability resistance and relatively higher strength [1,2]. However, welding of Mg alloys is a major challenge and limits the ability to fabricate large and complex components [3]. Therefore, joint efficiency can have a profound impact on expanding its applicability towards various sectors in the near future. In the past decade, friction stir processing was demonstrated as a powerful tool to locally modify the microstructure by Mishra et al. [4]. This led to a series of efforts to optimize the process and obtain high strength alloys. Extensive study on Al-based alloys and a lucid understanding of microstructural evolution by friction stir processing has been formulated and available in the literature [5,6]. Starting from Al alloys, a variety of Mg alloys have also been studied.

Feng et al [7] studied the effect of friction stir processing on an AZ91 alloy and reported the dissolution and breakup of coarse eutectic $Mg_{17}Al_{12}$ phase. Park et al. [8] demonstrated the importance of texture and related to the mechanical properties of an AZ61 alloy subjected to FSP. Ma et al. [9] suggested that FSP plays the role of solution treatment in AZ91 and saves time. Cao et al. [10] reported values of 69-78% for joint efficiencies in an AZ31-H24 alloy with failure occurring predominantly between stir zone (SZ) and thermo-mechanically affected zone (TMAZ). Several studies have been carried out on the precipitation strengthened Mg alloys and indicate a strong dependency of strength on the evolution of hardening precipitates [11,12,13,14] However, there is a strong demarcation with respect to the global value of strength, contributing factors and evolution path as a function of alloy chemistry during FSW. The thermal stability of the precipitates strongly determines the process conditions to be used for achieving a desired microstructure. In comparison to the dissolution of precipitates in the AZ

series (Mg-Al-Zn), strengthening in Mg-Al-Ca and rare earth containing GWZ (Mg-Gd-Zn), and WE43 (Mg-4Y-3Nd) series is determined by the ability to control the intermetallic phases [7,12,13,14].

Freaney et al. [13] showed enhancement of the mechanical properties by breakage and dissolution of the second phases in a cast EV31 alloy. Xiao et al. [12] showed a large increase in the strength of a cast GW103 alloy after post FSP aging. This was achieved by dissolving the Mg_5Gd intermetallics during processing. However, Zhang et al. [14] showed that the breakage and homogeneous distribution of Al_2Ca increased the strength and recommended faster welding speeds and lower heat input. Considering a variety of intermetallics (Mg_2Y , Mg_{24}Y_5 , $\text{Mg}_{41}\text{Nd}_5$) that form in a WE43 alloy during casting and remain during subsequent shaping operations, it would be interesting to study their response as a function of processing parameters [15,16,17]. Investigations indicate that different starting tempers can have a huge impact during processing and result in different final values of strength. Freaney et al. [18] studied the effect of FSP on a cast WE43 alloy and obtained a nugget strength equivalent to 120% of the base material. Though a large amount of literature exists on the friction stir welding of Mg alloys, the domain of industrially important WE43 alloys has been left untouched. To the best of our knowledge, no report exists on the microstructure-joint efficiency relationship in a wrought WE43 alloy.

The present study aims at correlating the effect of process parameters on the microstructure and mechanical property of a T5 temper WE43 alloy

2.2. Experimental Details

In this study, 3.5mm thick plates of WE43 sheet in the rolled condition was provided by Magnesium Elektron. The nominal composition of the alloy was 4% Y-3%Nd-0.5%Zr –balance Mg (all in weight %). The alloy was subjected to aging at 210 °C for 48 h to maximize the base strength. The samples were longitudinally friction stir welded by employing a conical threaded pin made of tool steel with a concave shaped featureless shoulder. The pin height, pin diameters at the tip and root of the pin were 1.4 mm, 3.4 mm and 5.6 mm respectively. A single pass FSW was performed at tool rotation rates of 600 and 800 rpm and a constant traverse speed of 102 mm/min.

The specimen for microstructural examinations were cross sectioned perpendicular to the FSW direction. A standard sequential metallurgical procedure such as cutting, mounting and polishing with alcohol based diamond polishing compound was employed. Structural features were subsequently revealed by etching for duration of 10s in a mixture of acetic glycol (20 mL), (1 mL) HNO₃, (60 mL) ethylene glycol, and (20 mL) water, and washing with ethanol. Microstructural analysis and characterization was extensively carried out by employing the scanning electron microscope (FEI Nova NanoSEM 230). Samples for EBSD analysis were prepared using diamond based compounds to a final polishing step of 0.02 µm. These samples were subsequently electro-polished (40% H₃PO₄ and 60% ethanol at 20°C) using a voltage of 2–3V for 10–15s and washed using ethanol. A FEI Nova NanoSEM 230 (20 kV, 3.1 mA, tilting 70°, 0.3 µm step size) was used to record the EBSD patterns for stir zone (SZ).

The microhardness measurements (Vickers microhardness tester) were done using a load of 1.961 N and a dwell time of 10 seconds. These measurements were performed through the

center of the transverse cross section in the SZ and extending into the base matrix on either sides for a distance of 15mm. Quantitative analysis was done using the ImageJ software package. The grain size determination was done using the linear intercept method.

2.3. Results and Discussion

2.3.1 Initial Microstructure: T5 Temper (As-Rolled + Aged)

The as-rolled microstructure was subjected to aging based on the optimal conditions reported in literature. This heat treatment has been reported to precipitate strengthening β'' and β' phases [19,20,21]. However lower values of hardness as compared to the values reported in literature can be attributed to the following: 1) an inhomogeneous microstructure 2) prior precipitation during the course of rolling operation. Extensive analysis of the microstructure depicted three interesting features: Shear bands, Intermetallic clusters of RE and precipitation gradients. Figure 2.1 (a) showed patches of inhomogeneity in the rolled structure suggesting preferential shear localization during rolling. Jin et al. [22] studied the deformation behavior of a coarse grained AZ31 alloy and observed such inhomogeneous structures. The observation was reasoned based on dissimilar recrystallization magnitude of different grains owing to their orientation with respect to the compressive stress. Serajzadeh et al. [23] employed modelling and related the microstructural inhomogeneity to the inherent and inevitable strain gradients. The study also suggested that the extent of inhomogeneity would be directly proportional to the reduction per pass. In the present case, a greater reduction per pass at lower temperature substantiates the microstructural features. Another plausible reasoning could be the persistence of the solute that segregated to the interdendritic spaces during solidification. This mechanism of chemical partitioning must have led to a local supersaturation and subsequent precipitation of

non-strengthening precipitates. Thus, the prior microstructure plays a crucial role in the subsequent evolution of microstructure and mechanical variables during isothermal aging. The grain size was observed to be $35 \pm 15 \mu\text{m}$.

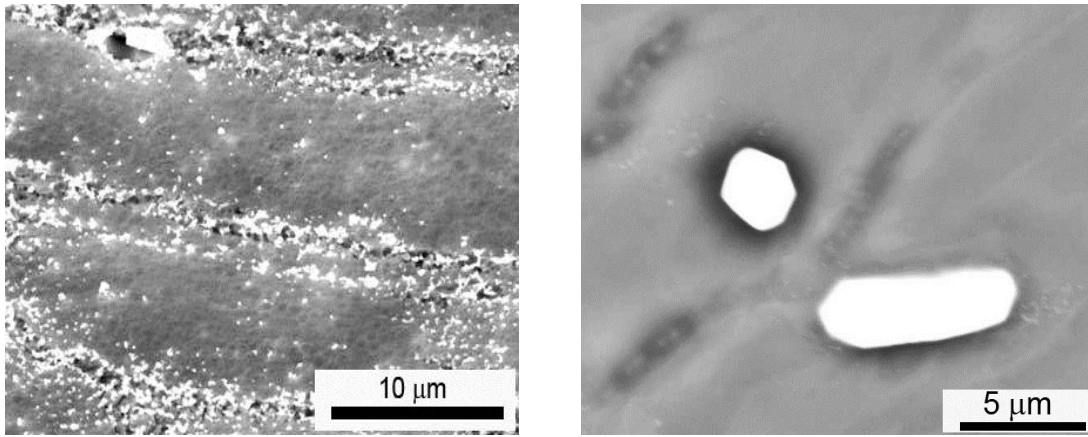


Figure 2.1. (a) Scanning electron (SE) micrograph depicting shear localization and precipitation gradients (b) Back scattered electron (BSE) micrograph showing cuboidal $\text{Mg}_2\text{YZr}_{0.3}$ and plate shaped $\text{Mg}_{41}\text{Nd}_5\text{Zr}$ intermetallics.

Figure. 2.1 (b) shows the presence of large cuboidal intermetallics of Mg_2Y . These intermetallics have been reported to form during the course of solidification and persisted during rolling operations [15-17]. Such cuboidal precipitates have been reported by numerous researchers in Gd containing alloys [12]. High thermal stability of these precipitates has been reported and their melting point has been quoted to be around 620°C . The presence of such giant particles around $4\text{-}5 \mu\text{m}$ would be inefficient in serving as an obstacle to dislocation motion. Therefore, it would be highly interesting to note the behaviour of these particles subjected to FSW.

2.3.2 Friction Stir Welding (FSW)

This study aims at reasoning the evolution of microstructure as a function of process condition. The major contributing factors to strengthening in a WE43 alloy are grain size and precipitate descriptors. Therefore, it is necessary to understand the competing aspects of strain, strain rate and temperature. The deformation strain, peak temperature and the grain size are correlated employing the Zener- Holloman parameter Z (s^{-1}). Table 2.1 summarizes the mathematical equations employed to establish the Zener-Holloman parameter from the literature.

Table 2.1. Equations for process parameters based calculations [24-27].

| | | |
|---|--|--|
| $Z = \dot{\varepsilon} \exp\left(\frac{Q}{RT}\right)$ (1) | $\varepsilon = \ln\left(\frac{l}{APR}\right) + \left \ln\left(\frac{APR}{l}\right)\right $ (2) | $l = 2r \cos^{-1}\left[\frac{r-x}{r}\right]$ (3) |
| $\dot{\varepsilon} = \frac{\varepsilon}{t}$..(4) | $t = \frac{APR}{v}$..(5) | $\ln d = A1 - A2 \ln Z$..(6) |

where $\dot{\varepsilon}$: strain rate, R : gas constant, T : temperature, Q : activation energy, l : Maximum deformed length, APR : Advance per revolution, r : pin radius, x : perpendicular distance to welding direction from RS to AS of the tool, v : welding speed ($mm\ s^{-1}$), d : grain size.

The peak temperature was determined by using the Arbegast model: [28]

$$\frac{T}{T_m} = K \left(\frac{\omega^2}{2.362v \times 10^4} \right)^\alpha \quad (7)$$

where T_m (K): melting temperature (893 K for WE43), ω (r.p.m.) and v ($mm\ s^{-1}$) are the tool rotational and welding speeds used during FSW. In the present study the values of K and α were averaged over the reported values by Chang et al. [29] and Commin et al.[30] for AZ 31 and Mg

alloys. The activation energy was assumed to be the lattice diffusion of Mg and taken to be 135 kJmol⁻¹. Table 2.2 summarizes the process parameter based calculations using equations from Table 1.

Table 2.2. Summary of process parameter based calculations.

| Rotational speed (RPM) | Welding speed (mm/min) | Strain | Strain rate (s ⁻¹) | Peak temperature (K) | Zener-Holloman parameter, Z (s ⁻¹) |
|------------------------|------------------------|--------|--------------------------------|----------------------|--|
| 600 | 102 | 8.03 | 80.29 | 621 | 1.82*10 ¹³ |
| 800 | 102 | 8.6 | 114.73 | 660 | 5.55*10 ¹² |

Examination of OIM micrographs reveal fine grained structures indicating extensive event of dynamic recrystallization. This is indicative of extremely high deformation rates postulated by Table 2.2. Figures 2.2 (a) and (b) show the grain sizes of 600/102 and 800/102 to be around 1.7 and 2.7 μm respectively. This observation can be rationalized based on the Z parameter, strain rate and peak temperature. A process parameter of 600/102 yields a lower peak temperature and higher strain rate leading to a higher Z value. This would imply that at any particular instant, a 600/102 sample experiences a higher strain per volume and a greater driving force to recrystallize. Freeney et al. [13] reported the grain size to be 6.1 μm for a cast EV31A processed at 400/102. Investigations for a T5 WE43 exhibits grain refinement by a magnitude of 4x subjected to a higher heat input as compared to EV31A. A higher grain refining sensitivity in a WE43 alloy could be reasoned based on a greater extent of second phases and Zr content that would auger pinning, predeformed microstructure and higher extent of solute elements. In comparison to the cast WE43 alloy processed at 400/102, T5 temper exhibited a finer grain size substantiating the importance of initial microstructure. Though, DRX is unanimously accepted,

there is a conflict over the mechanistic mode triggering recrystallization.

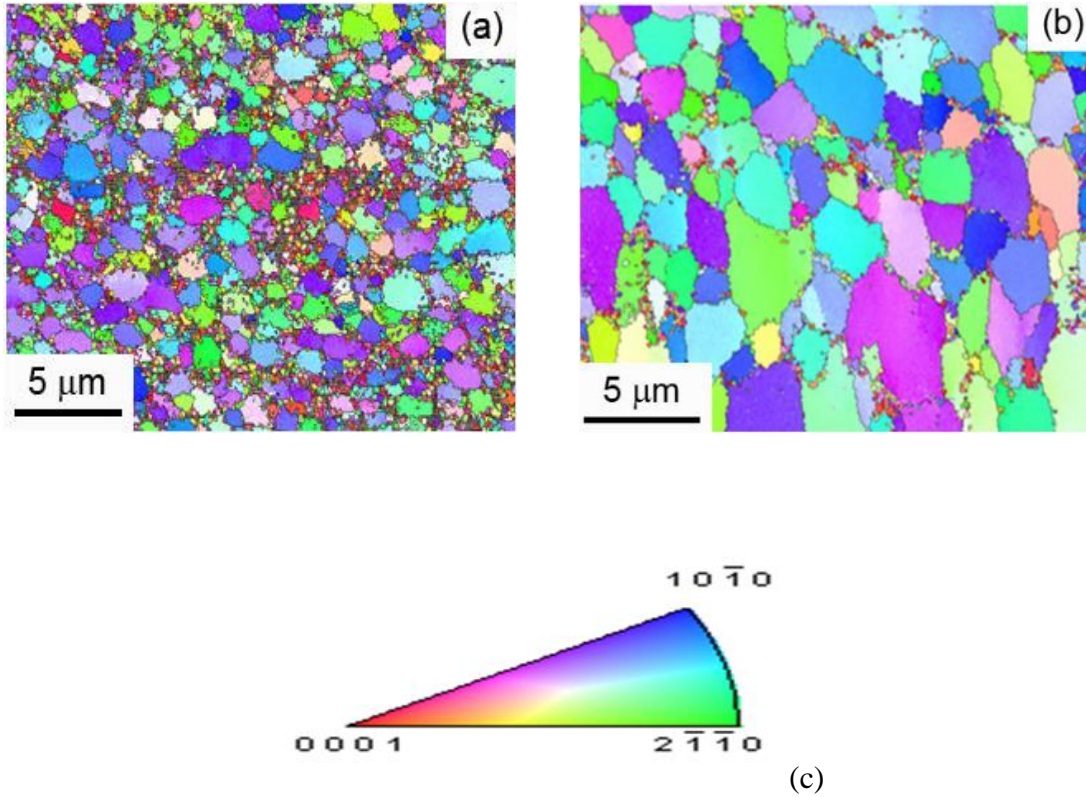


Figure 2.2. EBSD micrographs of (a) 600/102, (b) 800/102 and (c) IPF color code.

Figures 2.3 (a-e) shows various zones and the features embedded in the microstructure. The area fraction of the precipitates was evaluated using imageJ and decreased from 24.1 % in the T5 state to 16.1 % and 17.4 % in 600/102 and 800/102 sample respectively. From Figure 2.3(a), it can be concluded that FSP led to partial homogenization. For a sample processed at a higher rotational speed (Figure 2.3d), it showed preferential precipitate coarsening at the grain boundaries as compared to 600/102. Since coarsening is dependent on the thermal profile and mechanical attrition, the evolution becomes a complex function of the competing factors. For an 800/102 sample, the peak temperature is above the dissolution temperature of strengthening

precipitates and would soften the matrix to a greater extent. Non equilibrating reprecipitation would then favor the formation of non-strengthening β precipitates at grain boundaries. Figures 2.3 (c) and 2.3 (e) depict formation of necklace structures and fragmentation of prior grains leading to finer grains by recrystallization and break up. This is due to high bulk diffusivity of Mg at a certain temperature in comparison to Al alloys.

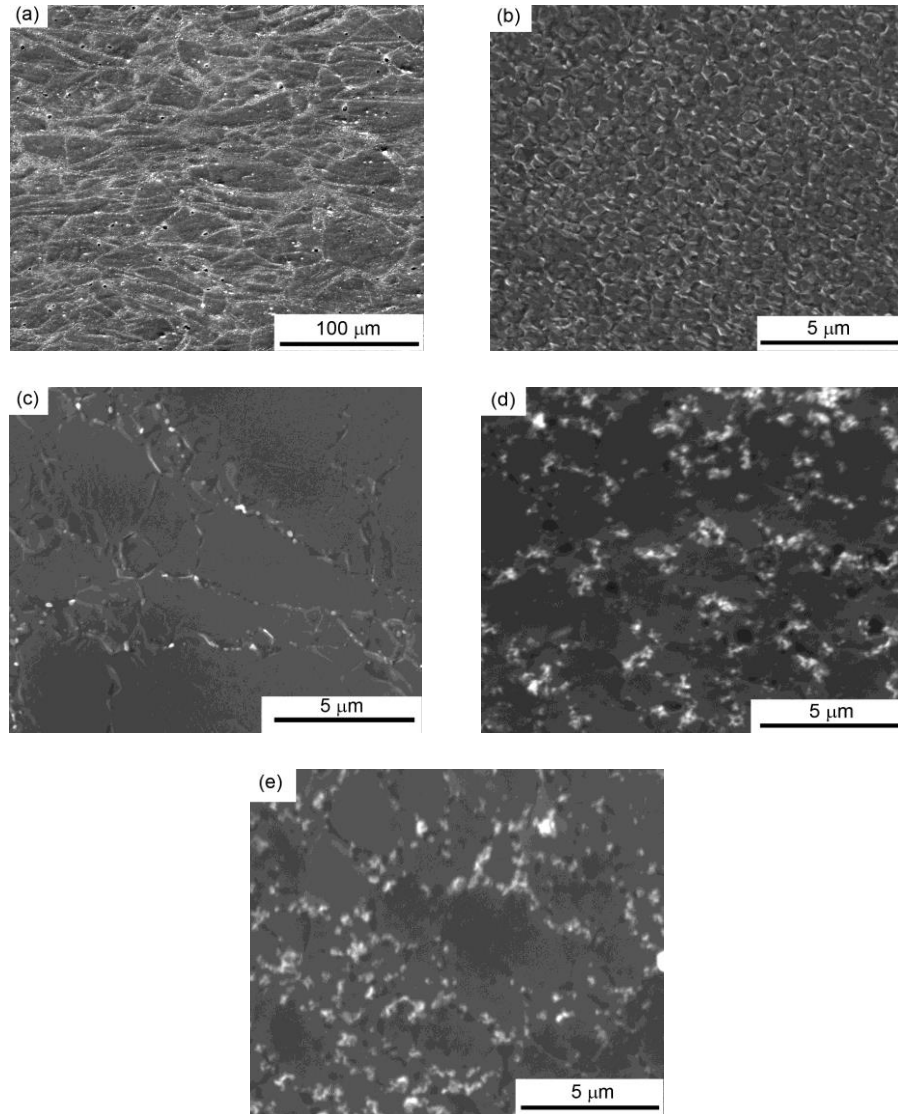


Figure 2.3. SEM micrographs of different conditions; (a) AR+T5 (210 °C/48h), (b) 600/102 SZ, (c) 600/102 TMAZ, (d) 800/102 SZ, (e) 800/102 TMAZ.

2.3.3 Mechanical Properties and PWHT (Post Weld Heat Treatment)

Differences exhibited by 600/102 (Figure 2.3b) and 800/102 (Figure 2.3d) in terms of precipitate characteristics and grain size markedly affected the strength levels by an order of 6-7HV in the HAZ and 5 HV in the nugget as shown in Figure 2.4 (a). A W shaped curve was observed and can be reasoned based on the far-reaching effect of shoulder. The shoulder diameter (d)/Plate thickness (t) ratio was approximately thrice resulting in greater accumulation of heat. This is analogous to a heat pumping source containing a greater temperature field over a smaller distance. Thus the HAZ would experience higher temperatures with a severe knockdown in properties. PWHT markedly increased the SZ, TMAZ and HAZ strength by marginally lowering the strength of the base metal. Therefore the joint efficiency values considerably increase after aging.

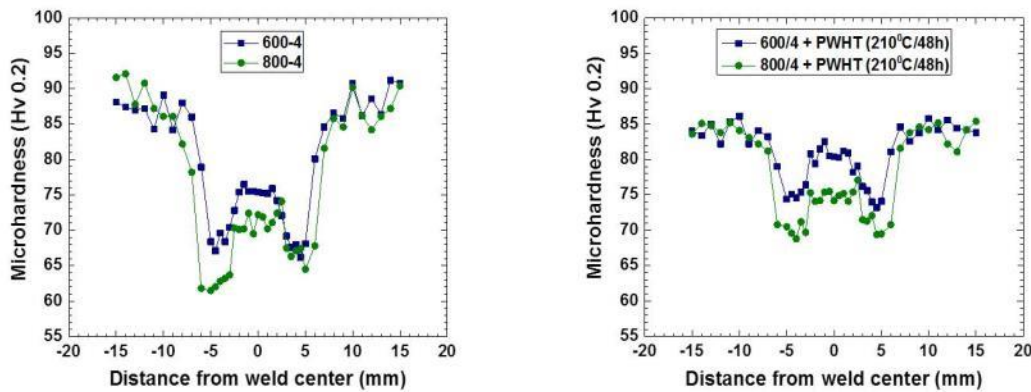


Figure 2.4. Microhardness data for as processed and PWHT samples.

2.4. Conclusions

The effect of processing conditions on the joint efficiency of a T5 temper WE43 alloy was investigated. Based on the study, the following conclusions are made:

- 1) The FSW of WE43 resulted in grain refinement and attrition of second phase particles leading to homogenization. The grain size reduced from $35 \pm 15 \mu\text{m}$ in the T5 state to $1.7 \pm 0.2 \mu\text{m}$ and $2.7 \pm 0.26 \mu\text{m}$ in a 600/102 and 800/102 samples.
- 2) The shoulder diameter to plate thickness ratio was thrice resulting in a concentrated temperature field. This caused the shoulder to act as a constricted heat generator and spread the HAZ over a long distance.
- 3) The HAZ served as the weakest link with a joint efficiency of 73.5 % and 67 % for a 600/102 and 800/102 samples. These values increased to 85 and 79.5 % after PWHT respectively. A better understanding of microstructure evolution coupled with aging optimization needs to be done.

2.5. References

1. Development of highly creep resistant Magnesium alloys, B.L Mordike, Journal of Materials Processing and Technology, 117 (2001) 391-394
2. Recent development in light alloys, I.J Polmear, Materials transactions, 36 (1996) 12-31
3. Welding and Joining of Magnesium Alloys, Frank Czerwinski, Magnesium alloys- Design, processing and properties
4. R.S. Mishra, M.W. Mahoney, S.X. McFadden, N.A. Mara, A.K. Mukherjee, Scripta Mater. 42 (2000) 163
5. Integrated modeling of friction stir welding of 6xxx series Al alloys: Process, microstructure

- and properties, A. Simar, Y. Bréchet, B. de Meester, A. Denquin, C. Gallais, T. Pardoen, *Progress in Materials Science* 57 (2012) 95-183
6. Friction stir welding of aluminium alloys, Threadgill PL, Leonard AJ, Shercliff HR, Withers PJ *Int Mater Rev* 54 (2009) 49–93
 7. Enhanced mechanical properties of Mg–Al–Zn cast alloy via friction stir processing, A.H. Feng and Z.Y. Ma *Scripta Materialia* 56 (2007) 397–400
 8. Effect of micro-texture on fracture location in friction stir weld of Mg alloy AZ61 during tensile test, Seung Hwan C. Park, Yutaka S. Sato, Hiroyuki Kokawa *Scripta Materialia* 49 (2003) 161–166
 9. Microstructural refinement and property enhancement of cast light alloys via friction stir processing, *Scripta Materialia* 58 (2008) 361–366
 10. Effect of welding speed on the quality of friction stir welded butt joints of a magnesium alloy, X. Cao, M. Jahazi, *Materials and Design* 30 (2009) 2033–2042
 11. Effect of microstructural evolution on mechanical properties of friction stir welded ZK60 alloy, G.M. Xie , Z.Y. Ma, L. Geng, *Materials Science and Engineering A* 486 (2008) 49–55
 12. Enhanced mechanical properties of Mg–Gd–Y–Zr casting via friction stir processing, B.L. Xiao, Q. Yang, J. Yang, W.G. Wang, G.M. Xie, Z.Y. Ma, *Journal of Alloys and Compounds* 509 (2011) 2879–2884
 13. Effect of Friction Stir Processing on Microstructure and Mechanical Properties of a Cast-Magnesium–Rare Earth Alloy, T.A. Freeney, R.S. Mishra, *The Minerals, Metals & Materials Society and ASM International* 2009
 14. Microstructural evolution of a heat-resistant magnesium alloy due to friction stir welding, Datong Zhang, Mayumi Suzuki, Kouichi Maruyama, *Scripta Materialia* 52 (2005) 899–903

15. Microstructures and mechanical properties of high performance Mg-4Y-2.4Nd-0.2Zn-0.4Zr alloy, Zaijun Su, Chuming Liu, Yingchun Wan, *Materials and Design* (2012)
16. Effect of T5 and T6 Tempers on a Hot-Rolled WE43 Magnesium Alloy, Kun Yu, Wenxian Li, Richu Wang, Bo Wang and Chao Li, *Materials Transactions* 49 (2008) 1818 -1821
17. Corrosion resistance of WE43 and AZ91D magnesium alloys with phosphate
18. PEO coatings, R. Arrabal, E. Matykina, F. Viejo, P. Skeldon, G.E. Thompson, *Corrosion Science* 50 (2008) 1744–1752
19. T.A. Freeney, R.S. Mishra, G.J. Grant, and R. Verma: *Friction Stir Welding and Processing IV*, TMS, Warrendale, PA, 2007
20. Structure evolution of a WE43 Mg alloy submitted to different thermal treatments, P. Mengucci, G.Barucca, G. Riontino, D. Lussana, M. Massazza, R. Ferragut, E. Hassan Aly, *Materials Science and Engineering A* 479 (2008) 37-44
21. Structural examination of aging precipitation in a Mg-Y-Nd alloy at different temperatures, Renlong Xin, Ling Li, Ke Zeng, Bo Song, Qing Liu, *Materials Characterization* 62 (2011) 535-539
22. Characterisation of strengthening precipitate phases in a Mg-Y-Nd alloy, J.F Nie, B.C Muddle, *Acta mater.* 48 (2000) 1691-1703
23. Correlation of microstructural evolution and formation of basal texture in coarse grained Mg-Al alloy during hot rolling, Qinglin Jin, Sung-Yong Shim and Su-Gun Lim, *Scripta Materialia* 55 (2006) 843-846
24. An investigation on strain inhomogeneity in hot strip rolling process, S. Serajzadeha, A. Karimi Taheria, M. Nejatib, J. Izadib, M. Fattahi, *Journal of Materials Processing Technology* 128 (2002) 88–99

25. Twinning, dynamic recovery and recrystallization in hot worked Mg–Al–Zn alloy, Myshlyayev, M.M., McQueen, H.J., Mwembela, A. and Konopleva, E., *Materials Science and Engineering A*, 337, (2002), 121-133.
26. Dependence of Zener parameter on the nanograins formed during friction stir processing of interstitial free steels, Dehghani, K. and Chabok, A., *Materials Science and Engineering A*, 528, (2011), 4325-4330.
27. Flow visualization and simulation in FSW, *Scripta Materialia*, Reynolds, A.P, 58 (2008), 338-342.
28. Analysis of microstructural evolution during friction stir welding of ultrahigh-strength steel, *Scripta Materialia*, Ghosh, M., Kumar, K. and Mishra, R.S., 63 (2010), 851-853.
29. Hot Deformation of Aluminum Alloys III, Arbogast, W.J., TMS, Warrendale, PA (2003).
30. Relationship between grain size and Zener–Holloman parameter during friction stir processing in AZ31 Mg alloys, Chang, C.I., Lee, C.J. and Huang, J.C., *Scripta Materialia*, 51 (2004), 509-514
31. Friction stir welding of AZ31 magnesium alloy rolled sheets: Influence of processing parameters, Commin, L., Dumont, M., Masse, J.E. and Barrallier., *Acta Materialia*, 57 (2009), 326-334.

CHAPTER 3

EFFECT OF INITIAL MICROSTRUCTURE ON THE MICROSTRUCTURAL EVOLUTION AND NUGGET EFFICIENCY OF A WE43 ALLOY DURING FRICTION STIR WELDING

Overview: In chapter 2, a W-shaped hardness profile was shown with a knock down in the HAZ. This chapter shows that hardness profile is sensitive to the tool dimensions, initial microstructure and weld parameters. Therefore, the objective of this study was: (i) to improve the nugget efficiency in a precipitation strengthened WE43 alloy and understand the role of initial microstructure and welding parameters on subsequent microstructural evolution during friction stir welding. A major thrust is laid out on comprehending the microstructural evolution as a function of welding parameters and the initial microstructure. The overall goal is to understand the physical metallurgy of a WE43 alloy subjected to FSW. These efforts would serve as a tool to understand the physical principles operative and correlate to the dynamic response of microstructure to process variables and the initial microstructure.

3.1. Experimental Details

3.1.1 Friction Stir Welding

For this study, rolled WE43 sheets of different thickness (nominal composition: Mg-4wt%Y-3wt%Nd-0.5wt%Zr) were obtained from Magnesium Elektron. These sheets were subsequently subjected to friction stir welding. FSW was done using a right handed stepped spiral pin made of tool steel with a concave shaped featureless shoulder. A tilt angle of 1.5° was used to contain the material beneath the featureless shoulder. Figure 3.1 shows the schematic of

the process and also the tool macrograph with the dimensions used in the current study. Three different tool rotation rates of 700, 1400 and 2000 rpm were used at a constant traverse speed of 102 mm/min. To enhance the strength, the samples were peak aged after FSW at 180°C for 60 hours.

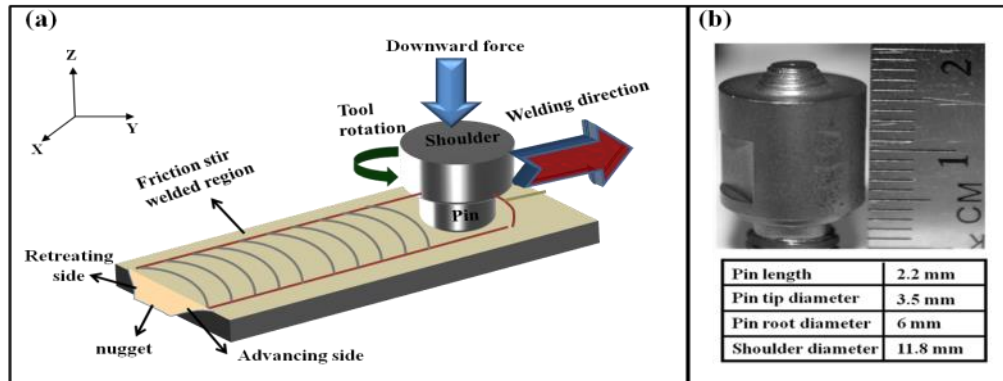


Figure 3.1. (a) Schematic illustration of friction stir welding. (b) Tool used in the current study.

3.1.2 Microstructural Characterization and Mechanical Testing

The specimen for microstructural examination and hardness evaluation were cross sectioned perpendicular to the welding direction (Y-Z plane). A standard sequential metallurgical procedure such as cutting, mounting and polishing with alcohol based diamond polishing compound was employed. Microstructural analysis and characterization was extensively carried out by employing a scanning electron microscope (FEI Nova NanoSEM 230) and a transmission electron microscope (Technai G2 F20 STEM). For TEM analysis, circular discs of 3 mm were prepared using the conventional dimple grinding and ion milling procedure. To ensure one to one comparison, extensive care was taken to ensure that these samples came from the same depth corresponding to the center of the sample. For comparison with the peak aged rolled condition, a

disc was also extracted from the base metal after aging. Samples for EBSD analysis were prepared using diamond based compounds till 1 μm followed by final polishing steps of 0.05 and 0.02 μm in colloidal silica. During the final step, the sample was intermittently washed with ethanol to avoid surface corrosion. A FEI Nova NanoSEM 230 (20 kV, 3.1 mA, tilting 70°, 0.17 μm step size) was used to record the EBSD patterns from the base and the nugget/stir zone (SZ). The Vickers microhardness measurements were done at a load of 1.961 N with a 10 sec dwell time. These measurements were performed along the centerline of the SZ using an interval of 0.5 mm (Y axis). The grain size was determined by using the grain diameter method in the TSL-OIM software. Uniaxial tensile testing was done for the samples with the tensile axis parallel to the weld direction (X axis). This was done to estimate the strength and ductility in comparison to the aged base material and translate the observed hardness numbers. The gauge dimension for the mini tensile sample was 2mmx1mmx1mm. The tensile tests were performed at room temperature at a strain rate of 10^{-3} s^{-1} and the data was averaged over three samples.

3.2. Results and Discussion

3.2.1 Path Dependent Microstructural Evolution in Rolled Sheets

The initial microstructure plays a vital role in determining the subsequent properties. In the present case, the rolled microstructures that were subjected to different thermal routine and percentage reduction were analyzed. Several important observations have been made: Firstly, thinner sheets exhibited the highest strength and such an observation is well expected due to the higher amount of strain incorporated into the material. Since, a higher amount of strain implies higher dislocation storage, these dislocations would aid in the process of precipitation leading to a higher number density and decreased inter-particle spacing. Furthermore, these defects recover

during the aging operation at 180 °C leading to recrystallization. Figure 3.2 experimentally validates this behavior in alloy 1 and 2 after aging. The formation of these necklace beads as shown in the figure can be attributed to the nucleation of small recrystallized grains at the grain boundary during the aging operation [1].

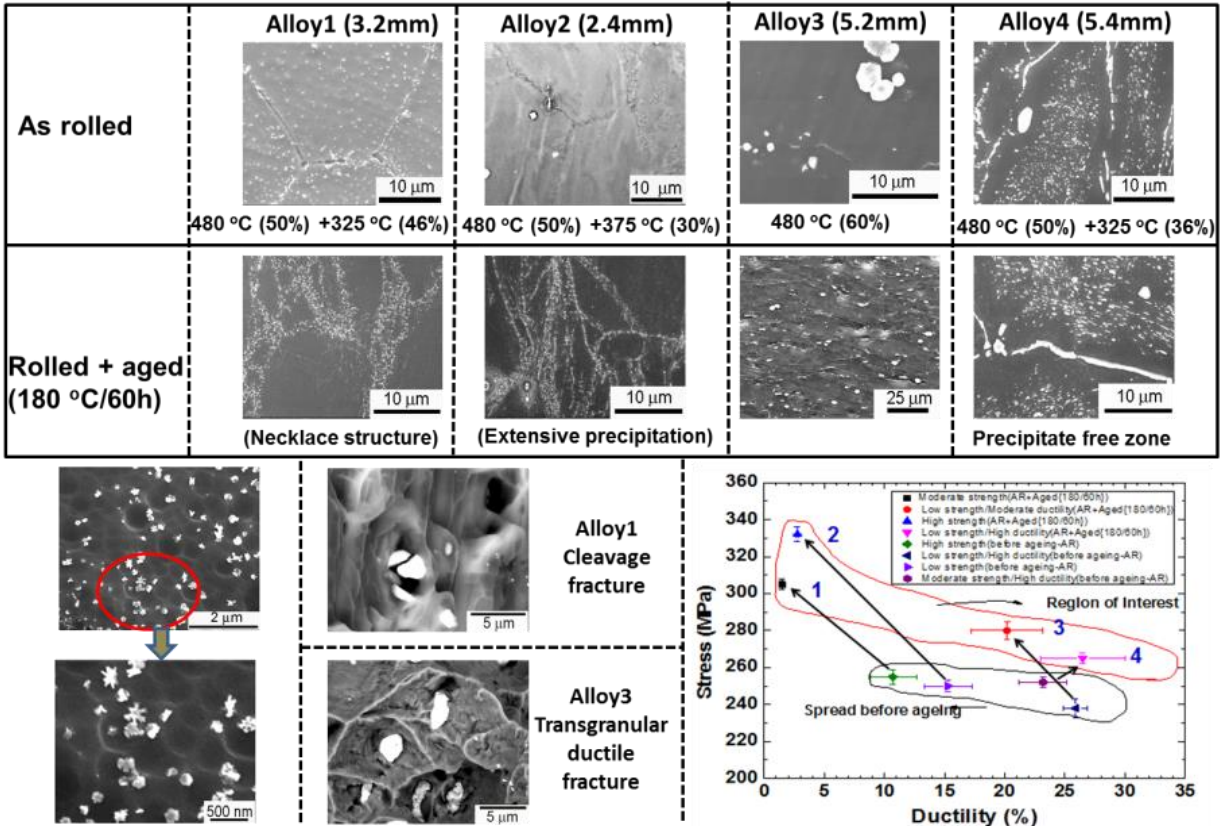


Figure 3.2. Path dependent microstructural and strength evolution in a WE43 alloy. Note that alloy numbering through 1-4 is representative of different rolling reductions of a WE43 alloy.

In regard to the strength, though the yield reaches closer to 325 MPa in alloys 1 and 2 after aging the rolled microstructures (ARA), the ductility drops below 5% and would not meet the requirement for a majority of the structural design. Therefore, the drawback of working the

material to a higher extent is the increase in the extent of inhomogeneity and a reduction in formability. Figure 3.3(a) shows the SEM micrograph for alloy 1 in the aged condition. Based on the microstructure, two regions can be identified. Regions I and II correspond to microstructurally clean and densely populated region with precipitates respectively. Furthermore, the TEM micrograph in Figure 3.3(b) shows extremely fine grains based on the diffraction pattern shown in the inset. Such an observation is in conformity with the process of static recrystallization during aging as mentioned above. In addition, these recrystallized grains act as heterogeneous nucleation sites leading to inhomogeneous precipitation with a precipitate size of 100 nm as shown in Figure 3.3(c). Recently, Kumar et al. stated that the presence of non-conforming grains would increase the resistance to plastic deformation [2]. On similar lines, the presence of region I surrounded by region II can increase the yield strength but would also have a very high work hardening rate and lead to a brittle failure with the crack propagating through region I. This clearly imposes a limitation in a way that any one, either ductility, strength or the extent of homogeneity has to be sacrificed to improve the other by the existing wrought operations.

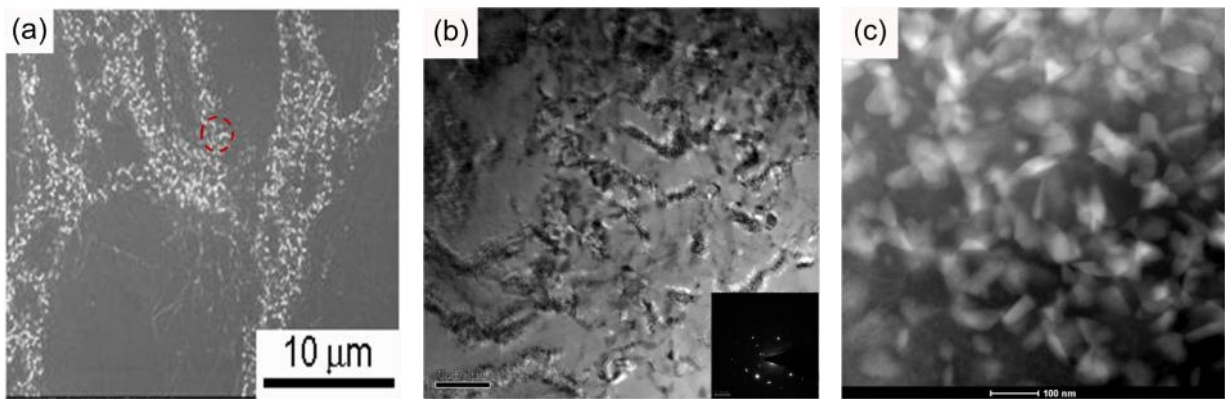


Figure 3.3. (a) SEM micrograph of alloy 1 showing the extent of inhomogeneity, and (b) enlarged image of the circled portion in (a). Diffraction pattern is shown in the inset and corresponds to extremely fine grains, (c) HAADF-STEM image showing coarsened precipitates

in the size range of 100-150 nm. These images have been recorded after peak aging at 180 °C for 60 hours.

Based on the micrographs shown in Figure 3.2, a major demarcation can be made with respect to the precipitate morphologies between alloy 1 and 2. Interesting floral shaped precipitates were observed in alloy 1 that coarsened and transformed to bug shaped precipitates after longer time. These floral precipitates with a size of 200 nm are currently hypothesized to consist of a high temperature β core that forms while cooling from the first reduction step followed by the shooting of β_1 arms on the prismatic planes during the second cooling step. However, such a feature was completely absent in alloy 2 that was rolled at a higher temperature. Such unique morphologies are highly encouraging and can pave way to designing microstructures for specific applications by controlling the processing route.

In contrast, alloys 3 and 4 did not recrystallize during the aging operation suggesting that the strain was below the critical value to initiate the nucleation of new grains. Secondly, alloy 4 showed the presence of precipitate free zones that increased in width after aging. The increase in ductility for alloy 4 after aging can be reasoned based on the increase in the width of the PFZ that would ease the movement of the dislocations. The sensitivity of the microstructure to the prior processing route can be appreciated by drawing a comparison between alloy 1 and 4. For similar thermal routines, a change in the extent of strain induced into the material by 10% causes a significant change in the ductility and a pronounced difference in the microstructure. Figure 3.4 compares the microstructure of alloy 4 with respect to alloy 1 as shown in Figure 3.3 after aging. The nature of precipitation is very distinct and the microstructure is representative throughout the

sample. Apart from the presence of PFZ's as shown in the SEM micrograph, the precipitates are plate shaped and are similar to β_1 . These precipitates are much coarse and have a long axis of 200 nm with the thickness corresponding to 50 nm. Figures (3.2-3.4) and Table 3.1 capture the entire essence of microstructural dependence on the processing route. These observations provide a profound insight into the path dependent sensitivity microstructural sensitivity in a Mg based WE43 alloy.

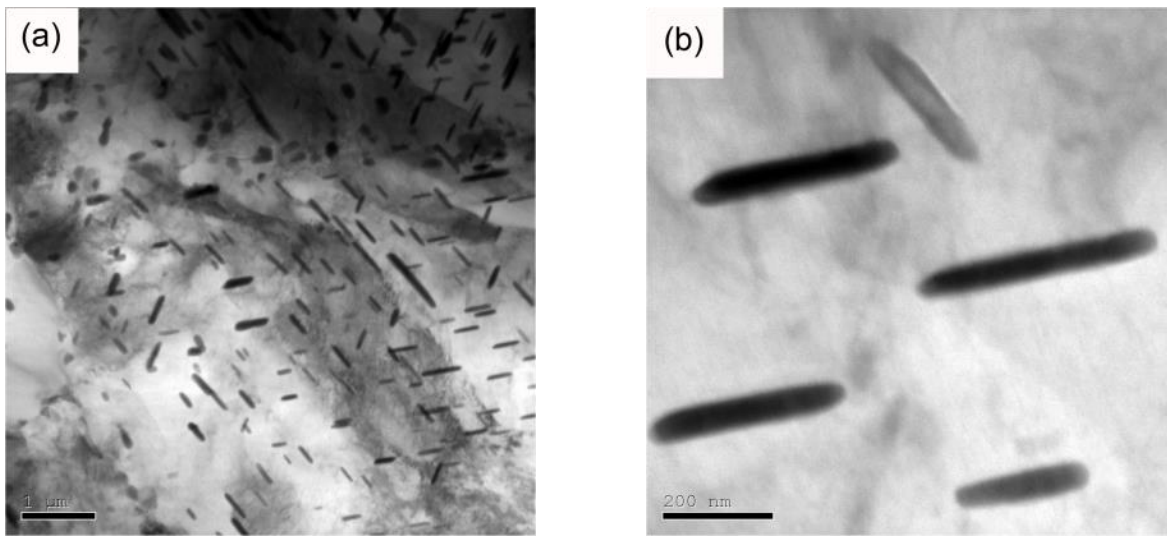


Figure 3.4. (a & b) Precipitate descriptors in alloy 4 after peak aging at 180°C for 60 hours.

Table 3.1. Comparison of mechanical properties and the microstructural characteristics as a function of rolling history

| Initial condition | Alloy 1 | | Alloy 2 | | Alloy 3 | | Alloy 4 | |
|----------------------|---------|-----|---------|-----|---------|-----|---------|-----|
| Yield strength (MPa) | 255 | 305 | 250 | 332 | 238 | 280 | 252 | 265 |
| U T S (MPa) | 301 | 359 | 286 | 379 | 280 | 358 | 294 | 320 |

| | | | | | | | | |
|---|--|-----|--|------|---|------|---|------|
| % E | 10.7 | 1.5 | 15.3 | 2.75 | 25.9 | 20.2 | 23.2 | 25.6 |
| Microstructural descriptors (As rolled) | Banded, intragranular precipitates, floral morphology | | Fine non-strengthening precipitates at grain boundary, greater supersaturation of solute elements (ΔX) | | Caterpillar morphology of intermetallics ($Mg_{41}Nd_5$), least precipitation | | Grain boundary precipitates of $Mg_{14}Nd_2Y$, presence of PFZ | |
| As rolled (AR) + aged ($180^\circ C/60h$) | Static recrystallization, necklace structure at grain boundaries | | Extensive precipitation at the boundaries and interior | | Lower degree of recrystallization, higher inhomogeneity | | Increase in the precipitate free zone width | |

3.2.2 Effect of Initial Microstructure on the Nugget Efficiency after FSW

In the previous section, it was shown that the microstructural identity was dependent on the prior thermo-mechanical routine experienced. Initial microstructure is one of the key variables that determines the final microstructure and hence the properties after FSW.

3.2.2.1 Mechanical Properties and Nugget Efficiency

To assess the effect of initial microstructure on mechanical properties, all the other variables were unchanged during FSW. Since nugget efficiency was a major parameter that was studied, it is of interest to define this term. Nugget/stir zone efficiency (SZ) can be defined as the ratio of yield strength in the nugget to the yield strength in the base material (initial microstructure). In the present case, the effect of initial microstructure was studied by comparing the strength at a higher heat input (2000/102) for different initial microstructures. Figure 3.5 shows this comparison graphically and in the tabular form.

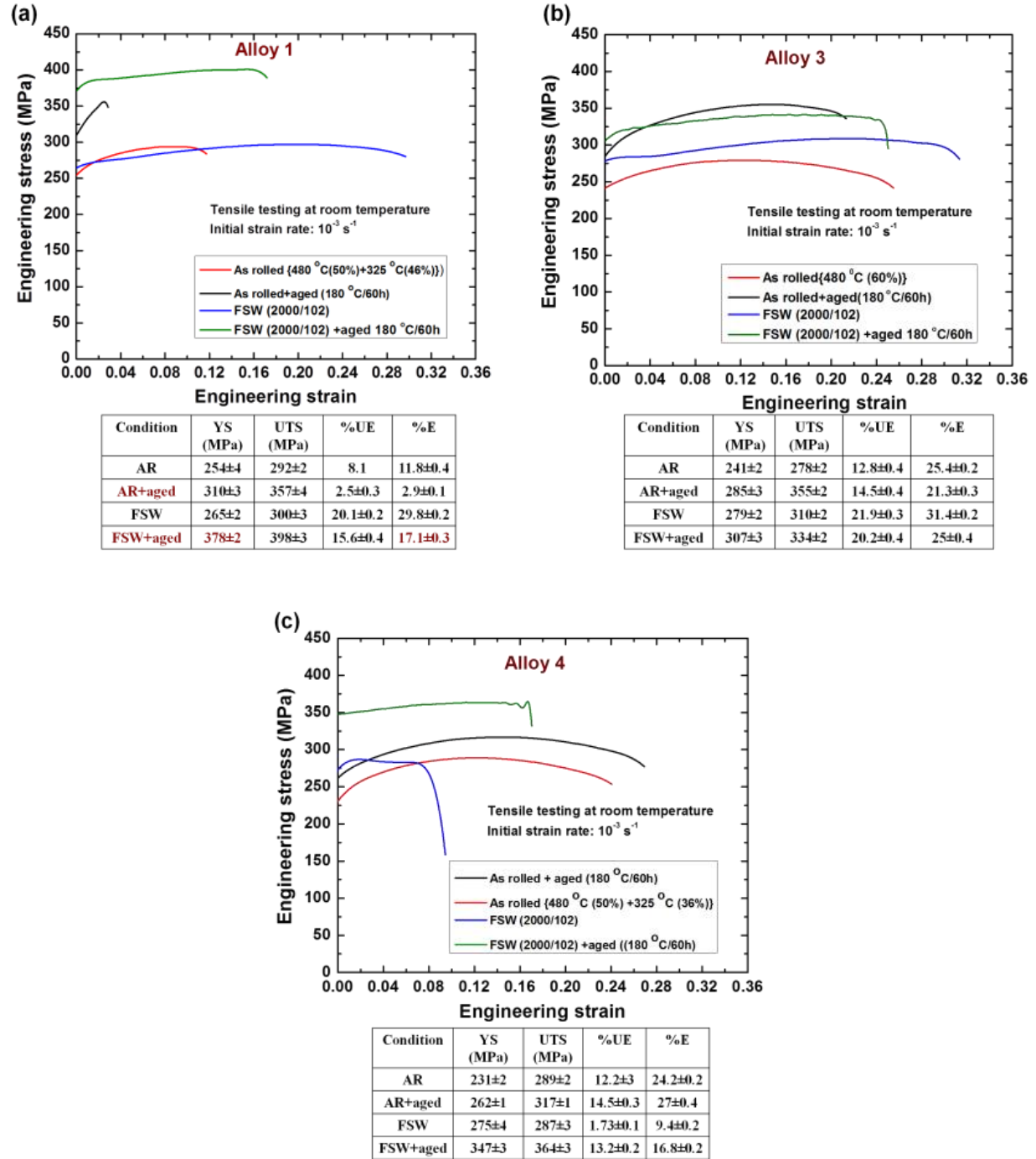


Figure 3.5. (a, b & c). Influence of initial microstructure on the mechanical properties during friction stir welding at 2000 rpm and 102 mm/min. The initial microstructures were in their peak aged condition. Post weld aging treatment was performed after FSW for further strengthening.

Peak aging was done for all the conditions at 180°C for 60 hours.

Several conclusions can be made based on Figure 3.5. Firstly, in comparison to the base material (ARA), a significant increase in strength and ductility was observed in the FSW+aged condition (FSWA). Such an increase in strength after post aging implies a higher amount of solute retention after FSW that was available during the later aging step. Higher temperatures coupled with a greater strain rate would dissolve the existing precipitates when welded at such a high rotational speed. The increase in strength after post aging indicates that the cooling rate was sufficient to quench the solute within the solid solution. Section 3.2.2.2 shows the TEM micrographs supporting the aforementioned statement. Moreover, the nugget efficiency was calculated to be 85% and 100% in the FSW and FSWA condition indicating the stir zone to be stronger in comparison to the base. Furthermore, a dramatic ten-fold increase in ductility was observed after FSW. Such high levels of ductility can be correlated to the favorable texture for slip and extremely fine grain sizes resulting after FSW. Previous studies by Koike et al. showed that dynamic recovery indeed took place during tensile deformation due to the cross slip of “a” type dislocations on the non-basal planes in an AZ31 alloy. The tendency to cross slip increased as the grain size decreased and was attributed to the intense grain boundary incompatibility stresses resisting further deformation [3]. These compatibility stresses reduce the yield anisotropy factor that is defined as the ratio between the non-basal and basal Schmid factor favoring the non-basal dislocations [3]. Calculations on the yield anisotropy factor by considering a few grains after FSW in alloy 1 is shown in the later part of this section. Since FSW leads to a finer grain size, greater non-basal activity can be visualized due to increased stress concentration. This in turn would have a bolstering effect on the ductility.

However, in the case of alloy 3, the increase in strength after post aging the FSWed sample is minimal but the ductility levels are higher than alloy 1. In addition, the natures of the curves are also very similar indicating a similar type of deformation mechanism. The nugget efficiency for this condition after FSW and FSWA was calculated to be 94% and 100%, respectively. In contrast, alloy 4 shows a unique stress-strain behavior after FSW that is significantly different from alloys 1 and 3. Unlike the other two conditions, a drop in ductility is observed after FSW of alloy 4 that restores in the FSWA condition. Nevertheless, an appreciable increase in strength was observed in the FSWA condition and the nugget efficiency was tabulated as 100%. after FSW and FSWA.

From the preceding discussion, it was evident that texture plays a major role in determining the extent of deformation. Moreover, the limited number of slip systems aided by a low CRSS for the activation of basal slip $(0001) \langle 11\bar{2}0 \rangle$ determines the ductility in magnesium alloys [4]. Figure 3.6 compares the texture between the base material and after FSW in alloys 1 and 4. These pole figures show the effect of initial texture on the final texture. A color coded intensity bar is located adjacent to these pole figures and represent the relative density of the poles recorded in the RD/WD - ND frame of reference. Texture strength is proportionate to the numbers mentioned on the intensity bar. As shown in Figures 3.6 (a,b), the $\langle 0001 \rangle$ poles are oriented at an angle of 30 and 20 degrees from the ND towards the TD. In addition a basal split is observed in ARA and is characteristic of the rare earth effect in Mg alloys. From Figures 3.6 (c,d), the basal poles are tilted at an angle of 38 degrees from ND toward RD/WD and 85 degrees from ND towards RD/WD. This implies that the basal planes are nearly parallel to ND in case of alloy 4 after FSW and tilted by 10 degrees in the direction of TD. Such an orientation would be

very hard to slip and is evident from the Schmid factor of 0.26 for basal slip with the tensile direction parallel to RD/WD.

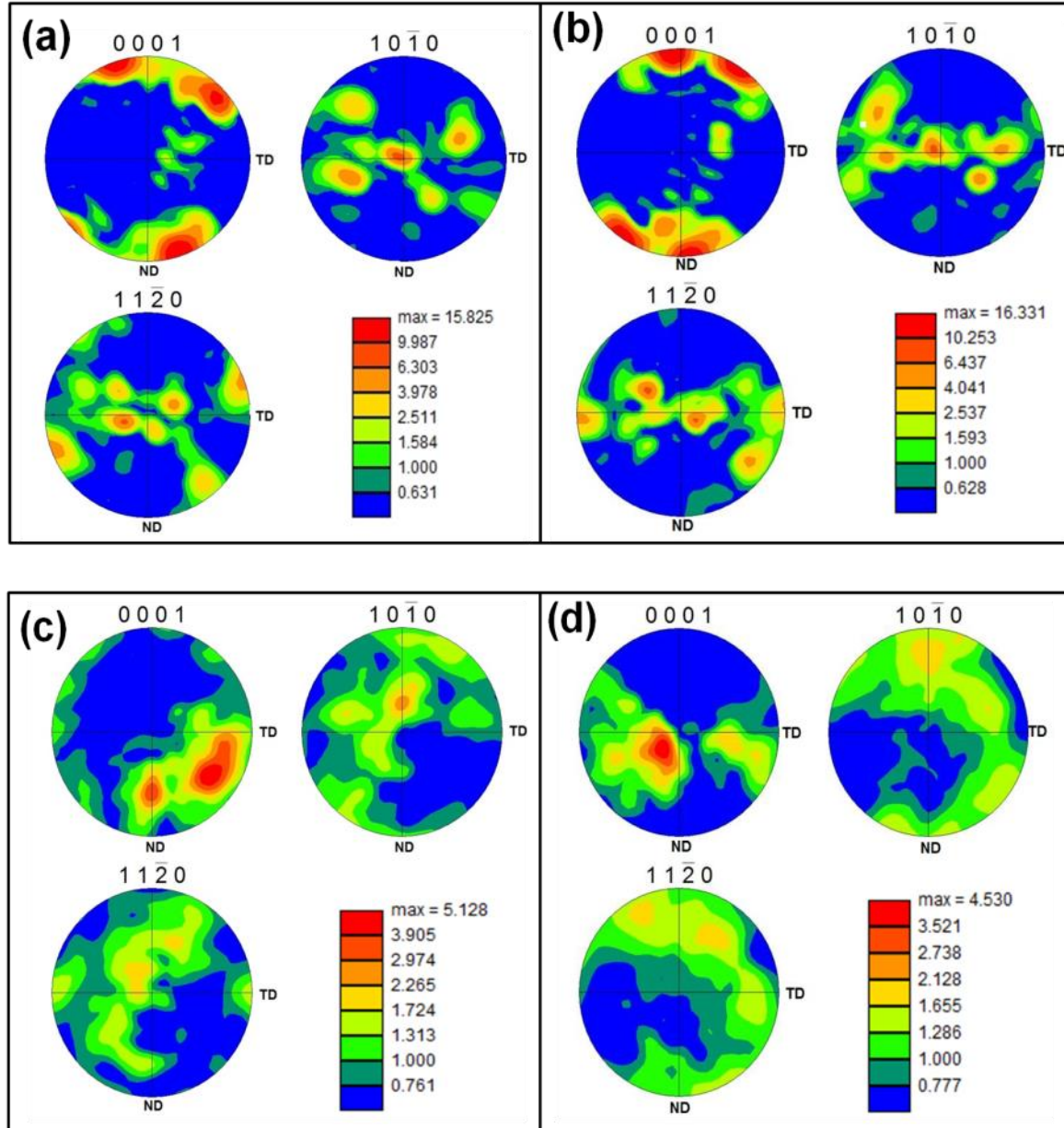


Figure 3.6. $\langle 0001 \rangle$, $\langle 10\bar{1}0 \rangle$ and $\langle 11\bar{2}0 \rangle$ pole figures of (a) alloy 1 (ARA), (b) alloy 4 (ARA), (c) alloy 1 (FSWA) and (d) alloy 4 (FSWA).

This reasons the lower ductility observed in case of alloy 4 after FSW. In comparison to alloy 4 subjected to FSW, alloy 1 would be amenable to slip due to the favorable orientation of basal planes and the calculation for Schmid factors yields a higher value of 0.35. These Schmid factors are in conformity with the observed tensile stress-strain curves for alloy 1 and alloy 4 in Figure 3.5.

In combination with the texture, finer grain size was also mentioned to play a crucial role in increasing the ductility after FSW. A few grains in alloy 1 were studied after FSW using the TSL-OIM software to show the decrease in the yield anisotropy factor and the preferred activity of non-basal slip. Figure 3.7 shows the grains that were examined and tabulates their respective yield anisotropies.

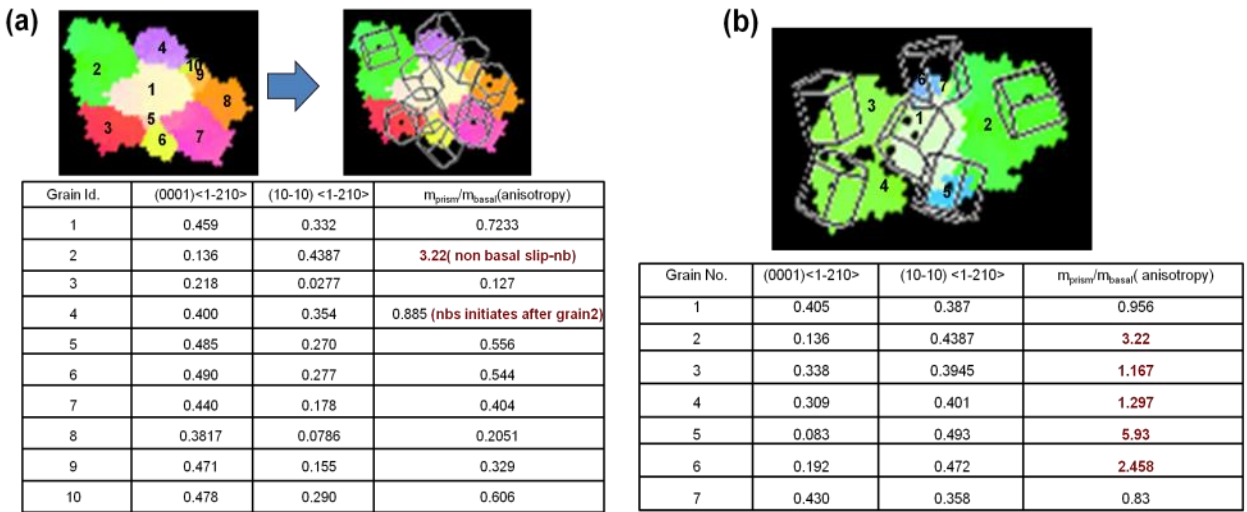


Figure 3.7. Yield anisotropy factor calculated by using the TSL-OIM software for alloy 1 after FSW at 2000 rpm and 102 mm/min (2000/102). (a) cluster showing higher tendency of basal slip, and (b) cluster showing higher tendency of non-basal slip.

There are two different clusters as seen from the figure. Figure 3.7 (a) shows the yield anisotropy values lesser than 1 in most of the cases whereas Figure 3.7 (b) shows the values to be greater than 1. Since, the values are greater than 1 in Figure 3.7 (b), non-basal slip would be highly favored and the extent would be maximum in grain 5. In case of Figure 3.7(a), non-basal activity is only favored in grain 2 as highlighted. The Schmid factors in the present case have been evaluated considering the tensile direction parallel to the rolling direction for comparison with the observed tensile tests. Figures 3.6 and 3.7 rationalize the increased levels of ductility based on the texture and the tendency for non-basal slip due to finer grain size.

3.2.2.2 Effect of Welding Parameter on the Microstructure and Mechanical Properties after FSW

Figure 3.8 shows the hardness at two different heat inputs and compares the effect of process parameters on the maximum hardness.

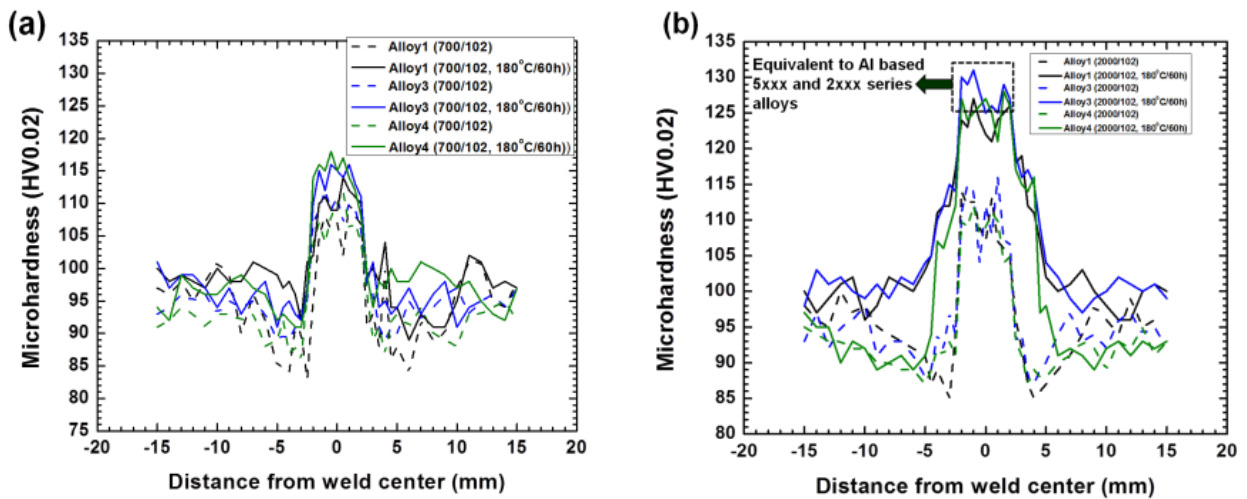


Figure 3.8 Hardness profiles across the centerline in the Y-Z plane for specimen welded at (a) 700/102 and (b) 2000/102.

It can be seen that post aging after FSW in the case of 2000/102 leads to hardness levels

similar to Al 2XXX alloys whereas 700/102 results in a lower hardness. Figure 3.9 shows the effect of the process parameters on the strength and ductility in alloys 3 and 4, respectively. A difference of 100 MPa is observed for alloy 4 after FSWA at two different heat inputs. From the present study, it is evident that a higher heat input leads to better strength values. The nugget efficiencies for alloys 3 and 4 processed using a rotational rate of 700 rpm and a traverse speed of 102 mm/min after FSW is 90, and 98% respectively. These numbers change to 78 and 98 % after post aging the respective conditions. These nugget efficiencies are much lower than their counterparts processed at a higher heat input (2000 rpm, 102 mm/min), where the efficiency is greater than 100 %.

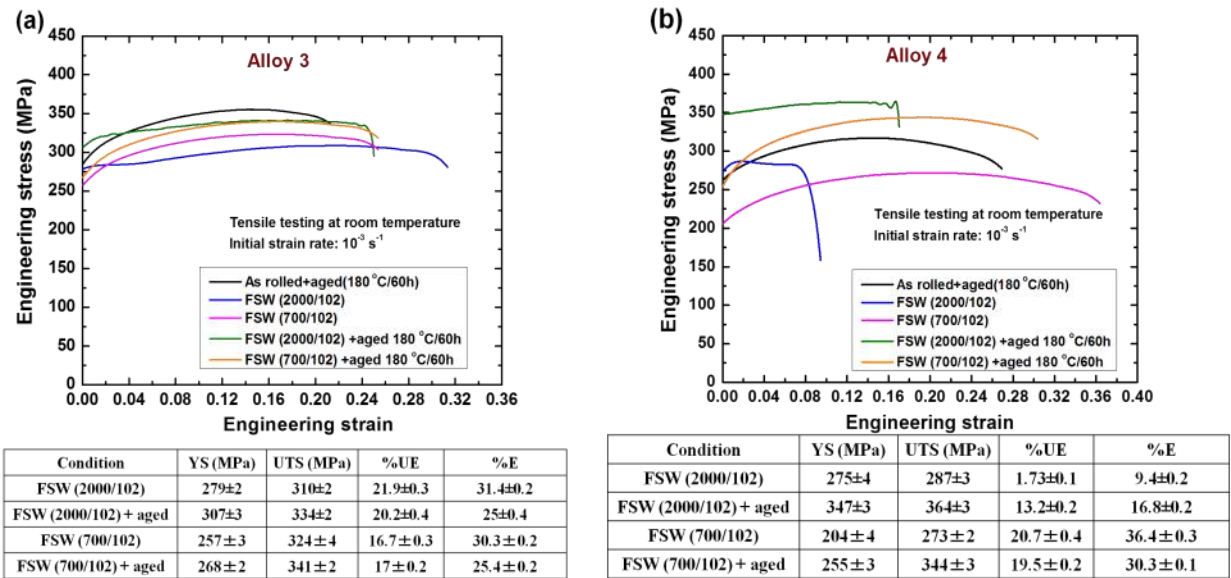


Figure 3.9. Effect of process parameters on the strength and ductility of (a) alloy 3, (b) alloy 4.

Though the nugget efficiency and strength are lower, the strain hardening ability is higher for a sample welded at 700/102 and has a net flow stress of 67 MPa in the case of alloy 3. However, the net flow stress is 30 MPa for alloy 3 processed at 2000/102. This behavior is captured in the nature of the tensile curves exhibiting a constant stress level at 2000/102 whereas

700/102 is markedly different showing similar trend as the rolled condition. A major difference in ductility can be noted in alloy 4 after FSW at two different welding conditions. As seen in Figure 3.9, welding at 2000/102 leads to a pronounced drop in ductility whereas welding at 700/102 exhibits good levels of ductility. Since, alloy 4 is very sensitive to the heat input, further microstructures to reason the nugget efficiency would be based on this alloy. It was mentioned in section 3.2.2.1 that a higher strength at 2000/102 can be attributed to the higher amount of solute retention and a greater dislocation density. In comparison to a sample welded at 2000/102, the tendency to coarsen is higher at 700/102 and knocks down the strength and hence the nugget efficiency. Figure 3.10 shows the precipitate descriptors in alloy 4 which was welded using a lower and higher heat input and reasons the observed values.

As shown in Figure 3.10 (a), coarsened precipitates belonging to the size range of 100-200 nm are formed during welding at 700/102. On further probing, these precipitates were found to be the equilibrium β precipitates (Mg_{12}NdY) with an orientation relationship of $[0001]_{\alpha} // [1-1-2]_{\beta}$ and $(-111)_{\alpha} // (10-10)_{\beta}$. These precipitates would have formed during the cooling cycle leading to a depletion of solute in the solid solution and would be ineffective in blocking the dislocations.

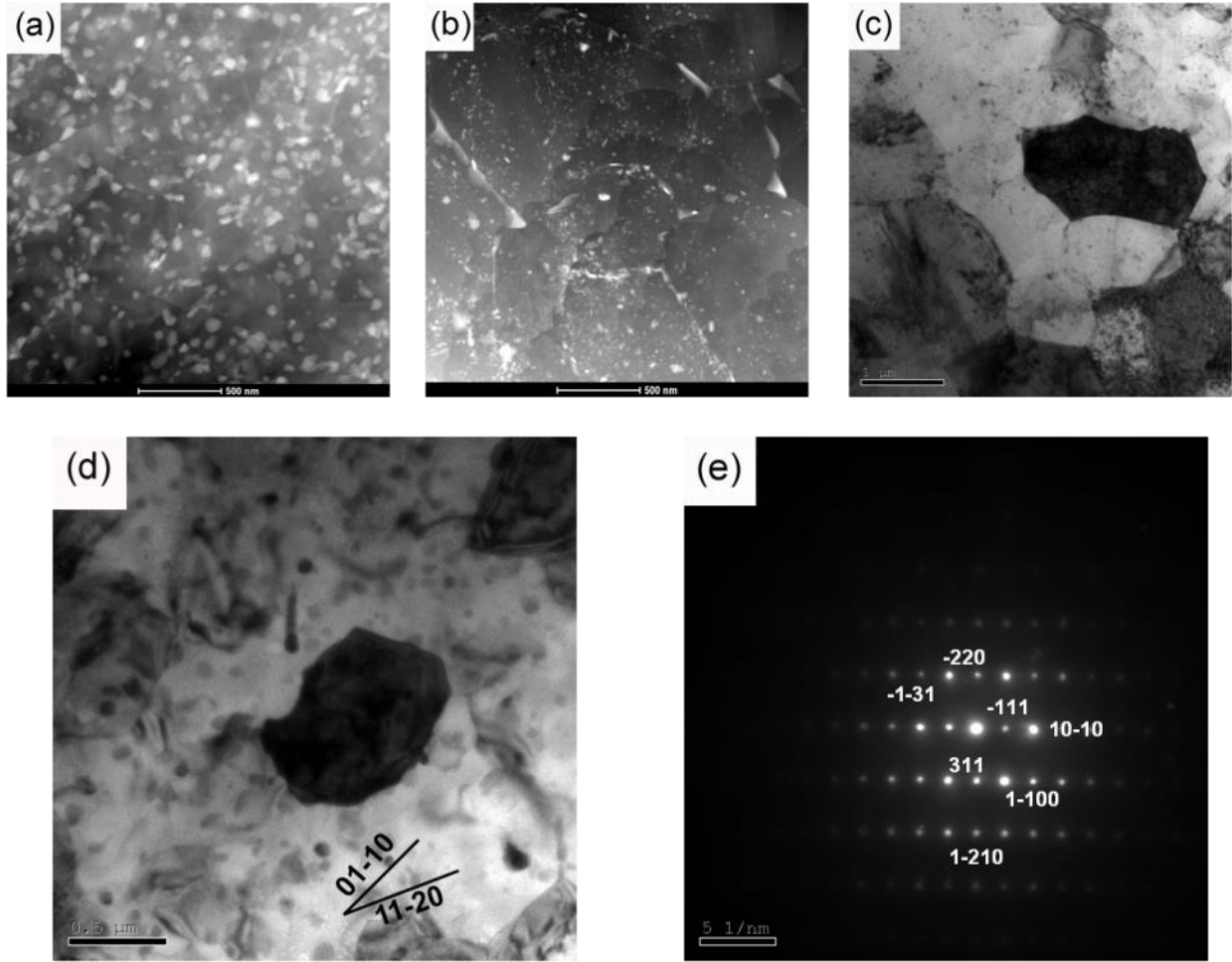


Figure 3.10. HAADF-STEM images showing the precipitate descriptors after FSW for alloy 4 welded at (a) 700/102, (b) 2000/102. Bright field images showing (c) higher amount of retained dislocation density in a sample welded at 2000/102, (d) the diffracting grain with the image recorded parallel to [0001] and (e) diffraction pattern showing the orientation relationship of the coarsened precipitates with the matrix. These precipitates are found to the equilibrium β precipitates (Mg_{12}NdY) with an orientation relationship of $[0001]_{\alpha} // [1-1-2]_{\beta}$ and $(-111)_{\alpha} // (10-10)_{\beta}$

3.2.3 Strain Rate Sensitivity of Rolled WE43 Alloy

Section 3.2.2 studied the tensile deformation behavior at a strain rate of $1 \times 10^{-3} \text{ s}^{-1}$. It was

shown earlier that the rolled microstructures were extremely sensitive to their rolling history. A wide variation in the microstructure led to various combinations of strength and ductility. Alloys 3 and 4 in the ARA condition were subjected to different strain rates to examine their strain rate sensitivity (SRS). Figures 3.11 (a&b) compares the SRS from the strain rate jump test between alloys 3 and 4.

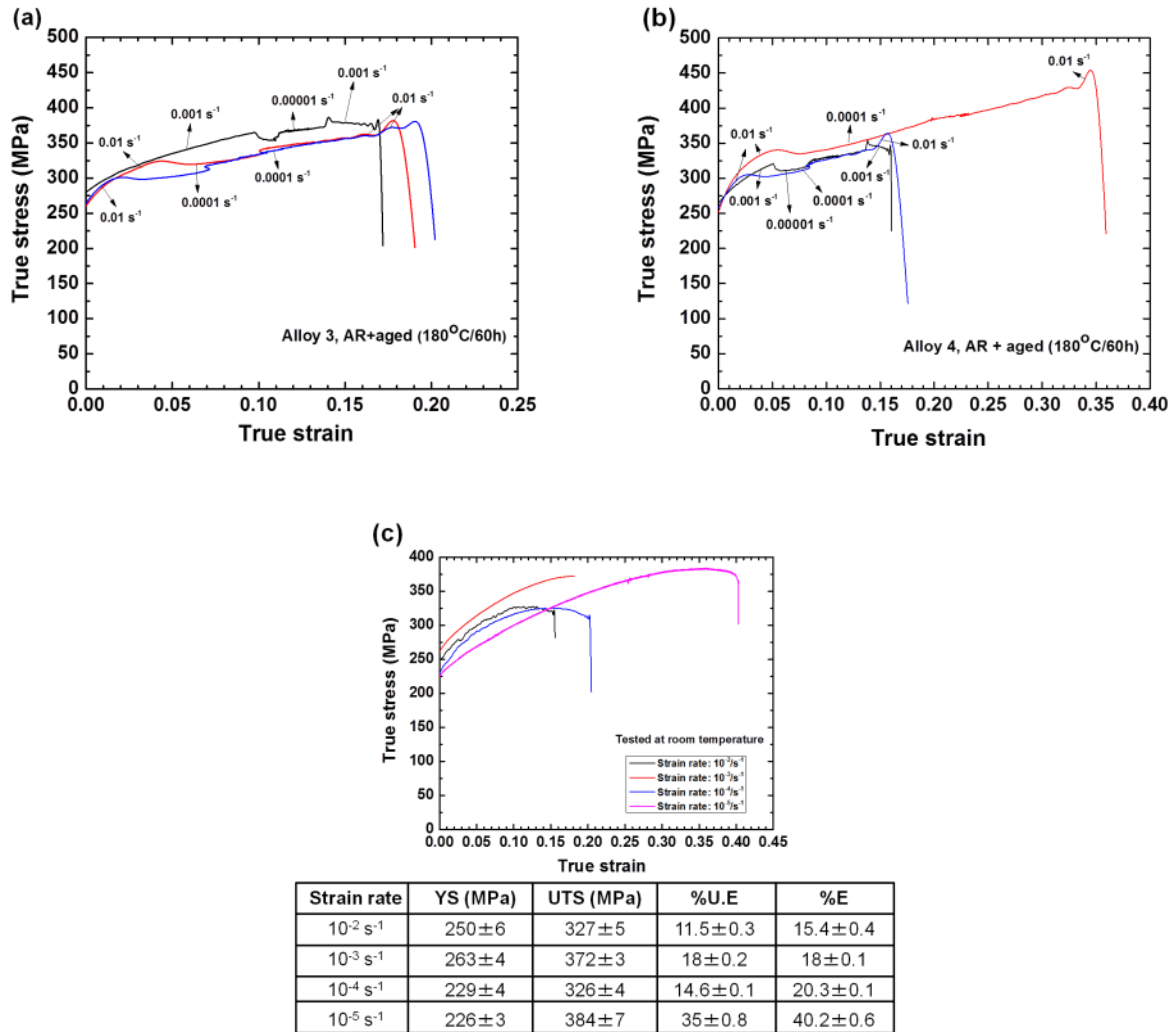


Figure 3.11. Strain rate jump test in the ARA condition for (a) alloy 3, (b) alloy 4. Effect of rate of loading on the tensile properties in, (c) alloy 4.

Alloy 4 showed a much higher dependence from the strain rate jump tests. Following this, the samples of alloy 4 in the ARA condition were tested at different strain rates independently. Figure 3.11 (c) shows the true stress-strain behavior of this alloy at different strain rates and tabulates the numerical values. The elongation values were highly susceptible to the rate of loading and are due to the composite microstructure in this alloy as shown in Figure 3.2. The varying rate of dislocation accumulation at the PFZ and the grain interior with respect to the strain rate controls the level of elongation. Therefore designing materials with such a microstructure in a WE43 alloy would not be suitable for applications involving varying loads. Usually, a generalized assumption is made with respect to the SRS in Mg alloys. However, such an assumption may not hold true at all levels and would strongly be a function of the microstructure.

3.3 Conclusions

The effect of the initial microstructure and welding parameter on the nugget efficiency of a WE43 alloy was investigated. Based on the study, the following conclusions are made:

- 1) The microstructure is extremely sensitive to the thermo-mechanical route employed during rolling. A minor variation in the microstructure manifests itself to a greater magnitude of variation in strength and ductility.
- 2) Different precipitate morphologies including floral and bug shaped are observed in alloy1. These morphologies signify the potential to obtain a wide range of precipitate descriptors.
- 3) Rolled microstructures show a greater extent of inhomogeneity that is exacerbated by a greater extent of precipitation on the recrystallized grains. Inhomogeneity extent is dependent on the deformation specifics. Generalization of rolled microstructures is not correct.

- 4) Nugget efficiency values have been tabulated for alloys 1, 3 and 4 with a higher heat input showing higher strength
- 5) A maximum yield strength of 380 MPa was achieved in alloy 1 after post aging at 180°C for 60 hours
- 6) Strain hardening was greater for a sample welded at 700/102 in comparison to the sample welded at 2000/102
- 7) Coarser precipitates with preferential orientation have been observed for alloys welded at lower heat input. On the other hand, finer precipitates with greater solute retention is observed in alloy 4 welded at 2000/102
- 8) The initial microstructure has a significant impact on the microstructural evolution during FSW with alloy 1 showing the highest strength. However, the nugget efficiency is 100% in most of the cases.
- 9) Rate of loading had a significant effect on ductility in alloy 4 and is due to the composite microstructure

3.4 References

1. S.K. Panigrahi, W. Yuan, R.S. Mishra, R. Delorme, B. Davis, R.A. Howell, K. Cho, “A study on the combined effect of forging and aging in Mg–Y–RE alloy”, *Materials Science and Engineering A* 530 (2011) 28-35
2. N. Kumar, N. Dendge, R. Banerjee, R.S. Mishra, “Effect of microstructure on the uniaxial tensile deformation behavior of Mg–4Y–3RE alloy”, *Materials Science and Engineering A* 590 (2014) 116-131.

3. J. Koike, T. Kobayashi, T. Mukai, H. Watanabe, M. Suzuki, K. Maruyama, K. Higashi ,
“The activity of non-basal slip systems and dynamic recovery at room temperature in
fine-grained AZ31B magnesium alloys”, *Acta Mater.* 51 (2003) 2055–2065.
4. X.Y. Lou, M. Li, R.K. Boger, S.R. Agnew, R.H. Wagoner, “Hardening evolution of
AZ31 Mg sheet”, *Int. J. Plast.* 23 (2007) 44-86.

CHAPTER 4

FRICTION STIR ADDITIVE MANUFACTURING FOR HIGH STRUCTURAL PERFORMANCE THROUGH MICROSTRUCTURAL CONTROL IN AN MG BASED WE43 ALLOY[‡]

Overview: In chapter 2, the major highlight was the ability to achieve high strength in a WE43 alloy after FSP. Driven by these initial results, in this chapter friction stir additive manufacturing (FSAM) is introduced as a potential technique to attain structurally efficient magnesium alloys. In this study, a multilayered stack of an Mg based WE43 alloy was built using FSAM at two different welding parameters. Formation of defects is sensitive to the heat input. In addition, dynamic recrystallization led to finer grain size (2-3 μm). Such fine grain size coupled with desirable precipitate characteristics culminated in superior mechanical properties. Maximum hardness of 115 HV was obtained in as-fabricated state and increased to 135 HV after aging. These levels are similar to Al 2XXX alloys. In fact, in terms of strength, it translates to 400 MPa and 17 % ductility and is significantly higher than the base material subjected to aging. Mechanical properties have been correlated with detailed microstructural observations. Texture is discussed for a higher heat input sample using orientation imaging microscopy. The objective of this chapter is to study the microstructure and correlate it to the properties layer wise and show that it is possible to achieve high strength WE43 builds.

4.1 Introduction

4.1.1 Current Metal based Additive Manufacturing Techniques and Key Challenges

[‡] This chapter is presented in its entirety from S. Palanivel, N. Phalgun, B. Glass, R.S. Mishra, “Friction stir additive manufacturing for high structural performance through microstructural control in an Mg based WE43 alloy”, *Materials & Design* 65 (2015): 934-952 with permission from Elsevier.

Additive manufacturing is touted to be the most significant manufacturing approach to have emerged over the past few decades. In its simplest form, additive manufacturing can be defined as, “the process of joining materials to make objects from three-dimensional (3D) model data, usually layer upon layer, as opposed to subtractive manufacturing methodologies such as machining” [1]. The current state of the additive manufacturing technology predicts tremendous economic growth in the market and an asset of \$3bn by 2016 [2]. Such a spur in the field of additive manufacturing was realized by the addition of several techniques and are comprehensively documented in a few review papers [3,4]. Though, additive manufacturing has come to the forefront by virtue of several innovations that have paved its way, numerous key challenges persist.

To highlight these challenges, an effort has been made to capture the characteristics of various existing technologies in a concise yet informative way. Figure 4.1 details the temporal evolution of the metal based additive technologies enlisting their advantages and disadvantages. Special attention is laid on the specific characteristics like layer thickness, build volume, build rate and the key challenges faced by these techniques.

As a paradigm, it would be suitable to consider a few techniques to elaborate on the concerns faced by several metal based technologies. At present, majority of multilayered metal fabrication methods are limited to laser based techniques, electron beam melting and shaped metal deposition [5-8]. Though a good surface finish is obtained by direct laser deposition, the process is limited by higher operating costs, small build volumes and low production rate [8]. Electron beam deposition leads to better mechanical properties at the expense of surface quality

but is limited by the cost factor relating to the provision of inert atmosphere. On the other hand, shaped metal deposition leads to higher production rates at the expense of surface finish and dimensional accuracy. Another issue that pertains to all the three techniques is contamination by the use of powder based substrate. Other alternative techniques like electroforming are limited by longer lead times and poses environmental hazards in the form of toxic slurry.

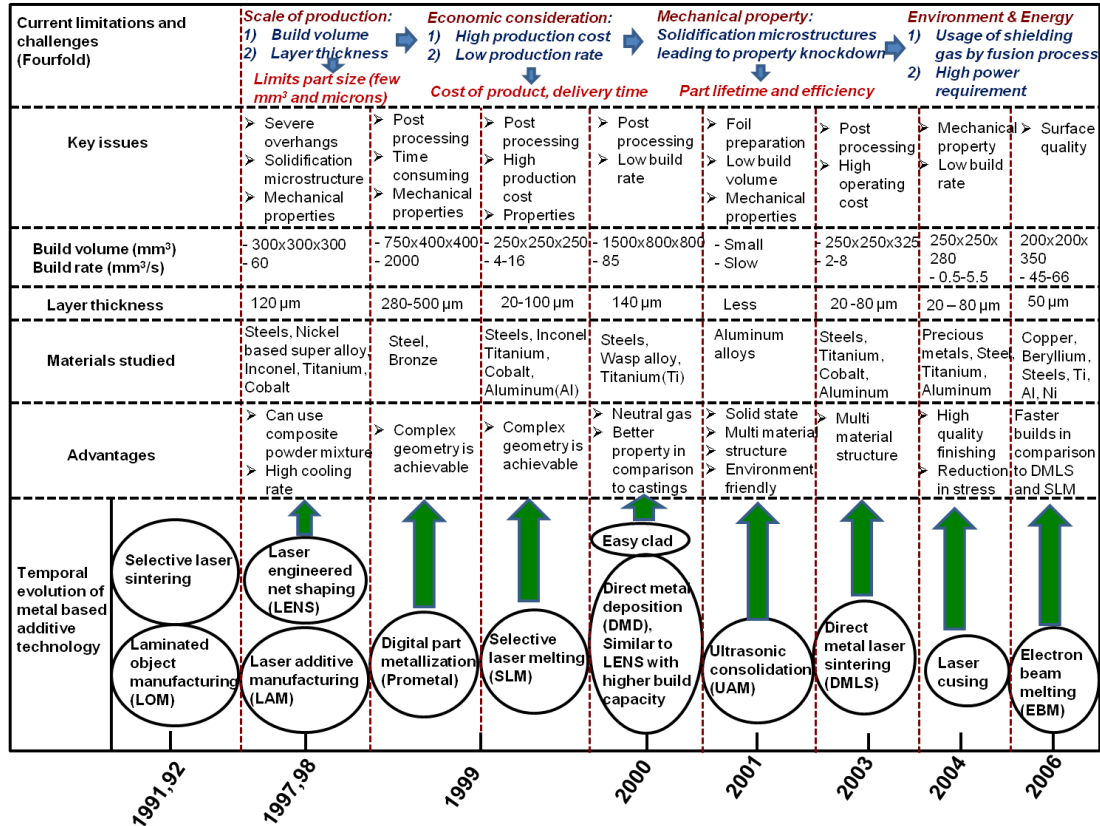


Figure 4.1. Temporal evolution of metal based additive technologies and a listing of key challenges [3-9].

Based on the foregoing discussion and from Figure 4.1, four key challenges that are germane to the field of additive manufacturing have been identified; (i) scale of production, (ii) cost of production, (iii) structural performance, and (iv) environment and energy. Therefore, industrial adoption of additively manufactured components requires overcoming these challenges

and hence set up the objective of this chapter. In the current study, focus is laid on highlighting friction stir additive manufacturing (FSAM) as a potential route to answer one such challenge “structural performance”.

4.1.2 Structural Performance: Future of Additive Manufacturing

Replacement of conventional techniques by the additive technology in the aerospace and automotive sector is a goal being pursued. A few parts pertaining to the cabin and cockpit have already been successfully installed and are attributed to the ability to fabricate complex shapes [10]. However, such applications are limited. Though, complicated shapes help in product customization, it is time to look beyond complex geometries to expand the horizons of additive manufacturing and cater to the stringent performance requirements laid by the aviation industry.

The ability to achieve higher structural performance is subjective to the ability to achieve model microstructures. A major concern pertaining to operations involving liquid based additive process is porosity and other solidification related defects [11]. In addition, microstructures are extremely inhomogeneous and mechanical properties are spatially dependent [12-15]. This has a tremendous effect on the part efficiency, lifetime and impairs additive technology to make an impact in the automobile and aviation sector. Exerting a greater control over the microstructure necessitates the incorporation of a solid state technique for structural components, which is capable of addressing a majority of the concerns present in conventional additive manufacturing techniques. In this regard, solid state ultrasonic additive manufacturing has been the frontline technology for solid state additive manufacturing [16]. Though, it has the ability to produce multifunctional, multimaterial parts, it is currently stifled by its own limitations. A fundamental

requirement for any structural material is to possess a homogeneous microstructure with enhanced properties. Ultrasonically fabricated components exhibit inferior properties in comparison to the bulk material. Moreover, substantial differences exist between interfacial and non-interfacial microstructures leading to inhomogeneous properties along specific sites and direction [17,18].

4.1.3 Mg Alloys: Lightweighting for Structural Applications

Recently, a major emphasis has been laid on enhancing the structural performance by using lighter materials. According to estimates, weight reduction in the aircrafts has led to a savings of 10 million gallons of fuel on an annual basis [19]. In addition to increased fuel efficiency, a reduction in CO₂ emission is also realized. In fact, the current impact of additive manufacturing in aviation sector is attributed to the ability to fabricate shapes that lead to lightweighting by virtue of design. One such example is the ability to fabricate complex shapes like the honeycomb patterns. In terms of material selection, the best opportunity to reduce weight is offered by Mg alloys that possess a density of approximately two thirds that of aluminum and one quarter that of steels.

At present, several concerted efforts to push the limits of Mg alloys are being attempted by various agencies and researchers [20,21]. This clearly indicates the potential it holds for the future. The ability to produce high performance Mg alloys is a challenge. By performance, the current work deviates from the conventional definition of density normalized performance to cost normalized performance. To realize the use of Mg alloys in aerospace and automotive industries, it is imperative that the strength be raised at a lower cost. FSAM being a versatile

technique has the capability to realize these objectives. In the following work, an Mg-4Y-3Nd (WE43) alloy is used. This alloy has been selected to demonstrate the versatility of the process and obtain higher strength by virtue of precipitation hardening.

Taking into account the discussion leading to this point, the purpose of this chapter has been categorized into four heads. These pertain to; 1) introducing friction stir additive manufacturing (FSAM) as a potential tool to fabricate multilayered structures and in the present case a built stack of a Mg based WE43 alloy, 2) studying the evolution of defects as a function of welding parameters, process forces and tool geometry, 3) correlating the variation in strength and assessing its sensitivity with respect to the welding parameter, and 4) characterizing and comparing the evolution of interfacial and non-interfacial microstructure as a function of welding parameter. The significance of this research lies in its potential to create an additive manufacturing technology capable of fabricating high structural performance lightweight materials for industrial applications.

4.2 Process Description and Experimental Procedure

4.2.1 Friction Stir Additive Manufacturing (FSAM)- Process Description

Friction joining for the purpose of additive manufacturing was patented in 2004 by White [22]. However, it is only recently that friction surfacing and friction welding have been shown as an possible route to build 3-D layers [23,24]. The first report on friction stir technology as a tool to additively manufacture components was published by Airbus in 2006 [25]. Airbus [25] and Boeing [26] claimed that the technology is capable of addressing two of the specified challenges, (i) achieving high throughput leading to faster production rates and (ii) less material wastage.

Following these claims, further studies on friction stir additive manufacturing has not been pursued leading to a lack of literature on FSAM. Table 4.1 draws a comparison between ultrasonic additive manufacturing, fusion based techniques and FSAM highlighting the key benefits of FSAM over the other two techniques. Distinctive characteristics of FSAM coupled with a competitive edge over the existing techniques render it as an ideal tool to leverage structural efficiency. However, FSAM also has a few disadvantages, which include: (i) scale of production where the build rate is limited by the machine dimensions and traverse speed of the tool, (ii) clamping the material is an issue, (iii) tool wear occurs over time, and (iv) significant amount of residual stresses can accumulate within the build.

Table 4.1. Key potential benefits of friction stir additive manufacturing as compared to ultrasonic additive manufacturing and fusion based additive techniques [13-19]

| Ultrasonic additive manufacturing (UAM) | Friction stir additive manufacturing | Fusion welding processes |
|--|--|---|
| <ul style="list-style-type: none"> • Build volume is limited by material thickness (Stiffness issue). • Only materials that can be rolled into foils can be built leading to limited material selection. • Preparation of foils is costly and time consuming. • Affected by linear weld density. • Difficult to bond materials with high work hardening rate. • Bonding is achieved by plastic deformation around the asperities. • Exhibit marginal fraction of the bulk | <ul style="list-style-type: none"> • Ability to fabricate large components. • Faying surface contamination is not as vital as in UAM. • Ability to bond a variety of materials that are rendered difficult by fusion welding and UAM (wide range of material selection). • Weld formation is dictated by process forces and tool geometry. • High degree of reproducibility. • Excellent metallurgical property in joint area • Ability to produce variable microstructures for specific applications (process flexibility). • Judicious use of materials leading to low buy | <ul style="list-style-type: none"> • Shielding gas and surface cleaning is required. • Shrinkage problems coupled with high residual stresses. • Poor metallurgical and mechanical properties due to directional and undesirable microstructures (low structural performance). • Environmental concerns and energy inefficient. • Loss of alloying elements. |

| | | |
|----------------------|---------------|--|
| material properties. | to fly ratio. | |
|----------------------|---------------|--|

Friction stir additive manufacturing (FSAM) is a modification of a well-established technique of friction stir welding (FSW). Therefore, the fundamentals of the process are similar and differ in their respective functions. The basic concept of FSAM is remarkably simple. A non-consumable rotating tool with a custom designed pin and shoulder is inserted into the overlapping surfaces of sheets or plates to be joined and subsequently traversed along the joint line. Figure 4.2 shows a self-explanatory schematic of the FSAM process labeling the process definitions for the tool and workpiece. Furthermore, the tool used in the current study has been shown adjacent to the schematic.

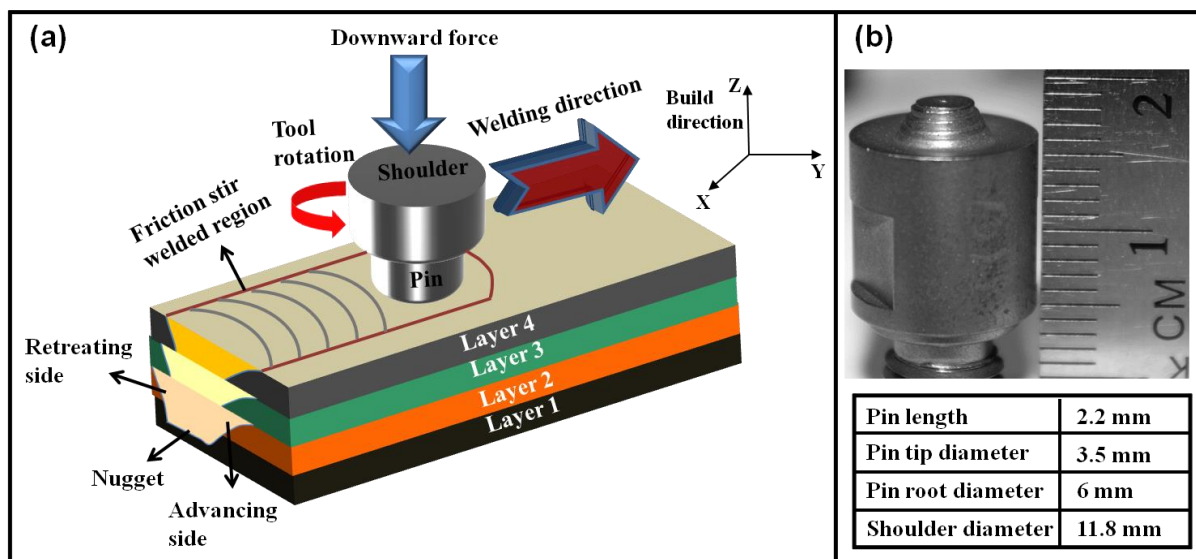


Figure 4.2. (a) Schematic illustration of the friction stir additive manufacturing (FSAM) process. Note that the build direction is perpendicular to the welding direction. (b) Photograph and dimensions of the tool used in the current study.

The heat necessary to weld the material is supplied by the frictional contact between the

shoulder and the workpiece coupled with intense plastic deformation achieved by the motion of the pin. Formation of weld nugget is facilitated by the movement of material from the front end to behind the pin and the macro shape is dependent on the geometrical features of the pin. From the virtue of the process, the joints are produced in solid state and involve no melting. For further details on the fundamentals of FSW, the reader is encouraged to refer the review article by Mishra and Ma [27].

In this study, a multilayered build is obtained by sequentially stacking layers over the previously welded layer and performing the lap joint. The final thickness of the joint can be controlled by the, (i) thickness of the sheets/plate, and (ii) number of assembly stages/layers. Several studies in the past have stressed on the importance of geometrical features on the tool and correlated to the resulting material flow and microstructural evolution in the nugget [28-30]. The overall kinetics of microstructural evolution is location sensitive and the effect of the process strain, strain rate and thermal cycle leads to fully recrystallized, equiaxed, fine grained microstructure. These fine grained microstructures result in excellent mechanical properties, fatigue properties, enhanced formability and exceptional superplasticity [31-35]. In addition to achieving fine grained microstructures, control can be exercised on the second phase precipitation to achieve desired properties.

For this study, 1.7 mm thick sheets of WE43 alloy (nominal composition: Mg-4wt.% Y-3wt.% Nd-0.5wt.% Zr) in the rolled condition was subjected to friction stir lap welding. A multilayered stack comprising of four sheets and a build height of 5.6 mm was produced by sequentially building and CNC machining of the welded layers. FSAM was performed using a

right handed stepped spiral pin made of tool steel with a concave shaped featureless shoulder. A tilt angle of 1.5° was used to contain the material beneath the featureless shoulder. The pin height, pin diameter at the tip and root of the pin were 2.2 mm, 3.5 mm and 6 mm, respectively. Two different tool rotation rates of 800 and 1400 rpm at a constant traverse speed of 102 mm/min were used; referred to as 800/102 and 1400/102 specimens in subsequent sections. This was done to compare the mechanical properties and the microstructural evolution as a function of heat input.

4.2.2 Microstructural Characterization and Mechanical Testing

The specimens for microstructural examination and hardness evaluation were cross-sectioned perpendicular to the welding direction (Y-Z plane). A standard sequential metallurgical procedure such as cutting, mounting and polishing with alcohol based diamond polishing compound was employed. Structural features were subsequently revealed by etching for duration of 10 seconds in a mixture of acetic glycol (20 mL), (1 mL) HNO_3 , (60 mL) ethylene glycol, and (20 mL) water, and washing with ethanol. Microstructural analysis and characterization were extensively carried out by employing a scanning electron microscope (FEI Nova NanoSEM 230) and a transmission electron microscope (Technai G2 F20 STEM). For TEM analysis, circular discs of 3 mm were prepared using the conventional dimple grinding and ion milling procedure. To correlate to the observed mechanical properties, extensive care was taken to ensure that these samples came from specific depths corresponding to the lowest and highest hardness point in a build manufactured at 1400/102. For comparison with the peak aged rolled condition, a disc was also extracted from the base metal after aging. Samples for EBSD analysis were prepared using diamond based compounds till $1\text{ }\mu\text{m}$ followed by final polishing steps of 0.05 and $0.02\text{ }\mu\text{m}$ in

colloidal silica. During the final step, the sample was intermittently washed with ethanol to avoid surface corrosion. A FEI Nova NanoSEM 230 (20 kV, 3.1 mA, tilting 70°, 0.17 µm step size) was used to record the EBSD patterns for nugget/stir zone (SZ). Vickers microhardness measurements were done at a load of 1.961 N with a 10 sec dwell time. These measurements were performed along the centerline of the SZ in the build direction at an interval of 0.2 mm (Z axis). The grain size was determined by using the grain diameter method in the TSL-OIM software. Uniaxial tensile testing was done for the 1400/102 sample with the tensile axis parallel to the weld direction (X axis). This was done to estimate the strength and ductility in comparison to the aged base material and translate the observed hardness numbers. The gage dimension for the mini tensile sample was 2 mm x 1 mm x 1 mm. The tensile tests were performed at room temperature at an initial strain rate of 10^{-3} s^{-1} and average values of three samples are reported.

4.3 Results and Discussion

4.3.1 Nugget Macrostructure and the Effect of Welding Parameter on the Formation of Defects

The complex nature of the material flow in a built-up structure involving multiple lap joints results in various kinds of defects. Most of these defects are also observed in single level friction stir lap welds and butt welds, and have been characterized in terms of friction stir process parameters in literature [36-41]. Additional complexity arises in FSAM due to various reasons, like the difference in the microstructures of the top and bottom layers during each successive weld, presence of defects from the previous lap joint, vertical overlapping of weld nuggets, etc. Figure 4.3 shows the defects observed in the cross-section of the 1400/102 build specimen. Hooking of the faying surface line is observed at all three interfaces. Furthermore, cavities occur at the bottom of each of the three successive lap weld nuggets. These are formed due to

inadequate material flow under the friction stir tool. Cracking is also observed to occur along the stir zone and TMAZ interface at the retreating side bottom.

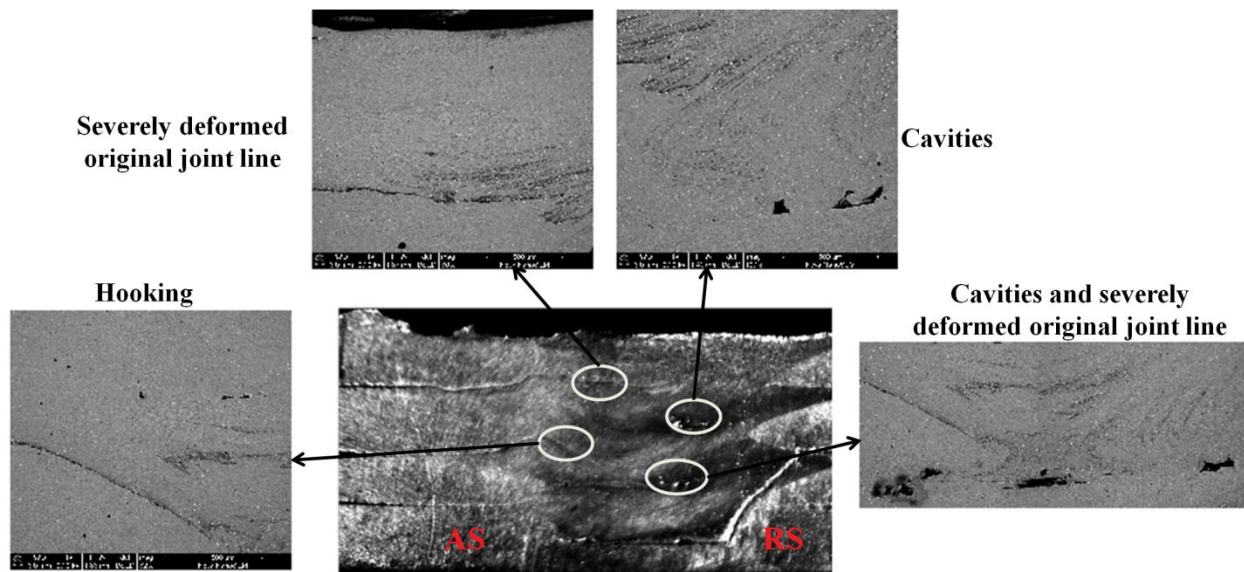


Figure 4.3. Defects in the 1400 /102 build specimen. The TMAZ-base metal interface at the bottom-right of the picture shows debonding.

The macrostructures of the weld cross-sections of the two build conditions, 1400/102 and 800/102 are compared in Figure 4.4. The build manufactured at the higher spindle speed (1400/102) exhibits a defective weld, whereas in comparison, the lower spindle speed weld shows a very sound macrostructure.

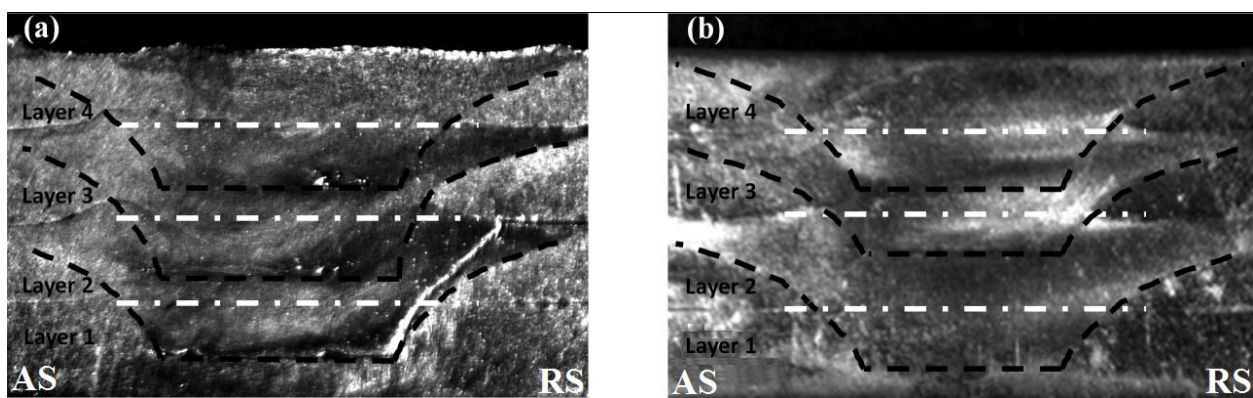


Figure 4.4. Transverse section macrograph of the friction stir welded build structures manufactured at (a) 1400/102, and (b) 800/102 specimens. Dashed horizontal white lines represent the original interface positions/locations.

As mentioned above, a number of defects usually observed in conventional friction stir welded joints were also present in the weld performed at higher spindle speed. In addition, there was considerable banding in the microstructure, with greater severity at the sheet interfaces. Section 4.3.2 provides a complete and detailed analysis of banding. In the present study, hooking defect was more prevalent in the build manufactured at a higher heat input. Hooking has been commonly observed during FSW of both butt and lap joints [41,42]. The faying surfaces of the lap weld sometimes do not completely bond and the unbonded interface extends into the weld nugget. This results in the decrease of the effective thickness and hence, lowers the strength of the weld joint. In this defect, the faying interface is severely deformed by the action of the tool pin, and the direction in which the “hook” bends follows the direction of material movement around the tool pin. By following the direction of bending of the hooking defect in Figure 4.3, it is evident that the material is being thrown down by the step features of the tool pin. Figure 4.3 also shows joint line reminiscence at each sheet interface. In Figure 4.4, the remnant original joint line is present in both the build conditions. The joint line has undergone severe plastic deformation by the action of the tool and in some places it is displaced significantly from the original line. Such a remnant line results from the oxide film at the original faying surfaces [42]. Cavities were observed in large numbers in the hotter weld condition, but were almost non-existent in the colder weld condition. These defects form when the amount of material flowing from the retreating side to the advancing side is not adequate to completely fill the volume of the

void left in the wake of the moving tool [36,42]. Ease of material flow depends directly on the heat input, the forge force of the tool on the work piece, and the containment provided by the tool shoulder during the FSW run [43].

It is interesting to note that the build manufactured at the hotter weld condition (1400/102) showed more defects compared to the build manufactured at 800/102. This observation highlights the role of material containment by shoulder at lower heat input. Higher spindle speed implies higher heat input, which in turn implies higher extent of material softening around the pin and easier flow both around the pin and under the shoulder. The defects observed, like hooking and cavity, are related to poor containment of material flow. In order to explain this observation further, the process forge forces for every FSW lap joint in the two builds are plotted as the tool moves along the weld line. This is shown in Figure 4.5.

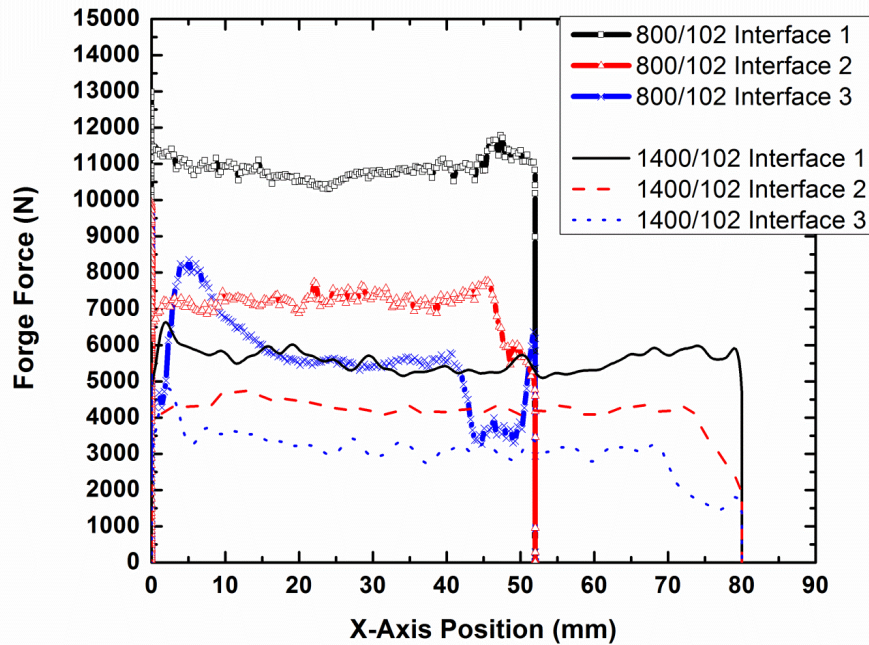


Figure 4.5. Forge forces, during the welding of the different interfacial lap joints, plotted against the distance along the weld line.

It is evident that the forge forces in the colder build condition are much higher than in the hot condition. The difference in the forge force values is greatest for the interface between the first two sheets (interface 1), a difference of around 5000 N. This is shown by the thick line with square boxes (representing 800/102) and the thin, solid line (representing 1400/102) in the plot. The difference in forge force values for the other interfaces is also significant, around 2000 N. This large difference in the Z-force explains the significant difference in the quality of the two builds. Higher forge forces provide the necessary compaction pressure required to push material under the rotating tool and close the voids and cavities that form in the wake of the tool.

The biggest, most prominent defect in the hotter weld is the cracking of the interface between the stir zone and TMAZ (bottom right in Figure 4.4a) and the crack continues along the bottom of the nugget, most probably aided by preexisting cavities from the first FSW lap joint. A likely explanation of the origin of this crack is that it is caused by residual thermal stresses across the weld nugget. The weld with the higher spindle speed has a higher temperature gradient across the weld cross-section. This gradient is translated into higher residual stresses once the workpiece cools down, causing the stir zone-TMAZ interface to be in a state of tensile stress. The direction of this tensile stress is in the transverse direction (left-right direction in Figure 4.4a) to the weld line. Section 4.4.4, which deals with the texture evolution in this microstructure, will provide a fuller understanding regarding the origin of cracking by correlating it to the thermal tensile stresses and texture.

4.3.2 Banding and its Origin

As mentioned in section 4.3.1, cyclic variations in the microstructure are observed for both the builds manufactured at 800/102 and 1400/102. However, their intensity is higher for a build manufactured using a higher heat input. A few interesting features are observed in association with the formation of these bands and one of them is their predominant existence at the interface. Several investigations on the nature of the periodicity of these bands have been reported for aluminum and copper alloys [44,45] attributing them to the base material, tool geometry and the welding parameters. However, during FSAM, presence of the interface increases the complexity. From the perspective of material flow, the genesis of such a periodically varying microstructure can be attributed to the unsteady nature of the flow. Such an unsteady flow usually results from the changes in the frictional condition at the pin-workpiece interface on temporal and spatial scales.

From Figure 4.6, the geometric profile of the band segment indicates a downward movement of the material at the pin threads and a subsequent curvature at the end indicating an outward and upward motion of the material to complete the circulation. A conical geometry of the tool coupled with a spiral design to facilitate the vertical movement of the material is in conformity to the geometrical feature of the observed band. In addition, the layered pattern spread in the Y-Z plane clearly indicates a layerly deposition process for the nugget as reported by several researchers. Previously, Colligan had related the formation of onion rings to the threads in the tool [46]. Furthermore, the periodic spacing between these bands have been correlated with the advance per revolution (APR). In some cases, the spacing has been observed

to be a fraction of the APR and has been attributed to the variation in process forces and additional effect of the tool pin features.

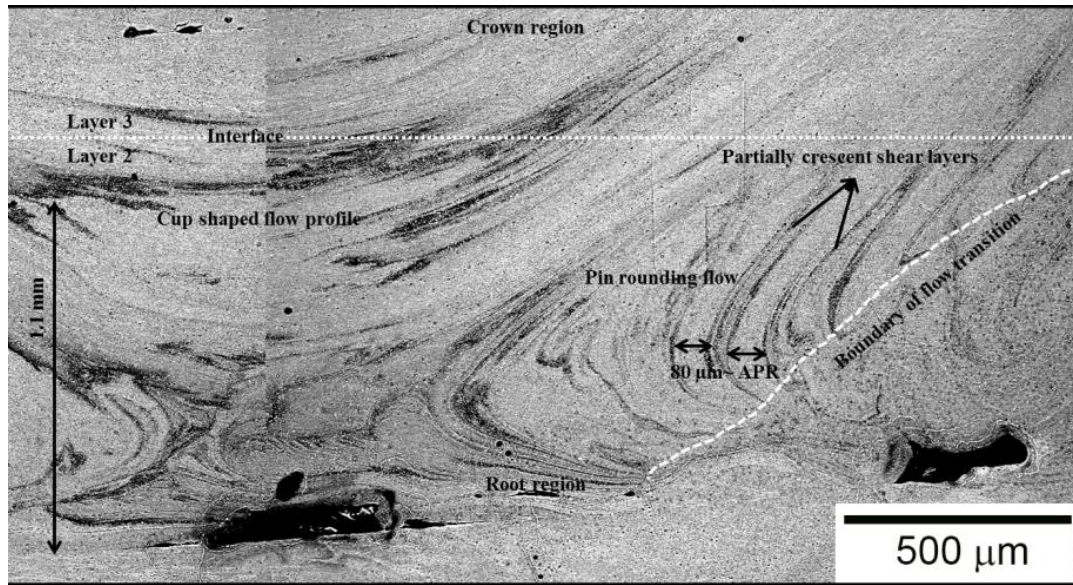


Figure 4.6. Spatial dependence of material flow and the microstructural features for a build manufactured at 1400 rpm and 102mm/min using FSAM.

From visual observation in Figure 4.6, the spacing between the shear layers is observed to be 80 μm for the higher heat input sample. Calculation of the APR using $\lambda=v/w$ for this build yielded a value of 73 μm and is in close agreement to the observation. In addition, a sudden transition is observed in the flow behavior at the retreating side and the outcome is a volumetric defect. A sharp transition is characteristic of the FSW process in the retreating side and is due to a steep change in the strain rate values over a spatial scale.

The generation of the volumetric defect is due to the excessive flash that resulted during the stacking of the third layer. Furthermore, a cup shaped flow profile is observed at the

interface. The resultant profile at the interface is due to the contributions from the crown dominated and the pin dominated flow regimes. The discussion regarding these two flows is pertinent as the sheets used for manufacturing the build are thin and hence the crown region of the weld would exert a greater impact. However, in the case of a build manufactured at a lower heat input, banding was minimal and is observed at the interfacial region. Hence the process parameters play significant role in determining the flow profile and therefore the mechanical properties at the interface. From the current observations, it can be concluded that the pin exercises a greater control over the crown on the interfacial macrostructure at a lower heat input. This statement is well supported by the banding profile in Figure 4.7 (a) that indicates a significant amount of vertical throw of the material. However, the key variable that would determine the interfacial macrostructure is its position from the shoulder.

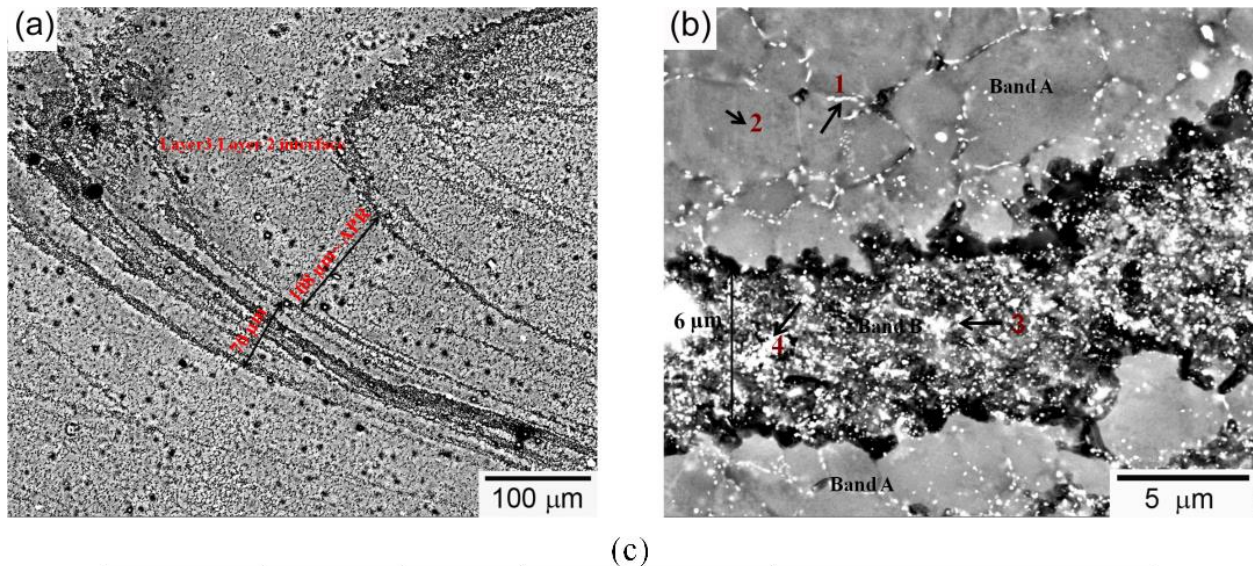


Figure 4.7. (a) Cyclic variation in the microstructure at 800/102, (b) Band spacing and the

difference in precipitation density, (c) Chemical composition of the marked positions in (b) by EDS.

Unlike, the structure built at 1400/102, a larger branch of a shear layer is bifurcated into several thinner layers as shown in Figure 4.7 (a). From Figure 4.7 (b), the spacing between these sublayers is 6 μm and is a fraction of the APR. Such layering is also noted in a build manufactured at 1400/102. Moreover, the differences in composition as evidenced by point EDS identify the variation in chemistry over a spatial scale. Figures 4.7 (b,c) specifies the location and tabulates the composition at various positions marked on the micrograph. Such a compositional variation indicates the sensitivity of the microstructural evolution to the strain, strain rate and temperature over distance. In simple mathematical form;

$$\frac{dc}{dx} = \frac{d(\epsilon, \dot{\epsilon}, T)}{dx} \quad (1)$$

where dc/dx is the compositional gradient, ϵ is the strain, $\dot{\epsilon}$ is the strain rate, and T is the temperature. Recently, Arora et al. [47] discussed about the strain and strain rate contributions during FSW and stressed on the spatial nature of these strains. Figure 4.8 (a) elucidates the gradient in the strain rate from the retreating side of the pin to the advancing side. These gradients in strain suggest a possible reason for the observation of the bands on the retreating and advancing sides. Moreover, a sudden transition in the material flow behavior is well supported by Figure 4.6 indicating a boundary for the transition in flow on the retreating side.

Another possibility that has not been discussed before is related to the temperature gradient. A change in temperature over the spatial scale implies the possibility of being above or

below the solvus temperature in a material with second phase. Such sensitive changes become important in the case of alloys that are rich in alloying elements due to the existence of multiple solvus curves. This argument becomes important as we consider the variation in strain. Since, plastic deformation contributes to the heat input, a gradient in strain also implies a gradient in temperature. In addition, the frictional heating occurs at tool/workpiece interface and the shear layer has strain and temperature gradients through the thickness of the shear layer. Therefore the temperature can be thought to decrease as we move across the shear layer towards the initial deformation zone that is yet to intersect the pin. These alternating bands can be clearly distinguished based on the precipitate density as shown in Figure 4.7 (b). A possible explanation in lieu of the observed variation in the microstructure can be based on the difference in Zr content. These Zr particles would serve two functions; (i) reduce the barrier to nucleation and aid recrystallization, and (ii) act as pinning centers to prevent further grain growth. Furthermore, Zr particles would also aid in preferential second phase precipitation that is supported by Figure 4.7 (b). A tentative mechanism can be framed based on the Zr elemental kinetics. Segregation of Zr rich clusters would occur during the heating cycle depending on the value of strain and temperature on a spatial domain. Such a segregation is characteristic of low diffusivity values of Zr in the magnesium matrix. Therefore during the cooling cycle, the second phases that precipitate out would consist of a Zr rich core capped by Y and Nd atoms leading to a composition of $\text{MgY}_{0.034}\text{Nd}_{0.016}\text{Zr}_{0.1}$. From the EDS results, it is evident that one Zr atom in Band A would combine with hundred Mg atoms whereas a single Zr atom in band B combines with ten Mg atoms. A tenfold ratio between these bands clearly relates to a significant variation in process variables and indicates the existence of gradient within a shear layer. The presence of this gradient in a second phase rich alloy with substantially different diffusivities would be

markedly higher.

The above mentioned discussion rendered an explanation based on the process variables like strain and temperature. In tandem, such a feature can also be based on the cyclic variation in the process forces. Figure 4.8 (b) plots the variation in the torque and the x force over the traverse distance. For a build manufactured at 800/102, the variation in the amplitude of the spindle torque and the traverse force with respect to the mean value is 52% and 3%. Similarly, for a build manufactured at 1400/102 these values are 70% and 9%. As shown by Figures 4.8 (b,c), a higher standard deviation for a build manufactured using higher heat input implies the greater magnitude of the discontinuous and unstable flow and therefore a greater probability to form bands. To elaborate, let us consider the variation in spindle torque as it can be directly correlated to the flow stress and the width of the shear layer. An assumption is made in regard to the width of the shear layer equating it to twice the APR. Such an assumption has been made considering the stick to slip ratio being 0.5 and satisfying the mass balance. Any change in the spindle torque can now be correlated to the change in flow stress by $\Delta\tau = r \cdot \Delta F$, where r is the shear zone width and ΔF is the change in the force. Moreover, ΔF can be directly correlated to the stress and therefore to strain. A simple calculation for the variation in torque over a single revolution for the builds manufactured at 1400/102 and 800/102 yields a value of 6.9 N-m and 2.5 N-m. In terms of strain, this translates to a variation of 0.42 and 0.05. It is to be noted that this calculation captures the change in strain over one revolution and is based on the instantaneous change in torque values rather than the accumulated strain as shown in Figure 4.8 (a). The intense nature of the changes in the process forces and hence the microstructure can be appreciated by correlating it to the variation in the strain rate from 10 s^{-1} to 0.7 s^{-1} for 1400/102

and 800/102 over the course of a single revolution. The above postulated mechanism of banding by virtue of process forces and process variables are highly interlinked and affect the evolving microstructure.

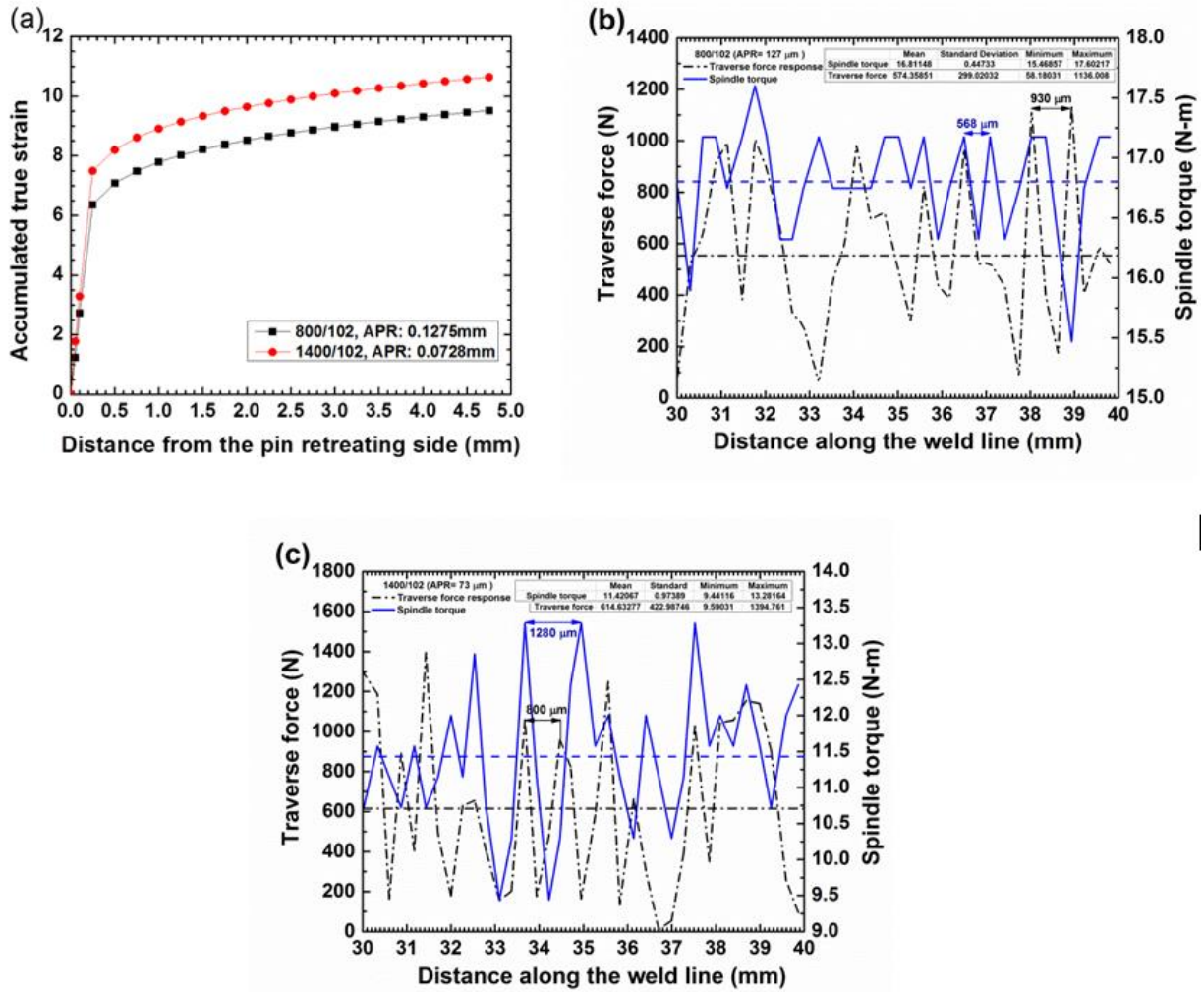


Figure 4.8. (a) Spatial variation of strain across the pin diameter. Spatial periodicity and variation of the traverse force(x) and the spindle torque over the welding distance for a build manufactured at (b) 800/102 and (c) 1400/102. To be in line with the observed micrographs in Figures 4.6 & 4.7, these process responses have been plotted for the stacking of the third layer and hence are representative of layer 2-3 interface.

4.3.3 Peak Temperature, Strain Rate and Zener-Hollomon Parameter

Based on the foregoing discussion, material flow, formation of defects and the evolution of microstructure during FSAM are strongly related to the peak temperature, strain rate and the Z-H parameter. Recently, a dimensionless correlation of the following form was proposed by Roy et al. [48] to estimate the non-dimensional peak temperature from the non-dimensional heat input,

$$T^* = a \log_{10}(Q^*) + b \quad (2)$$

where a and b are constants. Due to limited information on the peak temperature and heat input data on Mg alloys during FSW, the values of a and b are taken as 0.151 and 0.097 based on the previous reports for aluminum and steels [49]. T^* is the non-dimensional peak temperature expressed by [48],

$$T^* = T_{pk} - T_o / T_s - T_o \quad (3)$$

where T_{pk} is the peak temperature, T_o is the initial temperature of the workpiece and T_s is the solidus temperature. Q^* is a non-dimensional heat input defined by,

$$Q^* = \frac{\eta \sigma_{0.8} A \omega C_p}{k v^2} \quad (4)$$

where $\sigma_{0.8}$ is the yield stress of the workpiece material at $0.8 T_s$, ω is the tool rotation speed, v is the tool travel speed. For conformity in calculation, the units of ω and v are changed from rev min^{-1} to rad s^{-1} and mm min^{-1} to ms^{-1} . C_p and k are the specific heat capacity and thermal conductivity of the workpiece material and are tabulated at a temperature value averaged over the initial and solidus temperatures of the workpiece material ($T_{mean} = 0.5(T_o + T_s)$). A is the cross-sectional area of the tool shoulder. η represents the ratio at which the heat generated at

the tool shoulder-workpiece interface is transported between the tool and the workpiece and is defined as [48],

$$\eta = \sqrt{\frac{(k\rho C_p)_{wp}}{(k\rho C_p)_{tool}}} \quad (5)$$

The data used for the calculation of the peak temperature in a WE43 alloy is tabulated in Table 4.2. Thermal conductivity of H13 tool steel and WE43 at the mean temperature was obtained by interpolating the temperature dependent values existent in the literature [50,51]. Preheat during the tool plunge has been assumed as negligible and the initial temperature is substituted as 298 K.

Table 4.2. Summary of the tool dimensions and estimated material specific variables to compute the peak temperature.

| Workpiece | T _s (K) | C _p (J kg ⁻¹ K ⁻¹) | <i>k</i> (W m ⁻¹ K ⁻¹) | ρ (kg m ⁻³) | η | σ _{0.8} (MPa) | Shoulder radius (m) | Pin radius (m) |
|-----------|--------------------|---|--|----------------------------|-------|---------------------------|------------------------|-------------------|
| WE43 | 813 | 697 | 50.6 | 1843 | 0.741 | 30 | 0.0059 | 0.00237 |

Inserting the values from Table 4.2 into the equations (2)-(5) yields the value for the peak temperature. The maximum temperature at 800/102 and 1400/102 were evaluated to be 707 and 734 K, respectively. An alternative method to calculate the peak temperature is by using the analytical equation proposed by Arbegast and Hartley [52]. However, it does not take into account the various material parameters used in the dimensionless approach and relates the temperature directly to the tool traverse speed and tool rotation rate. Though, it is an empirical approach, the calculations using this approach predicted values in proximity to the computed ones using the dimensionless approach. The Arbegast model to compute the peak temperature is defined as:

$$\frac{T}{T_m} = K \left(\frac{\omega^2}{2.362v \times 10^4} \right)^\alpha, \quad (6)$$

where T_m (K) is the melting temperature and was considered as 913 K for the current Mg WE43 alloy. ω (r.p.m.) and v (mm s⁻¹) are the tool rotational and welding speeds used during FSW, respectively. The values of K and α were averaged over the reported values by Chang et al. [53] and Commin et al. [54] for AZ 31 and Mg alloys. Using this approach, the computed values for the peak temperature at 800/102 and 1400/102 was 698K and 785K. A convergence of the values for the peak temperature by two methods with a slightly greater error for a higher heat input suggests the obtained values are reasonable. Subsequent calculations will be based on the peak temperature values obtained by the dimensionless approach.

Formation of defects during friction stir welding can be mainly attributed to excessive or insufficient heat input. Section 4.3.1 correlated the defects to the process forces. Another tentative explanation can be based on the obtained value of peak temperature. A recent study found that defects can be avoided by operating at temperatures between $0.8T_s$ and $0.9T_s$ [55]. In the present study, the operating temperature for a sample built at 1400/102 was $0.902T_s$. The peak temperature calculation using the dimensionless approach is subject to an error of 3-9% [49]. Thus, the operating point is above the threshold of obtaining a defect-free run by virtue of a higher heat input and when adjusted for errors would lead to defects. Similarly, the operating temperature for an 800/102 build is $0.868 T_s$ and lies in the defect-free operating window.

In addition to the peak temperature, strain and strain rate provide a valuable insight on the extent of deformation and the resulting grain size. In the present study, strain is calculated by [56],

$$\varepsilon = \ln\left(\frac{l}{APR}\right) + \left|\ln\left(\frac{APR}{l}\right)\right| \quad (7)$$

where APR is the tool advance per revolution and l represents the length to which an element of initial length corresponding to the APR is stretched in one revolution. Equation (7) represents the tensile and compressive contribution to the strain experienced by a material element during one revolution. l is defined by,

$$l = 2d \cos^{-1} \left[\frac{d-x}{d} \right] \quad (8)$$

where d is the pin diameter and x is the distance perpendicular to the welding direction from the retreating side to the streamline in consideration. Average strain experienced by a material element is computed by assuming the streamline at the center of the weld. Considering, $x = d/2$, l was estimated as 9.94 mm. Computing ε from the obtained value of l , the strain rate during FSAM was calculated by using the following equation,

$$\dot{\varepsilon} = \frac{\varepsilon}{t} \quad (9)$$

where t is the time and related as $t = \frac{APR}{v}$, and v is the welding speed.

The calculated values of peak temperature and strain rate are employed to calculate the Zener–Hollomon parameter Z (s^{-1}) that is defined by [57]:

$$Z = \dot{\varepsilon} \exp\left(\frac{Q}{RT}\right) \quad (10)$$

where R is the gas constant, T is the temperature, and Q is the related activation energy. In the present discussion, the activation energy was assumed to be the lattice diffusion of Mg and is taken 135 KJmol^{-1} .

Table 4.3 summarizes the welding parameter based calculations obtained from Equations through (2)-(10). According to Equation (10), the changes in strain rate and temperature exhibit opposite effect on the grain size. It implies that lower temperature or higher strain rate leads to finer grains.

Table 4.3. Summary of welding parameter based calculations during FSAM

| Rotational speed (RPM) | Welding speed (mm/min) | Strain | Strain rate (s^{-1}) | Peak temperature (K) | Zener-Hollomon parameter, Z (s^{-1}) |
|------------------------|------------------------|--------|---------------------------------|----------------------|---|
| 800 | 102 | 8.73 | 116 | 707 | 1.09×10^{12} |
| 1400 | 102 | 9.83 | 229 | 734 | 9.27×10^{11} |

4.3.4 Effect of Welding Parameter on the Mechanical Properties of a Built Structure

4.3.4.1 Strength

Strength depends on the efficacy of solute elements, grain boundaries, dislocations and the second phases to block the gliding basal dislocations. In turn, these microstructural variables are strongly influenced by the processing route and the welding parameters. Figure 4.9 (a,b) shows the hardness profile of a build manufactured at 800/102 and 1400/102. Two immediate inferences can be drawn. Firstly, unlike the other additive manufacturing processes that are trying to catch up with the bulk properties, FSAM exceeds the strength of the rolled and aged condition by a significant margin. Secondly, for a build manufactured at 1400/102, a hardness of 115 HV is obtained in as fabricated state that improves to 135 HV after aging. These levels are

similar to Al 2XXX alloys. These results are encouraging as the observed hardness surpasses the maximum peak aged hardness achievable by conventional techniques/heat treatment routes that correspond to 110-120 HV [58,59].

Another pertinent issue is concerned with homogeneity. In comparison to the build manufactured at 800/102, the hardness is non-uniform for the build fabricated at 1400/102. A closer examination of the hardness profile reveals the low numbers (80-95 HV) to be associated with the interface positions. This is consistent with the discussion relating to the severity of banding as a function of welding parameters. In both the cases the hardness is seen to rise by an appreciable amount after aging as indicated by the horizontal arrows. The lowest hardness point (100 HV) is associated with layer 2-3 interface and is higher than the base material hardness after aging (97 HV) as shown by the vertical dashed line for a 1400/102 build. This is in stark contrast to the existing techniques that lead to a knock down in strength. The discussion is conservative due to the fact that 97 HV corresponds to the maximum hardness observed in the rolled and aged condition (henceforth designated as ARA). Moreover, a significant scatter of around 20 HV was observed with an average hardness of 90 HV. In order to appreciate the change in properties along the build direction, extensive characterization of the interfacial and non-interfacial microstructures for a 1400/102 stack is discussed in the succeeding section. Hardness can be correlated to the yield strength or in some cases; the UTS of the material. Site specific mini-tensile test as shown by the circle in Figure 4.9 (b) was done and compared to the ARA condition. Yield strength of 374 MPa and UTS of 400 MPa were obtained after FSAM. These values are considerably higher than the values obtained for ARA state that correspond to 310 and 357 MPa and signifies the potential to manipulate the microstructure by FSAM.

4.3.4.2 Ductility

In addition to strength, another important design consideration is ductility. Several metal working operations depend on the ability to form a material [60]. Usually, designers specify 5% ductility as a minimum requirement [61]. It is very well known that Mg alloys suffer from this drawback due to the limited number of slip systems. Following from the previous section, rolling combined with peak aging leads to higher strength but a severe knockdown in ductility. This is well supported by Figure 4.9 (c) and Table 4.4 that show an elongation of 2.9% for the ARA condition. Based on the design considerations, this condition would not qualify for structural application. Unlike this behavior, a dramatic ten-fold increase in ductility is observed after FSAM. Subsequent to the peak aging treatment performed in accordance with the literature for a wrought WE43 alloy [59], the uniform elongation remains very close to the initial value decreasing by a mere 5%. On the other hand, the yield strength increases by more than 100 MPa. Such a combination of ductility and strength is highly desirable.

To rationalize the observed differences, Figure 4.9 (d,e) draw a comparison on the plastic deformation behavior between the ARA, FSAM and FSAM+aged conditions. Figure 4.9 (d) shows a Kocks-Mecking type plot of strain hardening rate (θ) vs true strain at an initial strain rate of $1 \times 10^{-3} \text{ s}^{-1}$. The rolled condition exhibits a high initial hardening rate that decreases dramatically exhibiting a stage III behavior. From Figure 4.9 (e), the base material sustains a net flow stress of only 60 MPa before failure and is lesser than its FSAM counterpart. Similar initial hardening rate is also observed for the peak aged sample after FSAM. This is due to the presence of strengthening β' and β_1 precipitates that would act as dislocation barriers increasing the initial

θ value [58,61].

For the FSAM and FSAM+aged conditions, the work hardening plot can be divided into three domains. In the first domain, a steep decrease in the hardening rate is observed and is indicative of a sharp elastoplastic transition. This is followed by a minimum in the curve and a subsequent increase in the hardening rate. Domain III exhibits stage II type of linear hardening behavior before failure. Comparing the aged conditions after FSAM and rolling, the stage II type linear hardening behavior differentiates the two microstructures and hence the differences in resultant ductility. This linear hardening regime can be explained based on the activity of the non-basal dislocations that would intersect the primary slip planes leading to a balance between dynamic hardening and recovery. Previously, Koike et al. [62] showed that dynamic recovery indeed took place during tensile deformation due to the cross slip of “ a ” type dislocations on the non basal planes in an AZ31 alloy. The tendency to cross slip increased as the grain size decreased and was attributed to the intense grain boundary incompatibility stresses resisting further deformation. These compatibility stresses reduce the yield anisotropy factor that is defined as the ratio between the non-basal and basal Schmid factors favoring the non-basal dislocations [62]. Since FSAM leads to a finer grain size, greater non-basal activity can be visualized leading to an extended stage II linear hardening region.

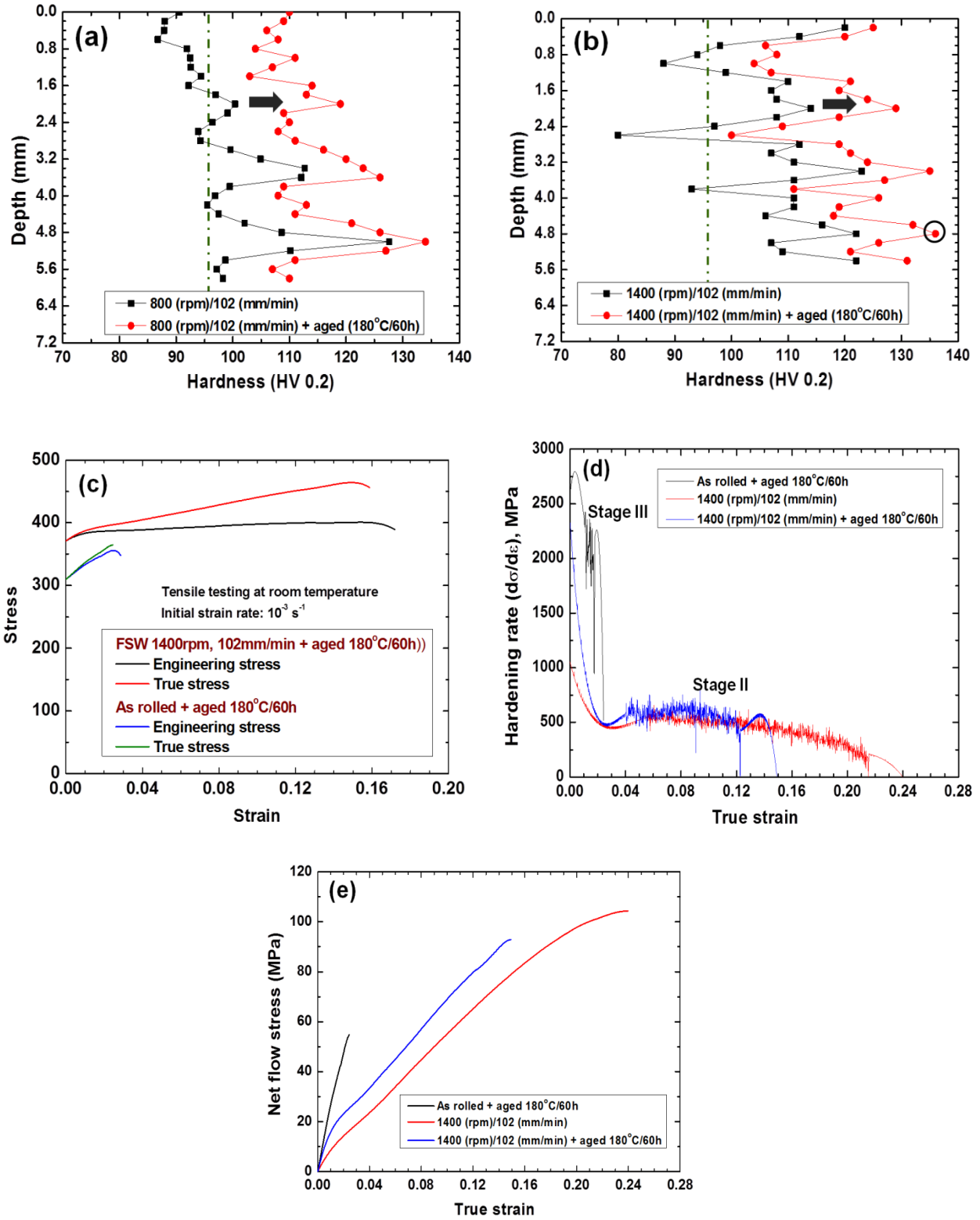


Figure 4.9. Hardness profiles along the build direction of (a) 800/102 stack, and (b) 1400/102

stack. The vertical line is representative of the hardness in the base material after aging and corresponds to 97HV. (c) Comparison between the uniaxial tensile stress-strain curves of the rolled and 1400/102 stack after aging, (d) work hardening behavior of the ARA sheet and build manufactured at 1400/102, and (e) net flow stress vs true strain to evaluate the strain hardening exponent. Testing was done parallel to the rolling/welding direction.

Another important parameter defined as the hardening capacity (H_c) was evaluated to correlate the observed work hardening response to the deformation behavior. H_c is defined as [63],

$$H_c = \frac{\sigma_{UTS}}{\sigma_{YS}} - 1 \quad (11)$$

where σ_{UTS} , σ_{YS} are the ultimate tensile and yield strengths. The hardening capacities are summarized in Table 4.4. FSAM leads to finer grain sizes and therefore higher yield strength and a lower hardening capacity. This can be attributed to the negligible difference in the flow resistance offered by the grain boundary and grain interior. To estimate the flow stress in the plastic deformation region, the strain hardening exponent was determined by a slight modification to the Ludwik's equation that is defined by [63],

$$\sigma - \sigma_y = K (\epsilon - \epsilon_y)^n \quad (12)$$

where σ , σ_y , K , ϵ , ϵ_y , n are the true stress, yield stress, strength coefficient, true strain, yield strain and the strain hardening exponent. The values are summarized in Table 4.4. The strain hardening exponent is in agreement with the hardening capacity with the rolled condition exhibiting a higher exponent. In the present study, anisotropy has not been accounted as the samples have been tested in the rolling/welding direction. The ease of deformation and the entire

discussion with respect to the work hardening behavior is intricately tied up with the crystallographic texture. Section 4.4.4 correlates the texture to the observed stress-strain behavior and explains the reduction/elimination of yield anisotropy after FSAM.

Table 4.4. Experimentally and empirically determined parameters after tensile deformation.

| Nomenclature | YS (MPa) | UTS (MPa) | %UE | %E | Hc | K | n |
|---------------------|-------------|--------------|----------|----------|-------|---------|------------|
| As rolled + aged | 310±3 | 357±4 | 2.5 | 2.9±0.1 | 0.151 | 1400±26 | 0.86±0.004 |
| FSAM (1400/102) | 265±7 | 300±9 | 20.1±0.2 | 29.8±0.2 | 0.132 | 356±1.5 | 0.81±0.02 |
| FSAM(1400/102)+aged | 374±3 | 400±6 | 15.8±0.1 | 17±0.3 | 0.07 | 394±2 | 0.76±0.002 |

4.4 Characterization of Interfacial and Non- Interfacial Microstructures

In the previous section, hardness was seen to depend on the spatial position for a 1400/102 build decreasing at the interfacial position. This is directly associated with the microstructure at that specific location. In order to examine the spatial dependence, and evaluate the accumulative effect on the microstructure, SEM, TEM and EBSD results are detailed in the following sections.

4.4.1 Base Material: Microstructure

Starting microstructure plays a significant role in the subsequent microstructural evolution. The rolled microstructure shown in Figure 4.10 (a) consists of a greater volume fraction of one type of intermetallic. From EDS, these cuboidal precipitates have been identified as $\text{Mg}_{3.5}\text{Y}_2\text{Nd}_{0.01}\text{Zr}$. These are very similar to the Mg_2Y precipitates reported in the cast, T5, T6 and solutionized states [64-66]. However, it is interesting to note that a considerable amount of Zr is also tied up with these intermetallics and has not been reported elsewhere. The presence of these particles render a two-fold explanation to the lower strength observed in the rolled condition. Firstly, these intermetallics would act as inefficient obstacles to dislocation motion by virtue of their size that ranges from 500 nm – 4 μm . Secondly, they consume a considerable portion of yttrium atoms and reduce the effectiveness of alloying elements and therefore the

solute for subsequent precipitation hardening. Even solutionizing treatments would be ineffective in harvesting the potential of the alloying elements as the melting point of these precipitates is greater than 620°C [67]. Moreover, as evidenced from the figure, it can be concluded that the strain and strain rates during the rolling operation are insufficient to dissolve these particles.

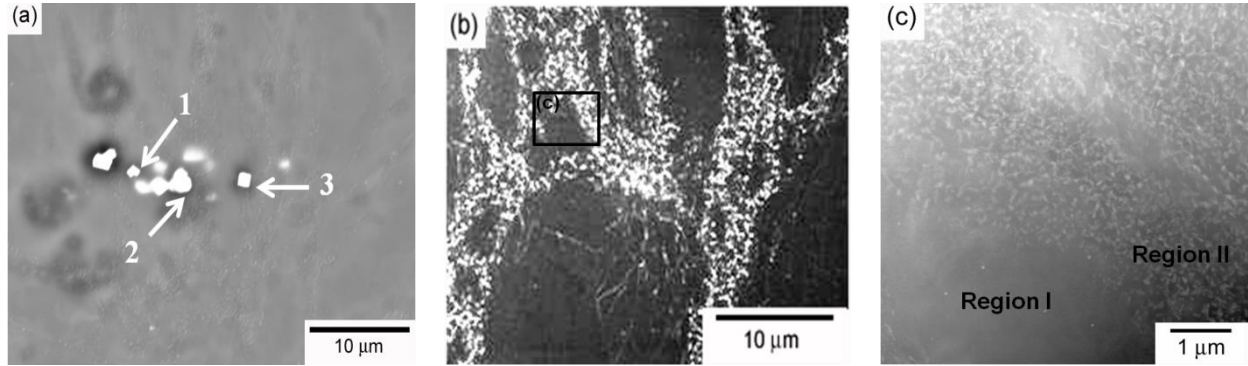


Figure 4.10. SEM micrographs showing, (a) Mg_2Y intermetallic cluster in the rolled state with their compositions tabulated in Table 4.4, (b) necklace structure along the grain boundaries after aging, (c) HAADF—STEM micrograph of the inset in (b) representative of the inhomogeneity in the rolled and aged condition.

Table 4.5. Summary of EDS results from Fig 10 (a)

| Position | Mg-K | Y-L | Nd-L | Zr-L |
|----------|-------|-------|------|-------|
| Point 1 | 52.28 | 31.52 | 1.46 | 14.73 |
| Point 2 | 52.66 | 30.61 | 2.83 | 13.88 |
| Point 3 | 71.71 | 18.6 | 1.13 | 8.59 |

In the previous section, it was mentioned that the ARA condition exhibited a significant scatter in the hardness values. Mechanical heterogeneity is directly tied to heterogeneous microstructures. Figure 4.10 (b) shows the formation of necklace structures after aging the rolled

microstructure. These necklace beads form due to the nucleation of small recrystallized grains at the grain boundary during the aging operation [59]. This observation clearly implies that the stored strain after hot rolling is sufficiently high and a temperature as low as 180°C can lead to recovered microstructures. Usually the contribution from dislocations in the hot rolled microstructure is neglected assuming a lower dislocation density. Such a generalized assumption may not always hold true as shown by the recrystallized grains in the present study. Now, such an observation has important implications. Achieving higher strength requires the introduction of a greater number of dislocations into the material and therefore a greater strain. But as shown, though the strength might scale, the extent of inhomogeneity would also scale in proportion leading to inhomogeneous properties. As mentioned previously, exercising the above route would lay a major impact on ductility. Figure 4.10 (c) is a HAADF- STEM micrograph and illustrates two different regions. Region I can be termed as a microstructurally clean region devoid of precipitation, whereas region II is densely populated with the second phases. Strength would be determined by the precipitate devoid region (Region I) rather than the stronger region (Region II). Recently, Nilesh et al. [61] stated that the presence of non-conforming grains would increase the resistance to plastic deformation. On similar lines, the presence of region I surrounded by region II can increase the yield strength but would also have a very high work hardening rate and lead to a brittle failure with the crack propagating through region I. This clearly imposes a limitation in a way that any one, either ductility, strength or the extent of homogeneity has to be sacrificed to improve the other by the existing wrought operations.

4.4.2 Microstructure of a 1400/102 Build at Different Locations

In section 4.3.4, FSAM was shown as an enabling technology in terms of improving

strength and ductility that are termed as the major drawbacks in Mg alloys. The major contribution to strength in a WE43 alloy stems from the precipitate descriptors and grain size. Therefore, this section is divided into two parts.

4.4.2.1 Precipitate Descriptors

In order to examine the differences in hardness along the build direction, SEM analysis was done at various locations. These locations have been annotated in the legend. Figure 4.11 (a-g) shows a considerable difference between the interfacial and non-interfacial microstructures. Depending on the peak temperature, strain rate and the thermal cycle, FSAM leads to dissolution, coarsening and/or reprecipitation. In majority of the cases, these processes occur simultaneously. The presence of intermetallics at the interfacial locations clearly indicates that the temperature and strain rate was insufficient to dissolve them. However, a majority of these are refined as compared to the base material. From Figure 4.11 (b, d) the grain size is significantly different. The grain size in layer 3 and interface 3 is seen to be 1.5 and 2.5 μm respectively. Secondly, precipitate banding is observed in interface 3. These observations imply that the strain rate and cooling rate experienced by the interface must have been lower in comparison to the individual layers.

In addition, from Figure 4.11 (a), the shoulder dominated flow at the crown surface leads to coarsened precipitates. Coarsening occurred due to a very high frictional heat supplied by virtue of the shoulder geometry. This microstructure corresponds to a depth of 0.6 mm from the top surface and is in agreement to the low hardness observed in Figure 4.9 (b). Moreover, a minor increase in the hardness from 98HV to 107 HV after aging in this region implies an

insignificant amount of retained solute after FSAM.

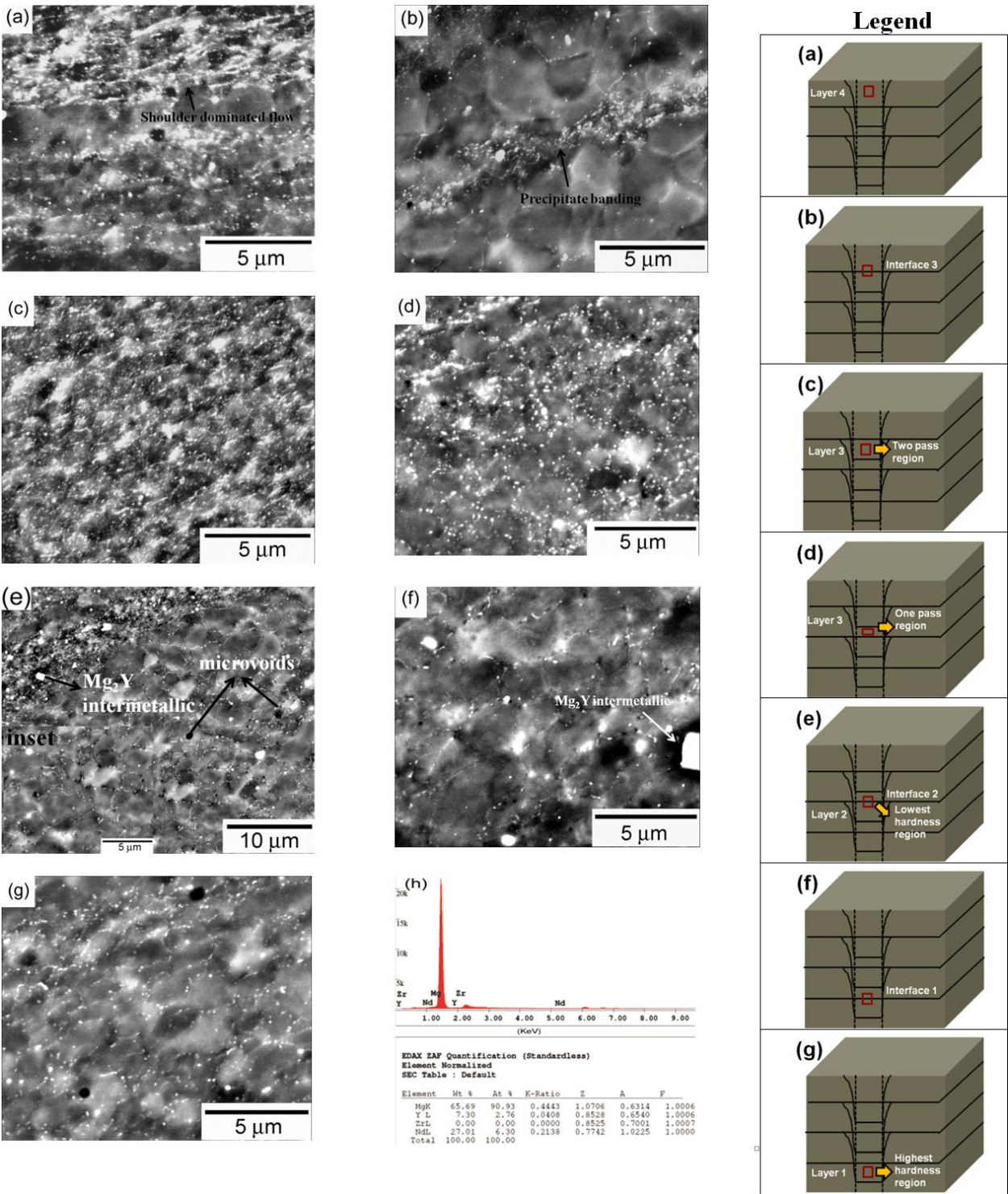


Figure 4.11. BSE images showing distribution of precipitates in (a) layer 4, (b) layer 3-4

interface, (c) two-pass region in layer3, (d) one pass region in layer 3, (e) layer 2-3 interface, (f) layer 1-2 interface and (g) layer 1. The examined regions have been annotated in the legend adjacent to these micrographs. EDS results for the grain boundary precipitates in Figure (d &g) have been shown in (h).

Figures 4.11 (d and g) refer to the pin dominated flow regimes and are representative of a single pass FSAM. Two features can be noted: (i) intermetallic dissolution, and (ii) grain boundary precipitation. From section 4.3.3, the peak temperature, Z-H parameter and the strain rate was calculated, as 734K, 9.27×10^{11} and 229 s^{-1} . Such high values of strain rate coupled with the high temperatures lead to dissolution of intermetallics and the consequence is increased solute supersaturation. The above explanation conforms to the hardness results in Figure 4.9 (b) that show a rise from 114-130 and 121-136 HV after aging. Furthermore, the peak temperature is above the solvus and when coupled with a very high cooling rate aids grain boundary diffusion at lower temperatures leading to precipitation at the grain boundaries. These are identified to be β precipitates with a composition close to $\text{Mg}_{14}\text{NdY}_{0.5}$ as shown by EDS in Figure 4.11 (h). Figure 4.11 (e) is representative of interface 2 and corresponds to low hardness values. In addition to the presence of intermetallics and banding, microvoids are observed in this region. These voids are responsible for lowering the hardness.

To examine further, HAADF-STEM was done to evaluate the precipitate morphology, size, density and distribution. TEM micrographs in Figure 4.12 (a-c) are representative of Figure 4.11 (e). From Figure 4.12 (a), two distinct regions are observed. Further analysis was done by magnifying the rectangular portions representative of these regions. Based on their size and

morphology, the second phases can be subdivided into four sets and are marked in Figure 4.12 (b). These sets correspond to, (i) very fine and spherical precipitates (3-8 nm), (ii) fine and globular shaped β' (15-20 nm), (iii) fine and plate shaped β_1 (25-35 nm), and (iv) coarse, irregular and partially faceted β (120-150 nm); based on their similarity with the available literature [58,68,69]. On the basis of precipitation density, such a microstructure is desirable to achieve higher strength due to a lower interparticle spacing. However, on the basis of size, extremely fine precipitates with a uniform distribution would be preferable.

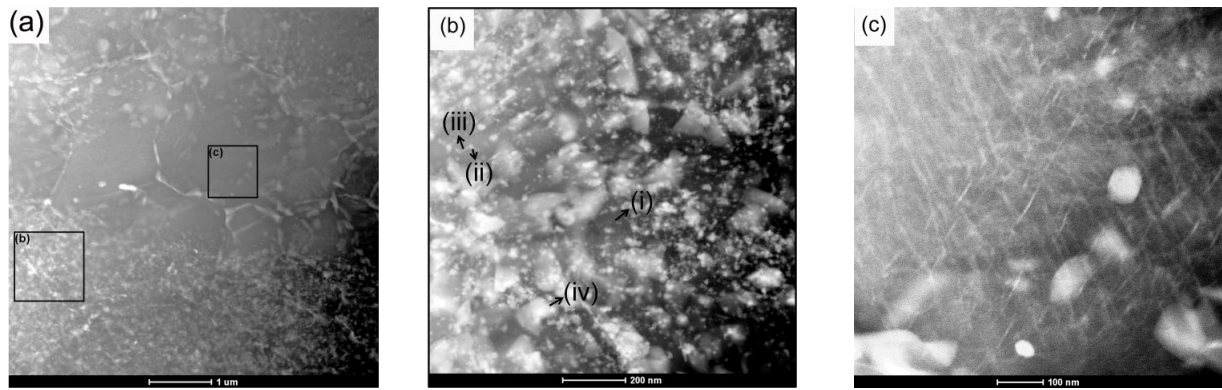


Figure 4.12 (a, b and c). HAADF-STEM images showing the precipitate descriptors after FSAM at interface 2. These images have been recorded after peak aging at 180°C for 60 hours. (2-column fitting image)

On the other hand, Figure 4.12 (c) shows a marked difference in precipitate size and morphology in comparison to Figure 4.12 (b). In this case, the matrix is populated with discontinuous fine needle/plate shaped precipitates [50 nm] and continuous vein like structures traversing the grain. In a recent study, Choudhuri et al. [70] showed the presence of the vein like structures in the rolled condition and reasoned their existence due to preferential precipitation at sub grain boundaries. Currently, these vein like structures are speculated to be associated with β_1

precipitates due to the tendency of Nd to partition at dislocations [70,71]. The formation of these structures in the present study clearly indicates the presence of a higher fraction of low angle grain boundaries (LAGBs) at the interface after FSAM. To confirm their presence, EBSD was done at the interface and the result has been shown in Figure 4.14 (b) and summarized in Table 4.6. It can be noted that the fraction of LAGBs resulting after FSAM constitute one-third of the scanned region at the interface. In comparison to the pin dominated bottom layer and the shoulder dominated top layer, a clear difference can be noted in the fraction of sub-grain boundaries that doubled at the interfacial position after FSAM. Based on the EBSD results and the TEM micrographs, it is obvious that the dislocation substructures play an important role on the precipitation behavior at the interface. Therefore mechanical properties in this region would be dependent on the nature of recovered dislocation structures. However, unlike the ARA microstructures that depicted a severe inhomogeneity due to the presence of precipitate free zone, the interfacial region exhibited precipitation throughout the matrix leading to a higher hardness. In reality, the precipitate number density would be lesser than the observed number as STEM imaging relies on thickness contrast. However, it accurately depicts the size and morphology. In addition, it is fair to draw a comparison on the number density between two STEM micrographs as they are subject to similar error.

Figure 4.13 shows the TEM micrographs obtained from the region corresponding to the highest hardness and has been extracted from layer1. As observed from the STEM micrographs, the microstructure is highly homogeneous and is in stark contrast to the ARA condition and the interfacial location. Furthermore, grain boundary precipitation is obvious and is in agreement with the SEM observation in Figure 4.11 (g). To analyze the observed tensile properties, a

magnified image of a specific location in Figure 4.13 (b) was recorded. As can be seen, a remarkable decrease in the relative intensity of the vein like structures is noted with respect to the interface. This observation is in line with the estimated fraction of LAGBs from EBSD in section 4.4.2.2. However, the underlying reason behind the higher strength values is not evident from the STEM images that show a clean matrix bereft of precipitation. To rationalize the observed tensile properties, the marked region in Figure 4.13 (c) was subjected to further probing by dark field imaging. Figure 4.13 (d) is a dark field micrograph of the corresponding region and is representative of the superlattice reflection circled on the inset. In contradiction to the observed STEM image, the local area marked in Figure 4.13 (c) was intensely populated with extremely fine and coherent precipitates (2-7 nm). Further efforts to identify the precipitate type have not been done in this study but they are expected to be associated with β'' or β' . As noted in the present case, such a uniform and fine distribution of the second phases throughout the matrix would serve as effective obstacles to dislocation motion and raise the strength. From design consideration, the microstructure shown in Figure 4.13 (d) would be highly desirable to push the limits of magnesium alloys.

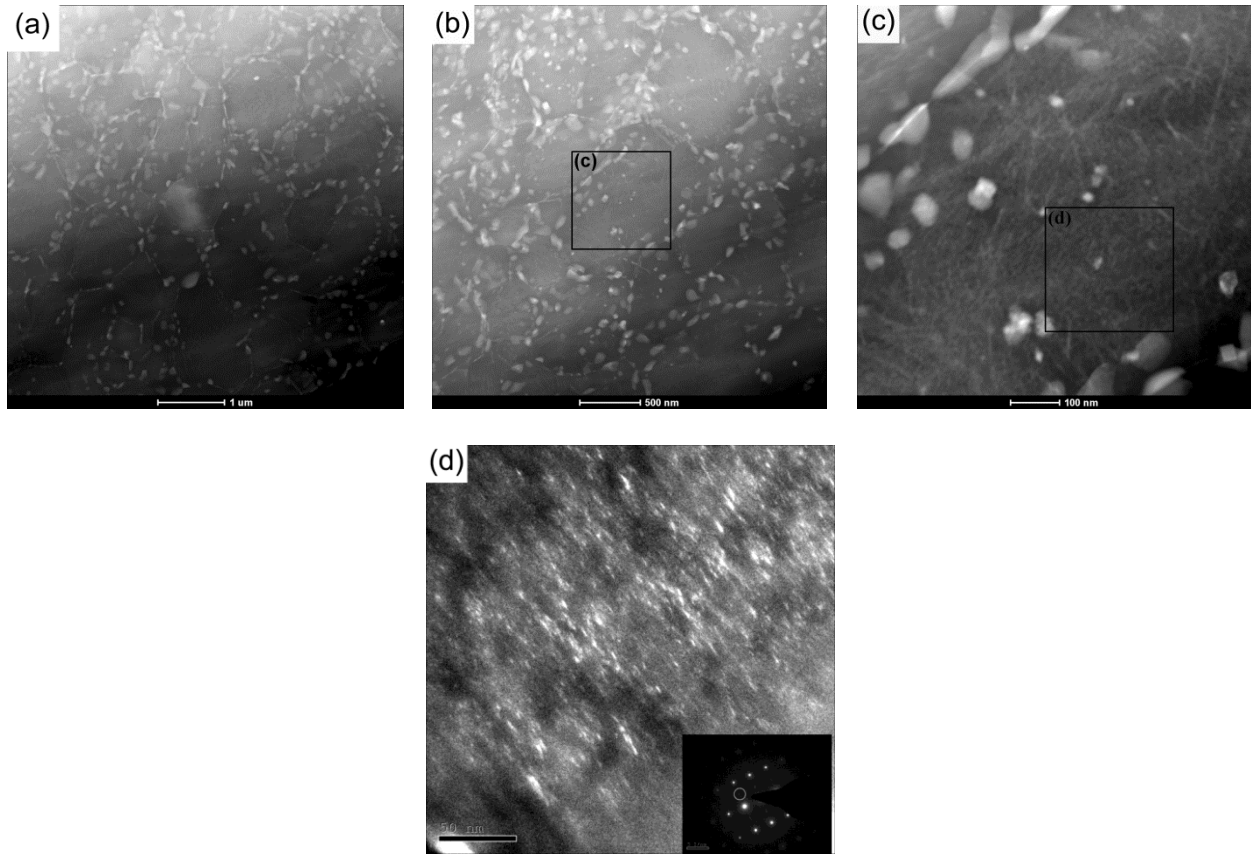


Figure 4.13 (a, b). HAADF-STEM images showing the precipitate descriptors at the bottom layer after FSAM. (c) Enlarged image of the location shown in (b). (d) A typical dark field micrograph obtained from the local area in figure (c). The reflection corresponding to the image has been marked in the diffraction pattern shown in the inset. Images were recorded parallel to [01-10]. These images have been obtained after peak aging at 180 °C for 60 hours. Note that the examined region corresponds to the highest hardness and strength of 400 MPa.

4.4.2.2 Grain Size

Figure 4.14 details the inverse pole figure (IPF) maps for a WE43 build manufactured at 1400/102. These maps were obtained from three specific locations to draw a comparison between the shoulder dominated top region, low hardness interfacial region and a high hardness

bottom region. In addition, the map was also obtained from the thermomechanically affected zone (TMAZ) to reason the stress induced cracking by correlating it to texture in section 4.4.4. A necklace type structure is seen in the TMAZ showing the occurrence of recrystallization at grain boundaries. Furthermore, an equal fraction of low angle grain boundaries (LAGBs) with respect to the high angle grain boundaries (HAGBs) suggest a higher dislocation density retained within the microstructure.

Comparing the three regions within the build, a clear microstructural difference can be noted. Table 4.6 gives a valuable insight on the magnitude of this variation. Two components are to be noted: (i) average grain size and (ii) grain size distribution, with the latter being a direct measure of microstructural homogeneity. A larger average grain size is observed at the interface followed by the pin affected bottom and the shoulder affected top layer. The smaller grain size at the top most layer is in agreement with a large amount of strain that the material experiences at the crown surface in comparison to the pin affected region. As quoted in section 4.4.2.1, a larger grain size at the interface can be linked to the insufficient strain rate and temperature. Though the grain size is larger at the interface, a higher retained dislocation density is observed in comparison to the top and bottom layers. Therefore, a similar value of strength can be expected at the interface by virtue of grain boundary strengthening. In addition to the grain size and dislocation density, the variation coefficient has been estimated and is a measure of dispersion in a probability distribution. A larger variation coefficient at the top indicates a greater distribution in the grain size and is associated with microstructural banding. These results conform to the observed micrograph in Figure 4.14 (a). Figure 4.14 (b) shows the IPF map corresponding to the interfacial region. Three regions are immediately identified and correspond to a (i) coarser grain

region, (ii) uniform grain size distribution (3.5 μm) and a (iii) very fine grain size distribution (250 nm)

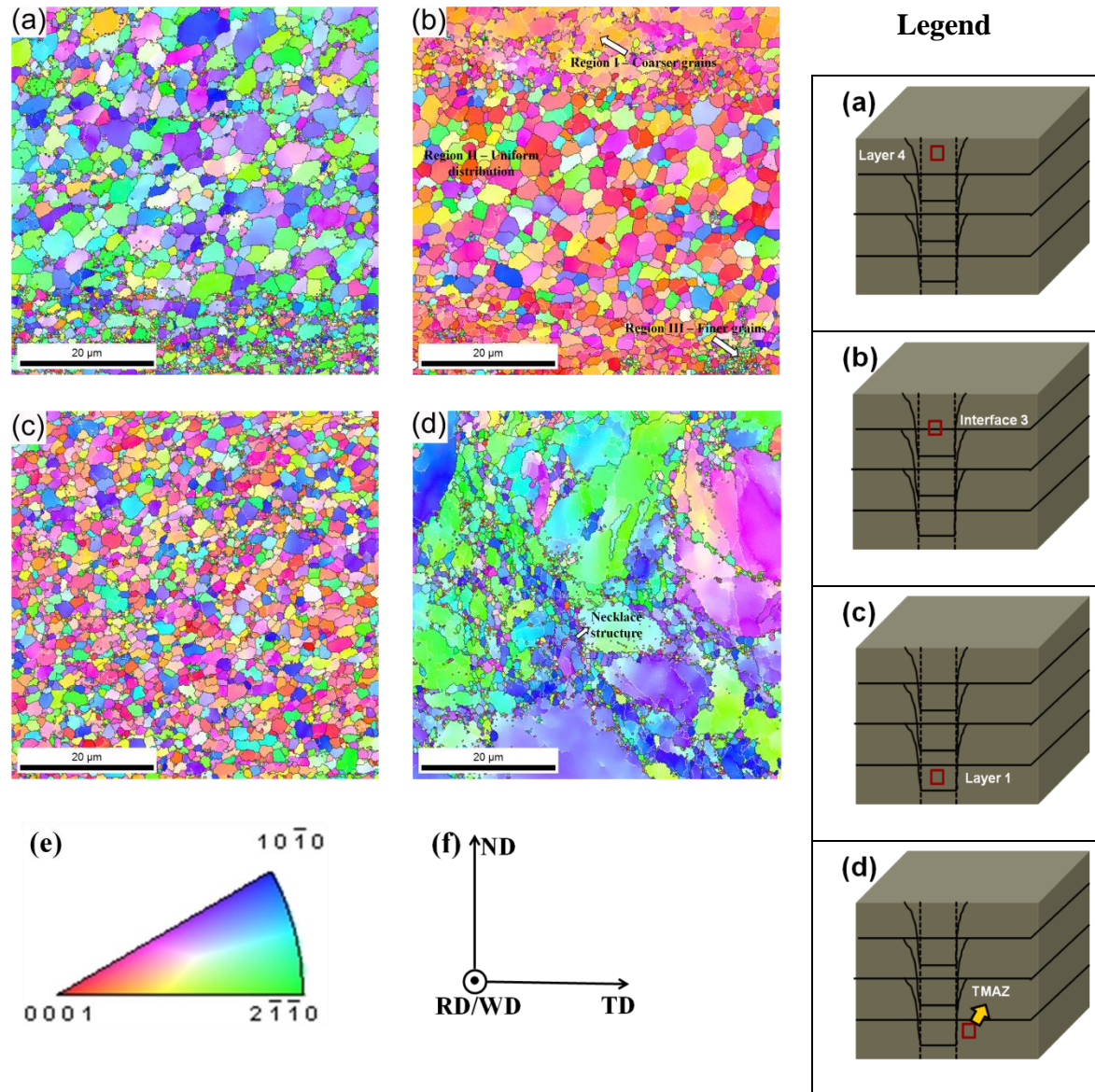


Figure 4.14. IPF maps depicting the distribution of grains in (a) layer 4, (b) layer 3-4 interface, (c) layer 1 corresponding to the tensile curve, and (d) thermo mechanically affected zone (TMAZ). The dark black lines and the faint white lines represent the high angle (HAGB) and low angle grain boundaries (LAGB). These analyzed regions have been annotated in the legend adjacent to these micrographs. Color correspondence scale and the sample coordinate system

have been shown in (e) & (f).

Table 4.6. Location specific grain size distribution in the 1400/102 build manufactured by FSAM

| Location | Average grain size (μm) | Maximum grain size (μm) | Minimum grain size (μm) | Standard deviation | Variation coefficient | $\frac{LAGB}{HAGB}$ |
|-------------|--------------------------------------|--------------------------------------|--------------------------------------|--------------------|-----------------------|---------------------|
| Layer 4 | 0.7 | 5.5 | 0.28 | 0.68 | 0.97 | 0.13 |
| Interface 3 | 0.98 | 6.2 | 0.26 | 0.83 | 0.85 | 0.3 |
| Layer 1 | 0.84 | 3.8 | 0.29 | 0.54 | 0.64 | 0.15 |
| TMAZ | 1.1 | 14.9 | 0.3 | 1.04 | 0.95 | 0.47 |

At present, the reason for the sandwiched microstructure at the interface is not known. However, it is speculated that such an observation is inevitably tied to the strain rate dependence in the build direction. Based on the results, the interfacial inhomogeneity exceeds the homogeneous bottom layer by 33%. From the above discussion, it is evident that the bottom layer that corresponds to a higher hardness has desirable precipitate characteristics coupled with a smaller grain size that is distributed consistently. In comparison to Al alloys, the Hall-Petch coefficient for Mg alloys is higher and would result in greater contribution to strength by grain size refinement.

4.4.3 Microstructure of a 800/102 Build at the Interface and Pin Dominated Bottom Layer

Figure 4.15 (a and b) have been shown to analyze and differentiate the microstructures from the build manufactured at 1400/102. These microstructures are representative of the pin dominated bottom layer and the interface, respectively. As previously discussed, the uniformity in the hardness profile at 800/102 can be attributed to the absence of microvoids unlike 1400/102. Furthermore, a lower hardness at the interface can be directly related to the coarser

grain size ($2.5\ \mu\text{m}$) in comparison to the very fine grains ($600\ \text{nm}$) attained in the pin dominated bottom region.

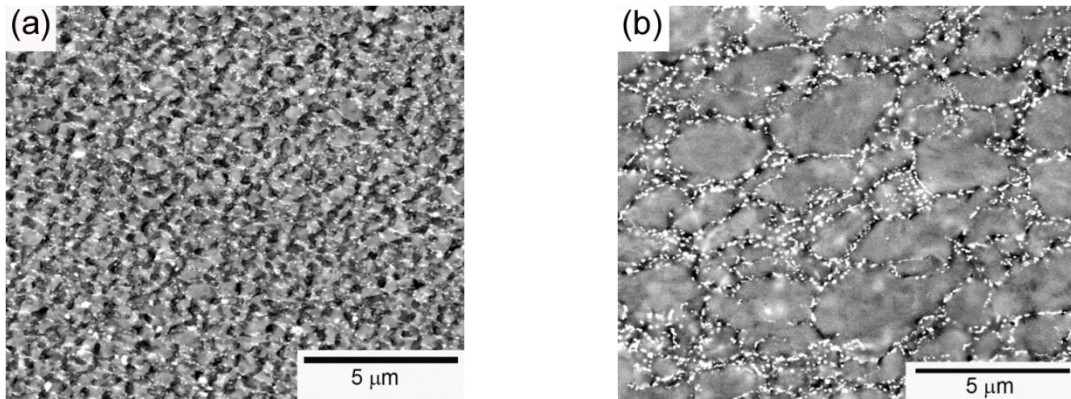


Figure 4.15. Back scattered electron (BSE) images showing, (a) bottom layer and (b) interface for a build manufactured using 800 rpm and 102 mm/min

To distinguish between the microstructures evolving from a higher and lower heat input, a comparison was drawn between Figure 4.11 (g) and 4.15 (a) as they embody the pin dominated bottom layer of the respective builds. By visual inspection, it is obvious that a lower heat input resulted in a very fine grain size. On similar lines, a comparison was drawn between the interfacial location from Figure 4.11 (f) and 4.15 (b). Unlike the refinement of intermetallics and their persistence at a higher heat input, they were absent in a build manufactured at a lower heat input. Their absence implied the sufficiency of strain and temperature to cause dissolution. Preceding calculations in section 4.3.3 for an 800/102 build estimated the Z-H parameter to be higher by an order with respect to the build manufactured at 1400/102. These calculations are in good agreement with the microstructural observation for both the builds.

4.4.4 Spatial Evolution of Texture for a Build Manufactured at 1400 rpm and 102 mm/min

Earlier, section 4.3.4.2 dealt with the deformation behavior of the pin dominated bottom layer and the base material. From the preceding discussion, it was evident that texture played a major role in determining the extent of deformation. Moreover, the limited number of slip systems aided by a low CRSS for the activation of basal slip $(0001) \langle 11\bar{2}0 \rangle$ determines the ductility in magnesium alloys [72]. In case of FSAM, the resulting texture is strongly connected to the mechanical action of the tool. Therefore to appreciate the observed orientation of the basal and prismatic planes, it is necessary to correlate those to the fundamentals of material flow that was previously discussed in sections 4.3.1 and 4.3.2. Figures 4.16 (a-d) show the orientation distribution of the basal (0001) , primary prismatic $(10\bar{1}0)$ and secondary prismatic $(11\bar{2}0)$ planes obtained from the marked regions in Figure 4.14. Consequently, these pole figures are representative of the IPF maps discussed in section 4.4.2.2 and render a quantitative explanation on the location specific deformation characteristics. A color coded intensity bar is located adjacent to these pole figures and represent the relative density of the poles recorded in the RD/WD - ND frame of reference. Texture intensity maximum is proportional to the numbers mentioned on the intensity bar.

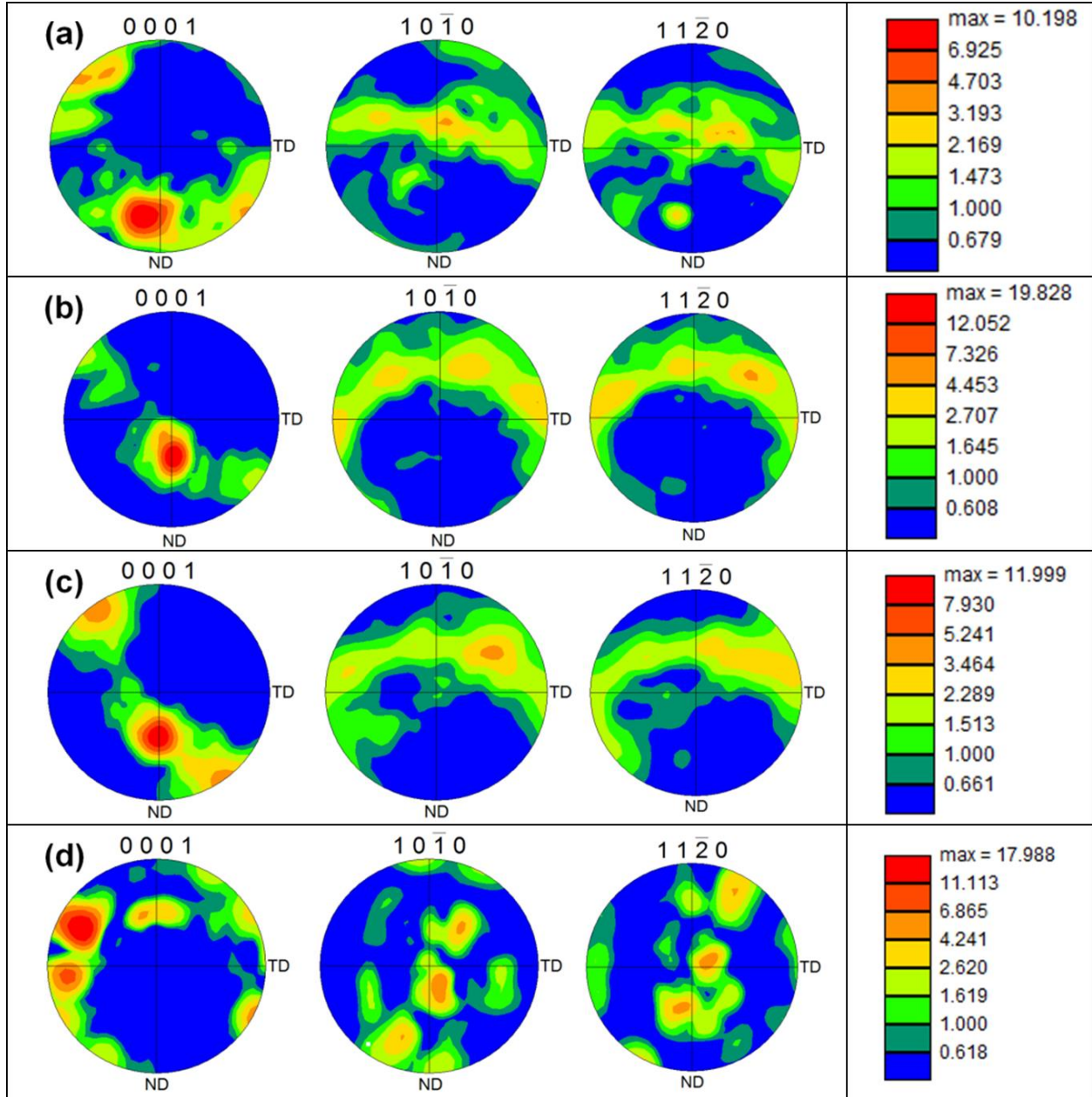


Figure 4.16. $\langle 0001 \rangle$, $\langle 10\bar{1}0 \rangle$ and $\langle 11\bar{2}0 \rangle$ pole figures of (a) shoulder affected layer 4 (top), (b) layer 3-4 interface, (c) pin affected layer 1 (bottom) and (d) thermo mechanically affected zone (TMAZ) after FSAM.

Firstly, the evolution of texture in the build is discussed. As shown in Figures 4.16 (a-c),

the $\langle 0001 \rangle$ poles are oriented at an angle of 30, 60 and 53 degrees from the ND towards the RD/WD. Hence, the basal planes would be closely oriented with respect to RD/WD at the top surface, whereas they would have a tendency to align towards the ND at the interface and bottom layer, respectively. From the observed inclination of the basal plane, it can be inferred that they tend to align with the pin surface except at the top. Such a textural evolution has also been reported in an AZ61 alloy [73]. It can be recalled that the base material was subjected to a severe rolling reduction and would have led to the parallel alignment of basal planes with respect to RD. The action of the shoulder at the top surface leads to in plane horizontal motion of the material leaving the basal planes alignment similar to the initial condition. However, the inclination with respect to WD can be attributed to the plunge and tilt coupled with a slight interaction with the pin surface. On the other hand, constraint free material flow and maximum vertical throw at the interface leads to a greater orientation of the basal planes with respect to WD. Moreover, the texture intensity is also very high in comparison to the bottom region that is constrained by the undeformed material and pin bottom.

In contrast to the orientation of the basal planes in the WD-ND plane for the build, their alignment in the TMAZ is complicated. It can be seen from Figure 4.16 (d), that the $\langle 0001 \rangle$ poles are inclined at an angle of 57 degrees from the ND towards RD and 65 degrees from the RD towards TD. It is to be recollected that residual stresses originating during the manufacturing process led to debonding across the TMAZ and nugget interface as shown in Figure 4.3 in section 4.3.1. This phenomena of debonding between layer 1 and the TMAZ is directly associated with the inability to accommodate stresses at the interface and can be correlated to the observed variation in texture. Figure 4.17 schematically illustrates the crack propagation path

along the nugget-TMAZ interface. Immediately, it can be noted that the path followed by the crack is determined by the basal plane trace in TMAZ. Such an observation clearly implies that the region in TMAZ was amenable to slip in comparison with the adjacent nugget.

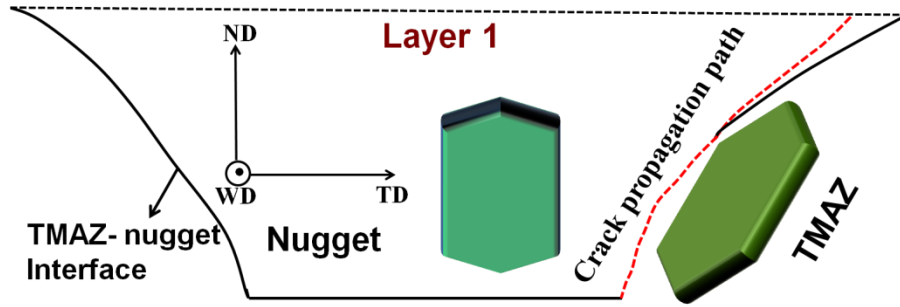


Figure 4.17. Schematic illustration of the crack propagation path along the trace of the basal plane at the nugget-TMAZ interface.

To confirm the aforementioned statement, the Schmid factors have been estimated in Table 4.7 using the TSL-OIM software for all the conditions shown in Figure 4.16 (a-d). Since the crack plane projection lies in the ND-TD plane, the stress experienced would be tensile in nature. The tensile stress in the transverse direction (TD) would be responsible for debonding. Hence, considering the tensile direction to be the transverse direction (TD), the Schmid factors were computed to be 0.27 and 0.34 at the bottom and TMAZ regions respectively. These values are in line with the observed macrograph in Figure 4.3. Therefore, as the residual stress builds up due to thermal cycle, the local stresses exceeded the fracture value. It is to be noted that the magnitude of the local incompatibility stress was higher because of a large orientation difference between the basal plane in the nugget and TMAZ. Such a situation results in strain gradient across the cross-section leading to crack nucleation and propagation along the energetically favorable basal plane trace in the TMAZ as shown in the schematic.

Table 4.7: Location specific Schmid factor of basal and non-basal slip system having two different tensile directions.

| Location | Schmid factor (0001) $\langle 11 \bar{2} 0 \rangle$ Tensile dir.// RD | Schmid factor (0001) $\langle 11 \bar{2} 0 \rangle$ Tensile dir.// TD | Schmid factor (10 $\bar{1}$ 0) $\langle 11 \bar{2} 0 \rangle$ Tensile dir.// RD | $\frac{m_{\text{prism}}}{m_{\text{basal}}}$ | Yield anisotropy $\frac{TD}{RD}$ |
|--------------------|--|--|---|---|-------------------------------------|
| Layer 4 (top) | 0.28 | 0.29 | 0.39 | 1.392 | 1.03 |
| Interface 3 | 0.38 | 0.2 | 0.22 | 0.578 | 0.526 |
| Layer1 (bottom) | 0.35 | 0.27 | 0.31 | 0.885 | 0.77 |
| TMAZ | 0.24 | 0.34 | 0.42 | 1.75 | 1.41 |

In section 4.3.4.2, increased elongation after FSAM was reported and discussed. These levels of elongation were related to the stage II linear hardening behavior and that in turn was associated to the activation of non-basal slip systems. But these non basal dislocations can be triggered only if the ratio between the Schmid factors of the “a” type non basal and basal dislocations is low. From Table 4.7, this ratio is seen to be the lowest at interface followed by the bottom layer. This is in agreement with the high value of elongation (30%) obtained after FSAM for a sample tested in layer1. Moreover, the yield strength was also observed to be low after FSAM and can be rationalized based on the favorable orientation of the basal planes ($m=0.35$) when tested in rolling direction. However, it can be recalled that these levels increased to 374 MPa after aging. Following on that, the Schmid factor is low in the TD (0.27) and if tested in this direction would have resulted in a much higher yield strength, closer to 400 MPa. On the other hand, the ARA condition exhibited very low ductility (2.5%). Presently, the texture in TMAZ can be approximated to the rolled condition as it carries the identity of the latter. Tensile testing

of the rolled material with the tensile axis parallel to the rolling direction led to a very low ductility due to the orientation of the c-axis within 20° (80% of the c-axis) of the transverse direction, which makes basal slip very difficult. This is well supported by the estimated Schmid factor of 0.24. Another significant factor that is a cause of concern in magnesium alloys is the yield anisotropy. From Table 4.7, the extent of anisotropy is also observed to decrease after FSAM in comparison to TMAZ, with the exception at the interface.

4.5 Conclusions

Friction stir additive manufacturing can be an effective route to fabricate high performance magnesium alloy components (WE43) with a higher strength (400 MPa) and considerable ductility (17%). The key findings are:

- 1) The origin of high uniform elongation of 16% in FSAM specimen results from stage II type linear hardening behavior.
- 2) Interface showed the presence of Mg_2Y intermetallics in a 1400/102 build. However, they were absent at non-interfacial locations due to enhanced strain rate. Furthermore, a higher Z-H parameter resulted in their dissolution at 800/102 irrespective of the location.
- 3) Superior strength, similar to Al 2XXX alloys, results from extremely fine, uniform and densely populated coherent precipitates in the size range of 2-7 nm.
- 4) Joint line reminiscence and cavities were predominant in a build manufactured at 1400/102. Their existence was associated with the presence of oxide particles and insufficient compaction of material under the tool pin. Similarly, banding is severe at a higher heat input and is due to a significant variation in the strain rate (10 s^{-1} vs 0.7 s^{-1}) and process forces in comparison to the build manufactured at 800/102.

- 5) Cracking in a 1400/102 build is due to the residual stresses originating from the immoderate thermal gradients experienced by the workpiece. The path of crack propagation follows the basal plane (0001) trace in the TMAZ due to incompatibility stresses.

4.6 References

1. Historical Standard: ASTM F2792-10 Standard Terminology for Additive Manufacturing Technologies, July 2010.
2. Terry Wohlers, Wohlers report: Additive Manufacturing and 3D Printing state of the industry, Annual Worldwide Progress Report, Wohlers Associate Inc., (2012) 1-287.
3. J.P. Kruth, M.C. Leu, T. Nakagawa, Progress in Additive Manufacturing and Rapid Prototyping, Annals of the CIRP, 47 (1998) 525-540.
4. P. Kulkarni, A. Marsan, D. Dutta, A review of process planning techniques in layered manufacturing, Rapid Prototyping Journal, 6 (2000) 18-35.
5. L.E. Murr, S.M. Gaytan, D.A. Ramirez, E. Martinez, J. Hernandez, K.N. Amato, P.W. Shindo, F.R. Medina, R.B. Wicker, Invited review: Metal Fabrication by Additive Manufacturing Using Laser and Electron Beam Melting Technologies, Journal of Materials Science and Technology, 28(1) (2012) 1-14.
6. K. Bartkowiak, S. Ullrich, T. Frick, M. Schmidt, New Developments of Laser Processing Aluminium Alloys via Additive Manufacturing Technique, Physics Procedia 12 (2011) 393–401.
7. R. Merz, F.B. Prinz, K. Ramaswami, M. Terk, L.E. Weiss, Shape Deposition Manufacturing, Proceedings Solid Freeform Fabrication Symposium, The University of Texas at Austin,

- (2004) 1–8.
8. K.M.B. Taminger, R.A. Hafley, Electron beam freeform fabrication: A rapid metal deposition process, Proceedings of the third annual automotive composites conference, Troy, MI, 2003.
 9. M. Aliakbari, Additive Manufacturing: State-of-the-Art, Capabilities, and Sample Applications with Cost Analysis, Master of Science Thesis, Production Engineering and Management, KTH, 2012.
 10. B. Lyons, Additive manufacturing in Aerospace; Examples and Research Outlook, The Boeing Company, 2011. Presentation can be accessed from <http://www.naefrontiers.org/File.aspx?id=31590> , Accessed on March 2014.
 11. E. Brandl, U. Heckenberger, V. Holzinger, D. Buchbinder, Additive manufactured AlSi10Mg samples using Selective Laser Melting (SLM): Microstructure, high cycle fatigue, and fracture behaviour, Materials and Design, 34 (2012) 159-169.
 12. E. Brandl, B. Baufeld, C. Leyens, R. Gault, Additive manufactured Ti-6Al-4V using welding wire: comparison of laser and arc beam deposition and evaluation with respect to aerospace material specifications, Physics Procedia, 5 (2010) 595-606.
 13. E. Brandl, A. Schoberth, C. Leyens, Morphology, microstructure, and hardness of titanium (Ti-6Al-4V) blocks deposited by wire-feed additive layer manufacturing (ALM), Materials Science and Engineering A, 532 (2012) 295–307.
 14. B. Baufeld, O. Van der Biest, Mechanical properties of Ti-6Al-4V specimens produced by shaped metal Deposition, Science and Technology of Advanced Materials, 10 (2009) 1-10.
 15. S.M. Kelly, S.M. Kampe, Microstructural Evolution in Laser-Deposited Multilayer Ti-6Al-4V Builds: Part I. Microstructural Characterization, Metallurgical Transactions, 35A (2004)

1861-1867.

16. C.Y. Kong; R.C. Soar; P.M. Dickens, Characterization of aluminium alloy 6061 for the ultrasonic consolidation process, *Materials Science and Engineering A*, 363 (2003) 99-106.
17. D.E. Schick, R.M. Hahnlen, R. Dehoff, P. Collins, S.S. Babu, M.J. Dapino, J.C. Lippold, Microstructural Characterization of Bonding Interfaces in Aluminum 3003 Blocks Fabricated by Ultrasonic Additive Manufacturing, *Welding Journal*, 89 (2010) 105-115.
18. R.R. Dehoff, S.S Babu, Characterization of interfacial microstructures in 3003 aluminum alloy blocks fabricated by ultrasonic additive manufacturing, *Acta Materialia*, 58 (2010) 4305–4315.
19. American Airlines “Fuel Smart” program literature, Information can be accessed from <http://hub.aa.com/en/nr/media-kit/operations/fuelsmart> , Accessed on Sept. 2014.
20. Mg Science and Technology Workshop, May 19-20, 2011, Arlington, VA, Sponsored by the National Science Foundation, report accessed from <http://www.virginia.edu/ms/research/agnew/conferences/>, Accessed on Dec. 2013.
21. S.R. Agnew, J.F. Nie, Preface to the viewpoint set on: The current state of magnesium alloy science and technology, *Scripta Materialia*, 63 (2010) 671-673.
22. Dawn White, Object consolidation employing friction joining, US patent, Patent No.:US 6,457,629 B1, October 2002.
23. J.J.S. Dilip, G.D. Janaki Ram, B.E. Stucker, Additive manufacturing with friction welding and friction deposition processes, *International journal of rapid manufacturing*, 3(2012) 56-69.
24. J.J.S. Dilip, S. Babu, S. Varadha Rajan, K.H. Rafi, G.D. Janaki Ram, and B.E. Stucker, Use of friction surfacing for additive manufacturing, *Materials and Manufacturing Processes*, 28

(2013) 1-6

25. P.H. Lequeu, R. Muzzolini, J.C Ehrstrom, F. Bron, R. Maziarz, Powerpoint presentation on: High performance friction stir welded structures using advanced alloys, Aeromat conference, Seattle, WA, 2006.
26. J.A. Baumann, Technical report on: Production of Energy Efficient preform structures, The Boeing Company, Huntington Beach, CA, 2012.
27. R.S. Mishra, Z.Y Ma, “Friction stir welding and processing”, Materials Science and Engineering R 50 (2005) 1-78.
28. A.P. Reynolds, Viewpoint paper: Flow visualization and simulation in FSW, Scripta Materialia, 58 (2008) 338–342.
29. R. Nandan, T. DebRoy, H.K.D.H. Bhadeshia, Recent advances in friction-stir welding – Process, weldment structure and properties, Progress in Materials Science, 53 (2008) 980–1023.
30. Y.C. Chen, K. Nakata, Effect of tool geometry on microstructure and mechanical properties of friction stir lap welded magnesium alloy and steel, Materials and Design, 30 (2009) 3913–3919.
31. R.S. Mishra, Preface to the Viewpoint Set on friction stir processing, Scripta Materialia, 58 (2008) 325.
32. C.G. Rhodes, M.W. Mahoney, W.H. Bingel, R.A. Spurling and C.C. Bampton, Effect of Friction Stir Welding on Microstructure of 7075 Aluminum, Scripta Materialia, 36 (1997) 69.
33. G. Liu, L.E. Murr, C-S. Niou, J.C. McClure and F.R. Vega, Microstructural aspects of the friction-stir welding of 6061-T6 aluminum, Scripta Materialia, 37 (1997) 355.

34. K.V. Jata, S.L. Semiatin, Continuous dynamic recrystallization during friction stir welding of high strength aluminum alloys, *Scripta Materialia*, 43 (2000) 743.
35. S. Benavides, Y. Li, L.E. Murr, D. Brown, J.C. McClure, Low-temperature friction-stir welding of 2024 aluminum, *Scripta Materialia*, 41 (1999) 809.
36. W.J. Arbegast, “A flow-partitioned deformation zone model for defect formation during friction stir welding”, *Scripta materialia*, 58 (2008) 372-376.
37. K.J. Colligan, R.S. Mishra, “A conceptual model for the process variables related to heat generation in friction stir welding of aluminium”, *Scripta Materialia*, 58 (2008) 327-331.
38. G. Padmanaban, V. Balasubramanian, “Selection of FSW tool pin profile, shoulder diameter and material for joining AZ31B magnesium alloy—an experimental approach”, *Materials & Design*, 30 (2009) 2647-2656.
39. H. Zhang, S.B. Lin, L. Wu, J.C. Feng, Sh.L. Ma, “Defects formation procedure and mathematic model for defect free friction stir welding of magnesium alloy”, *Materials & Design*, 27 (2006) 805-809.
40. Y.C. Chen, K. Nakata, “Effect of tool geometry on microstructure and mechanical properties of friction stir lap welded magnesium alloy and steel”, *Materials & Design*, 30 (2009) 3913-3919.
41. X. Cao, M. Jahazi, “Effect of welding speed on the quality of friction stir welded butt joints of a magnesium alloy”, *Materials & Design*, 30 (2009) 2033-2042.
42. X. Cao, M. Jahazi, “Effect of tool rotational speed and probe length on lap joint quality of a friction stir welded magnesium alloy”, *Materials & Design*, 32 (2011) 1-11.
43. K. Kumar, S.V. Kailas, “The role of friction stir welding tool on material flow and weld formation”, *Materials Science and Engineering A*, 485 (2008) 367-374.

44. B. Yang, J. Yan, M.A. Sutton, A.P. Reynolds, “Banded microstructure in AA2024-T351 and AA2524-T351 aluminum friction stir welds: Part I. Metallurgical studies”, *Materials Science and Engineering A*, 364 (2004) 55-65.
45. M. Guerra, C. Schmidt, J.C. McClure, L.E. Murr, A.C. Nunes, “Flow patterns during friction stir welding”, *Materials Characterization*, 49 (2003) 95-101.
46. K. Colligan, *Proceedings 1st international Symposium on friction stir welding*, Thousand oaks, California, The welding institute, Cambridge UK (1999).
47. A. Arora, Z. Zhang, A. De, T. Debroy, Strains and strain rates during friction stir welding, *Scripta Materialia*, 61 (2009) 863-866.
48. G.G Roy, R. Nandan, T. Debroy, Dimensionless correlation to estimate peak temperature during friction stir welding, *Science and Technology of Welding*, 11 (2006) 606-608.
49. A. Arora, T. Debroy, H.K.D.H. Bhadeshia, Back-of-the-envelope calculations in friction stir welding – Velocities, peak temperature, torque, and hardness, *Acta Materialia*, 59 (2011) 2020–2028.
50. S. Santhanakrishnan, N. Kumar, N. Dendge, D. Choudhuri, S. Katakam, S. Palanivel, H.D. Vora, R. Banerjee, R.S. Mishra, N.B. Dahotre, Macro- and Microstructural Studies of Laser-Processed WE43 (Mg-Y-Nd) Magnesium Alloy, *Metallurgical Transactions*, 44B (2013) 1190-1200.
51. S. Santhanakrishnan, F. Kong, R. Kovacevic, An experimentally based thermo-kinetic hardening model for high power direct diode laser cladding, *Journal of Materials Processing Technology*, 211 (2011) 1247–1259.
52. W.J. Arbegast, in: Z. Jin, A. Beaudoin, T.A. Bieler, B. Radhakrishnan (Eds.), *TMS Annual Meeting on Hot Deformation of Aluminum Alloys III*, San Diego, California, March 2–6

2003, 313.

53. C.I Chang, C.J. Lee, J.C Huang, Relationship between grain size and Zener–Holloman parameter during friction stir processing in AZ31 Mg alloys, *Scripta Materialia*, 51 (2004) 509-514.
54. L. Commin, M. Dumont, J.E. Masse, Barrallier, Friction stir welding of AZ31 magnesium alloy rolled sheets: Influence of processing parameters, *Acta Materialia*, 57 (2009) 326-334.
55. J. Qian, J. Li, F. Sun, J. Xiong, F. Zhang, X. Lin, An analytical model to optimize rotation speed and travel speed of friction stir welding for defect-free joints, *Scripta Materialia*, 68 (2013) 175-178.
56. A.P Reynolds, Flow visualization and simulation in FSW, *Scripta Materialia*, 58 (2008) 338-342.
57. M.M. Myshlyaev, H.J. McQueen, A. Mwembela, and E. Konopleva, “Twinning, dynamic recovery and recrystallization in hot worked Mg–Al–Zn alloy”, *Materials Science and Engineering A*, [337](#) (2002) 121-133.
58. G. Barucca, R. Ferragut, F. Fiori, D. Lussana, P. Mengucci, F. Moia, G. Riontino, “Formation and evolution of the hardening precipitates in a Mg–Y–Nd alloy”, *Acta Materialia*, 59 (2011) 4151–4158.
59. S.K. Panigrahi, W. Yuan, R.S. Mishra, R. Delorme, B. Davis, R.A. Howell, K. Cho, “A study on the combined effect of forging and aging in Mg–Y–RE alloy”, *Materials Science and Engineering A*, 530 (2011) 28-35.
60. J.R. Davis, I. ebrary, *Tensile Testing*, 2nd ed., ASM International, Materials Park, Ohio, 2004.
61. N. Kumar, N. Dendge, R. Banerjee, R.S. Mishra, “Effect of microstructure on the uniaxial

- tensile deformation behavior of Mg–4Y–3RE alloy”, *Materials Science and Engineering A*, 590 (2014) 116-131.
62. J. Koike, T. Kobayashi, T. Mukai, H. Watanabe, M. Suzuki, K. Maruyama, K. Higashi , “The activity of non-basal slip systems and dynamic recovery at room temperature in fine-grained AZ31B magnesium alloys”, *Acta Materialia*, 51 (2003) 2055–2065.
63. N. Afrin, D.L. Chen, X. Cao, M. Jahazi, “Strain hardening behavior of a friction stir welded magnesium alloy”, *Scripta Materialia*, 57 (2007) 1004-1007.
64. Z. Su, C. Liu, Y. Wan, “Microstructures and mechanical properties of high performance Mg-4Y-2.4Nd-0.2Zn-0.4Zr alloy,” *Materials and Design* (2012).
65. K. Yu, W. Li, R. Wang, B. Wang, C. Li, “Effect of T5 and T6 Tempers on a Hot-Rolled WE43 Magnesium Alloy”, *Materials Transactions*, 49 (2008) 1818 -1821.
66. S. Palanivel, R.S. Mishra, B. Davis, R. Delorme, K.J. Doherty, K.C. Cho, “ Effect of initial microstructure on the microstructural evolution and joint efficiency of a WE43 alloy during friction stir welding”, *Friction Stir Welding and Processing VII*, TMS, San Antonio, TX, 2013.
67. N. Hort, Y. Huang, K.U. Kainer, “ Intermetallics in magnesium alloys”, *Advanced Engineering Materials*, 8 (2006) 235-240.
68. J.F. Nie, B.C. Muddle, “Characterisation of strengthening precipitate phases in a Mg-Y-Nd alloy”, *Acta materialia*, 48 (2000) 1691-1703.
69. Y. Gao, H. Liu, R. Shi, N. Zhou, Z. Xu, Y.M. Zhu, J.F. Nie, Y. Wang, “Simulation study of precipitation in an Mg–Y–Nd alloy”, *Acta Materialia*, 60 (2012) 4819–4832.
70. D. Choudhuri, S. Meher, S. Nag, N. Dendge, J.W. Hwang, R. Banerjee, “Evolution of a honeycomb network of precipitates in a hot-rolled commercial Mg-Y-Nd-Zr alloy”,

Philosophical Magazine Letters, 93 (2013) 395–404.

71. J.F. Nie, “Precipitation and hardening in Magnesium alloys”, Metallurgical and Materials Transactions A, 43 (2012) 3891-3939.

72. X.Y. Lou, M. Li, R.K. Boger, S.R. Agnew, R.H. Wagoner, “Hardening evolution of AZ31 Mg sheet”, International Journal of Plasticity, 23 (2007) 44-86.

73. S.H.C. Park, Y.S. Sato, H. Kokawa, “Basal plane texture and flow pattern in friction stir weld of a magnesium alloy”, Metallurgical and Materials Transactions A, 34 (2003) 987-994.

CHAPTER 5

A FRAMEWORK FOR SHEAR DRIVEN DISSOLUTION OF THERMALLY STABLE PARTICLES DURING FRICTION STIR WELDING AND PROCESSING

Overview: In chapters 3 and 4, the increase in strength after FSP was attributed to increased alloying efficiency by the dissolution of undesirable Mg_2Y intermetallic. Though, dissolution of thermally stable particles is a well-documented phenomenon during FSP [1-5], a fundamental understanding on this subject is lacking. In this chapter, a framework is proposed to explain the dissolution and fragmentation of particles during friction stir welding and processing. Two major mechanisms dissolve the particle during the process: (i) thermally activated diffusion, and (ii) dislocation and grain boundary sweeping of atoms. We use a three-dimensional coupled viscoplastic flow and heat transfer model to quantify these mechanisms. For illustration purposes, calculations were done on a thermally stable Mg_2Y intermetallic that dissolved during processing. The framework is universal and applies to any second phase dissolution and fragmentation during friction stir welding and processing, thus enabling a science-based approach to tailor microstructures.

5.1 Introduction

Friction stir welding (FSW) and friction stir processing (FSP) fragments or dissolves second phases [1-5]. For over a decade, several researchers and engineers have used this ability to enhance performance in structural alloys. A few of these include cast A356, wrought AA2024, Mg-Al-Zn, and Mg-rare earth alloys [1-5]. In cast A356, Ma et al. [1] increased the strength by 100 MPa and ductility by an order of magnitude by refining the size of Si particles from an

average of 16 μm in the cast condition to an average of 3 μm after FSP. A recent study on AA 2024 by Pasebani et al. [2] showed a decrease in $\text{Al}_6(\text{Cu,Fe,Mn})$ constituent particle size from 3.7 to 0.8 μm by increasing the tool rotational rate from 300 to 1000 rpm. Their observation was consistent with the concept put forth by Mishra et al. [6], where low advance per revolution (APR) leads to a narrow shear layer, high process strain, and sufficient residence time to fracture the particle multiple times.

In addition to fragmentation of particles, an intriguing feature in FSW/FSP is the dissolution of thermally stable intermetallics. Xiao et al. [4] reported an increase in the crystal lattice parameters by dissolving heat resistant $\text{Mg}_5(\text{Gd,Y})$ intermetallic in GW103 casting after FSP. Similarly, Palanivel et al. [5] observed the dissolution of Mg_2Y intermetallic in WE43 after friction stirring. This ability to supersaturate the matrix by dissolving intermetallics is well used in precipitation strengthened Al and Mg alloys to enhance the mechanical properties [2, 4, 5].

Though dissolution and fragmentation of thermally stable particles are experimentally validated after FSW/FSP, a long-standing question in this research field is; how do these particles dissolve or break? At present, accelerated diffusion rate and shorter diffusion distance, coupled with intense-plastic-deformation enabled enhanced-material-mixing are speculated as the contributing factors [2, 5, 6, 7]. Although the process enables forced mixing, the mechanism by which particles dissolve or break is unknown and remains unanswered. In other words, a science-based fundamental framework is lacking to explain the aforementioned phenomenon in a field that is well-established.

The objectives of this study are to: (i) propose a theoretical model outlining the mechanisms that contribute to dissolution, (ii) quantify the individual mechanisms with the aid of numerical modeling, and (iii) state a criterion for fragmentation vs dissolution. For illustration purposes these mechanisms are quantified by taking the example of an Mg_2Y intermetallic in an Mg-Y-Nd alloy that dissolved during FSW/FSP.

5.2 Experimental and Computational Details

FSP was done on a rolled sheet (3 mm thick) of WE43 alloy (Mg-4wt%Y-3wt%Nd-0.5wt%Zr) at a tool rotation rate of 800 revolutions per minute and a traverse speed of 102 mm/min using a conical pin and concave shaped featureless shoulder. The shoulder diameter, pin height, pin diameter at the tip and root of the pin, tilt angle and the plunge force during processing were 11.8 mm, 2.2 mm, 3.5 mm, 6 mm, 1.5 degrees and 9 kN, respectively. Mg_2Y dissolution was experimentally confirmed after comparing the microstructures of the rolled, solutionized (525°C/8hours) and processed specimens using a scanning electron microscope (FEI Nova NanoSEM 230) equipped with energy dispersive spectroscopy (EDS).

To quantify dissolution, we used a three-dimensional heat transfer and material flow model to compute the thermal cycle, strain and strain rate during processing. Both strain and strain rate were calculated on an Mg_2Y intermetallic that was located 60 μm away from the pin surface and within the shear layer to avoid physical contact between the pin and the particle. Temperature and velocity distribution in three dimensions were computed by solving mass, momentum and energy conservation equations in non-uniform rectangular grid. A Cartesian coordinate system with origin fixed at the tool center was considered with material moving at

negative traverse velocity. Furthermore, a partial slip condition was considered at the tool and workpiece interface, where the velocity of the tool was partially transferred to the workpiece. Heat generated due to both friction and plastic deformation was considered at the tool-workpiece interface and divided among the tool and workpiece based on their density, thermal conductivity and specific heat. Heat generation from viscous dissipation was also considered away from the interface.

The computed velocity field was then used to calculate the strain rate tensor ($\dot{\varepsilon}_{ij}$) as the spatial gradient of the material velocity vector:

$$\dot{\varepsilon}_{ij} = \frac{1}{2} \left(\frac{\partial u_i}{\partial x_j} + \frac{\partial u_j}{\partial x_i} \right) \quad (1)$$

where u_i is a component of velocity vector and x_j is the distance vector. The three-dimensional material velocity field was used to trace streamlines corresponding to particle in the workpiece material. The streamlines were considered at 0.06 mm away from the tool pin surface and 1 mm from the top at the advancing and retreating sides. The strains experienced by the particle at these two locations were calculated by absolute integration of the strain rate along the corresponding streamlines:

$$\varepsilon_{ij} = \sum_{k=1}^{n-1} |\dot{\varepsilon}_{ij}|_k \times \left(\frac{\Delta x_s}{u_s} \right)_k \quad (2)$$

where x_s is the distance between two consecutive points, k and $k+1$ on the stream line, u_s is the velocity of the particle between the points and n is the total number of points along the streamline. The absolute value of strain rate was integrated to represent the cumulative effect of both tensile and compressive strains. To verify the proposed mechanism, transmission electron microscopy (Technai G2 F20 STEM) was done at 200 kV.

5.3 Results and Discussion

Figures 5.1 (a, b) show coarse (1.5-4 μm) and cuboidal intermetallics in the rolled and solutionized samples. EDS identified these intermetallics as Mg_2Y , which dissolved on the advancing side (AS, Figure 5.1(c)) and fragmented on the retreating side (RS, Figure 5.1(d)) during FSP. Considering only AS, on the basis of Figure 5.1(e), it is surprising that Mg_2Y particles dissolved at a peak temperature $\sim 100^\circ\text{C}$ lower than the solutionizing temperature and a fraction of the solutionizing time ($\sim 1/3000$). Compared to the studies on forced mixing [8, 9], dissolution of Mg_2Y is unusual because of a large lattice mismatch ($\frac{\Delta a}{a} \approx 87\%$), and difference in shear moduli ($\frac{\Delta G}{G} \approx 87\%$) between the thermally and mechanically stable intermetallic and Mg matrix [10, 11].

Since Mg_2Y destabilizes and melts at 780°C [11], which happens to be above the melting range of WE43 ($540\text{--}640^\circ\text{C}$), its existence in the solutionized condition is expected. However, its presence after rolling implies that the nature of strain (plane strain compression) and magnitude of strain rate were insufficient to dissolve the Mg_2Y particles by conventional thermo-mechanical processing. Figure 5.1 leads to two conclusions: (i) temperature alone is insufficient to cause dissolution, and (ii) high temperature combined with torsional shearing and extrusion during FSP leads to accelerated dissolution of thermally stable particles.

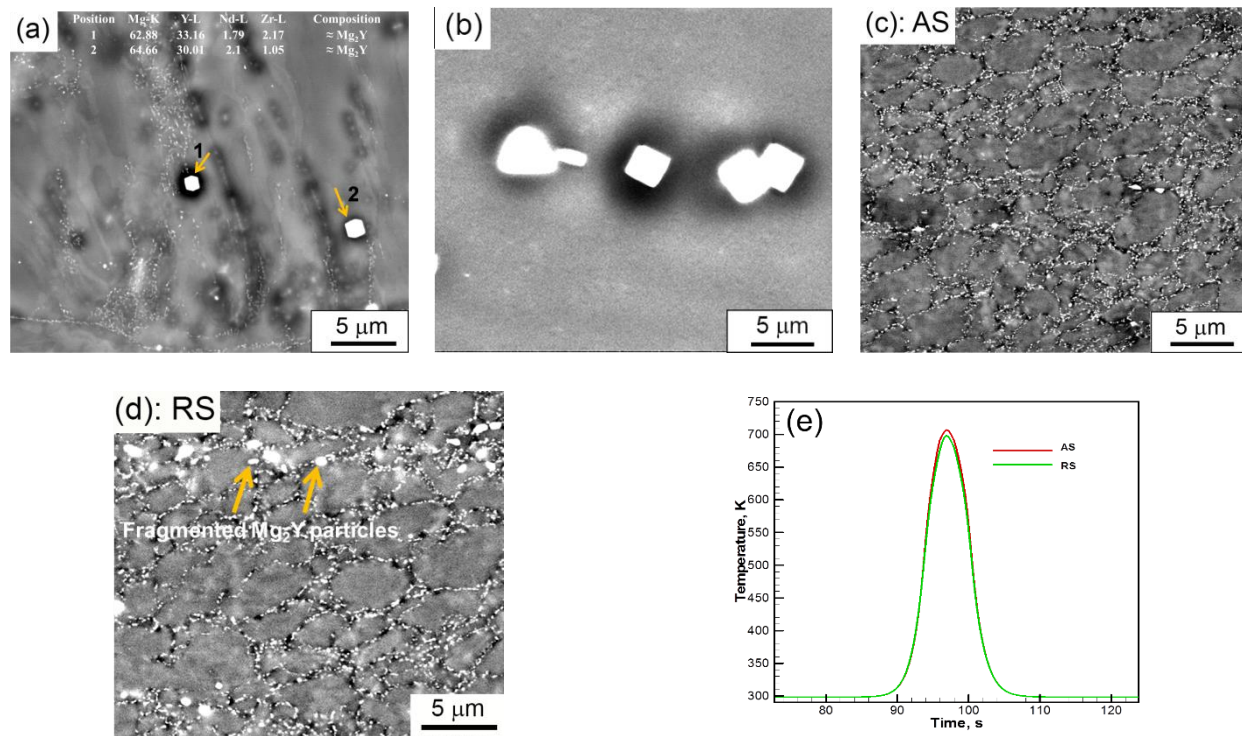


Figure 5.1. Back scattered electron images show thermally stable Mg₂Y intermetallics in (a) rolled, and (b) solutionised conditions. FSP leads to (c) dissolution of the intermetallic phase on the advancing side, and (d) fragmentation on the retreating side. (e) Predicted thermal cycle by numerical model shows lower peak temperature (435°C) and shorter times for diffusion in comparison to solutionising treatment.

Figure 5.2 shows a theoretical framework outlining the individual mechanisms that contribute to dissolution during FSW/FSP which are: (i) mechanically driven atomic transportation along the tool path, (ii) thermally aided solute transportation, and (iii) dislocation and grain boundary sweeping across the matrix-particle interface within the shear layer.

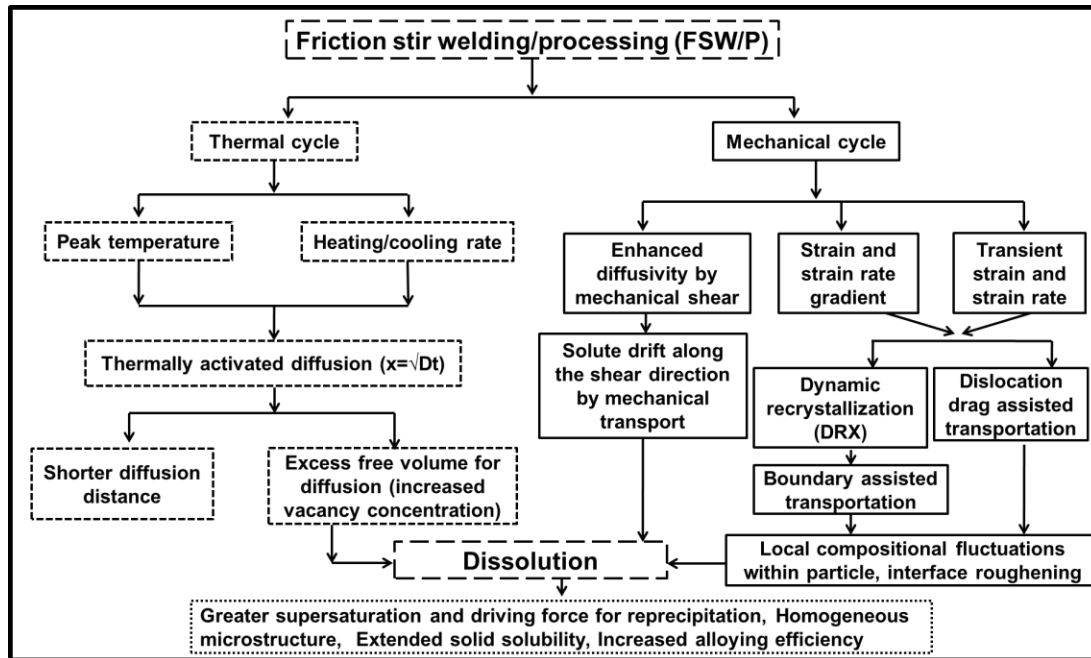


Figure 5.2. Theoretical model showing the basic mechanisms that dissolve particles during FSW/FSP.

To illustrate the effect of each mechanism, an independent treatment was given, and attention was directed to their mutually inclusive nature. Furthermore, for the sake of simplicity, a binary Mg-Y system was considered. As a consequence to the above assumption, the interaction between Nd and Y was neglected. Such an assumption introduces negligible error into the calculations because only the atomic diffusion of Y away from the Mg_2Y - α -Mg interface is considered. Moreover, mechanical action of the tool can be safely neglected because there is no physical contact between the pin surface and Mg_2Y particle. Therefore, only dislocation and boundary sweeping of the atoms aided by thermally activated diffusion dissolve the Mg_2Y particle.

Temperature activated solute diffusion arises from the rise in equilibrium number of vacancies increasing the excess free volume. The created free space accelerates atomic transport by vacancy-atom interchange mechanism due to low activation barrier for vacancy migration [12]. Additionally, thermal vibration assists atomic jumps from one lattice site to the other. If atoms are assumed to diffuse by uncorrelated jumps and a random walk process, and the diffusion distance is assumed to be 50 μm (grain radius), time required to dissolve the Mg_2Y particle at solutionizing temperature (525°C) can be calculated using:

$$t = \frac{x^2}{D} \quad (3)$$

where x , D and t are the diffusion distance, interdiffusion coefficient of Y in Mg, and time, respectively. Due to larger atomic size of Y (180 pm) compared to Mg (160 pm), diffusion of Y is considered to be the rate limiting step for dissolving Mg_2Y . Overriding the anisotropic diffusion on basal and non-basal planes where the ratio is ~ 1 at 525°C [13], diffusivity of Y in α -Mg can be calculated using [12]:

$$D = D_o \exp\left(\frac{-Q}{RT}\right) \quad (4)$$

where D_o is the pre-exponential factor, Q is the activation enthalpy for inter-diffusion jump, R is the gas constant and T is the temperature. Plugging in the values ($D_o = 3.21 \times 10^{-8} \text{ m}^2/\text{sec}$, $Q = 99.127 \text{ kJ/mol}$) obtained for impurity diffusion of Y in Mg by Das et al. [13], D is calculated as $1.04 \times 10^{-14} \text{ m}^2/\text{sec}$ at 525°C using equation (4). Inserting this value of D in equation (3), time required for dissolving Mg_2Y during solution heat treatment is 67 hours.

In the case of FSW/FSP, dislocation-plasticity-mediated-diffusion accelerates the dissolution of Mg_2Y . Using the velocity streamlines from Figure 5.3(a), total effective strain on the particle during its residence within the shear layer is calculated as ~ 22 in the AS (Figure 5.3(b)), where the value of effective strain (ϵ) is obtained by taking the square root of the squares of principal strains ϵ_1 and ϵ_2 :

$$(\sqrt{\epsilon_1^2 + \epsilon_2^2}) \quad (5)$$

These principal strains were calculated by plugging in the computed values of ϵ_{xx} , ϵ_{yy} , and ϵ_{xy} from the numerical model in:

$$\epsilon_{1,2} = \frac{\epsilon_{xx} + \epsilon_{yy}}{2} \pm \sqrt{\left(\frac{\epsilon_{xx} - \epsilon_{yy}}{2}\right)^2 + \epsilon_{xy}^2} \quad (6)$$

A lower total effective strain (Figure 5.3(b)) in the retreating side validates the concept that material from AS deposits on AS and RS on RS. This implies that material on RS was worked lesser with the imposed strain unable to dissolve Mg_2Y but sufficient to fragment it.

The individual components of strain and strain rate that were computed by the numerical model are shown in Figures 5.3(c, d). Since the particle dissolves when it resides in the shear layer, plugging $t=6.4$ seconds in equation (3), and assuming the diffusion distance as the intermetallic edge length $\sim 2 \mu\text{m}$, the apparent diffusivity (D_{app}) of Y in Mg matrix is calculated as $0.625 \times 10^{-12} \text{ m}^2/\text{sec}$. This value of D_{app} is 60 times greater than the diffusivity of Y in the absence of stress and is attributed to: (i) stress driven anisotropic transport of solute atoms by gliding dislocations and sweeping grain boundaries combined with (ii) pipe and boundary diffusion of solute atoms along the dislocation core and grain interfaces during FSW/FSP.

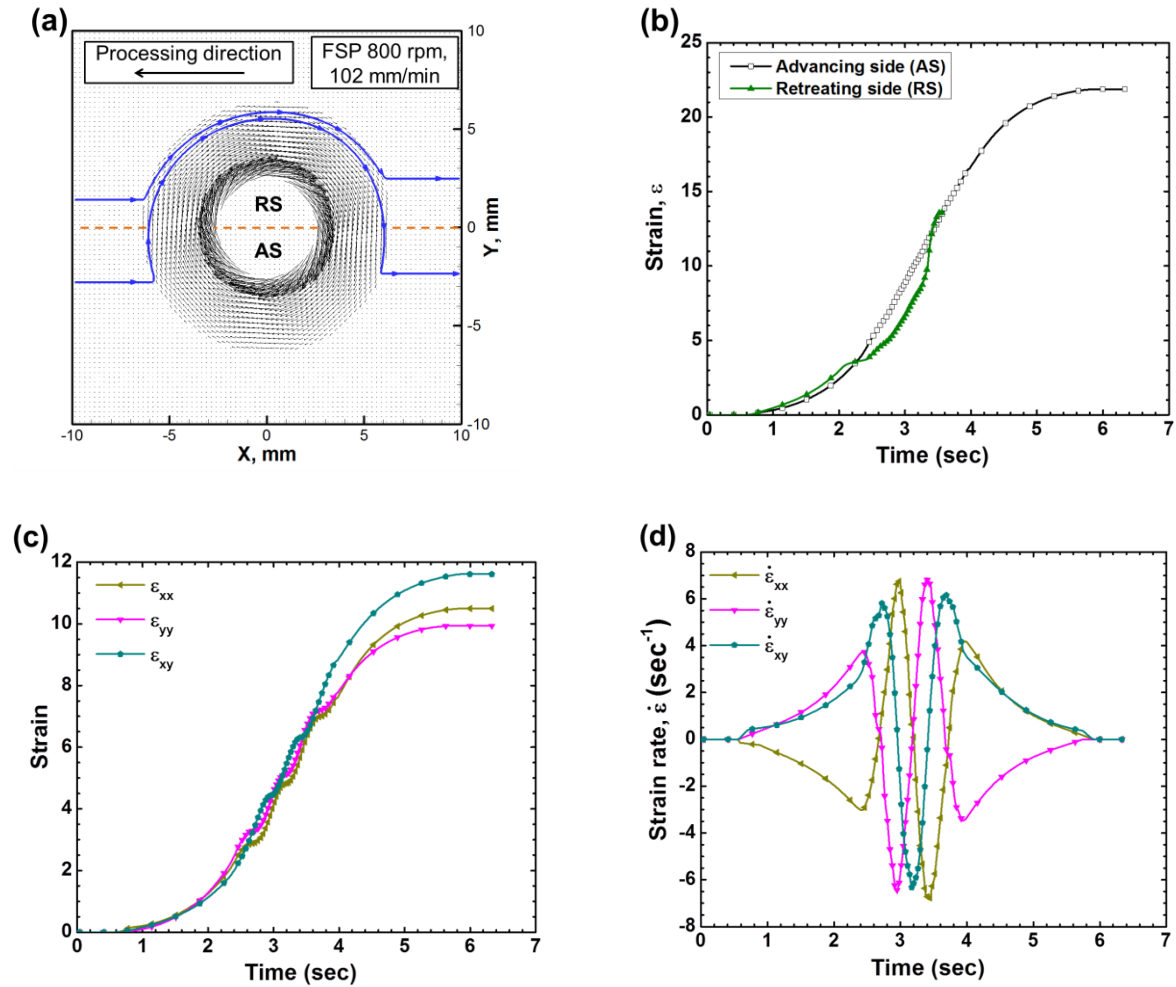


Figure 5.3. (a) Velocity profile and streamline used for computation of strain and strain rates during FSW/FSP, (b) calculated value of effective strain on Mg_2Y particle using Eqs (5, 6), and (c, d) computed strain and strain rate components on the particle situated at a distance of $60 \mu m$ from the pin surface within the shear layer.

Figure 5.4 shows a schematic of the 2-D geometric straining of the Mg_2Y particle around the pin circumference for a tool rotational rate of 800 rpm and traverse velocity of 102 mm/min. The strain values are quantified for a particle that engages with the pin on the leading–advancing

(L–A) side and is deposited on the trailing–advancing (T–A) side. Note that, to guide the reader’s eye, the particle dimensions are exaggerated with respect to the pin. Also, the shape change is plotted assuming that the strain is accommodated elastically. Throughout its interaction with the pin, the particle is under a state of shear (ϵ_{xy}) ranging from 2.56–7.85. Due to the shear on both x and y planes, the particle is twisted as observed in the plot. In addition to twisting, extrusion of the particle, parallel and antiparallel to the tool traverse direction elongates the particle along the y axis (ϵ_{yy}). The elongation of the particle decreases (3.28–1.48) from the L–A to the L–R side and increases (1.48–3.52) again as it travels from the trailing–retreating (T–R) to trailing–advancing (T–A) side of the pin. Perpendicular to the tool travel direction, the particle is compressed along the transverse direction for L–A, L–R, and T–R regions while it is elongated in the T–A region. The magnitude of compression along the transverse direction decreases from 2.87 to 0.93 as the particle travels from L–A to L–R before increasing again from L–R (0.93) to T–R (3.1). In the final stages, as the particle is deposited in the wake of the pin, ϵ_{xx} changes from -3.1 to 0.39 combined with heavy shear. Irrespective of the material, the nature of forces encountered by the particle during FSW/P will be similar, with its magnitude depending on process specifics. This figure provides the first account on the complex strain history experienced by the material adjacent to the pin surface and can be used to gain further understanding on the deformation history during FSW/FSP. Since particle dissolves on the AS, further discussion and quantification are limited to this region.

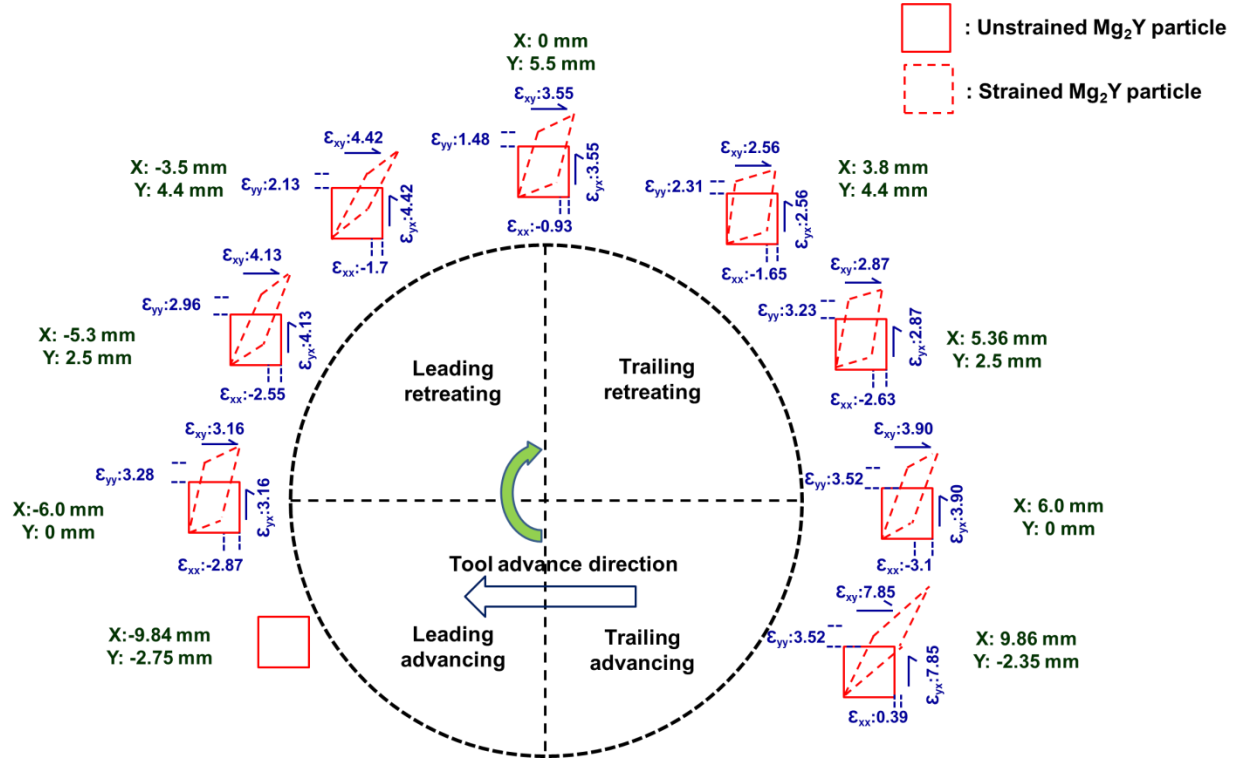


Figure 5.4. Schematic plot showing 2-D geometric straining of the Mg_2Y particle around the surface of the pin during FSW/FSP. The strain values are quantified at selected positions for a process parameter of 800 rpm and 102 mm/min. These positions can be cross-referenced with Figure 5.3(a) to enhance understanding. Negative sign of the strain value indicates that the particle is under compression.

To minimize the complexity, strain is considered to be accommodated by dislocations without the occurrence of dynamic recrystallization. This assumption allows for neglecting grain boundaries and considers solute flux to occur exclusively via moving dislocations. Using a two-parameter Kubin-Estrin model [14], the density of mobile (ρ_m) and immobile (ρ_f) dislocations with strain was calculated by solving these coupled differential equations:

$$\frac{d\rho_m}{d\varepsilon} = \frac{c_1}{b^2} - C_2\rho_m - \left(\frac{c_3}{b}\right)\rho_f^{0.5} \quad (7)$$

$$\frac{d\rho_f}{d\varepsilon} = C_2\rho_m + \left(\frac{C_3}{b}\right)\rho_f^{0.5} - C_4\rho_f \quad (8)$$

where b is the Burgers vector, C_1 is associated with the multiplication of mobile dislocations, C_2 accounts for dislocation annihilation and trapping, C_3 is related to the immobilization through interaction with forest dislocations, and C_4 relates to dynamic recovery. The negative terms that represent the loss of the mobile dislocation density in equation (7) due to various dislocations reactions, reappear as positive terms in equation (8) for the calculation of forest dislocations.

Though, $\frac{\tau_{CRSS}^{non\ basal}}{\tau_{CRSS}^{basal}}$ drops from 100 to ~ 1 at 400°C , we have considered basal slip ($b=0.32\text{ nm}$) for simplicity. Figure 5.5(a) plots the evolution of mobile and immobile dislocation densities as a function of strain by using the reported values of C_i for Mg [15] which are; $C_1=3.15\times 10^{-4}$, $C_2=0.606$, $C_3=0.077$, and $C_4=15$, while Figure 5.5(b) shows high dislocation density capturing the high strain processing nature of FSW/FSP. Note that post-mortem analysis of the processed sample was done under a TEM using a two beam condition to record the extent of deformation qualitatively.

For a $2\text{ }\mu\text{m}$ particle, the number of dislocations arriving at the interface is:

$$N = \rho_m L v t \quad (9)$$

where N is the number of dislocations arriving at the precipitate, t is the time, L is the particle diameter, and v is the mobile dislocation glide velocity calculated using the Orowan equation ($\dot{\varepsilon} = M\rho_m b v$) by setting M as 4.5, which is the value for randomly oriented Mg grains [16, 17]. We simplify the calculations for dislocation assisted solute flux by making two assumptions. First, the particle is considered not to fragment with its dissolution starting from the

instant it has contacted the shear layer. Second, solute atoms are transported by an intermediate step of diffusion across the particle-matrix interface into the pinned dislocation core. Although the first assumption is more applicable to small non-shearable particles because large particles are amenable to cracking as explained in the latter part of this article, the transfer of atoms by interfacial diffusion at elevated temperatures relaxes the stress-field around the dislocation core and leads to attractive dislocation-particle interaction [18]. Experimental evidence for this mechanism is provided in Figure 5.5(c) which shows departure side pinning of dislocation at a particle in a friction stir processed specimen.

With the above assumptions, a necessary condition that must be met for the particle to dissolve is that the dislocation wait time at the particle-matrix interface should be greater than the time for the solute to diffuse into the dislocation core. The waiting time (t_w) of a dislocation is: $t_w = \frac{\Omega}{\dot{\epsilon}}$, where Ω is the elementary strain and can be expressed as: $\Omega = \frac{\rho_m b}{\rho_f^{0.5}}$ [19]. The distance that the solute traverses over the dislocation wait time is: $x = (Dt)^{0.5}$. In the present case, D_Y^{Mg} at the shear layer temperature (435°C) is 1.55×10^{-15} m²/sec. Incorporating ρ_m and ρ_f from Figure 5.5(a) and inserting the obtained value of t_w in the diffusivity equation, the waiting time of the dislocation is sufficient to allow solute flux into its core. For example, consider the value of strain and strain rate on Mg₂Y particle at 2 seconds. For these values, the dislocation is pinned at the particle for 0.01 seconds. In the pinned time, the solute atoms can traverse a distance of 10 nm, which is higher than the distance for jumping across the Mg₂Y/Mg interface. This indicates that solute trapping occurs by interfacial diffusion into the dislocation core before it is forced by the external stress to speed past the particle.

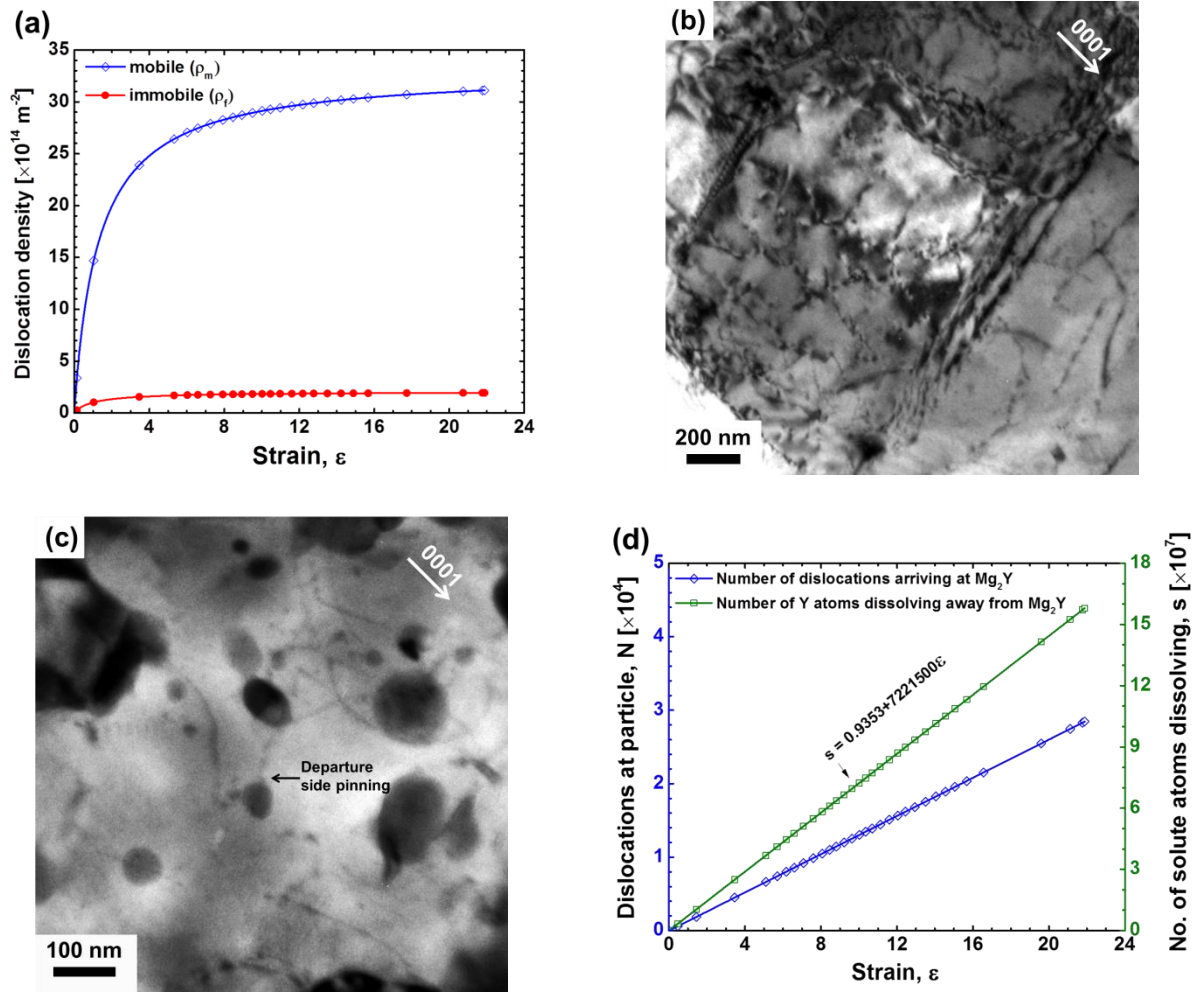


Figure 5.5. (a) Evolution of mobile and immobile dislocation density with strain calculated using Eqs. (5-8). (b) Processing strain captured in the form of high dislocation density in an Mg-4Y-3Nd alloy, (c) Departure side pinning supporting the mechanism of interfacial transport of solute atoms, and (d) Number of dislocations arriving at the particle, and solute atoms dissolving away from Mg_2Y as a function of strain.

To dissolve an Mg_2Y particle of a volume of $8 \mu\text{m}^3$, a total of 3.3×10^{12} Y atoms (N) must be transported away from the particle. This number is obtained from $N = \frac{\rho V N_a}{3W}$, where ρ is the

density of Mg_2Y (2.93 g/cc), V is the volume, N_a is the Avogadro number, and W is the molecular weight of Mg_2Y (137.5 gram/mole). We consider Mg_2Y to dissolve via mobile dislocations. Furthermore, from the above calculations on the waiting time and time required to diffuse the solute, a pragmatic consideration is complete decoration of the dislocation core resembling a condensed solute atmosphere. Here the equivalent line length for decoration is the edge length of the precipitate, which is 2 μm . Figure 5.5(d) plots the number of dislocations arriving at the particle along with the number of Y atoms dissolving away from Mg_2Y precipitate.

By this method, dislocations account for a minor fraction of the atoms and imply that grain boundary diffusion and particle shearing are important in disintegrating the particle. In the above calculation, we have considered that back diffusion of solute from the dislocation into the particle does not occur once the solute crosses the interface. This limitation is valid for solute atoms with a positive volume misfit ($\Delta V > 0$) as in the present case due to minimization of strain energy at the core where the stresses are tensile in nature [18]. In summary, the mechanism of dissolution of non-shearable particles via interfacial dislocations occurs in three steps. First, solute diffuses into the core (thermal event); second, solute moves along the core by pipe diffusion, and third, dislocation detaches from the particle and the solute is transported away from the particle at a rate equal to the dislocation velocity.

Although for simplifying the calculations, we have considered the mechanisms in the framework to act individually, events of fragmentation combined with dislocation and grain boundary sweeping along the particle-matrix interface will be followed by dislocation glide

within the particle, provided the particle has the same crystal structure as the matrix as in the present case. A simple criterion to explain the competing phenomenon of dissolution and fragmentation is: If the stress required for nucleating dislocations within the particle exceeds the fracture stress of the particle, the particle cracks; and if not, the particle dissolves. Brown and Stobes [20] expressed the local stress at a hard particle as; $\sigma_p = 4.2\alpha Gb\rho_f^{0.5}$. Using σ_p , the fracture strength (σ_f) of Mg_2Y is estimated as equal to or lesser than 85 MPa ($G=12.5$ GPa, $\alpha=0.5$ at 708 K). With decreasing particle size, the stress needed to fracture the particle increases. This signifies a cross-over from cracking to plasticity within the particle at a critical size, which in turn depends on the strain. Even after the particle deforms, an increase in the aspect ratio along the shear direction can lead to particle fracturing by a fiber loading mechanism. These arguments are supported by particle refinement on the RS (Figure 5.1 (d)) whereas, on the AS, the strain was high enough to cause the cross-over in mechanism to dislocation glide within the particle that completely dissolved the particles (Figure 5.1(c)).

For shear to be effective, a necessary condition is that the rate of arrival of dislocations at the particle must be greater than the back-diffusion time for the solute to avoid undoing the shear. As the size of the particle decreases by fragmenting multiple times, a cross-over from shaving to shearing will occur. This phenomenon of shearing validates the Molecular Dynamics (MD) simulation for other processes where forced mixing is involved [21, 22]. Similar to the other severe plastic deformation (SPD) processes modeled using MD, we believe that majority of dissolution will occur by superdiffusive mixing enabled by dislocation cutting of the precipitate. In fact, these MD models can be adapted to gain further insight into the process of friction stir welding.

5.4 Conclusions

A specific case of Mg_2Y dissolution was exemplified to propose physics based framework for the dissolution and fragmentation of particles during FSW/FSP. To the best of our knowledge, no such effort exists in the literature.

The highlights from this work are:

- 1) Thermally stable Mg_2Y (melting point: 780°C) intermetallic dissolved on the advancing side and fragmented on the retreating side indicating a strain gradient within the microstructure.
- 2) Particles dissolved even though the peak temperature (435°C) during FSP was $\sim 350^\circ\text{C}$ below the melting point of Mg_2Y . Diffusivity of Y in Mg matrix was calculated as 60 times faster during FSW/FSP ($0.625 \times 10^{-12} \text{ m}^2/\text{sec}$) than in the absence of stress ($1.04 \times 10^{-14} \text{ m}^2/\text{sec}$). Higher value of diffusivity is proposed to arise from (i) stress driven anisotropic transport of solute atoms by gliding dislocations and sweeping grain boundaries combined with (ii) pipe and boundary diffusion of solute atoms along the dislocation core and grain interfaces during FSW/FSP.
- 3) Strain and strain rates are computed for the particle located at $60 \mu\text{m}$ from the pin surface within the shear layer using a numerical model. The total effective strain on the particle is computed as 22. 2-D geometric strain mapping around the pin surface using the numerical model shows intense shearing and elongation of the particle along the travel direction. The particle is compressed in the transverse direction except for the trailing–advancing region where the particle experiences tensile stress.

- 4) Mobile (ρ_m) and immobile (ρ_i) dislocation density is quantified using the information obtained from the heat transfer and numerical model, and the Kubin-Estrin model. A total dislocation density of 3.1×10^{15} is predicted by this approach. Assuming solute transport to occur exclusively via mobile dislocations, calculations show that 1.6×10^8 solute atoms are swept from the Mg_2Y precipitate. The mechanism of dislocation sweeping is proposed to occur in three steps: (i) thermally activated diffusion of solute atom into dislocation core, (ii) transportation of solute atom along the core by pipe diffusion, and (iii) detachment of dislocation from the particle with the solute at a rate equal to the dislocation velocity. This mechanism is supported by the experimentally observed departure side pinning of the dislocation at a particle.
- 5) A criterion stated for fragmentation of precipitate over dissolution is: If the stress required for nucleating dislocations within the particle exceeds the fracture stress of the particle, the particle cracks; and if not, the particle dissolves.

In addition to advancing the understanding within the field, the proposed framework has utility to tailor microstructures by careful control of the process parameters.

5.5 References

1. Z.Y. Ma, S.R. Sharma, R.S. Mishra. "Microstructural modification of as-cast Al-Si-Mg alloy by friction stir processing". *Metallurgical and Materials Transactions A* 37.11 (2006): 3323-3336.
2. S. Pasebani, I. Charit, R.S. Mishra. "Effect of tool rotation rate on constituent particles in a friction stir processed 2024Al alloy". *Materials Letters* 160 (2015): 64-67.

3. A.H. Feng, Z.Y. Ma. “Enhanced mechanical properties of Mg–Al–Zn cast alloy via friction stir processing”. *Scripta materialia* 56.5 (2007): 397-400.
4. B.L. Xiao, Q. Yang, J. Yang, W.G. Wang, G.M. Xie, Z.Y. Ma. “Enhanced mechanical properties of Mg–Gd–Y–Zr casting via friction stir processing”. *Journal of Alloys and Compounds* 509.6 (2011): 2879-2884.
5. S. Palanivel, N. Phalgun, B. Glass, R.S. Mishra. “Friction stir additive manufacturing for high structural performance through microstructural control in an Mg based WE43 alloy”. *Materials & Design* 65 (2015): 934-952.
6. R.S. Mishra, P.S. De, N. Kumar. “Friction stir welding and processing”. Springer, Science and Engineering, 2014; ISBN: 978-3-319-07042-1
7. Z.Y. Ma, A.L. Pilchak, M.C. Juhas, J.C. Williams. “Microstructural refinement and property enhancement of cast light alloys via friction stir processing”. *Scripta Materialia* 58.5 (2008): 361-366.
8. A.R. Yavari, P.J. Desre, T. Benamer. “Mechanically driven alloying of immiscible elements”. *Physical review letters* 68.14 (1992): 2235.
9. N.Q. Vo, R.S. Averback, Y. Ashkenazy, P. Bellon, J. Wang. “Forced chemical mixing at Cu-Nb interfaces under severe plastic deformation”. *Journal of Materials Research* 27.12 (2012): 1621-1630.
10. O.B. Fabrichnaya, H.L. Lukas, G. Effenberg, F. Aldinger. “Thermodynamic optimization in the Mg–Y system”. *Intermetallics* 11.11 (2003): 1183-1188.
11. G. Chen, P. Zhang. “First-principles Study of Electronic Structures, Elastic Properties and Thermodynamics of the Binary Intermetallics in Mg–Zn–Re–Zr Alloy”. *Defence Technology* 9.3 (2013): 131-139.

12. D.A. Porter and K.E. Easterling, Phase Transformation in Metals and Alloys, 2nd ed., Chapman and Hall, New York.
13. S.K. Das, Y.B. Kang, T. Ha, I.H. Jung. “Thermodynamic modeling and diffusion kinetic experiments of binary Mg–Gd and Mg–Y systems”. *Acta Materialia* 71 (2014): 164-175.
14. L.P. Kubin, and Yu Estrin. “Evolution of dislocation densities and the critical conditions for the Portevin-Le Chatelier effect”. *Acta metallurgica et materialia* 38.5 (1990): 697-708.
15. J. Balík, P. Lukác, R. Kužel. “Basal to Non-Basal Transition for In-Plane Deformation of AZ31 Magnesium Alloys”. *Acta Physica Polonica-Series A General Physics* 122.3 (2012): 435.
16. C.R. Hutchinson, P.T. Loo, T.J. Bastow, A.J. Hill, J. da Costa Teixeira. “Quantifying the strain-induced dissolution of precipitates in Al alloy microstructures using nuclear magnetic resonance”. *Acta Materialia* 57.19 (2009): 5645-5653.
17. C.H. Cáceres, and P. Lukáč. “Strain hardening behaviour and the Taylor factor of pure magnesium”. *Philosophical Magazine* 88.7 (2008): 977-989.
18. D.J. Srolovitz, R.A. Petkovic-Luton, M.J. Litton. “Diffusional relaxation of the dislocation-inclusion repulsion”. *Philosophical Magazine A* 48.5 (1983): 795-809.
19. W.A. Curtin, D.L. Olmsted, L.G. Hector. “A predictive mechanism for dynamic strain aging in aluminium–magnesium alloys”. *Nature materials* 5.11 (2006): 875-880.
20. L.M. Brown, W.M. Stobbs. “The work-hardening of copper-silica v. equilibrium plastic relaxation by secondary dislocations”. *Philosophical Magazine* 34.3 (1976): 351-372.
21. Y. Ashkenazy, N.Q. Vo, D. Schwen, R.S. Averbach, P. Bellon. “Shear induced chemical mixing in heterogeneous systems” *Acta Materialia* 60.3 (2012): 984-993.

22. P. Bellon, R.S. Averbach, S. Odunuga, Y. Li, P. Krasnochtchekov, A. Caro. Crossover from superdiffusive to diffusive mixing in plastically deformed solids. Physical review letters 99.11 (2007) 110602.

CHAPTER 6
DISLOCATION TYPES AND CONFIGURATION IN A FRICTION STIR
PROCESSED MG—RARE EARTH ALLOY

Overview: From chapters 3 and 4, it was evident that dislocations play a key role in controlling the precipitate descriptors during post aging of the friction stir processed/AM WE43 specimen. Due to the limited formability of Magnesium, high temperature thermo-mechanical processing is done because of the difficulty in triggering non-basal dislocations at room temperature. However, studies on the defect structures resulting from high temperature severe plastic deformation processes are scarce in literature. Furthermore, to understand the types of dislocations that assist the nucleation of strengthening precipitates, it is important to document the defect structure in the as processed specimen. Therefore, we investigate the defect types and their configuration for the first time in a friction stir processed Magnesium—rare earth alloy to capture the slip activity that occurred during high straining at high temperatures. Post-mortem examination of the processed specimen showed three deformation signatures. First, copious amounts of basal $\langle a \rangle$ and non-basal (prism and pyramidal $\langle a \rangle$, $\langle c+a \rangle$, $\langle c \rangle$) dislocations were observed. Second, I_1 stacking faults were observed in the regions concentrated with non-basal $\langle c \rangle$ and $\langle c+a \rangle$ dislocations and basal $\langle a \rangle$ dislocations that dissociated into Shockley partials to form I_2 faults. Third, we speculate a possible source mechanism for the formation of $\langle c+a \rangle$ based on the experimental observations.

6.1 Introduction

Room temperature plasticity in Magnesium is limited by the ability to initiate five independent slip modes as required by the Taylor criterion for homogeneous deformation of a polycrystalline aggregate [1]. Such a limitation is imposed by pronounced plastic anisotropy in critical resolved shear stress required for basal activity as compared to the non-basal modes. The magnitude of this difference is approximately, $R = \frac{\tau_{CRSS}^{non\ basal}}{\tau_{CRSS}^{basal}} \sim 10^2$. However, as the temperature increases above 180°C, R drops to 2 [2]. This drop in the anisotropy at higher temperatures leads to the generation of prismatic and pyramidal $\langle a \rangle$ ($\{h0i0\}1/3\langle 11\bar{2}0 \rangle$, $\{h0i1\}1/3\langle 11\bar{2}0 \rangle$ along with $\langle c+a \rangle$ slip systems ($\{hkil\} 1/3\langle 11\bar{2}0 \rangle$) to accommodate deformation [3].

Among the above mentioned slip systems, tremendous attention has been paid on pyramidal slip ($\langle c+a \rangle$) activity in Mg alloys because of their ability to provide five independent slip systems [4-7]. Several reasons have been invoked to explain their activation at room temperature, a few of which are: (i) decreased c/a slip ratio with addition of solute [8], (ii) stabilization of the glissile $\langle c+a \rangle$ by reduction in the $(11\bar{2}2)$ stacking fault energy [5], (iii) reduced tendency to decompose on basal planes due to immobilization of the $\langle c+a \rangle$ edge dislocation [5], and (iv) increased basal stacking fault energy [5]. Though, there are multiple viewpoints on their activation mechanism, it is now widely accepted that stacking faults and $\langle c+a \rangle$ dislocations play a beneficial role in increasing the strength and ductility of Mg alloys [9, 10, 11]. For example, the study by Sandlobes et al. [9] showed an increase in ductility facilitated by the heterogeneous nucleation of $\langle c+a \rangle$ dislocations at the I_1 fault in an Mg-Y alloy.

Although, it is well-established that Mg-rare earth alloys exhibit enhanced non-basal slip and possess low basal stacking fault energy [7, 9], reports on the dislocation structures generated at high temperatures and intense strain and strain rates are limited for these alloys. Therefore, the purpose of this study was to evaluate the quenched-in structure of dislocations after friction stir processing (FSP) in a commercially available Mg-4Y-3Nd (WE43) alloy. It should be noted that, this is the first attempt on investigating the dislocation structures after FSP in an hcp metal.

6.2 Experimental Methods

For this analysis, 3 mm thick sheet of WE43 alloy (nominal composition: Mg-4wt% Y-3wt%Nd-0.5wt%Zr) was friction stir processed at a tool rotation rate of 2000 revolutions per minute and a tool traverse speed of 102 mm/min. To quench in the dislocations nucleated at high temperatures, copper backing plate was used for increased cooling. Peak temperature during processing was computed using a three dimensional heat transfer and material flow model of Arora et al. [12] and the details of the model can be obtained from the reference [12]. The above mentioned process parameter for friction stir processing was chosen to dissolve second phases so that only dislocations and grain boundaries contribute to room temperature deformation. After FSP, strength and ductility was measured by room temperature mini-tensile testing at an initial strain rate of $1 \times 10^{-3} \text{ s}^{-1}$.

To analyze the quenched-in dislocation structures after FSP, g.b=0 invisibility criterion was used in a transmission electron microscope (Technai G2 F20 STEM) operating at 200KV. Specimen for TEM was polished to a thickness of 80 μm followed by ion milling (Gatan PIPS) till perforation using an accelerating voltage of 3 KV. To identify the $\langle a \rangle$ type dislocations with

$b=1/3\langle 11\bar{2}0 \rangle$, $\langle c \rangle$ type with $b=\langle 0001 \rangle$, and $\langle c+a \rangle$ type with $b=1/3\langle 11\bar{2}3 \rangle$, two beam bright field (TBBF) and weak beam dark field imaging (WBDF) were used. Different reflections were excited by tilting the sample with respect to the $[10\bar{1}0]$ zone axis. This direction was chosen to view the basal plane edge on while imaging.

To use the invisibility criterion for investigating the dislocations, several two beam conditions were set up in the TEM by exciting different g reflections. Table 6.1 shows the $g.b$ values for the individual reflections in a hexagonal closed packed (hcp) crystal structure which are pertinent to this study. On the basis of the contrast generated in the TEM and Table 6.1, the Burgers vector of the dislocation was identified. Note that at least two invisibility criterion are required to determine the Burgers vector of the dislocation with certainty. For example, if $g_1.b=0$, and $g_2.b=0$, the burgers vector of the dislocation will be parallel to g_3 that is normal to g_1 and g_2 .

Table 6.1. $g.b$ values for selected reflections (g) in an hcp metal

| Reflection (g) | Burgers vector (b) of perfect dislocations ($\times \frac{1}{3}$) | | | | | | | | | |
|----------------------------|---|----------------------|----------------|----------------|----------------------|----------------|----------------------|----------------------------|----------------------|---------------|
| | $[11\bar{2}0]$ | $[\bar{1}2\bar{1}0]$ | $[\bar{2}110]$ | $[11\bar{2}3]$ | $[\bar{1}2\bar{1}3]$ | $[\bar{2}113]$ | $[11\bar{2}\bar{3}]$ | $[\bar{1}2\bar{1}\bar{3}]$ | $[\bar{2}11\bar{3}]$ | $[0003]$ |
| $[0001]$ | 0 | 0 | 0 | ± 2 | ± 2 | ± 2 | $\pm \bar{2}$ | $\pm \bar{2}$ | $\pm \bar{2}$ | ± 2 |
| $[11\bar{2}0]$ | ± 2 | ± 1 | $\pm \bar{1}$ | ± 2 | ± 1 | $\pm \bar{1}$ | ± 2 | ± 1 | $\pm \bar{1}$ | 0 |
| $[\bar{1}2\bar{1}0]$ | ± 1 | ± 2 | ± 1 | ± 1 | ± 2 | ± 1 | ± 1 | ± 2 | ± 1 | 0 |
| $[\bar{2}110]$ | $\pm \bar{1}$ | ± 1 | ± 2 | $\pm \bar{1}$ | ± 1 | ± 2 | $\pm \bar{1}$ | ± 1 | ± 2 | 0 |
| $[11\bar{2}2]$ | ± 2 | ± 1 | $\pm \bar{1}$ | ± 4 | ± 3 | ± 1 | 0 | $\pm \bar{1}$ | $\pm \bar{3}$ | ± 2 |
| $[11\bar{2}\bar{2}]$ | ± 2 | $\pm \bar{1}$ | $\pm \bar{1}$ | 0 | $\pm \bar{1}$ | $\pm \bar{3}$ | ± 4 | ± 3 | ± 1 | $\pm \bar{2}$ |
| $[\bar{1}2\bar{1}2]$ | ± 1 | ± 2 | ± 1 | ± 3 | ± 4 | ± 3 | $\pm \bar{1}$ | 0 | $\pm \bar{1}$ | ± 2 |
| $[\bar{1}2\bar{1}\bar{2}]$ | ± 1 | ± 2 | ± 1 | $\pm \bar{1}$ | 0 | $\pm \bar{1}$ | ± 3 | 0 | ± 3 | $\pm \bar{2}$ |
| $[\bar{2}112]$ | $\pm \bar{1}$ | ± 1 | ± 2 | ± 1 | ± 3 | ± 4 | $\pm \bar{3}$ | ± 3 | 0 | ± 2 |
| $[\bar{2}11\bar{2}]$ | $\pm \bar{1}$ | ± 1 | ± 2 | $\pm \bar{3}$ | $\pm \bar{1}$ | 0 | ± 1 | ± 1 | ± 4 | $\pm \bar{2}$ |

6.3 Results and Discussion

6.3.1 Room Temperature Stress-Strain Curve and Peak Temperature during FSP

Figure 6.1 (a) shows the tensile stress-strain curve of the friction stir processed specimen tested along the processing direction. A total elongation of 36% indicates increased non-basal activity at room temperature. In contrast to the annealed structure, where fine grains are solely responsible for triggering non-basal dislocations due to the incompatibility stresses generated at the boundary [4], in a severely deformed structure, prior dislocation sub-structure could play a significant role. Figure 6.1(b) shows the computed peak temperature (750 K) during FSP and will be recalled later to reason the observed high temperature dislocation structure.

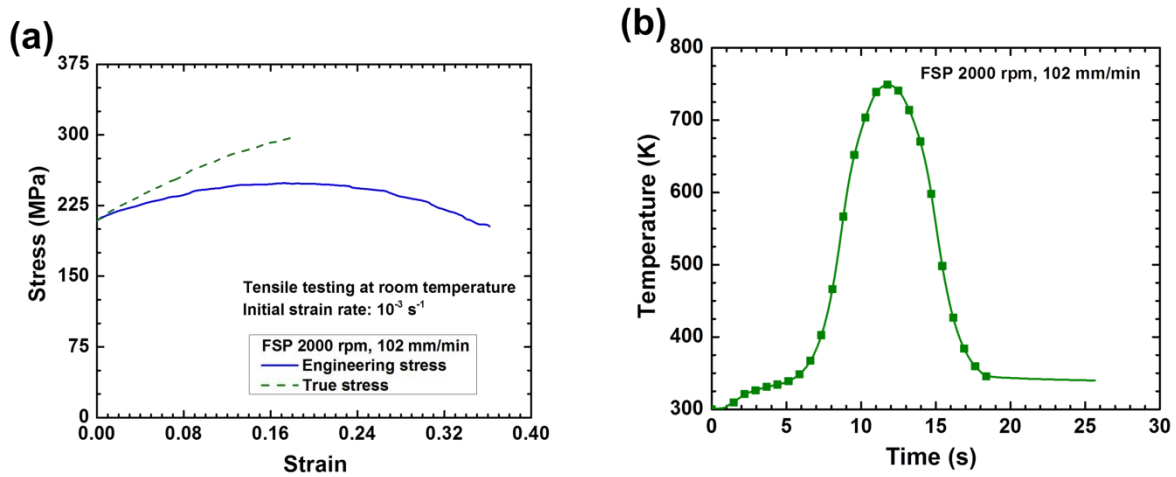


Figure 6.1. (a) Room temperature uniaxial tensile stress-strain curves of a friction stir processed specimen, and (b) computed thermal cycle in the shear layer during FSP.

6.3.2 Dislocation Structures after FSP

Typical dislocation density retained after FSP is shown in Figure 6.2(a). A majority of these dislocations were identified to have a $\langle c \rangle$ component on the basis of their visibility for $g=0002$ reflection near the $[10\bar{1}0]$ zone axis in Figure 6.2(b). Though, this analysis is shown for a single

grain, more than 10 grains were studied with all of them showing significant non-basal activities. Figure 6.2(c) shows an $\langle a \rangle$ type screw dislocation climbing out of the basal plane presumably by absorption of vacancies forming a sub-grain boundary. Nucleation of these non-basal dislocations and the process of climb are aided by the high temperature ($\sim 450^\circ\text{C}$, Figure 6.1(b)) and strains up to ~ 20 [12] imposed on the shearing layer.

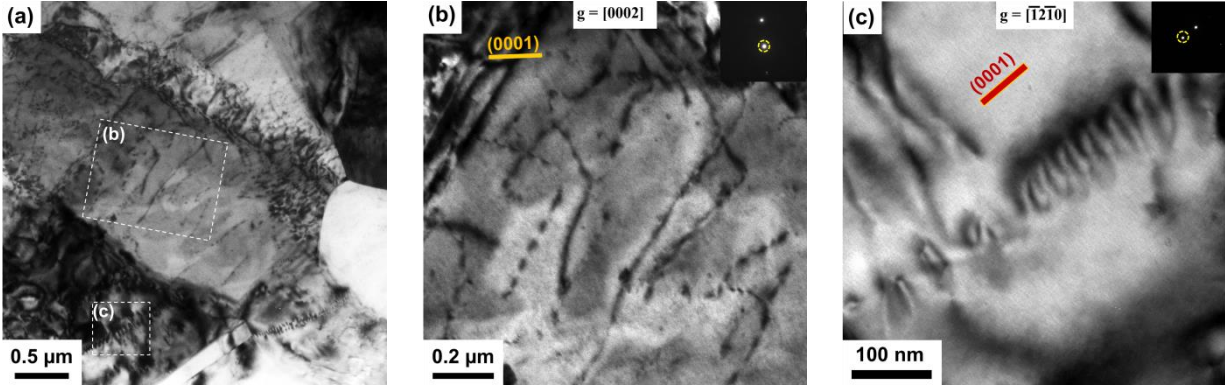


Figure 6.2. (a) Typical dislocation density in a friction stir processed specimen, (b) high density of $\langle c \rangle$ or $\langle c+a \rangle$ dislocations visible using $g=0002$ reflection, and (c) $\langle a \rangle$ type helical screw dislocations formed by absorption of vacancies during processing.

Such non-basal activities combined with the process of climb can serve as precursors to the formation of stacking faults [13]. This is supported by Figures 6.3 (a, b) which show a mixture of I_1 and I_2 faults in combination with basal $\langle a \rangle$ and non-basal $\langle c \rangle$, $\langle c+a \rangle$ dislocations. First, let us consider the formation of I_1 fault that requires the non-coplanar dissociation of $\langle c+a \rangle$ edge dislocation on a second order pyramidal plane according to the following reaction [5]:

$$\frac{1}{3}[11\bar{2}3] \rightarrow \frac{1}{6}[20\bar{2}3] + SF_{(11\bar{2}\bar{2})} + \frac{1}{3}[02\bar{2}3] \quad (1)$$

This reaction is accomplished by condensation of vacancies or interstitials on the basal plane followed by a shear in the $[10\bar{1}0]$ direction. On the basis of Figure 6.3, the chronological

sequence of deformation events is reconstructed to reason the presence of each defect. Since, the local stress state in FSP changes around the circumference of the pin, several grains can orient favorably for $\langle c \rangle$ axis compression leading to copious $\langle c+a \rangle$ activity. Once these dislocations are nucleated, they can easily climb at the peak temperature of 750 K (Figure 6.1(b)) which is well supported by a previous computational study [14] that showed $\langle c+a \rangle$ climb at temperatures as low as 1 K, provided $\langle c \rangle$ axis deformation occurs. The non-conservative motion of $\langle c+a \rangle$ dislocations serve as sources for the point defects and when followed by basal slip result in the formation of I_1 faults as observed in the present study. Zhang et al. [13] recently proposed the aforementioned $\langle c+a \rangle$ dislocation assisted mechanism for the nucleation of I_1 fault in an extruded Mg-Y alloy. Similar to their study, we also noted the presence of I_1 stacking fault in the vicinity of grain boundary presumably due to the ability of interfaces to nucleate $\langle c+a \rangle$ dislocations [15].

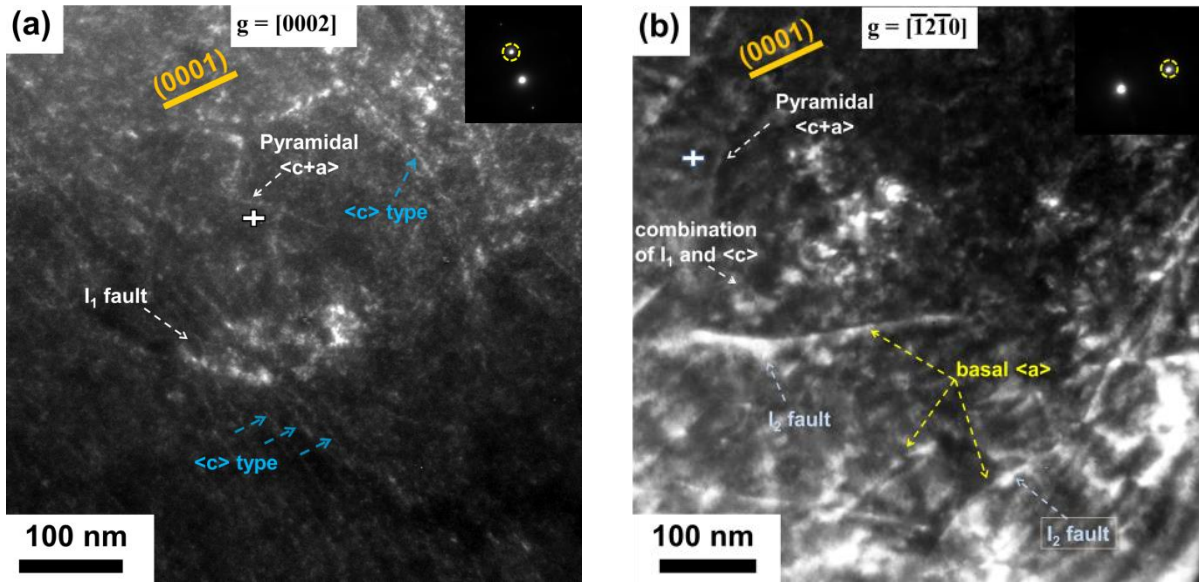


Figure 6.3. Weak beam dark field images recorded for an area using $g = 0002$ and $g = \bar{1}2\bar{1}0$ near $[10\bar{1}0]$ zone axis in a friction stir processed WE43 alloy showing (a) a mixture of I_1 stacking

fault and $\langle c \rangle$ dislocations, and (b) the presence of basal $\langle a \rangle$ dislocations and I_2 stacking fault near I_1 fault. Note the possible nucleation of pyramidal $\langle c+a \rangle$ dislocation at the I_1 fault.

In addition to the formation of I_1 stacking fault, Figure 6.3(a) shows the presence of $\langle c \rangle$ dislocations in the vicinity of the stacking fault. This can occur when the subsequently nucleated $\langle c+a \rangle$ dislocations are blocked by the sessile Frank partials bounding the I_1 fault resulting in the splitting of the $\langle c+a \rangle$ into pure $\langle c \rangle$ and basal $\langle a \rangle$ component by the following reaction [5]:

$$\frac{1}{3}[11\bar{2}3] \rightarrow [0001] + \frac{1}{3}[11\bar{2}0] \quad (2)$$

The energetic incentive for this reaction stems from the subsequent coplanar dissociation of the basal $\langle a \rangle$ dislocation into Shockley partials ($\frac{1}{3}[10\bar{1}0]$) bounding an I_2 fault. This dissociation reaction can be written as follows and is marked in Figure 6.3(b):

$$\frac{1}{3}[11\bar{2}0] \rightarrow \frac{1}{3}[10\bar{1}0] + SF_{(0001)} + \frac{1}{3}[01\bar{1}0] \quad (3)$$

In addition to the above mentioned deformation signatures, pyramidal $\langle c+a \rangle$ dislocation was observed adjacent to the I_1 stacking fault (Figures 6.3(a, b)). At this juncture, on the basis of the location of $\langle c+a \rangle$ dislocation with respect to the I_1 fault, we expect that I_1 fault served as nucleating source for $\langle c+a \rangle$ accommodating further deformation after its formation. This source mechanism for $\langle c+a \rangle$ was previously observed experimentally by Sandlobes et al. [9] and the recent results based on continuity modeling by Agnew et al. [10] reported the energetic incentive for $\langle c+a \rangle$ to nucleate at I_1 fault. In fact, we strongly believe that these faults have played a key role in contributing to higher tensile elongation values (36%) reported at room temperature.

Investigation on this aspect has not been attempted in this study.

The above figures provide sufficient evidence for the nucleation and glide of $\langle c+a \rangle$ dislocations. Using Figures 6.3(a,b), we stated the possibility of $\langle c+a \rangle$ nucleation from I_1 fault due to its proximity with the 2-dimensional defect. Further detailed analysis of the dislocation substructure in a different grain is shown in Figure 6.4(a) by using several two beam diffraction conditions (Figures 6.4(b-g)). The Burgers vector analysis is outlined in the schematic shown in Figure 6.4(h) which is a blueprint of the enclosed rectangular area and is based on the $g \cdot b = 0$ invisibility criterion. Note that only selective portions from the enclosed area have been sketched for explanation, and therefore the schematic is not exhaustive.

invoked. Hereafter, we call these possibilities as Case I, II and III. Case I refers to the possibility that the network is $\langle c+a \rangle$ dislocation with jogged segments. For this to be true, entire dislocation structure should be visible for all three $g = [\bar{1}2\bar{1}0]$, $g = [\bar{1}2\bar{1}2]$, and $g = [0002]$ reflections. Consider the individual segments forming node 1. We find that dislocation A is of $\langle c+a \rangle$ type on the basis of its visibility for all three selected reflections, as shown in Figures 6.4 (b-g). On the other hand, dislocation B is visible for $g = [\bar{1}2\bar{1}0]$ and $g = [\bar{1}2\bar{1}2]$, showing $\langle a \rangle$ component. The absence of this dislocation for $g = [0002]$ confirms the Burgers vector as $1/3\langle 11\bar{2}0 \rangle$. By a similar method, we identify the segments E, F, G, H, I in the schematic as $\langle a \rangle$ type dislocations where the curved segment F shows the cross slip of $\langle a \rangle$ type dislocations from the basal to non-basal slip systems. Since the basal planes are viewed edge on, the $\langle a \rangle$ dislocation segments that are straight and horizontal in lie on the (0001) planes (B, E, G, I) in Figures 6.4 (b-g). Also, the $\langle c+a \rangle$ segment denoted by A and D glides on the pyramidal plane. Similarly, dislocation C is invisible for $g = [\bar{1}2\bar{1}0]$ and appears in $g = [\bar{1}2\bar{1}2]$ and $g = [0002]$, confirming the $\langle c \rangle$ component.

From the above argument, it is clear that Case I is false and the sub-structure is a mixture of $\langle a \rangle$, $\langle c \rangle$ and $\langle c+a \rangle$ dislocations. For such a configuration, two reactions are possible; Case II: dissociation of $\langle c+a \rangle$ to sessile $\langle c \rangle$ and glissile $\langle a \rangle$ (equation 2) or, Case III: combination of sessile $\langle c \rangle$ and glissile $\langle a \rangle$ to form $\langle c+a \rangle$ gliding on $(11\bar{2}2)$ as per the following reaction:



Both the cases lead to the formation of nodes. In fact similar junctions were previously

reported [5] in an Mg-Li alloy to explain the dissociation of $\langle c+a \rangle$ and was based on the energetic incentive accompanying the dissociation of Shockley partials on the basal plane (equation 3). If we consider Case II to be solely operative, dissociation of each $\langle c+a \rangle$ dislocation should lead to two segments ($\langle a \rangle$, $\langle c \rangle$) implying a total of six segments for the three nodes shown in the schematic. Since we observe only four segments (B, C, E, J) for the three nodes in Figures 6.4 (c, e, g), we speculate a different mechanism that is a mixture of Case II and Case III. This mechanism is invoked based on the high driving force [15] to nucleate $\langle c+a \rangle$ (segment D in Figure 6.4(h)) at the grain boundary which is indicated by the black dashed arrows in Figures 6.4(b-g). Once this dislocation nucleates, depending on the local stress, it can dissociate into $\langle c \rangle$ (segment C) and $\langle a \rangle$ (segment E) dislocations which is Case II. Also, on a similar time scale, it is fair to assume the activity of basal $\langle a \rangle$ (Segment B) dislocations in the same area due to its ease of activation in Mg alloys. Once segment C intersects segment B, further motion of the node can occur in either of these two ways: (i) non-conservative motion of the node which requires the climb of $\langle c \rangle$ component or, (ii) nucleation of $\langle c+a \rangle$ by combining $\langle a \rangle$ and $\langle c \rangle$ due to the stress at the node. The micrographs indicate the operation of latter mechanism (Case III) providing a likely possibility for the source mechanism of $\langle c+a \rangle$. Note that, analysis of this area reveals the operation of Case II (dissociation) and Case III (combination) during FSP which is possible depending on the local stress state and given that both the reactions are equally favorable.

These post-mortem experimental observations suggest the nucleation of $\langle c+a \rangle$ dislocations at the nodes and the observed result is in accord with the qualitative statements which suggest that increasing stress at the junctions can nucleate $\langle c+a \rangle$ dislocations [16]. The critical dislocation arrangement shown for $\langle c+a \rangle$ nucleation in this study can be used for further

thermal activation analysis which was not possible in a previous study [5] due to a lack of information on the high temperature dislocation structure.

6.4 Conclusions

This chapter provides the first experimental account of the dislocation structures evolved during FSP of an hcp structure (WE43 alloy). The main conclusions are:

- (i) Non-basal ($\langle c \rangle$, $\langle c+a \rangle$) activity and climb of dislocations was observed in the microstructure
- (ii) I_1 stacking faults were generated due to the climb of $\langle c+a \rangle$ dislocations followed by shear on the basal plane. Subsequent $\langle c+a \rangle$ activity was blocked by these faults arresting the $\langle c \rangle$ dislocation followed by coplanar dissociation of the glissile $\langle a \rangle$ component into Shockley partials as noted by the presence of I_2 faults.
- (iii) I_1 fault served as nucleating center for pyramidal $\langle c+a \rangle$ dislocation accommodating continued deformation during FSP. This is verified from the $\langle c+a \rangle$ dislocation emanating from the fault tip in the micrographs.
- (iv) A mixture of $\langle c+a \rangle$ dissociation and nucleation was observed in the dislocation sub-structure subjected to post-mortem analysis after FSP. This resulted from a high activity of $\langle c \rangle$ and $\langle a \rangle$ dislocations, with the final microstructure being representative of all four (basal $\langle a \rangle$, non-basal ($\langle a \rangle$, $\langle c+a \rangle$, $\langle c \rangle$) components.

Further confirmation of the proposed $\langle c+a \rangle$ source-mechanism at the node requires computational validation or in-situ microscopy studies.

6.5 References

1. G. I. Taylor, "Plastic strain in metals", J. Inst. Met, 62 (1938), 307-338
2. Y. Wu, W. Hu, "Comparison of the solid solution properties of Mg-RE (Gd, Dy, Y) Alloys with Atomistic simulation", Research Letters in Physics, 85 (2008), 1-4.
3. B.C. Wonsiewicz, W.A. Backofen, "Plasticity of magnesium crystals", Trans. TMS –AIME, 239 (1967), 1422-1431.
4. J. Koike, T. Kobayashi, T. Mukai, H. Watanabe, M. Suzuki, K. Maruyama, K. Higashi, "The activity of non-basal slip systems and dynamic recovery at room temperature in fine-grained AZ31B magnesium alloys", Acta materialia, 51(2003), 2055-2065.
5. S. R. Agnew, J. A. Horton, M. H. Yoo, "Transmission electron microscopy investigation of $\langle c+a \rangle$ dislocations in Mg and α -solid solution Mg-Li alloys", Metallurgical and Materials Transactions A 33 (2002), 851-858.
6. A. Galiyev, R. Kaibyshev, G. Gottstein "Correlation of plastic deformation and dynamic recrystallization in magnesium alloy ZK60" Acta Materialia, 49 (2001), 1199-1207.
7. S. Sandlöbes, S. Zaefferer, I. Schestakow, S. Yi, R. Gonzalez-Martinez, "On the role of non-basal deformation mechanisms for the ductility of Mg and Mg–Y alloys" Acta Materialia, 59 (2011), 429-439.
8. S. Kamado, T. Ashie, H. Yamada, K. Sanbun, Y. Kojima, "Improvement of tensile properties of wrought magnesium alloys by grain refining", Materials science forum, 350 (2000), 65-72).
9. S. Sandlöbes, M. Friák, S. Zaefferer, A. Dick, S. Yi, D. Letzig, Z. Pei, L-F. Zhu, J. Neugebauer, D. Raabe, "The relation between ductility and stacking fault energies in Mg and Mg–Y alloys", Acta Materialia, 60 (2012), 3011-3021.

10. S. R. Agnew, L. Capolungo, C. A. Calhoun, "Connections between the basal II "growth" fault and $c+a$ dislocations" *Acta Materialia*, 82 (2015), 255-265.
11. Z. Wu and W. A. Curtin, "The origins of high hardening and low ductility in magnesium", *Nature*, 526.7571 (2015), 62-67.
12. A. Arora, Z. Zhang, A. De, T. Debroy, "Strains and strain rates during friction stir welding", *Scripta Mater.*, 61 (2009), 863-866.
13. D. Zhang, L. Jiang, J.M. Schoenung, S. Mahajan, E.J. Lavernia, "TEM study on relationship between stacking faults and non-basal dislocations in Mg", *Philosophical Magazine*, 95.34 (2015), 3823-3844.
14. Y. Tang, J.A. El-Awady, "Formation and slip of pyramidal dislocations in hexagonal close-packed magnesium single crystals", *Acta Materialia*, 71 (2014), 319-332.
15. M.H. Yoo, S.R. Agnew, J.R. Morris, K.M. Ho, "Non-basal slip systems in HCP metals and alloys: source mechanisms", *Materials Science and Engineering A*, 319-321 (2001), 87-92.
16. M.H. Yoo, "Slip, twinning, and fracture in hexagonal close-packed metals", *Metallurgical Transactions A*, 12.3 (1981), 409-418.

CHAPTER 7

DISLOCATION MEDIATED PRECIPITATION IN A MG-Y-ND ALLOY

Overview: In this chapter, using the information obtained from chapter 6, the role of defects on precipitation was studied by intermittent aging of an Mg-4Y-3Nd alloy. Aging the as processed microstructure (T5 temper) at 210°C showed heterogeneous nucleation of β' and β_1 precipitates on the dislocations. Furthermore, recovered hexagonal networks formed by the reactions between $\langle a \rangle$ type $[11\bar{2}0]$ screw dislocations were observed as early as 2 hours after aging. This self-guided hexagonal assembly was stabilized by the precipitation of β_1 on the individual arms of the network. Additional two beam imaging (g.b=0 invisibility criterion) coupled with diffraction of the specimen aged for two hours revealed nucleation of β_1 on the I_1 stacking fault. Nucleation of precipitates was also observed on $\langle c+a \rangle$ dislocations. An FCC crystal structure within I_1 fault provided the driving force for β_1 precipitation accelerating its formation at this site. On the basis of measured stress-strain curves and microstructural investigation, it is concluded that dislocations aid in the decomposition of supersaturated solid solution to β_1 without the presence of transition precipitate phases (β'' and β') that are involved in the conventional precipitation pathway (T6 temper). Based on the observations, a broader design strategy for obtaining high strength Mg alloys with strengthening precipitates on the $(10\bar{1}0)$ habit plane is proposed.

7.1 Introduction

Magnesium alloys are actively researched due to its potential for light-weighting in the transportation sector [1, 2]. However, to insert Magnesium into the automotive or aerospace

industry at a larger scale, strength equivalent to high strength Al (2XXX, 7XXX) alloys needs to be achieved. Over the years, increment in strength has either been realized by alloy design or thermo-mechanical processing, and in majority of the cases, a combination of both these traditional approaches. Utilizing the alloy design approach, addition of rare earth elements to Mg has shown enhanced age hardening response [3-8]. This is attributed to the formation of plate shaped precipitates with a prismatic habit plane effective in blocking the basal dislocations [8, 9]. In a majority of cases, additional thermo-mechanical processing of these alloys and subsequent aging referred as T5 temper, is done to refine these precipitates to achieve a good balance of strength and ductility. For example, WE54 alloy demonstrated enhanced aging response and a higher strength when pre-deformed before aging [10]. This observation provided an indirect evidence on the beneficial role of dislocations as a heterogeneous nucleation site for second phase precipitation from α -Mg supersaturated solution.

One such alloy within the class of Mg—rare earth alloys that has received considerable research interest from various quarters is Mg-4Y-3Nd (WE43). As a result of the concerted effort from various authors, the precipitation sequence, type, crystallography and morphology for this alloy are well-established [11-16]. From these studies, the precipitation sequence for this alloy has been documented as follows: Supersaturated solid solution (SSSS) \rightarrow ordered GP Zones \rightarrow β'' (DO 19) \rightarrow β' (orthorhombic) \rightarrow β_1 (FCC) \rightarrow β (FCC). Among these phases, β_1 ($a=0.74$ nm) is of technological importance due to its strengthening abilities and its nucleation from α -Mg matrix involves significant shear, tensile, and compressive strains at the broad interface and plate edges [12]. Therefore, the presence of any heterogeneous nucleation site in the form of stacking faults or dislocations can aid in its transformation by accommodating the strain energy of

transformation thereby increasing the driving force for its precipitation. A recent study [17] investigated the role of dislocations on the precipitation of β_1 in a Mg-3 wt.% Nd alloy using phase field modeling. The simulation results showed the variant selection and differing aspect ratios of β_1 on different $\langle a \rangle$ type dislocations [17]. While computational prediction exists, there is no experimental study devoted to this topic to the best of the author's knowledge.

The objective of this study is to experimentally investigate the role of dislocations on the precipitation of β_1 in an Mg-4Y-3Nd alloy. To achieve this objective, the study is categorized into three-heads. First, the age hardening response of WE43 alloy is examined by measuring the strength and ductility in as-processed and aged specimen. Second, the dislocation type and burgers vector resulting from friction stir processing are documented. Third, the role of these quenched-in defects on the nucleation of β_1 precipitate is investigated. On the basis of the observations, we propose a strategy based on defect engineering to tailor high strength Mg-rare earth alloys.

7.2 Experimental Procedure

For this study, a 3 mm thick sheet of WE43 alloy (nominal composition: Mg-4wt% Y-3wt%Nd-0.5wt%Zr) in hot rolled condition was subjected to friction stir processing (FSP). To cause the dissolution of the preexisting precipitates that formed during the hot rolling operation, a tool rotation rate of 2000 revolutions per minute and a tool traverse speed of 102 mm/min were used during FSP. Moreover, the cooling rate during FSP was increased by using a copper backing plate to enhance the solute retention which led to a higher supersaturation in the α -Mg matrix. Further details on FSP can be found in a review article by Ma and Mishra [18].

Subsequent to FSP, four pieces were cut from the processed region and aged for two, eight, twenty four and forty eight hours respectively at 210°C. Strength and ductility for all the five conditions were measured using a custom-built mini-tensile testing machine equipped with an LVDT for recording strain at an initial strain rate of $1 \times 10^{-3} \text{ s}^{-1}$. The gage length, width, and thickness of the mini-tensile specimen used in this study were 5 mm, 1 mm and 1 mm, respectively. For consistency, all the samples were tested with the tensile axis parallel to the processing direction with at least three samples tested in each condition.

Following processing and mechanical testing, microstructural analysis of as processed, processed + aged (2 hours), and processed + aged (8 hours) samples was done using a transmission electron microscope (Technai G2 F20 STEM) to study the role of dislocation mediated precipitation. For TEM analysis, circular discs of 3 mm were punched and mechanically ground to a thickness of 100 μm . Following mechanical polishing, these samples were reduced in thickness to about 25 μm by dimple grinding. Finally, the discs were ion milled at an ion accelerating voltage of 3 kV to render them electron-transparent. Dislocations were investigated by tilting the sample with the incident beam direction aligned parallel to the $[10\bar{1}0]$ direction. This was done to visually identify the basal and non-basal dislocation segments. Later, the dislocation analysis was done using the $g \cdot b = 0$ invisibility criterion. To ensure consistency, selected area diffraction (SAD) patterns from the precipitates were also recorded at the $[10\bar{1}0]$ zone axis.

7.3 Results and Discussion

7.3.1 Strength and Ductility in Friction Stir Processed and Aged Conditions

Figure 7.1 shows the age hardening response of the friction stir processed specimen heat

treated at 210 °C for 2, 8, 24 and 48 hours. A summary of the results from the stress-strain curve is listed in Table 7.1 which shows a rapid increase in strength (~60 MPa) for the first eight hours followed by a gradual rise (20 MPa) for the next forty hours of aging.

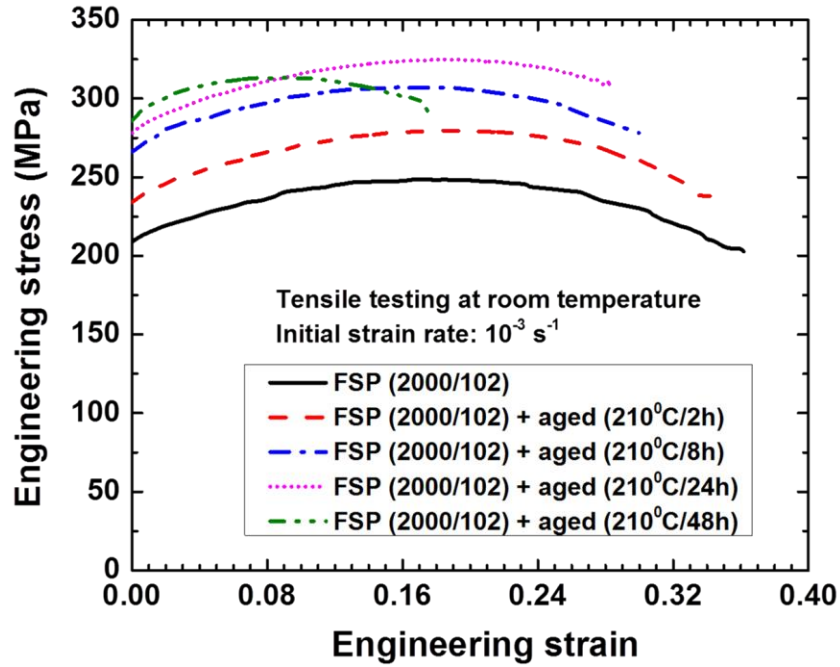


Figure 7.1. Age hardening response of an Mg-4Y-3Nd after friction stir processing. Note that the strength increases at a faster rate for the first eight hours from 208 to 268 MPa. Further aging leads to minimal rise in strength and a compromise in ductility.

Table 7.1. Summary of tensile properties from Figure 7.1

| Nomenclature | Tensile properties | | | |
|---|--------------------|--------------|----------------|----------------|
| | YS (MPa) | UTS (MPa) | %UE | %E |
| FSP (2000 rpm, 102 mm/min) | 208 ± 2 | 248 ± 32 | 16.5 ± 0.1 | 36 ± 0.2 |
| FSP (2000 rpm, 102 mm/min) + aged (2h) | 234 ± 1 | 280 ± 2 | 18.9 ± 0.1 | 34.1 ± 0.2 |
| FSP (2000 rpm, 102 mm/min) + aged (8h) | 266 ± 2 | 308 ± 3 | 18.2 ± 0.1 | 29.9 ± 0.3 |
| FSP (2000 rpm, 102 mm/min) + aged (24h) | 278 ± 3 | 325 ± 2 | 18.2 ± 0.1 | 28.5 ± 0.1 |
| FSP (2000 rpm, 102 mm/min) + aged (48h) | 286 ± 3 | 313 ± 2 | 9.3 ± 0.1 | 17.5 ± 0.1 |

From these results, it is conceivable that the strengthening precipitates nucleate as early as within two hours of aging with the processes of nucleation and growth occurring up to 24

hours. Aging this microstructure beyond 24 hours causes a significant trade-off between strength and ductility, where the rise in strength (8MPa) is minimal as compared to the drop in ductility (17% to 9%) suggesting coarsening of precipitates during this time period.

From these results, it is clear that the commonly used aging treatment (210 °C/48h) is not optimum for microstructures with quenched-in dislocations. In fact, a low temperature aging treatment will be apt to extract the benefits of the pre-existing dislocations. This suggestion is in agreement with other studies [19, 20] that showed excellent strength-ductility combination when the microstructure was aged at 180 °C after thermo-mechanical processing. To study the role and type of dislocations assisting the formation of strengthening precipitates during aging, further sections of the document are discussed based on the observed microstructural descriptors in as-processed and aged specimens (2 and 8 hours).

7.3.2 Defect Mediated Precipitation

The heterogeneous nucleation of plate like precipitates is shown in Figures 7.2(a, b) suggesting that dislocations act as preferred pathway for the diffusion of Y and Nd atoms. Analysis of another grain from the same specimen aged for eight hours shows the evidence for aligned and preferentially oriented precipitates along the [0001] direction. Diffraction from this grain confirms these precipitates as β_1 . Examining Figures 7.2 (a-d), it can be stated that Figure 7.2 (a,b) is a precursor to the observed microstructure in Figure 7.2 (c,d). Formation of these well aligned precipitates can be visualized to occur by the following four steps: (i) segregation of Nd and Y to the dislocation core, (ii) Nucleation of β_1 when the solute content reaches a critical concentration, (iii) growth of the precipitate leading to depletion of solute around the dislocation

core, and (iv) pinching off leading to well-defined preferentially oriented precipitates.

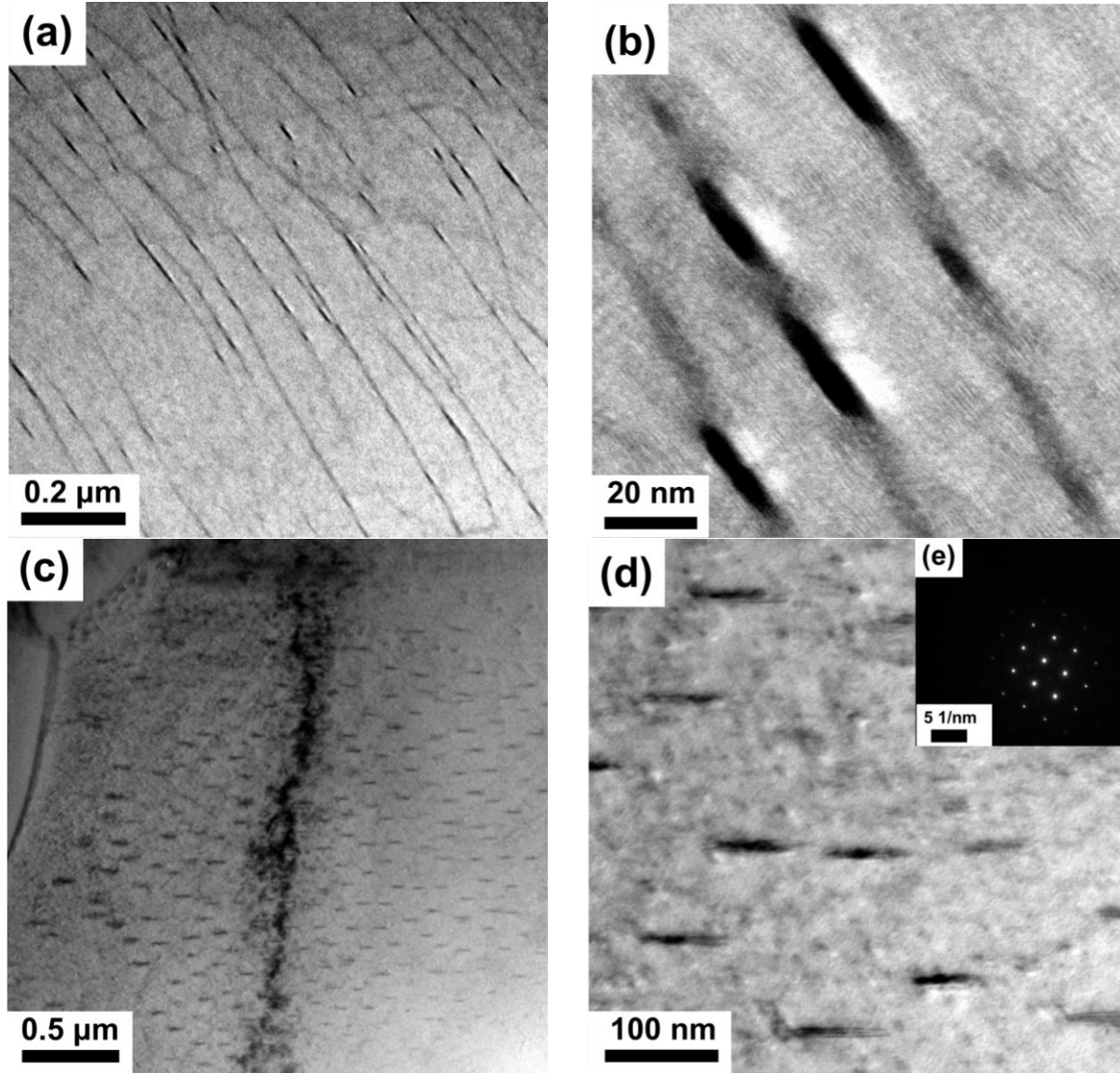


Figure 7.2. (a, b) Heterogeneous nucleation of β_1 precipitates on dislocations, (c, d) Micrograph at later stages after pinching off showing well aligned array of β_1 precipitates (e) Diffraction pattern of the micrograph in (d) recorded along the $[01\bar{1}1]$ zone axis showing superlattice reflections arising from β_1 precipitates

In addition to the formation of an array of precipitates with a specific directionality,

hexagonal networks guiding the precipitation of β_1 on its individual arms was observed. Figures 7.3 (a,b) shows these honeycomb networks.

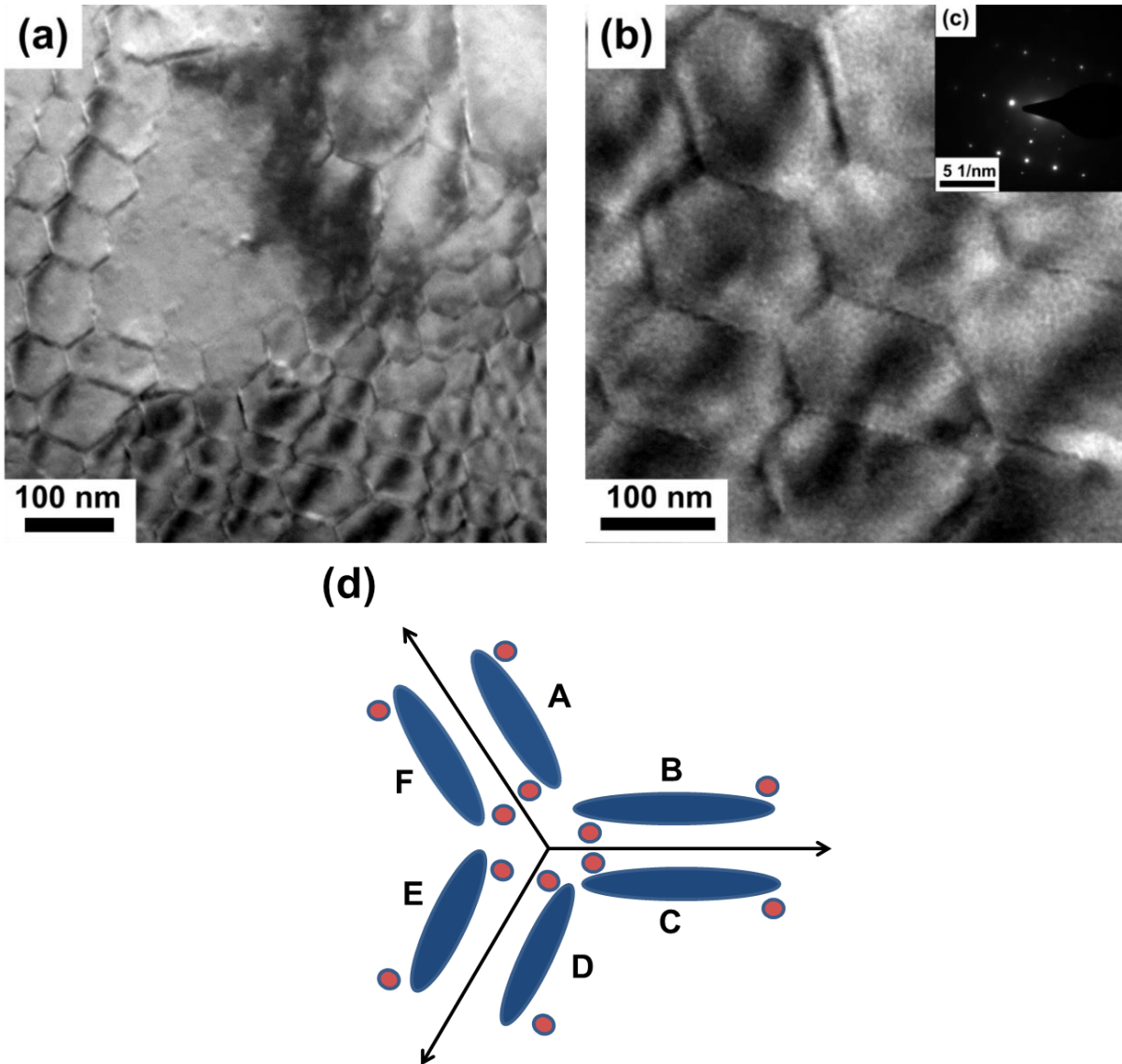


Figure 7.3 (a) Hexagonal network formed by the reactions between $a/3 \langle 11\bar{2}0 \rangle$ type screw dislocations, (b) Formation of β_1 precipitates on these individual dislocation lines as confirmed by the (c) diffraction pattern recorded along the $[10\bar{1}0]$ zone axis. (d) shows the six orientation variants resulting from three correspondence variants.

The precipitation of β_1 on the individual arms was identified from the diffraction pattern shown in Figure 7.3 (c). Such networks have been extensively studied [21,22], and form due to the reactions between the $a/3 \langle 11\bar{2}0 \rangle$ type screw dislocations which can form a twist boundary on the (0001) plane. Depending on the interaction energy between β_1 and α -Mg matrix, a specific orientation variant is chosen out of a total of six possible variants. These variants are shown in Figure 7.3(d) and originate by breaking the three-fold symmetry leading to the formation of triadic and hexagonal structures in Mg based alloys.

7.3.2.1 β_1 Nucleation on the I_1 Stacking Fault

The transformation of α -Mg to β_1 is achieved by a combination of shear on every second plane and an accompanying shuffle between them. These concomitant mechanisms correspond to a magnitude of 0.018nm ($a/18 \langle 11\bar{2}0 \rangle$) and occur in opposite directions parallel to the habit plane. Furthermore, to complete the transformation of the parent HCP to a BCC sub-lattice contained within the FCC precipitate, a shuffle of 0.046nm ($a/12 \langle 10\bar{1}0 \rangle$) normal to the habit plane is necessitated ($\epsilon_{zz}=0.08$). Clearly, a shear of 0.22 in magnitude along $(10\bar{1}0) \langle 11\bar{2}0 \rangle$ (ϵ_{yz}) constitutes the most critical step in β_1 generation [12]. Based on the transformation mechanism, it can be deduced that an $\langle a \rangle$ dislocation gliding on the prismatic plane with a screw component would be highly effective in neutralizing the shear term in the Bain deformation matrix. However, the energetic incentive by virtue of strain minimization parallel and normal to the habit plane would be higher in the case of a pre-existing planar defect in the form of a fault. Figures 7.4 (a-d) show the evidence for β_1 nucleation on a prior fault contained within a dislocation loop.

This observation has been made on a sample aged for two hours at 210°C after FSP. It can be noted that either extrinsic or intrinsic stacking faults can be generated within the loop, depending on whether it forms by interstitials or vacancies. To identify the nature of the fault, several images were recorded at different two beam conditions exciting specific reflections. A strong contrast was exhibited by the fault for $g = [0001]$ and $g = [01\bar{1}3]$. However, a weak residual contrast was observed for $g = [\bar{1}2\bar{1}0]$. Therefore, b could correspond to $[0001]$ or $\langle 11\bar{2}3 \rangle$. Further analysis using the $g = [1\bar{2}12]$ reflection led to the invisibility of bounding partials ruling out the $[0001]$ possibility. Using the extinction criterion corresponding to $g \cdot R = 0$, where R is the displacement vector, b was determined to be $1/6 \langle 2\bar{2}03 \rangle$. Further confirmation was obtained by orienting the specimen close to the $[11\bar{2}0]$ zone axis and exciting the $[1\bar{1}00]$ reflection. In this case, both the stacking fault and the bounding partials disappeared, verifying the anticipated Burgers vector.

Three possible faults can result based on the Burgers vector of the bounding partial, and these can occur on the $(\bar{2}112)$, $(11\bar{2}0)$ or (0001) planes. For the observed Burgers vector, the basal fault occurs, since the other two cases require the motion of a dislocation couple bounding them [23]. Since the temperature reached during processing was $\sim 0.9T_m$ [19], the number of vacancies in equilibrium would be tremendously high. Moreover, a higher cooling rate by virtue of the copper backing plate would lead to retention of quenched-in-vacancies. Vacancy condensation and shear lead to the I_1 stacking fault as shown through Figures 7.4 (a-d). The reaction is written as [23]:

$$\frac{1}{3}[1\bar{1}00] + \frac{1}{2}[0001] \rightarrow \frac{1}{6}[2\bar{2}03] \quad (1)$$

A diffraction pattern was subsequently recorded from the I_1 fault to assess its role in precipitate nucleation as shown in Figure 7.4(e). Faint superlattice reflections were generated within this area, and have been consistently indexed with the FCC crystal structure of the β_1 phase. It can be noted that the Burgers orientation relationship is maintained between α -Mg and β_1 , with $[10\bar{1}0]//[\bar{1}\bar{1}2]$ indicating that the transformation is complete.

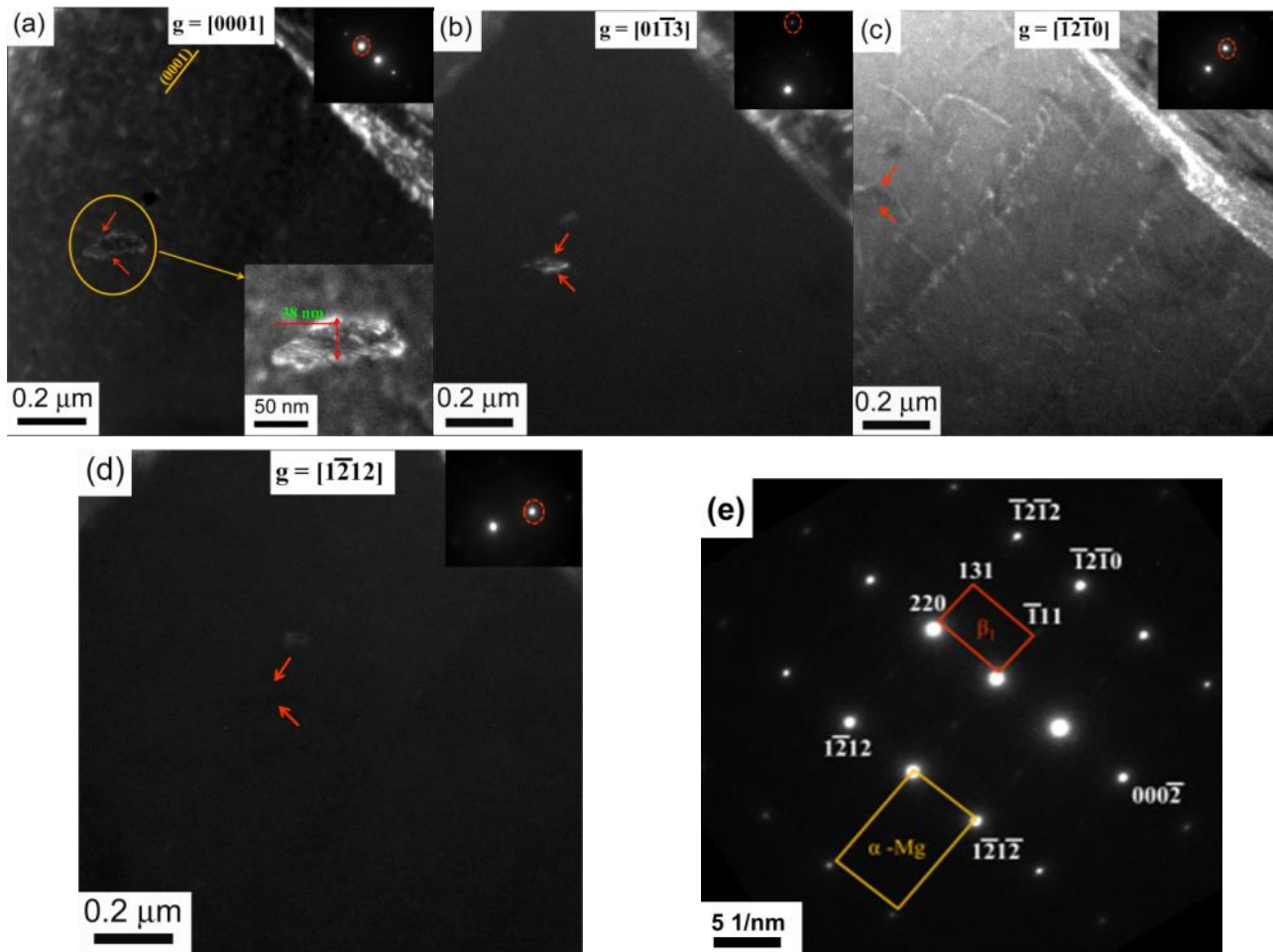


Figure 7.4 (a-d). Weak beam dark field images recorded with a series of two beam conditions showing the presence of an I_1 stacking fault bounded by a pyramidal Frank partial. The arrows point towards the same position in the above micrographs. Note that the feature is invisible in (d)

which highlights the dark field image captured using $g = [1\bar{2}12]$ reflection, as well as (e) selected area diffraction (SAD) patterns recorded parallel to $[10\bar{1}0]$ of α -Mg, showing β_1 spots generated within the I_1 stacking fault.

Therefore, it can be concluded that the presence of I_1 faults are desirable for β_1 nucleation and growth. Figure 7.5 shows the stacking sequence associated with the I_1 fault. As shown in the schematic, the I_1 fault is generated by condensing vacancies on the A layer and shearing the remaining crystal above the B layer by $1/3 [10\bar{1}0]$. The terminating sessile Frank partial ($1/6 [2\bar{2}03]$) can be easily visualized by drawing a Burgers circuit around the faulted region in Figure 7.5.

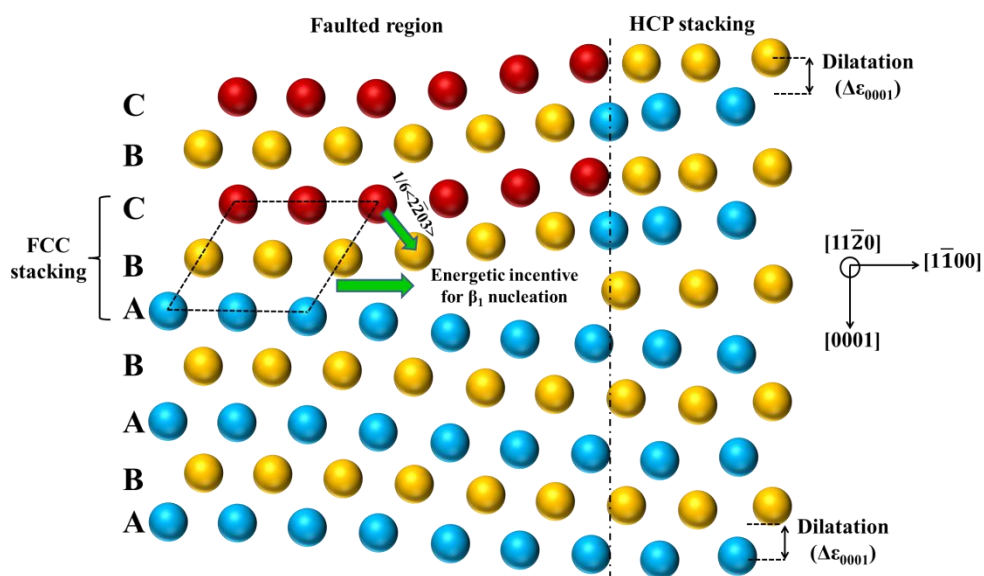


Figure 7.5. A schematic showing the driving force to nucleate β_1 on I_1 basal stacking fault. Note that the fault is terminated by a sessile Frank partial dislocation. Each individual layer/plane has been color coded.

Also, the terminating partial has a zonal nature and an FCC stacking is observed within the I_1 fault (...ABABABCBCBC...). Since β_1 has an FCC structure, there is a natural tendency and a high energetic incentive for its nucleation at this site. Furthermore, the strain accommodation normal to the habit plane coupled with a volume expansion at the fault with dilatation in [0001] would accelerate its formation. Analogous to FCC→BCC transformations creating the first Bogers-Burgers shear configuration by the movement of Shockley partials [24], the passage of a/n $[10\bar{1}0]$ associated with the fault would aid in the transformation of $(0001)_{HCP}$ to $(110)_{BCC}$, where n is an integer.

7.3.2.2 Nucleation of Precipitate on $\langle c+a \rangle$ Dislocations

Figure 7.6(a-c) shows a series of two beam images used to identify the dislocation highlighted by the pointed arrows. Contrast was exhibited by this dislocation for the three, $[\bar{1}2\bar{1}0]$, [0001] and $[\bar{1}2\bar{1}2]$ reflections, signifying the $\langle c+a \rangle$ characteristic. A few more reflections were analyzed, and the Burgers vector was determined as $1/3[\bar{1}2\bar{1}3]$. Moreover, from the plane traces, the dislocation line was parallel to the $(10\bar{1}0)$ plane. Subsequently, a diffraction pattern was recorded from this dislocation segment by centering the SAD, as shown in the inset of Figure 7.6 (d). Several super-lattice spots were detected, and could be indexed with the [110] FCC crystal structure. Based on the diffraction pattern, it was clear that precipitation occurred on the prismatic $\langle c+a \rangle$ dislocation. However, unlike the clear evidence for nucleation of β_1 on the I_1 stacking fault, the identity of the precipitate nucleating on $\langle c+a \rangle$ dislocation could not be determined from Figures 7.6 (a-d) and further studies are needed to unequivocally identify it.

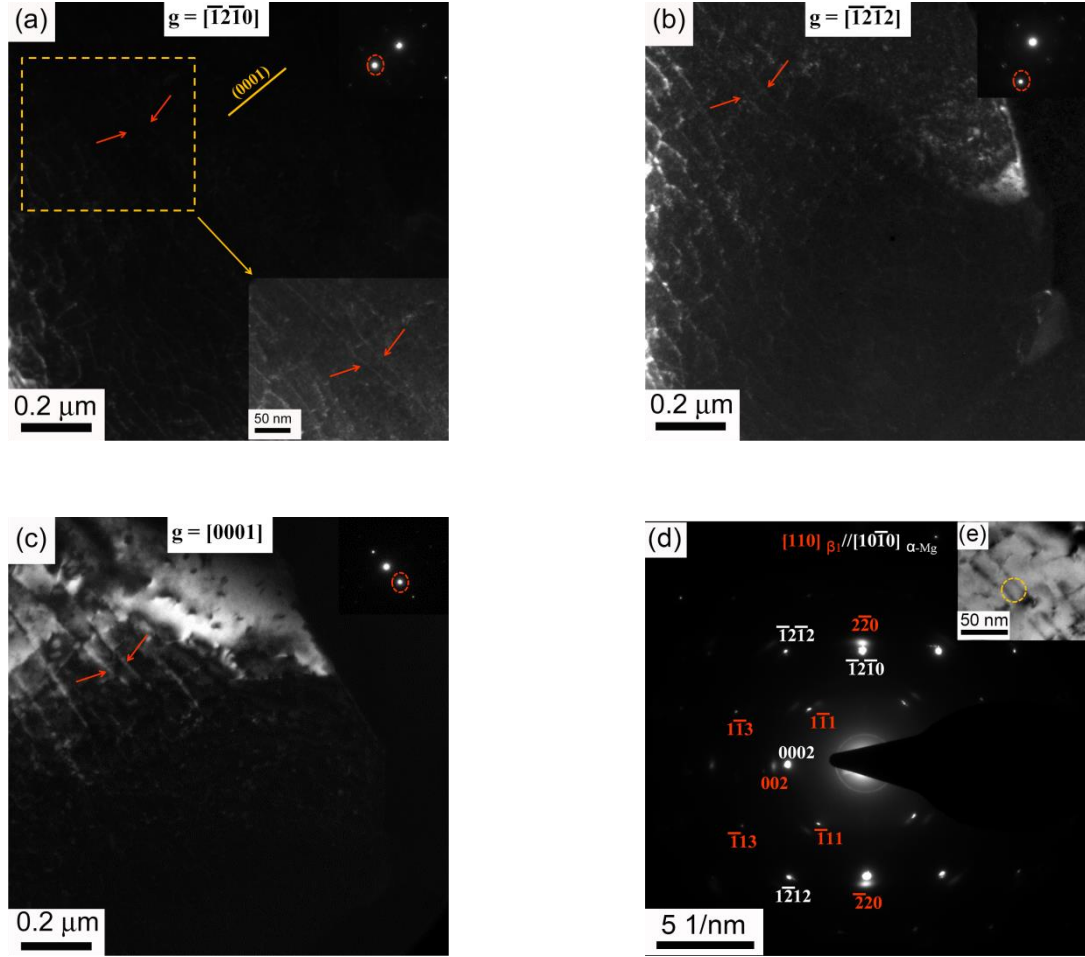


Figure 7.6 (a-c). Dark field images captured using two beam conditions, with the highlighted arrows pointing towards a $\langle c+a \rangle$ dislocation (d) a diffraction pattern recorded parallel to the $[10\bar{1}0]$ zone axis confirming nucleation of unidentified precipitate on the dislocation with a Burgers vector of $1/3 \langle 11\bar{2}3 \rangle$ (e) an inset displaying the region of SAD aperture centering.

Based on the results in section 3.2.1 and 3.2.2, β_1 nucleates directly from SSSS and does not involve transition phases like β'' and β' . In a previous study, yttrium has been reported to stabilize the I_1 fault and lead to higher ductility by acting as a $\langle c+a \rangle$ dislocation source [25].

This characteristic can be exercised to nucleate β_1 on the I_1 stacking fault and $\langle c+a \rangle$ dislocation. To generate such a combination, a high temperature processing route followed by a cold deformation is proposed.

7.4 Conclusions

This chapter provides the first experimental account on the type and role of defects nucleating β_1 precipitates in a WE43 alloy. The main conclusions are:

- (i) A well-defined directional array of β_1 precipitates formed due to the heterogeneous nucleation on prior existing line defects. Moreover, hexagonal dislocation network guided β_1 assembly formed due to the interaction between $a/3 \langle 11\bar{2}0 \rangle$ type screw dislocation and the nucleating β_1 plate.
- (ii) The I_1 stacking fault associated with faulting on the close packed basal plane promoted the nucleation of β_1 precipitate. The zonal nature and the composite Frank-Shockley partials bounding the fault provided strain accommodation normal and parallel to the $(10\bar{1}0)$ habit plane.
- (iii) The $\langle c+a \rangle$ dislocations gliding on the prismatic plane $(10\bar{1}0)$ might have served as the nucleating centers for the β_1 precipitate.

Therefore, a design strategy for increasing strength in a WE43 alloy would be to incorporate a high density of I_1 stacking faults, emitting $\langle c+a \rangle$ dislocations. In fact, this strategy can be utilized to guide the nucleation of semi-coherent precipitate plates formed on the $(10\bar{1}0)$ habit plane of any Mg alloy by shear transformation.

7.5 References

1. I. J. Polmear, Magnesium alloys and applications. *Materials science and technology* 10.1 (1994) 1-16.
2. B. L. Mordike, and Tü Ebert. Magnesium: properties—applications—potential. *Materials Science and Engineering. A* 302.1 (2001) 37-45.
3. C. Sanchez, G Nussbaum, P. Azavant, and H. Octor, Elevated temperature behaviour of rapidly solidified magnesium alloys containing rare earths. *Materials Science and Engineering: A*. 221(1) (1996) pp.48-57.
4. Y. Kawamura, K. Hayashi, A. Inoue. and T. Masumoto, Rapidly Solidified Powder Metallurgy Mg₉₇Zn₁Y₂Alloys with Excellent Tensile Yield Strength above 600 MPa. *Materials Transactions*. 42 (2001) pp.1171-1174
5. T. A. Freeney, and R. S. Mishra. Effect of friction stir processing on microstructure and mechanical properties of a cast-magnesium–rare earth alloy. *metallurgical and materials transactions A* 41.1 (2010). 73-84.
6. P. J. Apps, H. Karimzadeh, J. F. King, & G. W. Lorimer, Precipitation reactions in magnesium-rare earth alloys containing yttrium, gadolinium or dysprosium. *Scripta Materialia*. 48(8) (2003) 1023-1028.
7. M. Yamasaki, T. Anan, S. Yoshimoto and Y. Kawamura, Mechanical properties of warm-extruded Mg–Zn–Gd alloy with coherent 14H long periodic stacking ordered structure precipitate. *Scripta Materialia*. 53(7).(2005) pp.799-803.
8. J. F. Nie,. Precipitation and hardening in magnesium alloys. *Metallurgical and Materials Transactions A*. 43(11) (2012) pp.3891-3939.

9. J. F. Nie, Effects of precipitate shape and orientation on dispersion strengthening in magnesium alloys. *Scripta Materialia* 48.8 (2003) 1009-1015.
10. T. Hilditch, J.F. Nie, B.C. Muddle, The effect of cold work on precipitation in alloy WE54, editors: B.L. Mordike and K.U. Kainer, *Proc. Magnesium Alloys and their Applications*, Frankfurt, Germany (1998) 339–344.
11. J. F. Nie, B. C. Muddle, Precipitation in magnesium alloy WE54 during isothermal aging at 250°C, *Scripta Mater.* 40 (1999) 1089–1094.
12. J.F. Nie, B.C. Muddle, Characterisation of strengthening precipitate phases in a Mg-Y-Nd alloy, *Acta Mater.* 48 (2000) 1691-1703.
13. C. Antion, P. Donnadieu, F. Perrard, A. Deschamps, C. Tassin, A. Pisch, Hardening precipitation in a Mg–4Y–3RE alloy, *Acta Mater.* 51 (2003) 5335-5348.
14. P. Mengucci, G. Barucca, G. Riontino, D. Lussana, M. Massazza, R. Ferragut, E. Hassan Aly, Structure evolution of a WE43 Mg alloy submitted to different thermal treatments, *Materials Science and Engineering A.* 479 (2008) 37-44.
15. G. Barucca, R. Ferragut, F. Fiori, D. Lussana, P. Mengucci, F. Moia, G. Riontino, Formation and evolution of the hardening precipitates in a Mg–Y–Nd alloy, *Acta Mater.* 59 (2011) 4151–4158.
16. Renlong Xin, Ling Li, Ke Zeng, Bo Song, Qing Liu, Structural examination of aging precipitation in a Mg-Y-Nd alloy at different temperatures, *Materials Characterization.* 62 (2011) 535-539.
17. H. Liu, Y. Gao, Y.M. Zhu, Y. Wang, J.F. Nie, A simulation study of precipitation on dislocations in an Mg-rare earth alloy, *Acta Mater.* 77 (2014) 133-150.

18. R.S. Mishra, Z.Y Ma, Friction stir welding and processing, Materials Science and Engineering R. 50 (2005) 1-78
19. S. Palanivel, P. Nelaturu, B. Glass, and R. S. Mishra. Friction stir additive manufacturing for high structural performance through microstructural control in an Mg based WE43 alloy, Materials & Design 65 (2015) 934-952.
20. Panigrahi, S. K., W. Yuan, R. S. Mishra, R. DeLorme, B. Davis, R. A. Howell, and K. Cho,. A study on the combined effect of forging and aging in Mg–Y–RE alloy,. Materials Science and Engineering: A 530 (2011) 28-35.
21. D. Choudhuri,, S. Meher,, S. Nag, N. Dendge, J. Y. Hwang, and R. Banerjee, Evolution of a honeycomb network of precipitates in a hot-rolled commercial Mg–Y–Nd–Zr alloy, Philosophical Magazine Letters. 93(7) (2013) 395-404.
22. Liu, H., Gao, Y., Xu, Z., Zhu, Y.M., Wang, Y. and Nie, J.F. Guided Self-Assembly of Nano-Precipitates into Mesocrystals. Scientific reports. (2015) 5.
23. Partridge P.G., The Crystallography and deformation modes of hexagonal close-packed metals, Metallurgical reviews. 12 (1966) 169-194.
24. G.B. Olson, M. Cohen, A general mechanism of martensitic nucleation: Part II. FCC→BCC and other martensitic transformations, Metall. Trans. 7A (1976) 1905-1914.
25. S.Sandlobes, M. Friak, S. Zaefferer, A. Dick, S. Yi, D. Letzig, Z. Pei, L.F. Zhu, J. Neugebauer, D. Raabe, The relation between ductility and stacking fault energies in Mg and Mg-Y alloys, Acta Mater. 60 (2012) 3011-3021

CHAPTER 8

ACCELERATED AGE HARDENING RESPONSE BY IN-SITU ULTRASONIC AGING OF A MAGNESIUM—RARE EARTH ALLOY

Overview: Chapters 1-7 provided an insight into microstructural control in a WE43 alloy by thermo-mechanical processing routes and friction stir additive manufacturing. Using the fundamental knowledge from the prior chapters, this chapter utilizes an external field to modify the precipitate descriptors and hence strength. For this purpose, custom built in-situ ultrasonic aging equipment was used to investigate the precipitation hardening response in a commercial WE43 alloy at 210°C. Three powers (100, 300, 400 Watts) with interval times of 15, 30, and 60 seconds between sonication were used. The major highlight in this chapter is that the time to peak aging decreased from 48 hours during conventional aging to 2 hours in the specimen aged under the influence of ultrasonic waves. Though a higher power increased the peak hardness, shortening the interval time from 30-15 seconds did not have any influence. Well-developed β_1 variants were observed as early as 15 minutes in ultrasonically aged sample and are the reason for enhanced age hardening response.

8.1 Introduction

Precipitation rate depends on the thermodynamic driving force and to a large extent on the kinetics of the process. In cases, where the diffusion of the solute is sluggish, aging at high temperature results in coarsening and at low temperatures necessitates longer aging times. This holds true for WE43 alloy where the larger Nd and Y atoms have sluggish diffusion rates in Mg.

Since peak aging is attained in these alloys at lower temperatures but require longer times, any process that can assist in shortening the time to maximum hardness will be of great value.

In this regard, research in the 1960's focusing on the application of ultrasonic vibration to alloys during aging treatment is of immense interest [1-5]. Using ultrasonic vibration, Peslo [6] reported an increase in the age hardening response of an Al-Cu alloy by 30 to 100 times in comparison to the samples aged in the absence of stress. The increased rate of hardening was correlated to the formation of prismatic dislocation loops and the precipitation of fine Al_2Cu precipitates. Similar observations were documented by Ermakov [3] in a Nickel based alloy. In general, a majority of the studies reported the beneficial role of ultrasonic aging on the age hardening response and the mechanical properties irrespective of the system used and the alloy under investigation. These improvements were attributed to the stretching of the lattice and the increased rate of diffusion [1, 6, 7]. Inspired from these works, the objective of this study was to study the effect of in-situ ultrasonic aging on the age hardening response of an Mg-4Y-3Nd alloy.

8.2 Experimental Details

For this study, a 3 mm thick sheet of WE43 alloy (nominal composition: Mg-4wt% Y-3wt%Nd-0.5wt%Zr) in hot rolled condition was subjected to friction stir processing (FSP). To cause the dissolution of the preexisting precipitates that formed during the hot rolling operation, a tool rotation rate of 2000 revolutions per minute and a tool traverse speed of 102 mm/min were used during FSP. Moreover, the cooling rate during FSP was increased by using a copper backing plate to enhance the solute retention which led to a higher supersaturation in the α -Mg

matrix. Subsequent to FSP, nine pieces were cut from the processed region and aged for 15, 30, 45, 60, 90 minutes, and two, eight, twenty four and forty eight hours, respectively, at 210°C to track the age hardening response in the absence of stress.

After measuring the hardness profile in the absence of stress, discs of 19 mm in diameter and thickness of 2 mm containing the friction stir processed region were milled from the specimen for aging under the influence of ultrasonic vibration. Figure 8.1 shows the custom built ultrasonic set up for in-situ aging under the influence of sound waves.

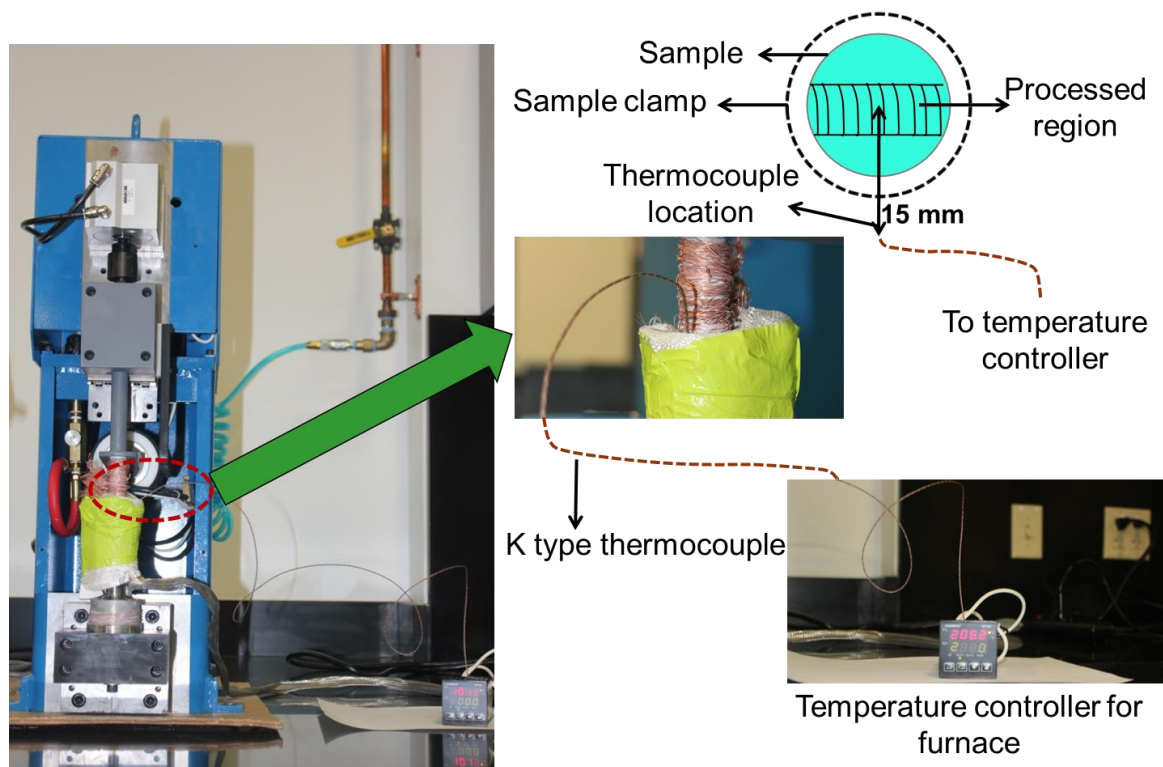


Figure 8.1. Custom built in-situ ultrasonic aging set up for studying the age hardening response of a WE43 alloy under the influence of sound waves.

The sample was placed within a customized clamp on the anvil. A band heater with the ability to reach temperatures up to 540°C was used as the furnace and was placed around the reed-anvil assembly. The temperature for aging was maintained at 210±0.2°C by a K-type thermocouple connected to a temperature controller as shown in Figure 8.1. Ultrasonic vibration to the samples was given for 3 seconds at 20 KHz using power of 100, 300 and 400 W. Three time intervals (15, 30, 60 seconds) were used between subsequent vibrations to study its effect on the age hardening response. Samples were aged for 15, 30, 45, 60, 90 and 120 minutes, respectively, for studying the effect of power and the number of cycles imparted on the hardening response.

Following aging and hardness testing, microstructural analysis of the ultrasonically vibrated + aged samples was done using a transmission electron microscope (Technai G2 F20 STEM) to study the number density, distribution and size of the precipitates. For TEM analysis, circular discs of 3 mm were punched and mechanically ground to a thickness of 100 µm. Following mechanical polishing, these samples were reduced in thickness to about 25 µm by dimple grinding. Finally, the discs were ion milled at an ion accelerating voltage of 3 KV to render them electron-transparent.

8.3 Results and Discussion

8.3.1 Effect of Power and Sonication Time on the Age Hardening Response of WE43 Alloy

Figures 8.2 (a), (b) and (c) show the age hardening response of WE43 aged using a power of 100, 300 and 400 Watts for different sonication time intervals.

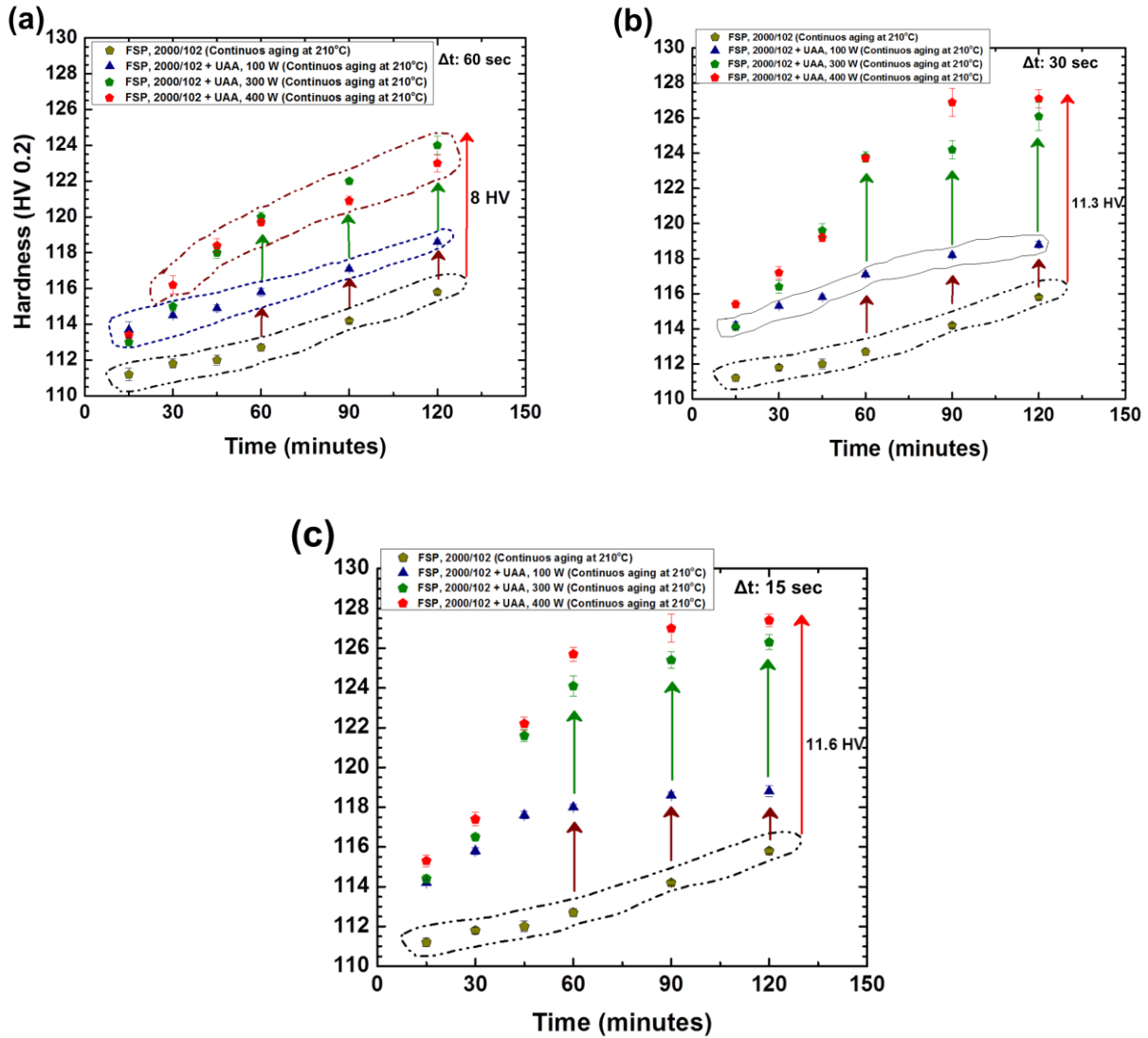


Figure 8.2. Effect of ultrasonic power on the age hardening response of a WE43 alloy for sonication time intervals of (a) 60 s, (b) 30 s, and (c) 15 s. Note that increasing the power from 100 W to 400 W accelerates the time to peak hardness. Furthermore, decreasing the sonication time from for 60 s to 30 s accelerates the hardening response.

From Figure 8.2(a), it can be noted that increasing the power from 100 to 400 W increases the hardness from 119 to 123 HV after two hours of aging. When the interval between

sonication was reduced to 30 s as shown in Figure 8.2(b), peak hardness of 127 HV was achieved for a power input of 400 W within two hours. Figure 8.2 (c) also shows a similar trend implying that shortening the interval time from 30 to 15 s has no change in the hardening response. The difference between the curves for a power input of 400 W is well captured in the plots where the hardness is increasing for the case of 60 s interval while saturation has occurred at the peak hardness for 30 and 15 s interval, respectively. In other words, increasing the sample time under the influence of vibration from 10 to 20 minutes does not affect the hardening response. Also, at 100 W, irrespective of the interval between sonication, the hardness after two hours is around 118 HV suggesting that at this power, there is no recognizable effect of time. Table 8.1 summarizes the hardness values for different powers and sonication time intervals and compares it with the conventionally aged sample at the end of 2 hours.

Table 8.1. A comparison of age hardening response between conventionally aged and ultrasonically aged specimen

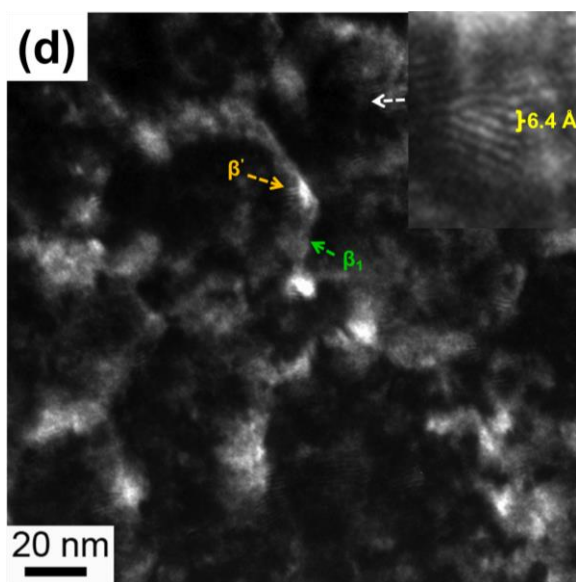
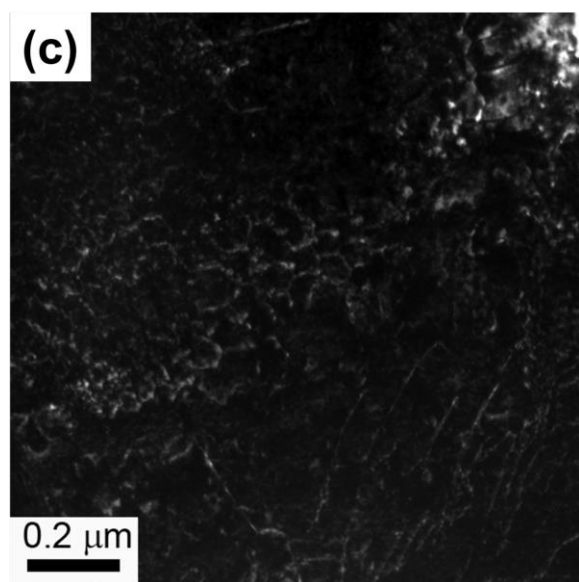
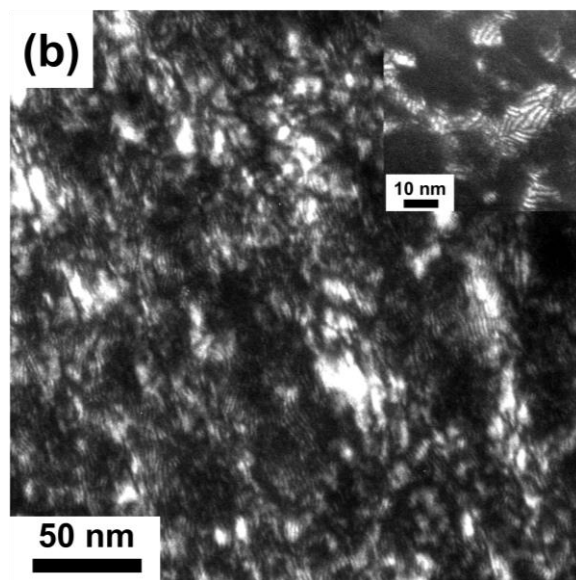
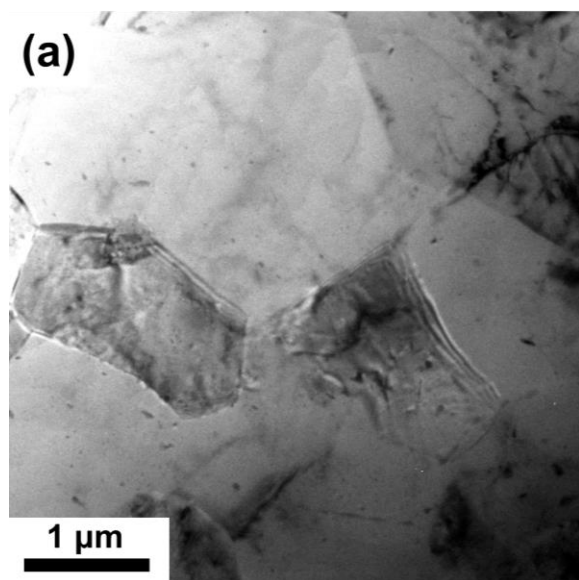
| Condition | FSP + aged | | | |
|-------------------|--|-------|--------|--------|
| Time | 2 hrs | 8 hrs | 24 hrs | 48 hrs |
| Hardness (HV 0.5) | 115.1 | 121.2 | 124.3 | 127.2 |
| Condition | Ultrasonic assisted aging (UAA), (hardness values reported after 2 hrs,) | | | |
| Ultrasound power | Time interval between sonication (seconds) | | | |
| | 60 s | 30 s | 15 s | |
| 100 W | 119 | 118.8 | 118.8 | |
| 300 W | 124 | 126.1 | 126.3 | |
| 400 W | 123.1 | 127.1 | 127.6 | |

A major highlight that emerges from Figure 8.2 and Table 8.1 is that the time to peak hardness is reduced by a factor of 24 when aged under the influence of sound waves. Though the

peak hardness remains same in the absence or presence of stress, the time is considerably reduced.

8.3.2 Microstructure of the Ultrasonically Aged Specimen

Figure 8.3 tracks the change in precipitate descriptors as a function of time for a sample aged under a power of 400 W. The as-processed microstructure is shown in Figure 8.3 (a) and is comparatively clean with the absence of strengthening (β' and β_1) precipitates. Figure 8.3(b) is a dark field image and shows the pocketing of Nd homogeneously within the matrix after 15 minutes of UAA at 400 W. Such an observation was made in an Mg-Nd alloy after 5 hours of isothermal aging by Choudhuri et al. [8]. Also, in the previous chapter, such pocketing for this alloy was shown after two hours of aging. The development of these isostructural Nd rich pockets within the Mg matrix was correlated to the presence of a miscibility gap by thermodynamic modeling which provides the driving force to phase separate. Furthermore, in the same study [8], the composition of these pockets was determined as 2.75 at.% Nd by reconstructing the atom probe data which implies that a local supersaturation is needed for phase separation to occur. Even more significant is that such pocketing is observed as early as 15 minutes in the UAA sample in comparison to 5 hours as reported in the literature. A conceptual schematic is hypothesized in the later section to explain the accelerated response under the influence of ultrasonic vibration. Figures 8.3(c, d) show the precipitation of β' and β_1 precipitates as hexagonal networks clearly indicating the role of dislocations in accelerating the age hardening response. This micrograph was recorded after 30 minutes of aging at 400 W.



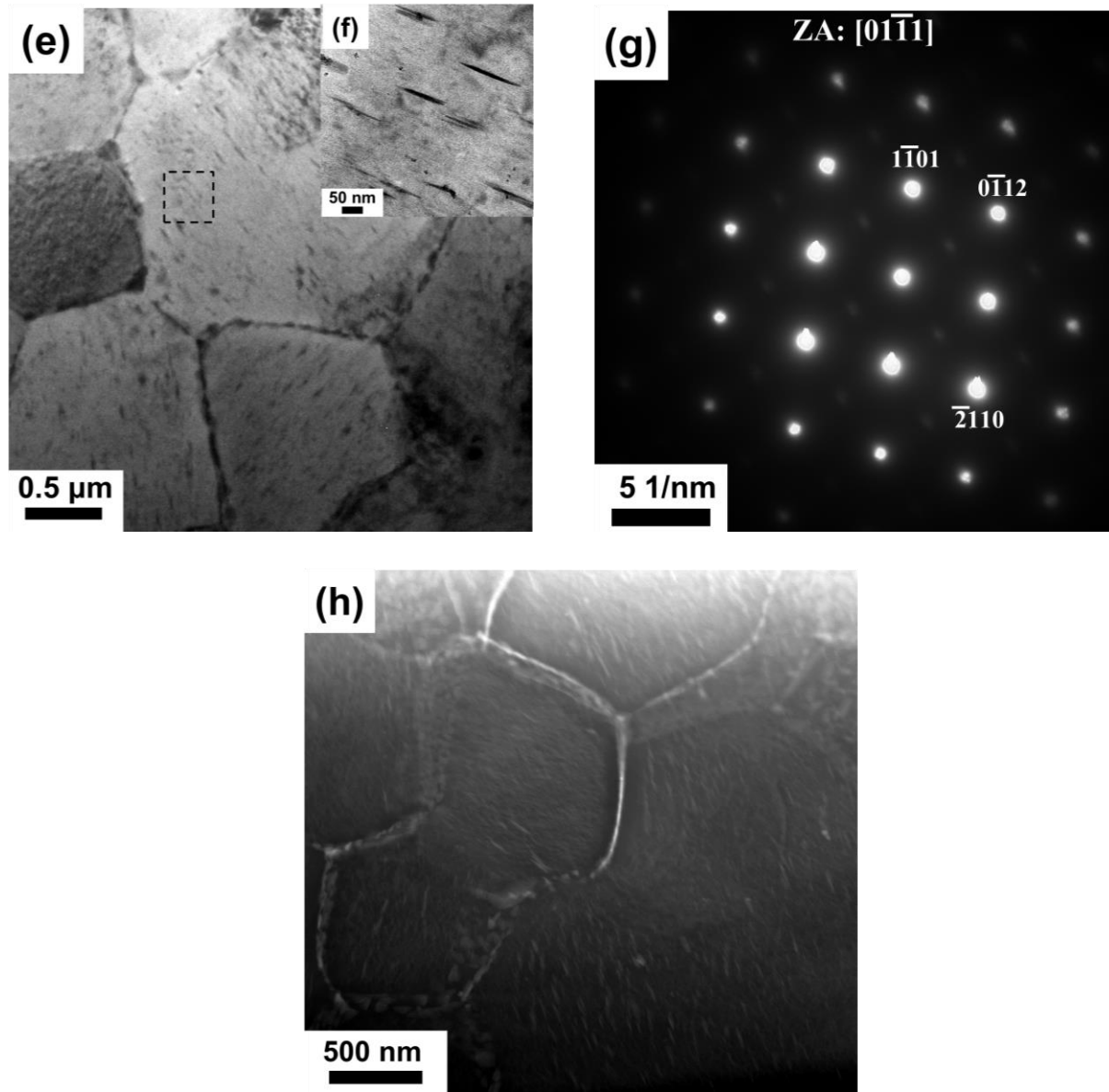


Figure 8.3. (a) TEM micrograph of as processed specimen showing a cleaner matrix with the absence of strengthening precipitates. TEM micrographs tracking the evolution of microstructure for a specimen aged at 210°C using a power of 400 W after (b) 15 minutes of aging showing pockets rich in Nd, (c, d) 30 minutes of aging showing the formation of hexagonal networks and Nd rich regions, (e) 60 minutes of aging showing well aligned β_1 precipitates. Note that the inset in (e) labelled as (f) corresponds to the dashed square and shows well grown β_1 precipitates with

a plate diameter of 50 nm. This is further confirmed from the diffraction pattern in (g) which shows bright superlattice reflections emerging from (f). (h) TEM micrograph showing a high number density of well aligned precipitates after ultrasonic aging for two hours. Note the accelerated nucleation and growth of the β_1 precipitates under the influence of ultrasonic stress which otherwise takes 48 hours to reach peak aged condition during conventional aging.

From Figure 8.3(d) which is an enlarged section of an area in the micrograph in Figure 8.3(c), an interesting observation is the concomitant pocketing of Nd within the hexagonal network. This observation implies that Nd pocketing can precede and also occur on the same temporal scale as the precipitation of β' and β_1 . Moreover, development of β' close to the pockets suggest that these Nd enriched regions might have served as nucleation sites and transitioned to the strengthening phases. Note that in the previous chapter, such hexagonal networks were shown to form after 8 hours of isothermal aging under the absence of stress indicating the accelerated kinetics of formation during ultrasonic vibration. Figures 8.3 (d) and (e) are taken after 60 minutes and 2 hrs of aging and clearly shows the presence of well-defined β_1 precipitates. These precipitates are aligned in specific directions indicating nucleation on prior dislocations that might have been induced by the ultrasonic stress or by the directional propagation of sound waves. To accurately envision the mechanism, further studies would be required on such field effects that need to be tied to the physics of the process.

8.3.3 Conceptual Thermodynamic and Kinetic Hypothesis for Accelerated Age Hardening Response under the Influence of Sound Waves

Precipitate shape, crystallographic orientation, aspect ratio and spatial arrangement are

controlled by a set of complex variables. Broadly, these variables can be classified as a subset of three major interacting features: elastic strain energy, interfacial energy and chemical free energy of the system. Further complexities would involve the formation of dislocation loops, dependence of interfacial energy and misfit strain on orientation, etc. A framework for the evolution of individual morphological descriptor is presented as a function of stress and correlated to the thermodynamic and kinetic aspects. Figure 8.4 depicts the influence of stress on the micromechanistic mode of atom transport. The effect of ultrasonic wave might result in effective reduction of diffusion distance from the matrix to precipitate thereby enhancing the kinetics. This would lead to accumulation of solute at the proximity of the interface increasing supersaturation and growth kinetics of planar front. The ratio of the flow of the solute atoms driven by stress to the diffusional flow would determine the mechanistic mode of growth. Higher stress driven solute transport might therefore enhance the diffusion rate.

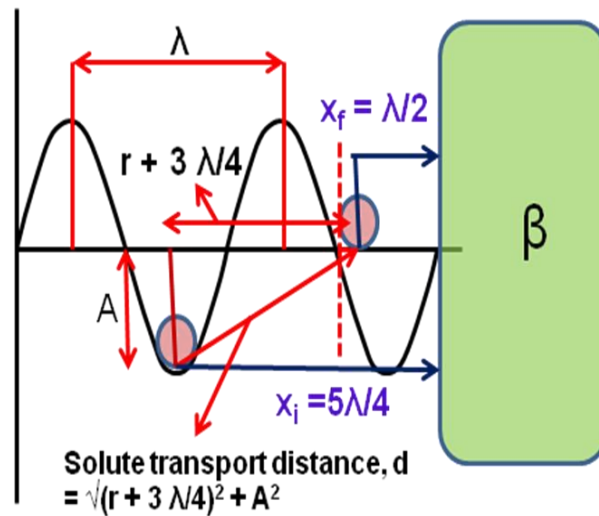


Figure 8.4. Stress wave induced transportation of solute enhancing the diffusional rate and hence the precipitation kinetics.

The driving force for precipitate evolution stems from the fundamental G-X plots. The application of stress can result in differential positioning of G-X minima. Such shifts in curves have been postulated to occur as a result of the interplay between elastic strain energy and changes in interfacial structures [9]. Thus, the thermodynamic conditions provide the basis for enhanced or decelerated growth kinetics. Figure 8.4 correlated the local compositional fluctuations to diffusion and hence growth. Figure 8.5 builds on this hypothesis and provides a two sided thermodynamic and kinetic interpretation of an external stress on change in aspect ratio. In the present case, it is postulated that the application of stress increases the driving force for precipitation by decreasing the strain energy and increases the growth rate by enhanced diffusion kinetics.

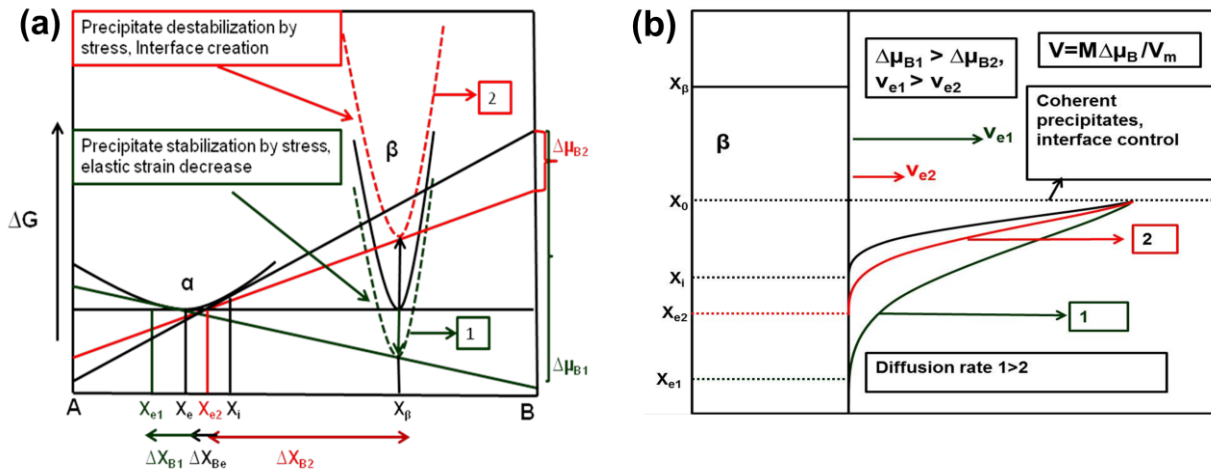


Figure 8.5. (a) Effect of stress on G-X plot of a binary AB alloy, and (b) correlation of growth kinetics to stress modified G-X plot ($\Delta \mu$: chemical potential, M : interface mobility, v : Interface velocity).

8.4 Conclusions

The effect of ultrasonic vibration on age hardening response of a WE43 alloy was

studied. The major highlights from this work are:

- (i) In comparison to the conventionally aged specimen, time to achieve a peak hardness of 127 HV was reduced from 48 hrs to 2 hrs in the specimen aged under the influence of ultrasonic waves. In short, ultrasonic assisted aging was 24 times faster than conventional aging.
- (ii) Increasing the power from 100 W to 400 W increased the hardness irrespective of the time interval between subsequent sonication.
- (iii) Changing the interval time from 60 seconds to 30 seconds had a significant effect on the age hardening response. Further decrease from 30 to 15 seconds did not influence the hardening response.
- (iv) Nd pocketing was observed as early as 15 minutes and well defined hexagonal networks formed within 30 minutes of aging in a sample aged at 400 W. The high number density of β_1 precipitates at the end of two hours was responsible for the observed hardness response.

8.5. References

1. K. M. Pogodina-Alekseeva, G.I Eskin, Effect of Ultrasonic Vibrations on the Precipitation Hardening and Tempering of Some Alloys. Henry Bratcher Translation (1956), vol: 4551
2. F.K. Gorskiu, and V. I. Efremov, Influence of Ultrasonic Vibrations on the Decomposition of Solid Solutions. Izvest. Akad. Nauk Beloruss (1953), vol:3, 155-164
3. V.S. Ermakov, and E.A. Al' ftan, Aging of Creep-Resisting Nickel-Base Alloy El 437 B, Accelerated by Ultrasonic Vibrations. Henry Bratcher Translation (1958), vol: 4278
4. Anon, Investigation of the Effects of Ultrasonics on the Deformation Characteristics

of Metals. Wien Univ., Austria, 1964.

5. V.S. Mes'kin and E. A. Al'ftan, Investigation of the Effect of Ultrasonics on the Results of the Heat Treatment of Alloys, *Phys. Metals Metallography* (1961), vol: 11, 53-62.

6. A. Peslo, Ultrasonic hardening of aluminum alloys, *Ultrasonics* (1984), vol: 22, 37-41.

7. H. V. Fairbanks, Effect of Insonation during the Precipitation-Hardening of Alloys. *Sound* (1962), vol:1, 35-39.

8. D. Choudhuri, N. Dendge, S. Nag, S. Meher, T. Alam, M. A. Gibson, R. Banerjee, Homogeneous and heterogeneous precipitation mechanisms in a binary Mg–Nd alloy." *Journal of Materials Science* (2014), vol: 49, 6986-7003.

9. .D. Embury, A. Deschamps, Y. Brechet, The interaction of plasticity and diffusion controlled precipitation reactions, *Scripta Materialia* (2003), vol:49, 927–932.

CHAPTER 9

COMPUTATIONAL DESIGN OF HIGH STRENGTH LOW ALLOY MAGNESIUM ALLOYS

Overview: Leading to this point, either processing methods or an external field has been used to influence the microstructure and hence strength in a WE43 alloy. Referring back to the concepts of alloying and microstructural efficiency in Chapter 1 which set the premise for this dissertation, it can be inferred that alloy design is a key component to achieve high strength Mg alloys. Furthermore, to have any impact on the real world, it is necessary to decrease the alloying elements and hence cost of the alloy in comparison to WE43 which has 8-9 wt% of alloying elements including minor additions. This chapter therefore shifts the focus from experimentation to using theoretical approaches and CALPHAD based methodology to architect high strength low alloy Magnesium alloys. A thermo-physical-structure-kinetic approach is outlined for the selection of microalloying elements. Based on this approach, two alloys are designed and proposed for high strength: (i) Mg-3Nd-1.2Y-1.2Ce-0.5Ag-0.5Ca-0.4Zr, (ii) Mg-5Al-3.5Ca-1Mn-0.5Ag. The proposed strategies and approach are universal and can be applied for further design of Magnesium alloys for achieving high strength.

9.1 Introduction

Revisiting Chapter 1, strength was stated as a major bottleneck for Magnesium alloys driving the entire effort. For the convenience of the reader, Figure 9.1 is re-mentioned from Chapter 1 with an additional data-point of FSP and shows the current state of strength that is achievable in the existing Mg alloys by using various processing methods.

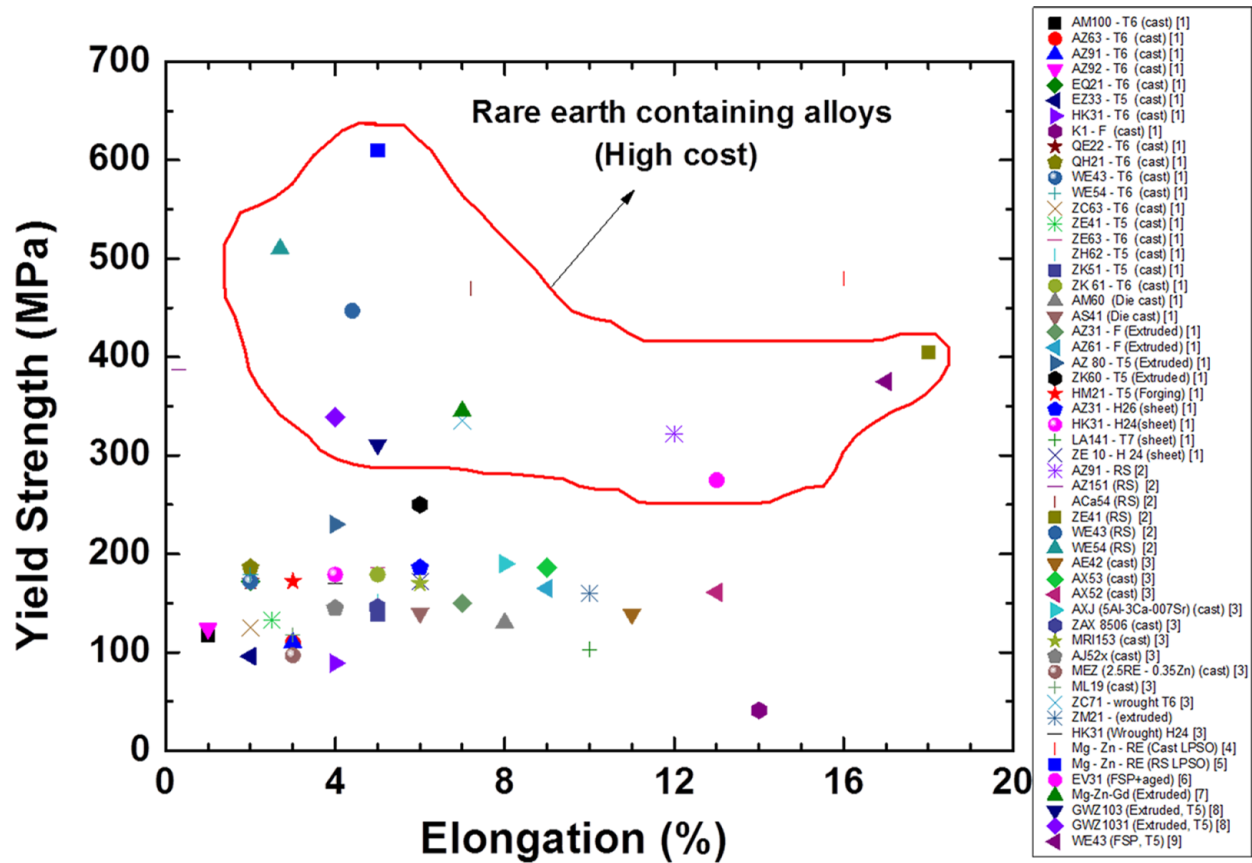


Figure 9.1. Comprehensive summary of strength in Magnesium alloys [1-9].

Two highlights emerge from this figure. First, high strength (300-650 MPa) magnesium alloys contain rare earth elements. In fact this was the reason for choosing WE43 alloy because the rare earth content stabilizes prismatic precipitates which in turn are favorable for blocking the basal slip and increasing strength. Second, the maximum yield strength that was achieved in WE43 using a wrought process (FSP/AM, refer Chapters 2 and 3) was 380 MPa. Till this point, the entire effort has been directed towards increasing the strength in this alloy by utilizing processing routes or the application of external fields. However, at this stage it is prudent to ask a question: What is the microstructural efficiency of WE43 alloy?

9.1.1 Microstructural Efficiency of WE43 Alloy

To calculate the microstructural efficiency, a theoretical microstructure was considered, where the strength was calculated by using the following additivity rule:

$$\sigma_{tot} = \sigma_{ss} + \sigma_{gb} + M(\Delta\tau_{dis}^2 + \Delta\tau_{ppt}^2)^{0.5} \quad (1)$$

where σ_{tot} is the total strength, σ_{ss} is the contribution from solid solution, σ_{gb} is the contribution from grain boundary, $\Delta\tau_{dis}$ is the contribution from dislocations and $\Delta\tau_{ppt}$ is the strengthening contribution from the precipitates. Among these, precipitate descriptors have the greatest influence in a WE43 alloy. The value for the Taylor factor (M) was taken as 4.5 based on the reports for random Mg polycrystals [10]. Using equation 1, the microstructural efficiency in WE43 alloy was calculated as 33% and is shown in Figure 9.2.

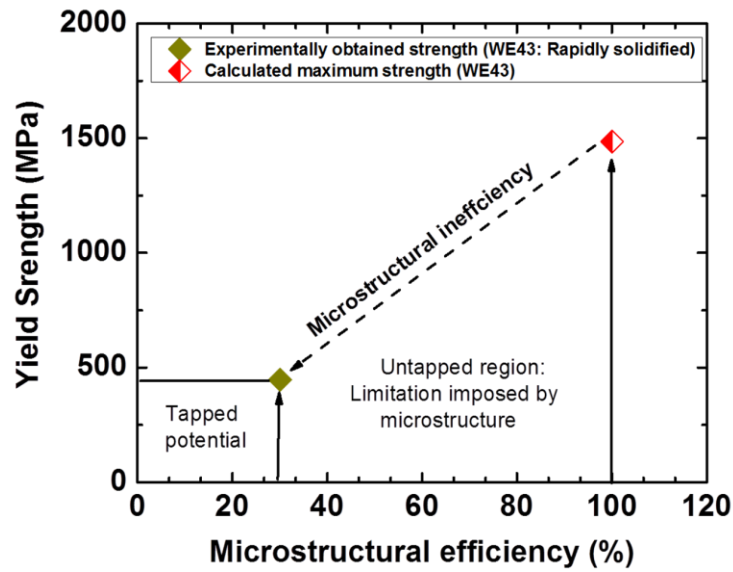


Figure 9.2 Calculated microstructural efficiency in a WE43 alloy.

For calculating the maximum possible strength, the theoretical microstructure was

assumed to be populated with the potent β_1 precipitate in the form of closed triangular networks and a plate aspect ratio of 100. Furthermore, the volume fraction of β_1 was calculated as 0.332 by considering that the entire Nd (3 wt%) precipitated out as β_1 precipitate and is a reasonable assumption due to its near zero solubility in Mg at the aging temperature. Using equation 2 [11], which is for the interaction of basal dislocations with prismatic precipitate plates, the strength contribution from β_1 precipitate was calculated as 1300 MPa.

$$\Delta\tau = \frac{Gb}{2\pi\sqrt{1-\nu}\left(0.825\sqrt{\frac{dt}{f}} - 0.393d - 0.886t\right) \times \ln\frac{0.886\sqrt{dt}}{b}} \quad (2)$$

where G : 17GPa, b :0.321 nm, f :0.332, d_t : 370 nm, t_t : 3.7 nm, ν : 0.27. Contributions from grain boundary, dislocations and solid solution were calculated as 101, 44 and 82 MPa, respectively resulting in yield strength of 1485 MPa for the theoretical microstructure.

Clearly, the alloying and microstructural efficiency is low for the alloy. Using the fundamental science and understanding gained through Chapters 1-7, a design driven research to establish a predictive methodology can be embraced. Therefore, the objectives of this chapter are to develop a theoretical approach and utilize Calphad based design to: (i) optimize WE43 alloy to achieve 500 MPa yield strength, and (ii) design a low-cost—rare-earth-free-alloy.

9.2 Background: Formation of β_1 Precipitate from α —Mg Solid solution and the Concept of Microalloying

However, to develop a theoretical methodology for the design and optimization of WE43 alloy, it is important to understand the formation of the strengthening precipitate (β_1) in this alloy. Transformation of α -Mg to β_1 is achieved by a combination of shear on every second plane

and an accompanying shuffle between them. These concomitant mechanisms correspond to a magnitude of 0.018nm ($a/18 \langle 11\bar{2}0 \rangle$) and occur in opposite directions parallel to the habit plane. Furthermore, to complete the transformation of the parent HCP to a BCC sub-lattice contained within the FCC precipitate, a shuffle of 0.046nm ($a/12 \langle 10\bar{1}0 \rangle$) normal to the habit plane is necessitated ($\epsilon_{zz}=0.08$). Clearly, a shear of 0.22 in magnitude along $(10\bar{1}0) \langle 11\bar{2}0 \rangle$ (ϵ_{yz}) constitutes the most critical step in β_1 generation. Therefore, addition of elements that are effective in neutralizing the shear term in the Bain deformation matrix will assist in the nucleation of β_1 . Since shearing generates compressive and tensile regions, addition of larger solutes with higher vacancy binding appears promising. Figure 9.3 depicts the transformation from α -Mg to β_1 by sketching a schematic of the $(10\bar{1}0)$ plane. For further details regarding the precipitation of β_1 , the reader should refer Chapter 6.

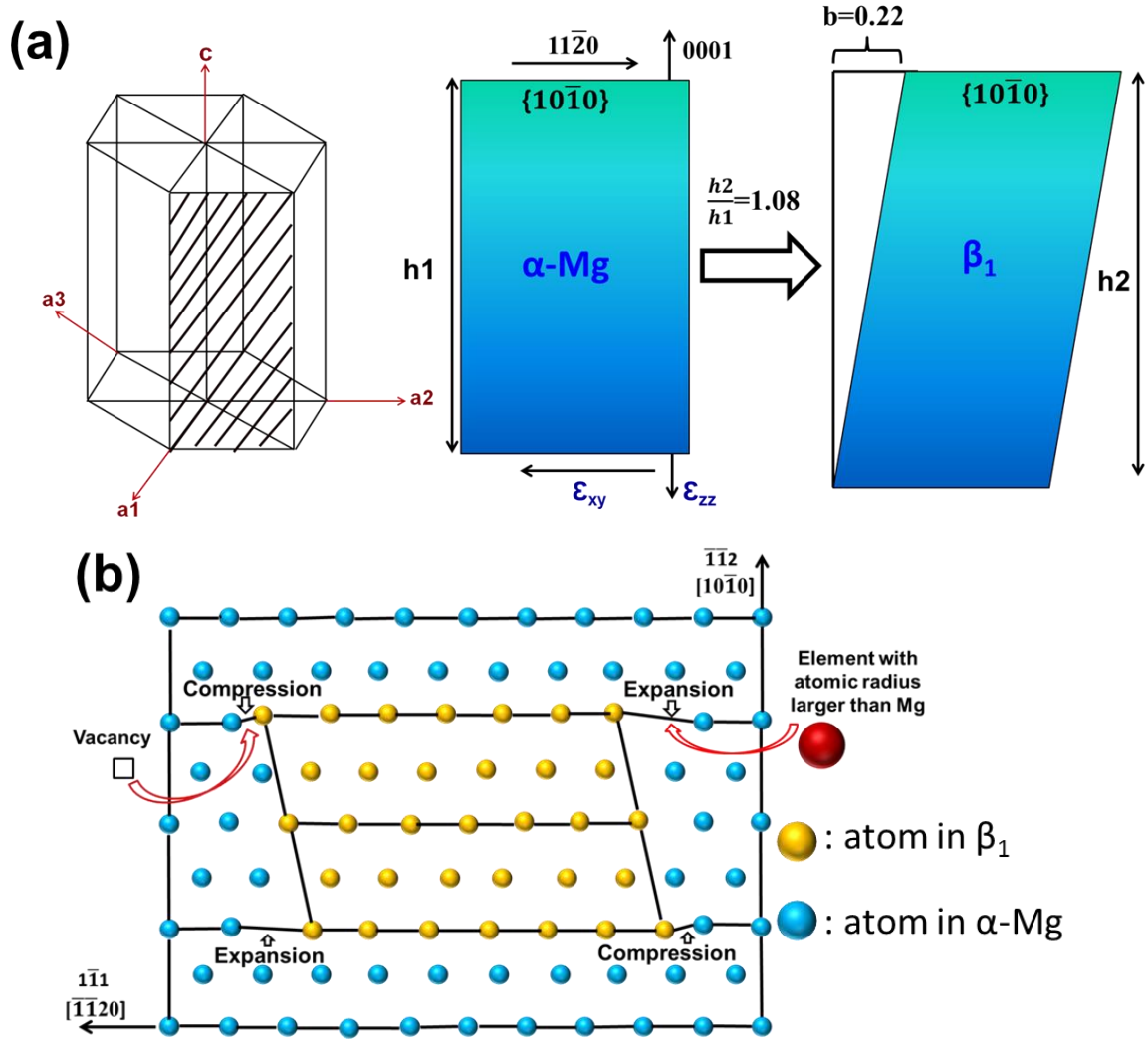


Figure 9.3 Schematic showing (a) transformation of α -Mg to β_1 in a WE43 alloy and, (b) relieving transformation strain by diffusion of a larger atom to the expansion and a vacancy to a compression region.

A traditional yet elegant method that has been adopted over the years to tailor the precipitate characteristics is “microalloying”. Whether an element will qualify as a potential microalloying addition depends on the interaction of the element with the major alloying elements and vacancies. A chapter by Nie [12] outlines the following mechanisms by which the microalloying

addition would aid in the nucleation of strengthening precipitate and affect the age hardening response:

- (i) Preferential interaction with vacancies, leading to reduced diffusion rates and nucleation rate of GP zones.
- (ii) Raising the GP zones solvus, altering the temperature ranges over which precipitate phases are stable.
- (iii) Stimulating nucleation of an existing precipitate by reducing the interfacial energy or elastic strain between precipitate and matrix.
- (iv) Promoting formation of a different precipitate phase by changing the free energy relationships in an alloy system.
- (v) Providing heterogeneous sites at which existing or new precipitates may nucleate. These sites include clusters of solute atoms.
- (vi) Increasing supersaturation so that the precipitation process is stimulated.

In fact, a majority of the microalloying elements are added to increase the number density of the strengthening precipitates leading to a reduction in inter-particle spacing and increased strength. Since, number density has the maximum effect on strength in comparison to other precipitate descriptors; further discussion will be limited to microalloying for the purposes of increasing the volume fraction of strengthening precipitates. In other words, trace additions that enhance the nucleation rate will be considered due to their positive influence on strength. The homogeneous nucleation rate (N) for the nucleation of the precipitate is expressed as [13]:

$$N = \omega N_o \exp\left(-\frac{\Delta G^*}{kT}\right) \exp\left(-\frac{\Delta G_m}{kT}\right) \quad (3)$$

where N is the homogeneous nucleation rate, ΔG^* is the activation energy barrier to nucleation, ΔG_m is the activation energy for atomic migration. Mathematically, ΔG^* takes the following form for a plate shaped precipitate [13]:

$$\Delta G^* = \frac{8\pi\gamma_e^2\gamma_b}{(\Delta G_v - \Delta G_s)^2} \quad (4)$$

where ΔG_v is the free energy change per unit volume, ΔG_s is the misfit strain energy per unit volume, γ_e and γ_b are the interfacial energy per unit area for the edge surface and the broad surface of the plate, respectively. From Equations 3 and 4, it is evident that the trace element addition should be capable to reduce the interfacial energy and strain energy of transformation to increase the nucleation rate and hence the number density of the strengthening precipitate. In the next section, using these fundamentals, a theoretical criterion is developed for the selection of microalloying elements to increase the number density of the strengthening precipitates.

9.3 Thermo-Physical-Structure-Kinetic Approach to Select Microalloying Elements for Design and Optimization of WE43 Alloy

Figure 9.4 shows a flowchart highlighting the theoretical criterion for the selection of microalloying elements.

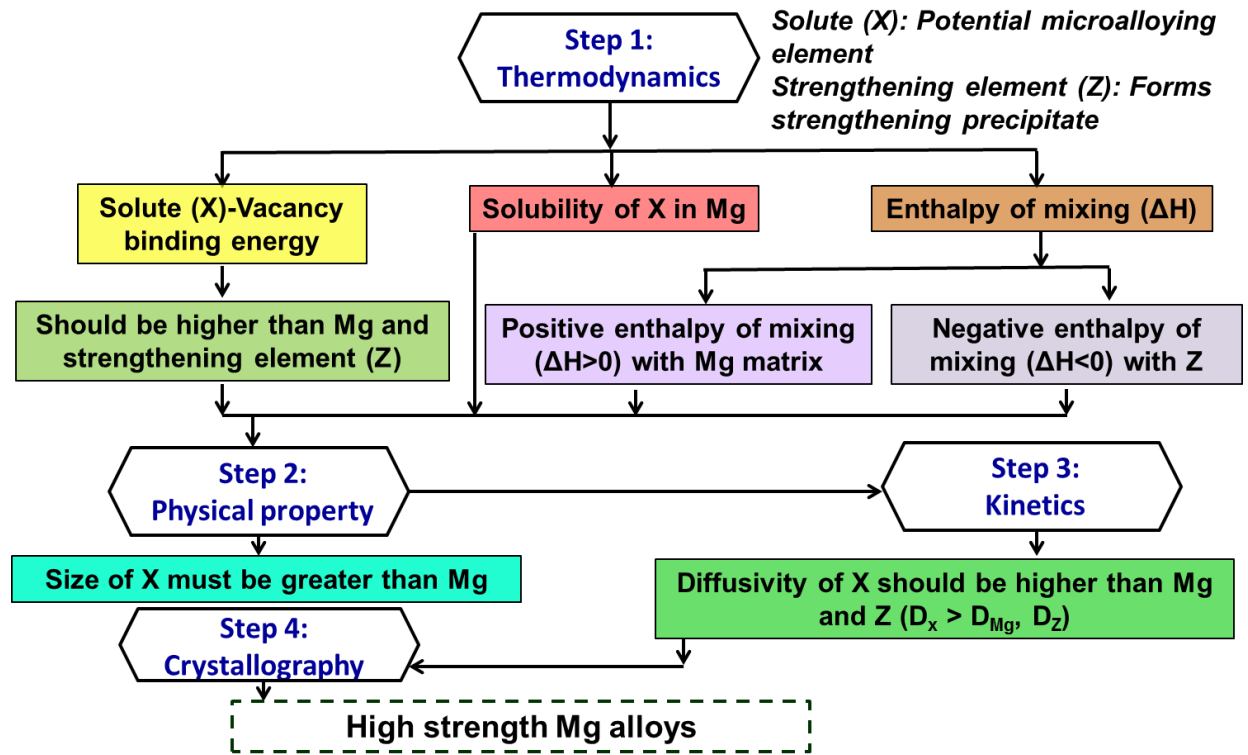


Figure 9.4 Design framework for architecting high strength Mg alloys.

On the basis of this figure, four factors were identified to play a key role in the selection of the microalloying element: (i) thermodynamic (X-□ binding energy, H of X and Z, □: vacancy), (ii) physical property (size of X), (iii) kinetics (diffusivity of X), and (iv) crystallography. Since, the entire effort is based on trace addition, it is important to know the solubility of the trace element (X) in α -Mg matrix. The first and the most important step in the selection of trace elements is that the thermodynamic condition should be satisfied. Figure 9.5 (a) shows the plot between the solute-vacancy binding energy and the solubility while Figure 9.5 (b) shows the plot for vacancy binding energy and the size of the trace element.

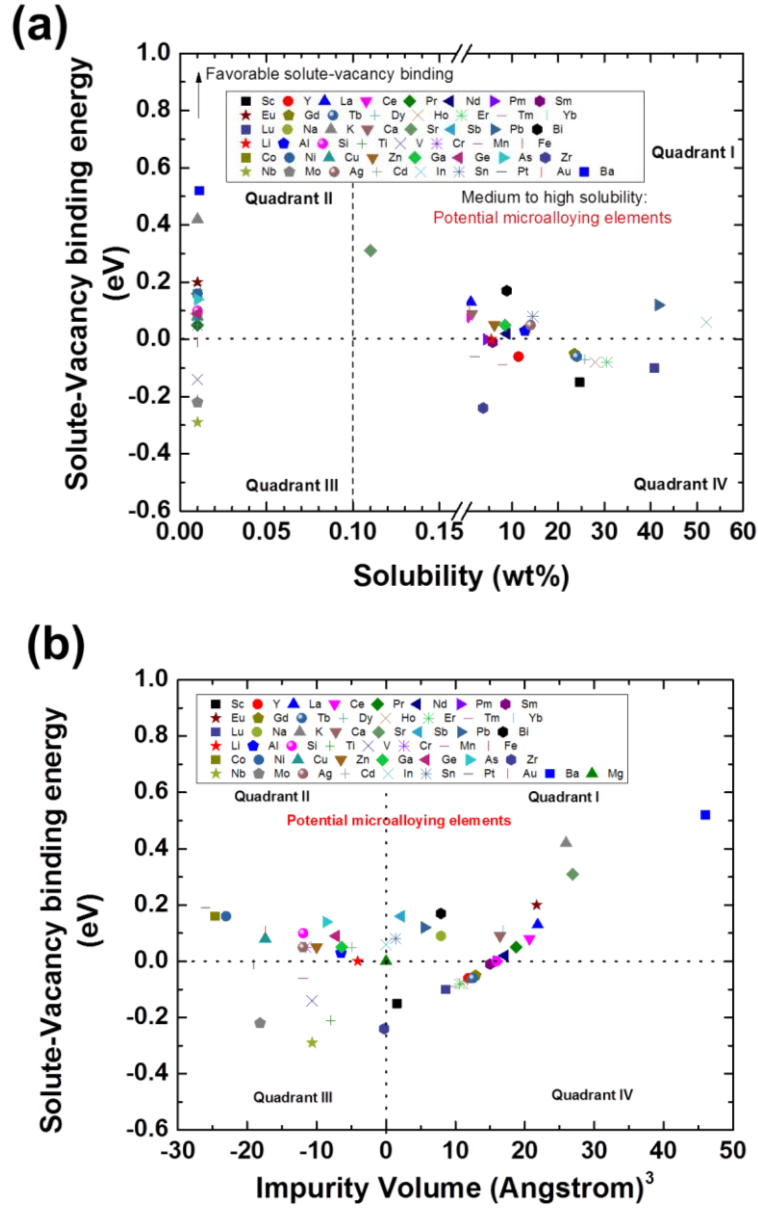


Figure 9.5 Potential microalloying elements based on (a) solute-vacancy binding energy—solubility, and (b) solute vacancy-binding energy—size plots for Mg. The data for plotting is taken from [14-18].

In this section, note that the terminologies “trace element – vacancy binding energy” and “solute-vacancy binding energy” are used interchangeably. The reason to do so is two-fold: (i)

the macroalloying elements (solutes) are plotted in addition to microalloying elements to draw a comparison and to have a baseline for selecting trace additions from the same plot, and (ii) the plots can be used for selecting the trace additions for alloys other than Mg-rare earth series. In such a scenario, the solutes cannot be fixed. The data plots for 49 elements have been generated in Figures 9.5 (a), and (b). This is quite comprehensive in nature. From Figure 9.5 (a) alone, 17 possible trace additions for design of Mg alloys are eliminated since 32 elements have a higher vacancy binding energy than Mg. Applying other boundary conditions from the theoretical design framework shown in Figure 9.4, trace elements are screened and outlined in Table 9.1.

Table 9.1. Theoretical screening of potential microalloying elements for the design of high strength Mg alloys.

| Criteria I: Thermodynamic | | Criteria II: Physical | Potential microalloying additions |
|--|---|--|---|
| Elements with vacancy binding higher than Mg | Elements having high vacancy binding and $\Delta H > 0$ with Mg | Elements with high vacancy binding and size larger than Mg | Elements satisfying criteria I and II |
| Medium to high solid solubility | La, Ce, Nd, Pm, Ca, Sr, Pb, Bi, Li, Al, Zn, Ga, Ag, In, Sn, Au | La, Ce, Ca, Sr | La, Ce, Nd, Pm, Ca, Sr, Pb, Bi, In, Sn |
| Restricted solid solubility | Pr, Eu, Yb, Na, K, Sb, Si, Cr, Co, Ni, Cu, Ge, As, Cd, Pt, Ba | Eu, Yb, Na, K, Cr, Co, Ni, Cu | La, Ce, Ca, Sr (Ag, In, Sn, Au can also be potential additions: Lack of enthalpy of mixing data) |
| | | Pr, Eu, Yb, Na, K, Sb, Ba | Eu, Yb, Na, K (Ba will also be a potential microalloying addition: Lack of enthalpy of mixing data) |

Though, the physical dimension of the trace element is important, it is not a necessary and requisite condition for the selection of microalloying elements. From a total of 49 elements, 13 elements are screened as potential additions as shown in Table 9.1. Applying crystallographic bounds for a match with the lattice of β_1 precipitate and cost considerations, 8 elements are identified for computational design. These are: Ce, Ca, Sr, Ag, Sn, Na, K and Ba. Furthermore, a ranking is established based on the theoretical criterion and is shown in Table 9.2.

Table 9.2. Ranking the microalloying additions on the basis of crystallographic and thermodynamic criterion for the nucleation of β_1 precipitate a Mg-rare earth alloy.

| Crystallographic criterion: Ranking by structural driving force (in descending order) | Thermodynamic criterion: Ranking by solute-vacancy binding (in descending order) | Overall ranking |
|--|---|---|
| Sr Yb Ca Ag Au La Ce K Ba Na Eu Sn, In | Ba K Sr Eu La Yb,Au Ca,Na Ce,Sn In Ag | Sr Yb Ca Au Ag K Ba La Ce Eu Sn, In |

Such a ranking mechanism is simple yet effective to identify the microalloying additions for a designated alloy system. In fact, this method can be extended beyond Mg alloys and can be used with effectiveness for other material systems with a plate shaped strengthening precipitate

and where vacancies play a major role. Furthermore, the validity of these theoretical predictions is shown in Table 9.3, where the predicted trace elements are in good agreement with the experimental observations.

Table 9.3. Theoretically predicted vs. experimentally observed effect of trace elements in a few Mg alloys. Note that the effect of predicted elements is in good agreement with experiments [19,20,21].

| Alloy | Trace element | Effect on strength | Effect on microstructure | Nucleating Mechanism |
|---|---------------------------------------|------------------------------|---|---|
| Mg-Al-Zn | Pb, Ag, Ca, Ba, Li, B, Ti, Sr, Mo, Si | No effect | — | — |
| Mg-Zn-Z Where Z is macroalloying element (X: Co, Cu, Ba) | Ca, Ag | Increase in overall hardness | Increases the number density of β_1' and β_2' | Cosegregation of Ca and Zn as precipitate clusters. Role of Ag is unclear |
| | Sn, In | Little effect | — | — |
| Mg-Zn -Al | Ca, Ag | Increase in hardness | Increases number density of ϕ | Cosegregation of Ca and Zn as precipitate clusters. Role of Ag is unclear |
| Mg-Sn-Zn | Cu, Na, Ag, Ca | Increase in hardness | Increases the number density of β | Precipitate clustering |

Though, theoretical principles are effective in narrowing the options, further computational approach is needed to determine the exact alloy composition. For this reason, a Calphad based approach was used and is detailed in further sections.

9.4 Computational Design to Achieve High Strength Mg Alloys

9.4.1 Basic Principle of Calphad based Approach

In this section, the focus is on the fundamental science behind the Calphad approach. Equations 5 through 9 provide the mathematical basis for the Calphad method where the free energy of a phase is computed as a function of composition and temperature. For a system with n components, the Gibbs free energy (G), can be written as:

$$G^n = \sum_{i=1}^n x_i G_i^\circ + RT \sum_{i=1}^n x_i \ln x_i + \sum_{\substack{i,j=1 \\ i < j}}^n G_{ij}^{ex} + \sum_{\substack{i,j,k=1 \\ i < j < k}}^n G_{ijk}^{ex} \quad (5)$$

where the first term $x_i G_i^\circ$ corresponds to the contribution from pure components, the second term $RT \sum_{i=1}^n x_i \ln x_i$ is the configurational entropy term and $\sum_{\substack{i,j=1 \\ i < j}}^n G_{ij}^{ex} + \sum_{\substack{i,j,k=1 \\ i < j < k}}^n G_{ijk}^{ex}$ are the excess

free energy terms. Note that the excess free energy is zero for ideal solutions. For binary and ternary non ideal solutions, Equation 5 can be written as:

$$G^{binary} = \sum_{i=1}^2 x_i G_i^\circ + RT \sum_{i=1}^2 x_i \ln x_i + x_1 x_2 L_{12} \quad (6)$$

$$G^{ternary} = \sum_{i=1}^3 x_i G_i^\circ + RT \sum_{i=1}^3 x_i \ln x_i + x_1 x_2 L_{12} + x_1 x_3 L_{13} + x_2 x_3 L_{23} + x_1 x_2 x_3 L_{123} \quad (7)$$

In these equations, L_{ij} , and L_{ijk} are the interaction parameters accounting for the communication between the elements and are computed using quantum based calculations or determined experimentally. For the case of quaternary or higher order systems which will be dealt while design and optimization of high strength Mg alloys in the subsequent sections, interactions between four or more elements will be neglected. This approximation is valid because of the negligible effect of such an interaction on the computation and is supported from Equations 8 and 9:

$$G_{ijkl}^{ex} = x_i x_j x_k x_l L_{ijkl} \quad (8)$$

$$x_i x_j x_k x_l \leq \frac{1}{4} \frac{1}{4} \frac{1}{4} \frac{1}{4} = 0.00391, G_{ijkl}^{ex} \rightarrow 0 \quad (9)$$

From equations 5-9, it is evident that well-grounded thermodynamic databases are required for accuracy in the computation. For this effort, ThermoCalc software with Mg database was used for designing the alloy.

9.4.2 Computed Mg-Rare Earth Alloy Space based on Strength and Cost Considerations

Two factors were considered while designing the alloy: (i) yield strength, and (ii) cost. First, a target property was set driving the effort towards strength limiting design. To calculate the extent of precipitation strengthening needed to achieve yield strength of 500 MPa, empirical strengthening models (Equations 1 and 2) were used. Based on these models, the precipitate contribution needed to achieve 500 MPa yield strength was calculated as 300 MPa. Note that the grain boundary (grain size: 3 μ m), solid solution, and dislocations combined together contribute 200 MPa. Considering that precipitates should contribute 300 MPa, the volume fraction of the strengthening precipitate required to achieve this value was calculated as 0.1218 based on Equation 2. For this calculation, the plate aspect ratio was inserted as 20 with the plate diameter (d) as 40 nm and plate thickness (t) as 2 nm. These values are based on experimental observations of the size of strengthening precipitates in a WE43 alloy.

Figure 9.6 shows the optimized alloy space based on strength and cost considerations. Here, the cost of the alloy was calculated using the cost of pure elements. From Figure 9.6, it can

be observed that the commercially available WE43 alloy has a higher cost (\$160/lb) and lower yield strength of 200 MPa. In comparison, alloys with Nd:Y ratio greater than 2 have an yield strength approaching 500 MPa at a reduced cost.

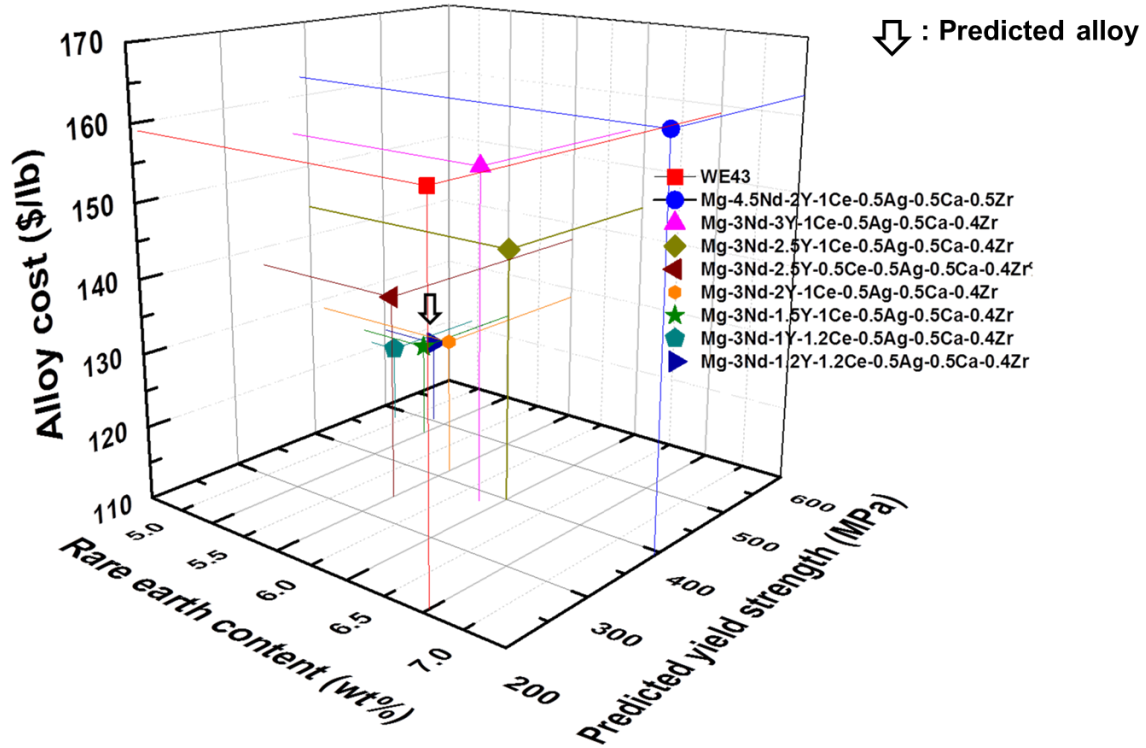


Figure 9.6 Calphad based optimized alloy space for an Mg-Y-Nd system. Note that a reduction in Y and Nd content with Nd:Y ratio greater than 2 results in higher yield strength and reduced cost.

Using the Calphad approach, in contrast to the existing Mg-4Y-3Nd (WE) system that is rich in Y, an Mg-3Nd-1.2Y-1.2Ce-0.5Ag-0.5Ca-0.4Zr (EW) alloy is proposed with Nd as the primary alloying element. The major highlight is that the cost of the proposed alloy is less by \$50/lb in comparison to the commercially available WE43 alloy and achieves higher strength.

Figure 9.7 shows the mass fraction of the phases computed using ThermoCalc for WE43 and the predicted alloy. The new alloy was optimized to avoid the undesirable Mg_{24}Y_5 and $\text{Mg}_{41}\text{Nd}_5$ intermetallics which decrease the alloying efficiency while increasing the mass fraction of the strengthening Mg_{12}R precipitate. Table 9.4 summarizes these values.

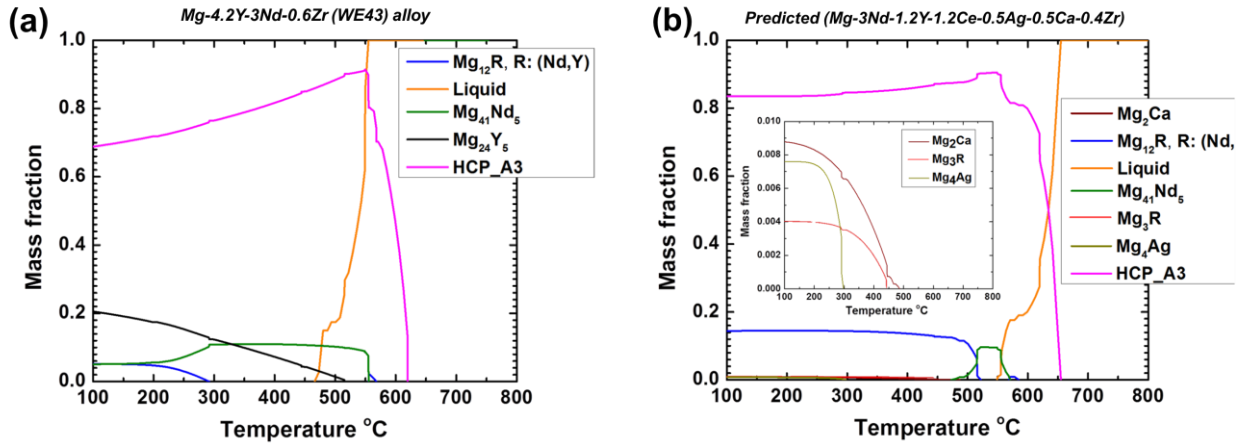


Figure 9.7 Computed mass fraction of metastable and stable phases in the commercially available WE43 and predicted EW alloy.

Table 9.4. Summary of the computed mass fractions of different phases for WE43 and predicted alloy from Figure 9.7.

| Phases | Mg_{12}R | Mg_3R | Mg_{24}Y_5 | $\text{Mg}_{41}\text{Nd}_5$ | Mg_4Ag | Mg_2Ca |
|-----------------|--------------------------|-----------------------|----------------------------|-----------------------------|------------------------|------------------------|
| WE 43 alloy | 0.049 | — | 0.186 | 0.049 | — | — |
| Predicted alloy | 0.144 | 0.004 | — | — | 0.007 | 0.0084 |

Based on Figure 9.7 and Table 9.4, it is clear that the presence of Mg_2Ca and Mg_4Ag will serve as nucleating sites for the precipitation of strengthening phases in the predicted alloy. Furthermore, the absence of undesirable intermetallics will lead to increased alloying efficiency in the predicted EW alloy. However, for nucleation rate to be higher, the driving force for the precipitation of the strengthening Mg_{12}R phase should be higher in the predicted alloy. Figure

9.8 compares the driving force for precipitation of $Mg_{12}R$, Mg_3R and $Mg_{24}Y_5$ phases between WE43 and the predicted alloy.

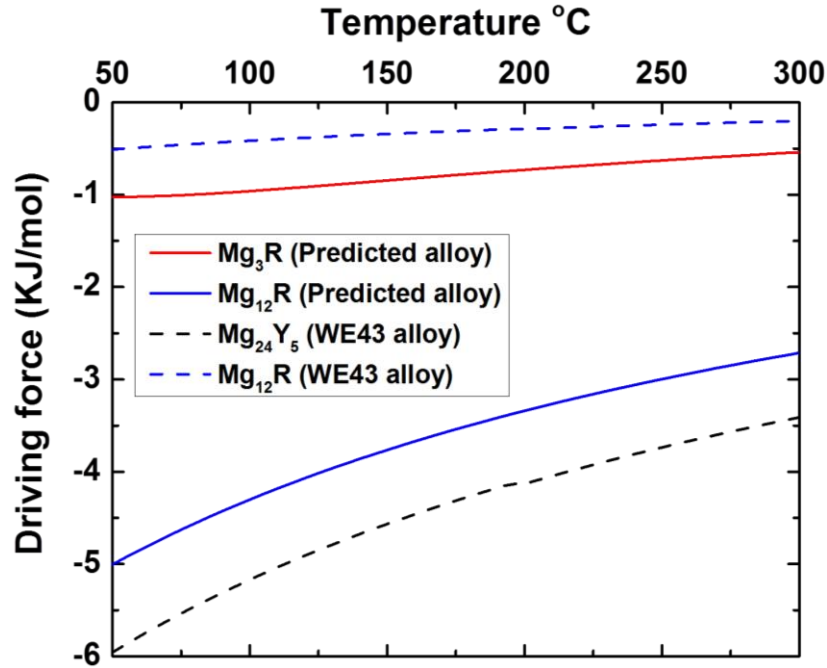


Figure 9.8 A comparison on the computed driving force for precipitation of $Mg_{12}R$ and other relevant phases in WE43 and the predicted alloy at the aging temperature ($180^{\circ}C$). Note that the driving force to precipitate $Mg_{12}R$ is an order of magnitude higher in the predicted alloy when compared to WE43.

Two points can be stated from Figure 9.8: (i) driving force to nucleate strengthening $Mg_{12}R$ type precipitate is higher in the predicted alloy (-3.49 kJ/mol at $180^{\circ}C$) than WE43 (-0.304 kJ/mole at $180^{\circ}C$, and (ii) driving force to precipitate the undesirable intermetallic is zero in the predicted alloy in comparison to the higher value in WE43. These observations indicate that the predicted alloy has a higher driving force to precipitate the strengthening phase and also has a higher volume fraction leading to high strength. Though, the cost is reduced in comparison

to WE43, for Mg-based alloys to make an impact, rare earth free alloys need to be designed.

9.4.3 Design of a Cheaper Mg-Al-Ca Alloy for High Strength

Figure 9.9 shows the optimization of the Mg-Al-Ca system with a few iteration routines shown. Again, a strength limiting design was used and the alloys were designed to maximize the volume fraction of spherical Al_2Ca precipitates to achieve strength above 400 MPa.

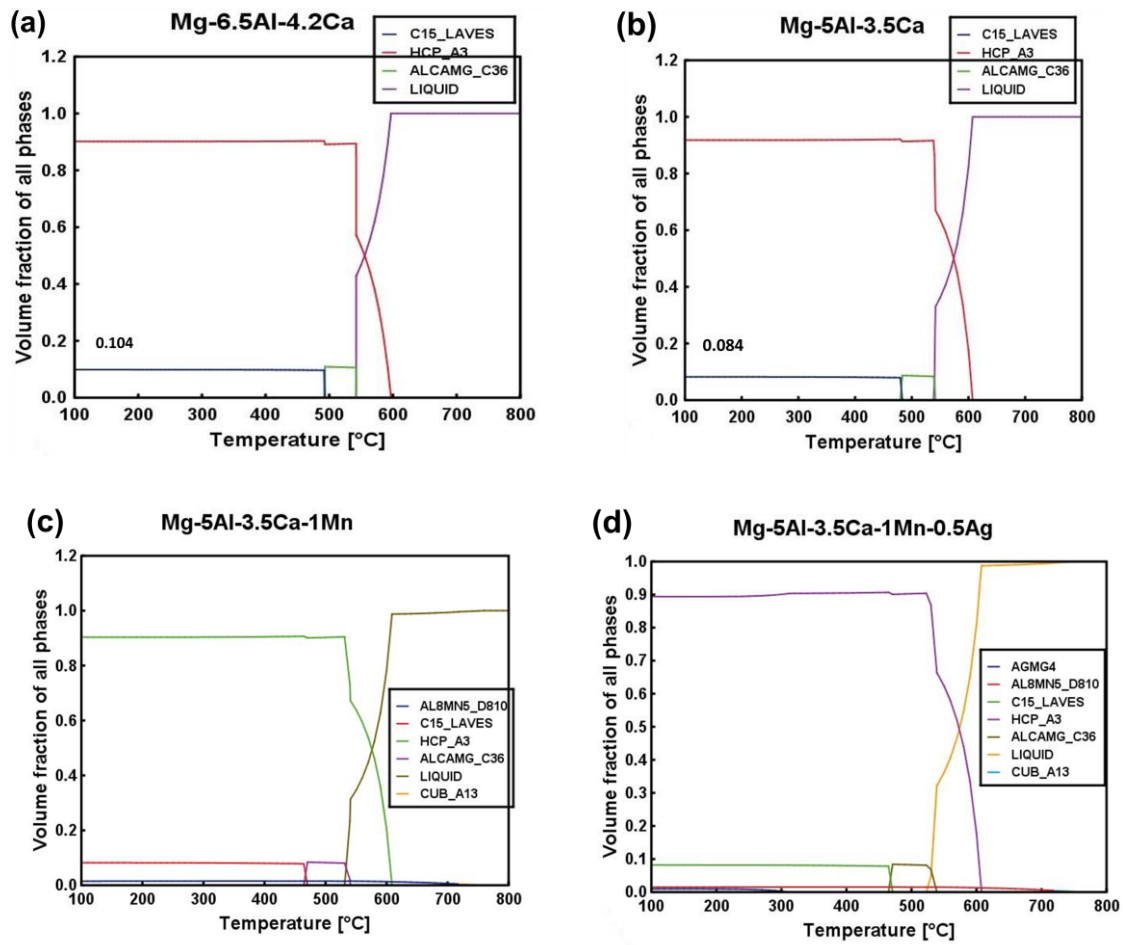


Figure 9.9 Design optimization of Mg-Al-Ca alloy system to achieve strength greater than 400 MPa.

Trace additions of Mn and Ag were made to increase the volume fraction of Al_2Ca and

form pre-precipitate clusters of Mg_4Ag . Ag was chosen due to its favorable interaction with Ca and beneficial effect on strength as shown in Table 9.3. The predicted alloy $\text{Mg-5Al-3.5Ca-1Mn-0.5Ag}$ has the highest volume fraction of Al_2Ca and the calculated strength for this alloy is 450 MPa. In comparison to the high cost associated with the Mg-rare earth alloys, the predicted rare earth free alloy costs \$25/lb and is $1/5^{\text{th}}$ the cost of the predicted Mg-rare earth alloy.

9.5 Conclusions

This chapter details a fundamental framework for the selection of microalloying elements to develop high strength Magnesium alloys. The theoretical approach outlined in this work is based on the fundamentals of phase transformation coupled with the observations in the literature. Furthermore, the alloy compositions are predicted based on the Calphad approach. There are four major take away points from this work:

- (i) Applying the thermo-physical-structure-kinetic approach, an order of preference is computed based on the potency of the microalloying addition to nucleate strengthening precipitates. According to this ranking; Ag, Ca, Ce are proposed as preferable micro alloying additions for Mg-rare earth alloys and are narrowed down from a total of 49 elements.
- (ii) Utilizing a Calphad based approach, WE43 alloy was optimized to achieve a strength of 500 MPa at a reduced cost. Based on the computational optimization, the predicted alloy ($\text{Mg-3Nd-1.2Y-1.2Ce-0.5Ag-0.5Ca-0.4Zr}$) had a leaner composition in comparison to WE43 with a cost saving of $\sim \$50/\text{lb}$.
- (iii) The predicted Mg-rare earth alloy has a Nd:Y ratio greater than 2 and is an EW type alloy rather than WE type. For the predicted composition, Mg_{24}Y_5 and $\text{Mg}_{41}\text{Nd}_5$

intermetallics are absent increasing the alloying efficiency. Furthermore, the driving force to precipitate the strengthening Mg_{12}R precipitate was an order of magnitude higher than the commercially available WE43 alloy.

- (iv) A low cost (\$25/lb) rare earth free Mg-5Al-3.5Ca-1Mn-0.5Ag alloy is predicted to achieve ~450 MPa strength.

In cases, where the microalloying additions have been experimentally tried, the theoretical predictions are in good agreement with the observed results. The theoretical approach outlined in this chapter is universal and can be applied to choose elements for designing any Mg based alloy with plate shaped strengthening precipitates.

9.6 References

1. ASM Handbook on Mg alloys (Desk edition)
2. C. Sanchez, G. Nussbaum, P. Azavant, H. Octor, Mater. Sci. Eng A 221 (1996)
3. Z. Yang, J. P. Li, J.X. Zhang, G.W. Lorimer, J. Robson, Acta Metall.Sin. 21 (2008) 313-328
4. T. Honma, N. Kunito, S. Kamado, Scripta Mater. 61 (2009) 644 –
5. Y. Kawamura, K. Hayashi, A. Innoue, T. Masumoto, Mater. Trans. 42 (2001) 1172 –
6. T.A Freeney, R.S. Mishra, Metall and Materials Trans. A 41 (2010) 73-84
7. M. Yamasaki, T. Annan, S. Yoshimoto, Y. Kawamura, Scripta Mater. 53 (2005) 799-803
8. X. B. Liu, R.S. Chen, E.H. Han, Journal of Alloys and Compounds 465 (2008) 232-238
9. S. Palanivel, N. Phalgun, B. Glass, R.S. Mishra, Materials & design 65 (2015) 934-952
10. C.H. Caceres, P. Lukac, Philos. Mag. 88 (2008) 977–989
11. J.F. Nie, Scripta Mater. 48 (2003) 1009–1015.

12. J. F. Nie, Ch: 20 Physical metallurgy of light alloys, 2009-2147, Physical Metallurgy Volume III, Fifth Edition (2014), Edited by: David E. Laughlin and Kazuhiro Hono.
13. David A. Porter, Kenneth E. Easterling, Mohamed Y. Sherif, Phase transformations in metals and alloys, Third edition (2008).
14. D. Shin, C. Wolverton, Acta Mat. 58 (2010) 531-540
15. J.E. Sall, C. Wolverton, Acta Mat. 60 (2012) 5151-5159
16. ASM handbook, vol. 2, 10 th ed. (ASM International, 1990)
17. A.A. Nayed-Hashemi, J.B. Clarke, Bulletin of Alloy phase diagrams 5 (1984) 348-358
18. L.L. Rokhlin, Magnesium alloys containing Rare earth Metals, Edited by: J.N. Fridlyander and D.G. Eskin, (2003) 18-63
19. C.J. Bettles, P. Humble, J.F. Nie, 1997. In: Lorimer, G.W. (Ed.), Proceedings 3rd International Magnesium Conference. The Institute of Materials, London, 403–417.
20. S.C. Park, J.D. Lim, D. Eliezer, K.S. Shin, Mater. Sci. Forum 419–422 (2004) 159–164.
21. K. Oh – Ishi, R. Watanabe, C.L. Mendis, K. Hono, Mat. Sci. Eng. A 526 (2009) 177-184

CHAPTER 10

CONCLUDING REMARKS AND FUTURE DIRECTIONS

10.1 Concluding Remarks

Microstructural design has been attempted to achieve high strength in an Mg-Y-Nd alloy using thermomechanical processing, additive manufacturing and application of external fields. Furthermore, computational optimization to design low cost Mg alloys for high strength has been done by combining theoretical and Calphad-based approaches. Major highlights from this effort are presented under the following three heads: (i) thermomechanical processing and additive manufacturing, (ii) external field effects, and (iii) alloy design.

10.1.1 Thermomechanical Processing and Additive Manufacturing

Hot rolling and friction stir processing was performed to investigate the strength values in a WE43 alloy. The microstructure was tailored using friction stir processing to achieve high strength and the role of specific variables like tool dimensions, processing parameters and the effect of starting microstructure was studied. Furthermore, defect structures and defect-mediated precipitation was studied. On the basis of these investigations, a defect engineering route is proposed to enhance strength in Mg-rare earth alloys. In addition, this dissertation also presents a framework for the dissolution of precipitates which is of value to the friction stir welding community and extends beyond the examined alloy system. The highlights from this section are:

- (i) Issues pertaining to the rolled microstructures were identified. Inhomogeneous microstructures with large intermetallics of Mg_2Y and $\text{Mg}_{41}\text{Nd}_5$ were observed in the rolled condition. A simple calculation showed the alloying efficiency of Y in WE43

- as 76%. This limits the maximum yield strength that can be achieved in an highly rolled (80% reduction) alloy to 310 MPa.
- (ii) Rate of loading had a significant effect on ductility in a rolled microstructure characterized by the grain boundary precipitate free zone due to the composite response to deformation.
 - (iii) The incoming microstructure has a major role on the microstructural evolution during FSW. A highly worked alloy ends up with a higher strength after friction stir welding. The maximum yield strength achieved was 380 MPa after post aging of the friction stir welded alloy.
 - (iv) Based on the promise for obtaining high strength by controlling the microstructure in a WE43 alloy, friction stir additive manufacturing method is shown as an effective route to fabricate high performance magnesium alloy components (WE43) with a higher strength (400 MPa) and considerable ductility (17%). Such superior strength, similar to Al 2XXX alloys, results from extremely fine, uniform and densely populated coherent precipitates in the size range of 2-7 nm. Moreover, alloying efficiency is increased in the non-interfacial locations by the dissolution of undesirable Mg_2Y intermetallics. Work based on FSAM has led to the first publication in this field and has potential to address the issue of structural performance.
 - (v) The origin of high uniform elongation of 16% in FSAM specimen results from stage II type linear hardening behavior. This arises due to a low ratio of the Schmid factors between the “a” type non-basal and basal dislocations and hence reduces the anisotropy effect.

- (vi) For the first time, physics-based framework for the dissolution and fragmentation of particles during FSW, FSP and FSAM is proposed. In addition to advancing the understanding within the field, the proposed framework has utility to tailor microstructures by careful control of the process parameters.
- (vii) Effective diffusivity of Y in Mg matrix was calculated as 60 times faster during FSW/P than in the absence of concurrent deformation. Higher value of effective diffusivity is proposed to arise from (i) stress driven anisotropic transport of solute atoms by gliding dislocations and sweeping grain boundaries combined with (ii) pipe and boundary diffusion of solute atoms along the dislocation core and grain interfaces during FSW/P.
- (viii) Dislocation sweeping is quantified based on the strain and strain rate computed by the numerical model, and mobile and immobile dislocation density calculated from the Kubin-Estrin model. The mechanism of dislocation sweeping is proposed to occur in three steps: (i) thermally activated diffusion of solute atom into dislocation core, (ii) transportation of solute atom along the core by pipe diffusion, and (iii) detachment of dislocation from the particle with the solute at a rate equal to the dislocation velocity. This mechanism is supported by the experimentally observed departure side pinning of the dislocation at a particle.
- (ix) The role of prior dislocations on the evolution of precipitate descriptors during aging is critical. Since, formability of magnesium is limited at room temperature, a high temperature thermomechanical process is used. In this dissertation, the high temperature dislocation structure resulting from FSP was studied for the first time in an Mg alloy. Post mortem analysis after friction stir processing showed activity of

- basal $\langle a \rangle$, and non-basal $\langle a \rangle$, $\langle c+a \rangle$, and $\langle c \rangle$ components. These non-basal $\langle c \rangle$ and $\langle c+a \rangle$ dislocations aided the formation of I_1 stacking faults.
- (x) Evidence for nucleation of pyramidal $\langle c+a \rangle$ dislocation from I_1 fault is presented. Also, I_2 stacking faults were observed in the regions concentrated with I_1 stacking faults and non-basal dislocations.
 - (xi) A source mechanism for $\langle c+a \rangle$ nucleation is invoked on the basis of the observed dislocation substructure. This resulted from a high activity of $\langle c \rangle$ and $\langle a \rangle$ dislocations, with the final microstructure being representative of all four (basal $\langle a \rangle$, and non-basal ($\langle a \rangle$, $\langle c+a \rangle$, $\langle c \rangle$) segments.
 - (xii) Dislocation-mediated precipitation was studied with an emphasis on the type and role of defects nucleating β_1 precipitates in a WE43 alloy. Hexagonal honeycomb $\langle a \rangle$ type screw dislocation network guided β_1 assembly was documented. Furthermore, well-defined directional array of β_1 precipitates also formed due to the heterogeneous nucleation on prior existing line defects.
 - (xiii) I_1 stacking fault promoted the nucleation of β_1 precipitate. Zonal nature and the composite Frank-Shockley partials bounding the fault provide strain accommodation normal and parallel to the $(10\bar{1}0)$ habit plane

10.1.2 Effect of External Field on the Precipitation Hardening of a WE43 Alloy

Based on the information obtained from the first section, in this section the objective was to study the effect of sound waves on the age hardening response in Mg-4Y-3Nd alloy. A major highlight from this section is:

- (xiv) Ultrasonic—assisted aging increased the age hardening response by a factor of 24 in comparison to the conventionally aged specimen and was due to the accelerated kinetics of precipitate nucleation and growth.

10.1.3 Theoretical and Computational Design of High Strength Magnesium Alloys

In this section, guided by theoretical principles, Calphad—based approach was utilized to design high strength-low cost Magnesium alloys. Two tracks were adopted in this section. First, the WE43 alloy was optimized to achieve the above objectives. Second, a rare earth free alloy was designed to reduce the cost. Major highlights from this section are:

- (xv) WE43 alloy was optimized to achieve strength of 500 MPa. Based on the computational optimization, Nd—rich alloy was proposed with the following composition: Mg-3Nd-1.2Y-1.2Ce-0.5Ag-0.5Ca-0.4Zr. In comparison to the commercially available WE43, the predicted alloy imparts a cost saving of ~ \$50/lb.
- (xvi) Using strength limiting design, a low cost (\$25/lb) rare earth free Mg-5Al-3.5Ca-1Mn-0.5Ag alloy is predicted to achieve ~450 MPa strength.

10.2 Future Directions

This dissertation presents results in the field of thermomechanical processing which includes hot rolling and friction stir processing of WE43 alloy, friction stir additive manufacturing of WE 43, field effects and computational alloy design to achieve high strength Mg alloys. Further research on the following would advance the understanding to some of the questions that remain unsolved in this dissertation.

- (i) A composite microstructure with the presence of precipitate free zones was shown to be extremely sensitive to the rate of loading. Furthermore, high ductility was recorded for this specimen. At this stage, the deformation mechanisms that lead to this behavior is unknown. The present hypothesis is that $\langle c+a \rangle$ dislocations will be nucleated within the sandwiched region by virtue of incompatibility stresses on either sides of the precipitate free zone. This hypothesis needs to be checked for correctness.
- (ii) In this dissertation, only dislocation sweeping of atoms is considered to quantify the dissolution of thermally stable particles. Further improvement to this model by accounting for grain boundary assisted transportation will be of value. Furthermore, a detailed study to identify the conditions for particle fragmentation vs. dissolution is needed.
- (iii) Friction stir additive manufacturing is introduced as a technique to achieve high performing magnesium builds. In this study, though the build is characterized in great detail relating the properties to microstructure, the effect of anisotropy is not paid attention. Since, Mg is highly anisotropic, a study on this aspect will be critical. Furthermore, FSAM can be used to explore other alloy systems that exhibit excellent properties when friction stir processed. This direction is open to further studies.
- (iv) Post mortem analysis after friction stir processing revealed the role of defects in nucleating strengthening precipitates in WE43. Further in-situ studies and modeling will aid the field of defect engineering to achieve high strength in Magnesium-rare earth alloys.

- (v) An interesting observation is the enhanced age hardening response of the ultrasonically aged specimen in comparison to conventional aging. Though, the observations are correlated to the microstructure, a sound understanding of the field effects on the microstructure is lacking. This dissertation presents a conceptual hypothesis for the accelerated aging response in terms of thermodynamics and kinetics. Further efforts are required to establish the fundamentals of field assisted aging by understanding the interaction of sound waves with the nucleating precipitates.
- (vi) Theoretical and computational approaches have been used to design high strength Mg alloys. These alloys need to be validated experimentally. Using the proposed approach, additional alloys need to be designed to accelerate the insertion of Mg alloys into applications.

LIST OF RELATED PUBLICATIONS

1. S. Palanivel, N. Phalgun, B. Glass, R.S. Mishra, “Friction stir additive manufacturing for high structural performance through microstructural control in an Mg based WE43 alloy”, *Materials & Design* 65 (2015): 934-952
2. S. Palanivel, H. Sidhar, R.S. Mishra, “Friction stir additive manufacturing – Route to high structural performance”, *JOM* 67 (2015): 616-621
3. S. Palanivel, R.S. Mishra, B. Davis, R. Delorme, K.J. Doherty, K.C. Cho, “ Effect of initial microstructure on the microstructural evolution and joint efficiency of a WE43 alloy during friction stir welding”, *Friction Stir Welding and Processing VII*, TMS, San Antonio, TX, 2013